LEHRSTUHL FÜR BIOMEDIZINISCHE PHYSIK
TECHNISCHE UNIVERSITÄT MÜNCHEN

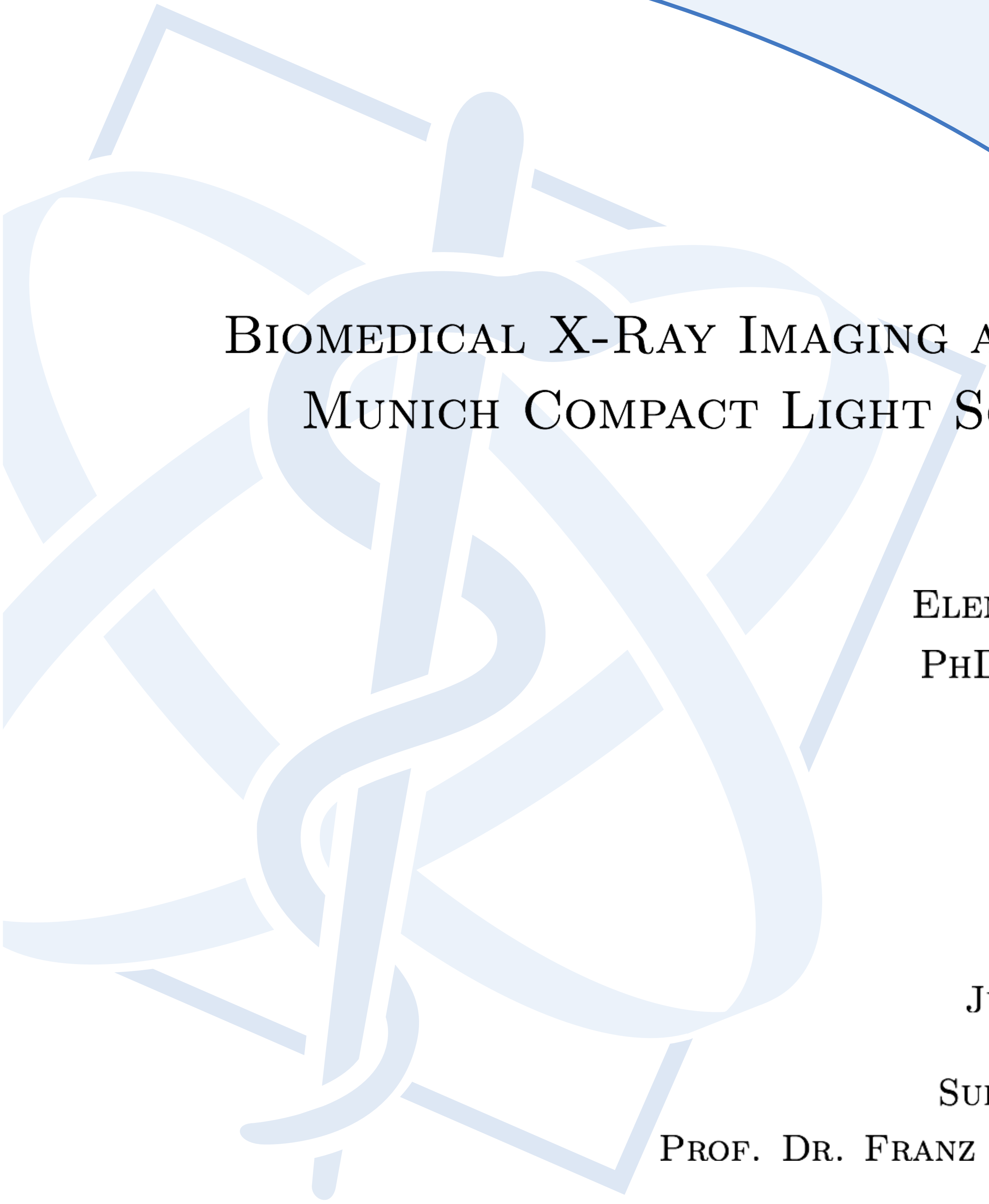

BIOMEDICAL X-RAY IMAGING AT THE MUNICH COMPACT LIGHT SOURCE

ELENA EGGL
PHD THESIS

JULY 2017

SUPERVISOR:
PROF. DR. FRANZ PFEIFFER

Technische Universität München

Technische Universität München
Physik-Department
Lehrstuhl für Biomedizinische Physik

Biomedical X-Ray Imaging at the Munich Compact Light Source

Elena Eggl

Vollständiger Abdruck der von der Fakultät für Physik der Technischen Universität München zur Erlangung des akademischen Grades eines

Doktors der Naturwissenschaften (Dr. rer. nat.)

genehmigten Dissertation.

Vorsitzender:	Univ.-Prof. Dr. Martin Zacharias
Prüfer der Dissertation:	1. Univ.-Prof. Dr. Franz Pfeiffer
	2. Univ.-Prof. Dr. Reinhard Kienberger

Die Dissertation wurde am 23.05.2017 bei der Technischen Universität München eingereicht und durch die Fakultät für Physik am 23.06.2017 angenommen.

Abstract

Between conventional x-ray tube sources and third-generation synchrotrons, a large gap in performance exists with respect to monochromaticity, brilliance and coherence of the x-ray beam, but they also differ greatly in costs and availability. Compact synchrotron sources have strongly been researched during the last decades and are expected to fill this gap in the near future. This thesis focuses on the first commercially installed compact synchrotron source based on inverse Compton scattering, the Munich Compact Light Source (MuCLS). We evaluate x-ray beam characteristics including flux and source size, also analyzing their stability over time. The unique properties of the MuCLS – quasi-monochromaticity, energy tunability, and high partial coherence – are exploited for a range of relevant biomedical imaging applications. Beneficial effects for grating-based small-animal imaging are investigated and pre-clinical studies on coronary angiography and mammography are conducted. Coronary angiography relies on the application of contrast agents to the coronary arteries for the diagnosis of coronary disease. We demonstrate that the mono-energetic x-ray beam provided by the MuCLS would allow for a significant dose reduction at equal contrast levels. Grating-based x-ray phase-contrast and dark-field imaging are known to provide increased soft-tissue contrast and small-angle scattering information. We investigate the potential of this technique at the MuCLS for tomographic imaging of small-animal samples and for pre-clinical mammographic imaging, exploiting the monochromatic and highly partially coherent beam. The analysis of freshly dissected mastectomy specimens and a mammography phantom showed enhanced diagnostic content at lower or equal dose levels compared to clinical mammography. The presented results highlight the potential of compact synchrotron sources for biomedical imaging and pre-clinical research.

Zusammenfassung

Zwischen konventionellen Röntgenröhren und Synchrotronen der 3. Generation bestehen große Unterschiede bei der Leistungsfähigkeit in Bezug auf Monochromatizität, Brillanz und Kohärenz, aber auch hinsichtlich der entstehenden Kosten und der Verfügbarkeit. In den letzen Jahrzehnten wurden kompakte Synchrotronquellen verstärkt erforscht und es wird erwartet, dass sie diese Lücke in naher Zukunft füllen können. Diese Arbeit konzentriert sich auf die erste kommerziell in Betrieb genommenen Kompakt-Synchrotronquelle, welche auf inverser Compton-Streuung basiert, der Munich Compact Light Source (MuCLS). Wir evaluieren die charakteristischen Eigenschaften des Röntgenstrahls, darunter Fluss und Quellgröße und analysieren zudem deren zeitliche Stabilität. Die einzigartigen Eigenschaften der MuCLS – quasi-Monochromatizität, Anpassbarkeit der Energie und hohe partielle Kohärenz – werden in bedeutungsvollen biomedizinischen Bildgebungs-Anwendungen ausgeschöpft. Die Vorteile für gitterbasierte Bildgebung an Kleintieren werden untersucht und prä-klinische Studien zu den Themen Koronarangiographie und Mammographie werden durchgeführt. Koronarangiographie basiert auf der Kontrastmittelgabe in Koronararterien um koronare Herzerkrankungen diagnositzieren zu können. Wir weisen nach, dass bei gleichbleibendem Bildkontrast die Kontrastmittelgabe dank des von der MuCLS erzeugten, monoergetischen Röntgenstrahls deutlich reduziert werden könnte. Gitterbasierte Phasenkontrast- und Dunkelfeld-Bildgebung ist bekannt dafür, besseren Weichgewebekontrast und Informationen über Kleinwinkelstreuung zu ermöglichen. Wir erkunden das Potential dieser Technik an der MuCLS bei der Tomographie von Kleintieren und für prä-klinische Anwendung in der Mammographie, welche vom monochromatischen und hoch partiell kohärenten Strahl profitieren. Die Analyse von frisch abladierten Mastektomieproben und eines Mammographiephantoms zeigte im Verlgeich zur klinischen Mammographie erweiterte diagnostische Aussagekraft bei niedrigerer oder gleicher applizierter Dosis. Die präsentierten Resultate unterstreichen das Potential von Kompakt-Synchrotronquellen in der biomedizinischen Bildgebung und der prä-klinischen Forschung.

Contents

1. Introduction

In this chapter, the main topic of this PhD thesis is briefly introduced in the context of research developments in the field. Section 1.2 presents the outline of this thesis.

1.1. Motivation

X-ray imaging has become an indispensable tool in medical diagnostics. As first observed by Wilhelm Conrad Röntgen in 1895, x-rays have the ability to penetrate through opaque materials and a sample will cast a shadow on a photographic plate behind it, depending on the attenuation of the materials in the sample. As an example, the attenuation in bone is by far higher than in soft tissues, thus casting a stronger shadow as less photons will hit the detector. Today, many clinical diagnostic methods rely on radiography or x-ray Computed Tomography (CT), such as the detection of bone fractures, coronary angiography or mammography. In materials science research, x-ray CT is used for the non-destructive evaluation and testing of materials and structural components.

X-ray tube sources reliably provide x-rays for medical and also materials science research applications, while the cost of purchase and maintenance is relatively small. With the development from Coolidge x-ray tubes to rotating anode x-ray tubes, a significant increase in power output was achieved that allows for very short acquisition times in the medical field. One of the drawbacks of x-ray tube sources is their broad polychromatic x-ray spectrum, which may lead to beam hardening artifacts in tomographic imaging. Furthermore, the contrast can suffer from the broad bandwidth. The insufficient coherence of the x-ray beam makes it impossible for several sophisticated imaging approaches to be applied at x-ray tube sources.

These limitations can be overcome with the use of highly coherent, monochromatic x-ray beams, like those provided by synchrotrons. Synchrotrons offer very brilliant x-rays that can be highly monochromatized and are higly coherent, allowing to exploit coherence effects as it is done in coherent diffraction imaging, holography, ptychography or phase-contrast imaging [Tegze and Faigel, 1996, Weitkamp et al., 2005, Thibault et al., 2008, Robinson and Harder, 2009, Dierolf et al., 2010]. However, due to their large electron storage rings, synchrotrons are limited to large-scale research facilities and impose high financial requirements for installation and maintenance. In addition, the available beamtime at synchrotrons is limited and requires long-term application procedures with long wait times.

Various research teams worldwide have dedicated their efforts during the last few decades to developing laboratory-scale x-ray sources that are capable of bringing the synchrotron beam benefits - monochromaticity, high partial coherence and small source sizes - to the researchers' laboratories where these beam properties can be exploited on a daily basis and in close vicinity to hospitals, laboratory animal infrastructure and

	MuCLS	ESRF
Undulator type	laser undulator	permanent magnet undulator
Undulator period	0.5 µm	1-5 cm
Number of periods	10^4	80
Storage ring circumference	4.2 m	844.4 m
Electron energy	20-45 MeV	6 GeV
$\gamma = \frac{E_e}{mc^2}$	40-90	12000
Beam current	80 mA	200 mA
Brightness $\left[\frac{\text{photons}}{\text{s}\,\text{mm}^2\,\text{mrad}^2\,0.1\%\,\text{BW}}\right]$	10^{10}	10^{20}
Typical bandwidth	4%	$10^{-4}\%$

Table 1.1.: Comparison of typical parameters for the Munich Compact Light Source (MuCLS) and the European Synchrotron Radiation Facility (ESRF) [ESRF, 2017], an example for a 3rd generation synchrotron.

chemistry or biological laboratories.

Most of the mainly followed approaches apply highly dedicated laser systems in the generation of x-rays. The most commonly researched and developed sources - often called tabletop synchrotron sources or compact synchrotron sources - are inverse Compton sources [Huang and Ruth, 1998], laser-wakefield sources [Kneip et al., 2010] and high-harmonic generation [Popmintchev et al., 2012].

Many of these sources are still strongly under development. Very recently, the first commercially sold inverse Compton source was installed in Munich, Germany: the Munich Compact Light Source (MuCLS) [Eggl et al., 2016a]. This work will focus on the characterization of the MuCLS and the examination of various possible imaging applications.

The functioning principle of the MuCLS is, as often used to name these kinds of sources, inverse Compton scattering, where a laser photon collides with a relativistic electron and is backscattered with its energy increased to the x-ray range [Huang and Ruth, 1998].

Possibly more intuitive when comparing the MuCLS to a synchrotron and explaining why it is "compact", is to regard the laser photons as electromagnetic waves. Then the counterpropagating laser pulse can be described like a localized electromagnetic field which will act on the electrons like a permanent magnet undulator at a synchrotron: the electromagnetic field causes the relativistic electrons to follow small oscillations during which the radiation in the x-ray regime is emitted. The main part of the radiation is emitted in the forward direction (propagation direction of the electrons) and when collimated using an aperture the spectrum is quasi-monochromatic with a few percent bandwidth.

When now comparing the laser undulator to a permanent magnet undulator, as done in table 1.1 for the MuCLS and the European Synchrotron Radiation Facility (ESRF) [ESRF, 2017], it becomes clear why a laser undulator source can be built so compact. While the undulator period of the permanent magnet undulator is in the order of a few centimeter, the period of the laser undulator is given by half of the laser wavelength, i.e. ~ 0.5 µm in the case of the infrared laser chosen for the MuCLS, which is about a factor of 20000 smaller than for the permanent magnet undulator. As the wavelength of the undulator radiation scales with the undulator period and γ^2, i.e. the energy of the electron beam, the electron energy - and subsequently the storage ring circumference - can be reduced by a factor of $\sim \sqrt{20000} \approx 150$. This allows for the MuCLS storage ring have such a small circumference of only 4.2 m and therefore the whole machine can be installed in a regular-sized laboratory, a photograph is shown in figure 1.1.

While the spatial and financial requirements imposed by the MuCLS are compatible with laboratory - or possibly, in the future, even clinical - environments, it offers benefits over conventional x-ray tube sources that so far have only been available at synchrotrons. The x-ray beam is quasi-monochromatic, with the energy freely tunable between currently 15 and 35 keV. The beam is highly partially coherent. The chosen angular collimation of 4 mrad provides a FOV that is larger than those commonly available at synchrotrons and well-suited for small-animal imaging.

Various biomedical and materials science research x-ray imaging applications and even radiation therapy benefit from one or several of these source properties, as illustrated in figure 1.1. The aim of this thesis is to explore the potential of some of these applications and to investigate their clinical relevance.

High partial coherence of the x-ray beam is necessary for **phase-sensitive imaging techniques** like propagation-based phase-contrast imaging or grating-based phase-contrast imaging. These methods allow to resolve tiny phase shifts of the x-ray wavefront, providing a tremendous improvement in soft-tissue contrast over conventional absorption imaging [Pfeiffer et al., 2007a, Tapfer et al., 2013].

Grating-based imaging simultaneously provides a third contrast besides the **absorption contrast** and the **phase contrast**, namely the **dark-field contrast** signal [Pfeiffer et al., 2007b], which provides information on the small-angle scattering properties of the sample on a sub-pixel resolution [Yashiro et al., 2010]. Grating-based phase-contrast and dark-field imaging have been proven to work also with conventional x-ray tubes with low coherence [Pfeiffer et al., 2006] but can be applied at the highly partially coherent beam provided by the MuCLS with a simplified setup geometry as done at synchrotrons [Bech et al., 2009]. Moreover, the image quality will improve compared to polychromatic sources due to the monochromaticity of the source as the x-ray energy can be adjusted precisely to the design energy of the interferometer.

The monochromaticity of the x-ray beam is beneficial for CT imaging since no beam hardening artifacts are introduced [Achterhold et al., 2013]. In addition, **quantitative CT**, i.e. the reconstruction of absorption coefficients and (in the case of grating-based phase-contrast CT) electron densities, is feasible without the need for calibration measurements.

Two **clinical applications** that could benefit from the quasi-mono-energetic x-ray spectrum are angiography and mammography.

In **coronary angiography**, an invaluable tool in the diagnosis of coronary heart disease, a contrast agent is injected into the coronary artery in order to detect blockages from arteriosclerotique plaque. The substances used as contrast media, like for example iodine, exhibit a sudden increase in their absorption coefficient at the so-called K-edge energy of the medium. The energy of a mono-energetic x-ray beam can be tuned to be directly above the K-edge energy in order to yield optimal contrast-to-noise ratio. This thesis provides a quantitative analysis how the contrast agent concentration can possible

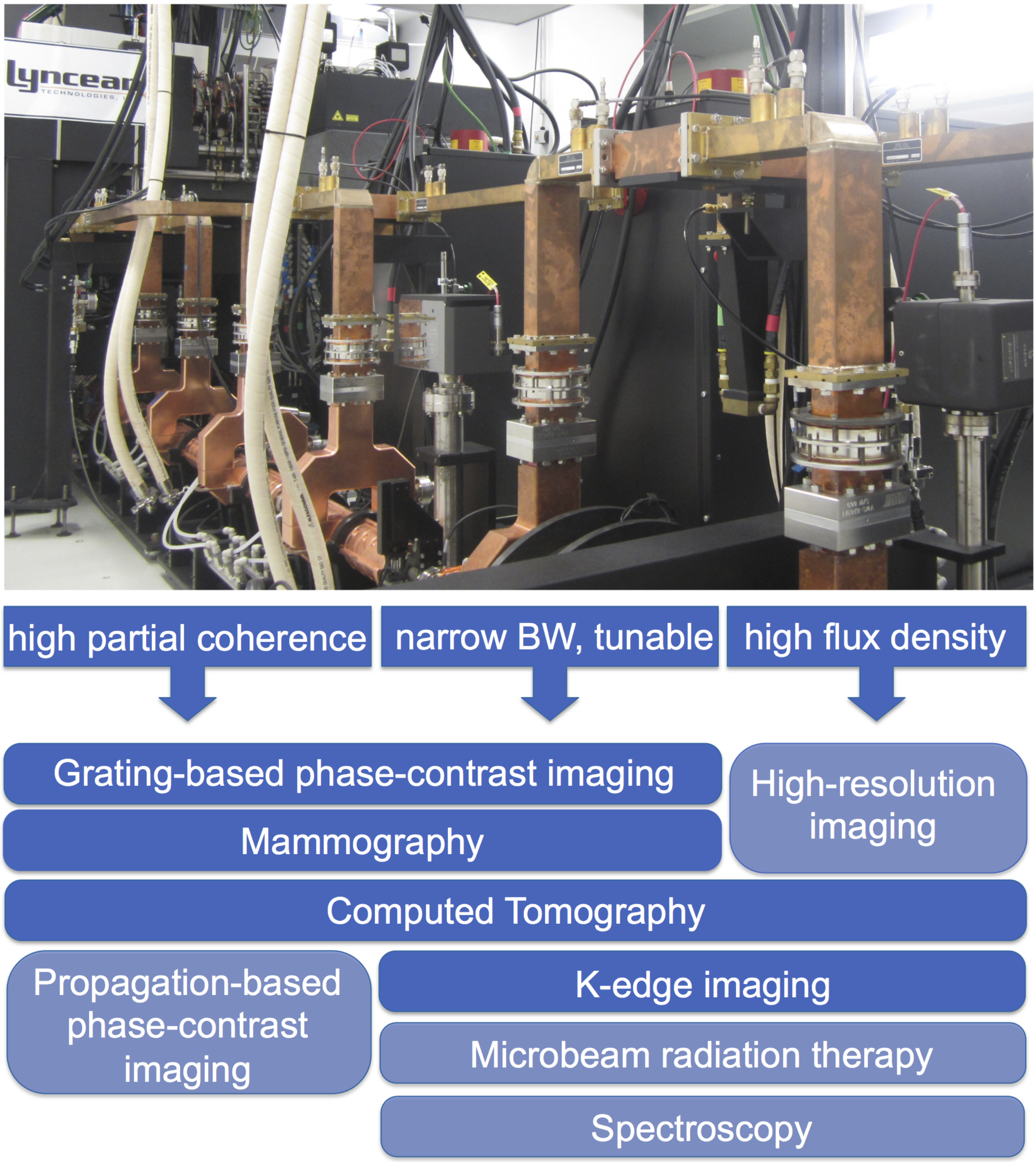

Figure 1.1.: The MuCLS: x-ray beam properties and applications that benefit from them.

reduced through this energy tunability. In the future, this approach can be extended to K-edge subtraction (KES) imaging, where two images are recorded (one slightly above and one below the K-edge energy) and subtracted such that only the structure filled with contrast media will remain in the image [Dix et al., 1986, Rubenstein et al., 1986].

Mammography relies on the visualization of small tumor nodules and microcalcifications for the early detection of breast cancer which is complicated by the inherently low absorption contrast in soft tissue. A recent patient study with synchrotron radiation showed that monochromatic phase-contrast enhanced mammography has the potential to clarify cases with unclear diagnosis after initial mammography and ultrasonography while keeping the mean glandular dose lower than or equal to the clinical value [Longo et al., 2014]. The quasi-monochromatic beam of the MuCLS in combination with grating-based phase-contrast and dark-field mammography has the potential to yield improved diagnostic image quality at lower or equal dose compared to clinical mammography. This thesis investigates the possibilities of mammography with the MuCLS.

1.2. Outline

The outline of this thesis is briefly described hereafter.

Chapter 2 introduces the principles of x-ray interaction with matter and how different image contrasts form from these interactions and can be extracted. The basic ideas of computed tomography are summarized and the concept of grating-based phase-contrast and dark-field imaging is explained.

Chapter 3 gives an overview of different types of x-ray sources and how they can be compared through different figures of merit. The major part of the chapter is dedicated to present the essential physical principles of inverse Compton sources and the technical realization in case of the MuCLS. The main aspects of the MuCLS operation and some of its challenges are illustrated as well.

In chapter 4, the experimental setup installed at the MuCLS is presented, with focus on the grating interferometer. A short summary of the software code used for the mammography project is provided.

In chapter 5, beam properties as well as performance parameters and their stability are presented and discussed, illustrating the further development of the MuCLS before and after the installation in Munich. The quasi-monochromatic spectrum was measured for different peak x-ray energies (chapter 5.3).

The main experimental results are shown in chapters 6 through 8. In chapter 6, the possibility of reducing the contrast medium concentration in coronary angiography by applying a quasi-mono-energetic x-ray beam instead of a conventional polychromatic spectrum from an x-ray tube is investigated. A first experimental demonstration of coronary angiography of a porcine heart is presented (chapter 6.3).

Chapter 7 presents several possible applications of grating-based phase-contrast and dark-field CT imaging. The quantitative reconstruction of the attenuation coefficient and the refractive index decrement is demonstrated for a fluid phantom (chapter 7.2). Grating-based multimodal CT reconstructions of three biomedical samples (infant mouse and bird) illustrate the superior soft-tissue information that is provided by the phase-contrast modality (chapters 7.3 and 7.4).

The potential of the MuCLS for mammography applications is explored in chapter 8. First (chapter 8.2), different concepts for calculating the applied mean glandular dose are discussed and the chosen method for dose calculation at the MuCLS is explained. A proof-of-principle study on grating-based phase-contrast and dark-field tomosynthesis is shown in chapter 8.3. Chapter 8.4 investigates the feasibility of dose-compatible mammography (with and without gratings) and possible benefits for diagnostic image quality.

The main scientific results are summarized and discussed in chapter 9 and an outlook on possible future applications and developments of the MuCLS is provided.

2. Principles of X-ray imaging

This chapter first introduces the most important processes for the interaction of x-rays with matter that contribute to the formation of image contrast. The principle of Computed Tomography (CT) is presented and the concept of measuring the x-ray phase-shift using a grating interferometer is explained.

2.1. X-ray interaction with matter

2.1.1. X-rays: photons and electro-magnetic waves

In the wave-particle dualism, x-rays can be regarded as either one: electro-magnetic waves (with wavelengths of around one Angstrom, 1 Å$= 10^{-10}$ m) or photons (with an energy of typically 10-150 keV for hard x-rays, below 10 keV for soft x-rays). The short wavelength region of the electro-magnetic spectrum is shown in figure 2.1, with the hard x-ray regime to the higher end of the spectrum with respect to photon energy.

X-rays as waves

An electro-magnetic wave is characterized by its wavelength λ, which is related to the wavenumber k by [Als-Nielsen and McMorrow, 2011]

$$k = \frac{2\pi}{\lambda}. \tag{2.1}$$

Even though an x-ray beam never is perfectly collimated, it can usually be approximated as a plane wave. The spatial and temporal evolution of a plane wave traveling along the

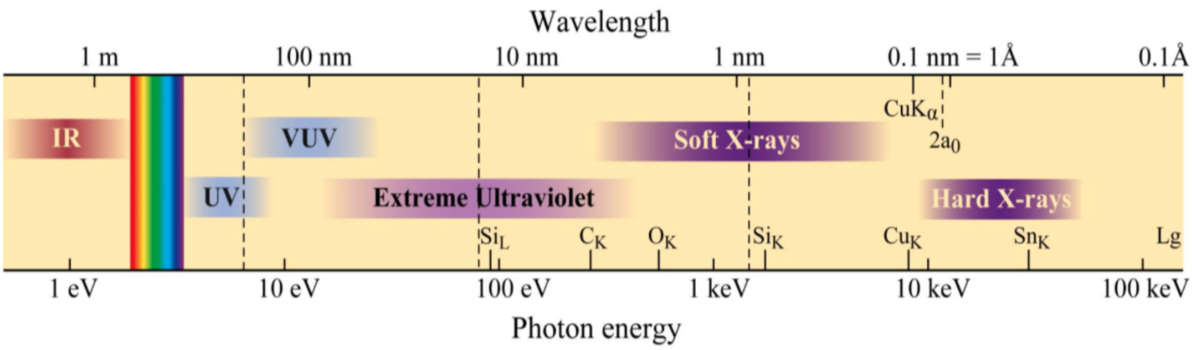

Figure 2.1.: The electromagnetic spectrum. Shown is the short wavelength region ranging from the infrared (left) to the hard x-ray regime (right). Adopted from [Attwood, 2007].

z-direction can be expressed as [Als-Nielsen and McMorrow, 2011]

$$E(z,t) = E_0 e^{i(kz-\omega t)}, \tag{2.2}$$

i.e. the classical description of a linearly polarized, electro-magnetic plane wave.

X-rays as photons

In the quantum-mechanical picture, an x-ray beam is regarded to be quantized into photons of energy $\hbar\omega$ and momentum $\hbar k$ [Als-Nielsen and McMorrow, 2011].

The intensity of an x-ray beam is given by the number of photons per area per unit time, or, in terms of the wave picture, the square of the electric field.

The wavelength λ and the photon energy E_x are related by the equation [Als-Nielsen and McMorrow, 2011]

$$E_x = \frac{hc}{\lambda}, \tag{2.3}$$

$$\lambda[\text{Å}] = \frac{hc}{E_x} = \frac{12.398}{E_x[\text{keV}]}, \tag{2.4}$$

where $h = 6.626 \cdot 10^{-34}$ Js is Planck's constant and $c = 2.998 \cdot 10^{8}$ m/s is the speed of light in vacuum.

An x-ray photon can interact with an atom through absorption or scattering, and it can be refracted at the boundaries of different media. These processes and how they are utilized for x-ray imaging will be discussed in the following sections.

2.1.2. Scattering

For x-rays in a medium, scattering mainly occurs with electrons. The scattering can be elastic (Thomson scattering) or inelastic (Compton scattering).

Thomson scattering

In the classical picture, i.e. for electrons that are moving at non-relativistic speeds, the scattering is elastic: the wavelength of the scattered wave is equal to that of the incident wave. The electromagnetic field of the incident x-ray beam forces the electron to vibrate, and the electron will radiate a spherical wave (dipole radiation) [Als-Nielsen and McMorrow, 2011].

The ability of an electron to scatter an x-ray photon is described by the scattering length. In the case of the quasi-free electron, the commonly used unit is the Thomson scattering length (also called 'classical' radius of a free electron) [Willmott, 2011],

$$r_0 = \frac{e^2}{4\pi\epsilon_0 mc^2} = 2.82 \cdot 10^{-5}\text{Å}. \tag{2.5}$$

The Thomson differential scattering cross-section for unpolarized radiation is given by [Als-Nielsen and McMorrow, 2011]

$$\frac{\mathrm{d}\sigma}{\mathrm{d}\Omega}_{\text{Thomson}} = \frac{r_0^2}{2}\left[1+\cos^2\theta\right], \tag{2.6}$$

where θ is the scattering angle. The total Thomson scattering cross-section is found by integrating over all possible scattering angles, which yields [Als-Nielsen and McMorrow, 2011]

$$\sigma_{\text{Thomson}} = \frac{8\pi r_0^2}{3}, \tag{2.7}$$

hence the cross-section for scattering of an electromagnetic wave by a free electron is independent of energy.

Compton scattering

In the quantum mechanical picture, the description of elastic scattering no longer holds true and a transfer of kinetic energy between the electron and the scattered photon has to be considered. The scattered photon lost part of its energy to the electron.

The change in wavelength is proportional to the Compton scattering length [Als-Nielsen and McMorrow, 2011, Willmott, 2011],

$$\lambda_C = \frac{h}{mc} = 2.43\cdot 10^{-2}\text{Å}. \tag{2.8}$$

The fractional loss of the photon energy increases with increasing scattering angle and incident photon energy. The Compton scattering cross-section is strongly peaked in the forward direction.

The total scattering cross-section for Compton scattering is given by the Klein-Nishina equation [Klein and Nishina, 1929],

$$\sigma_{\text{Compton}} = 2\pi r_0^2\left[\left(\frac{1+\mathcal{E}}{\mathcal{E}^2}\right)\left(2\frac{(1+\mathcal{E})}{1+2\mathcal{E}^2} - \frac{\ln(1+2\mathcal{E})}{\mathcal{E}}\right) + \frac{\ln(1+2\mathcal{E})}{2\mathcal{E}} - \frac{1+3\mathcal{E}}{(1+2\mathcal{E})^2}\right], \tag{2.9}$$

where $\mathcal{E} = h\nu/(m_e c^2)$ is the reduced energy of the incoming photon and r_0 is the classical electron radius.

The two fundamental scattering lengths for x-rays, the Thomson scattering length r_0 and the Compton scattering length λ_C are related through the fine structure constant α [Als-Nielsen and McMorrow, 2011],

$$\alpha = \frac{r_0}{2\pi\cdot\lambda_C} \approx \frac{1}{137}. \tag{2.10}$$

2.1.3. Complex refractive index

Regarded in the wave picture, x-rays should undergo a refraction at the interface of different media. The media are described by their refractive index n, while in vacuum n is unity. For x-rays, the difference of the refractive index is very small (in the order

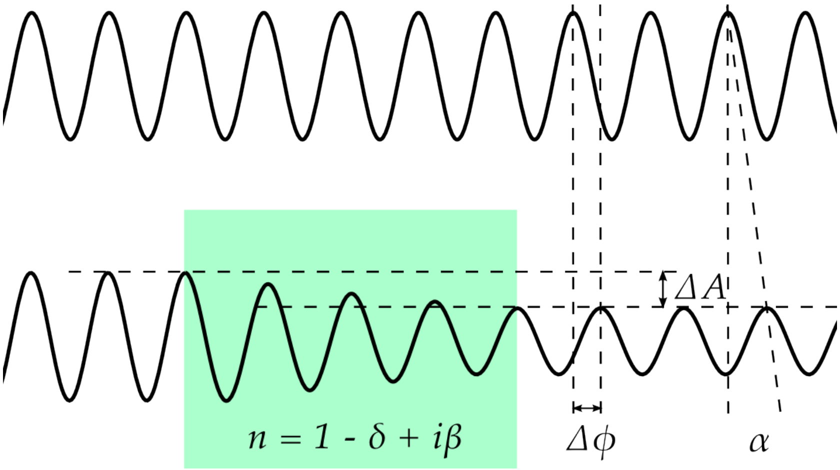

Figure 2.2.: Complex refractive index. Displayed are two waves of a monochromatic plane wavefront. While the upper wave propagates through vacuum and thus stays unchanged, the wave traveling through a medium with complex refractive index n experiences an amplitude decay ΔA and a phase shift $\Delta\Phi$. The phase shift corresponds to a refraction by a (very small) angle α.

of 10^{-5}) and therefore usually is expressed as the complex number [Als-Nielsen and McMorrow, 2011]

$$n = 1 - \delta + i\beta, \tag{2.11}$$

where $\delta \approx 10^{-5}$ for solids and $\delta \approx 10^{-8}$ for air, and the imaginary part β being even smaller.

δ and β can be related to the real and imaginary parts $f_1^0(\omega)$ and $f_2^0(\omega)$ of the atomic scattering factor [Attwood, 2007, Als-Nielsen and McMorrow, 2011]:

$$\delta = \frac{n_a r_0 \lambda^2}{2\pi} f_1^0(\omega) = \frac{2\pi n_a r_0}{k^2} f_1^0(\omega), \tag{2.12}$$

$$\beta = \frac{n_a r_0 \lambda^2}{2\pi} f_2^0(\omega) = \frac{2\pi n_a r_0}{k^2} f_2^0(\omega), \tag{2.13}$$

where n_a is the average atomic density, r_0 is the classical electron radius/Thomson scattering length and λ is the x-ray wavelength.

Alternatively, δ and β can be expressed by material properties [Als-Nielsen and McMorrow, 2011]:

$$\delta = \frac{2\pi\rho r_0}{k^2}, \tag{2.14}$$

$$\beta = \frac{\mu}{2k}, \tag{2.15}$$

where ρ is the electron density in condensed matter, k is the wavevector and μ is the absorption coefficient.

As δ is in the order of 10^{-6}, the critical angle $\alpha_c = \sqrt{2\delta}$ is approximately 1 milli-radian and therefore, refraction phenomena for x-rays are very difficult to observe.

2.1.4. X-ray attenuation and phase shift

When the x-ray wave propagates through medium, the dispersion relation contains the index of refraction [Attwood, 2007]:

$$\frac{\omega}{k} = \frac{c}{n} = \frac{c}{1-\delta+i\beta}. \tag{2.16}$$

Solving for the wavevector k gives

$$k = \frac{\omega}{c}(1-\delta+i\beta). \tag{2.17}$$

This can be substituted into the wave equation (2.2),

$$E(z,t) = E_0 e^{-i[wt-\frac{\omega}{c}(1-\delta+i\beta)]}, \tag{2.18}$$

which can be separated into three exponential factors:

$$E(z,t) = \underbrace{E_0 e^{-i\omega(t-z/c)}}_{\text{propagation in vacuum}} \underbrace{e^{-i(2\pi\delta/\lambda)z}}_{\text{phase shift}} \underbrace{e^{-(2\pi\beta/\lambda)z}}_{\text{amplitude decay}} \tag{2.19}$$

where the first one represents the propagation of the wave in vacuum, the second one (containing $2\pi\delta z/\lambda$) the phase shift due to refraction in the medium and the third factor (containing $2\pi\beta z/\lambda = \mu z$) gives the decay of the wave amplitude.

Attenuation of x-rays

Looking at the intensity of the wave, i.e. the square of the wave equation (2.19), and substituting $\beta = \frac{\mu}{2k} = \frac{\mu\lambda}{2\cdot 2\pi}$, we get

$$I(z) = |E(z,t)|^2 = E_0^2 e^{-\mu z}, \tag{2.20}$$

which can be rearranged (with $E_0^2 = I_0$) to

$$\frac{I(z)}{I_0} = e^{-\mu z}, \tag{2.21}$$

i.e. the commonly known Beer-Lambert law for the attenuation of x-rays, with the attenuation coefficient μ being related to the imaginary part of the refractive index.

Phase-shift of x-rays

Considering the wave equation in medium (2.19), the phase shift $\Delta\phi$ for a wave traveling in medium compared to propagation in vacuum is given by

$$\Delta\phi = \left(\frac{2\pi\delta}{k}\right) z = k\delta z. \tag{2.22}$$

As indicated in fig. 2.2, the phase shift introduced in medium corresponds to a refraction angle α,

$$\alpha(x) = \frac{\lambda}{2\pi}\frac{\partial\phi}{\partial x}, \tag{2.23}$$

i.e. when measuring the refraction angle the derived quantity is the first derivative of the phase shift.

2.1.5. Material and energy dependency

Both the attenuation coefficient μ and the electron density δ depend on the material and the x-ray energy. Therefore, for a non-homogeneous medium and a polychromatic x-ray beam, equations 2.21 and 2.22 need to be adjusted:

$$\ln\left(\frac{I}{I_0}\right) = -\int_{E_{\min}}^{E_{\max}} \int_0^z \mu(z,E)\mathrm{d}z\mathrm{d}E, \tag{2.24}$$

$$\Delta\phi = \int_{E_{\min}}^{E_{\max}} \int_0^z k\delta(z,E)\mathrm{d}z\mathrm{d}E. \tag{2.25}$$

Linear attenuation coefficient

The linear attenuation coefficient μ is defined as

$$\mu = 2k\beta = \rho_{at}\sigma_a, \tag{2.26}$$

where ρ_{at} is the atomic number density ($\rho_{at} = \rho_M N_A/M$ with mass density ρ_M, Avogadro number N_A and molar mass M) and σ_a is the total atomic absorption cross section . The linear attenuation coefficient follows the dependency of the total atomic cross section on the atomic number Z, $\sigma_a \propto Z^4$ and on the x-ray energy, $\sigma_a \propto \frac{1}{E^3}$ [Als-Nielsen and McMorrow, 2011].

The E^{-3}-dependency is not valid near so-called absorption edges: when the energy of the x-ray is greater than or equal to the binding energy of a shell electron, the electron can be expelled from the atom through photoelectric absorption [Als-Nielsen and McMorrow, 2011], hence leading to a sudden increase in absorption cross section at the binding energy, and the E^{-3}-dependency is resumed afterwards. For the K-shell electrons, the absorption edge is often called K-edge, and the sudden increase in absorption cross section is exploited in K-edge imaging, to be discussed in chapter 6 in this work. Figure 2.3 (a) displays a plot of the attenuation coefficient of iodine, a material well known for its use as contrast agent and in K-edge imaging. Figures 2.3 (b) and (c) show the absorption coefficient of two clinically relevant materials (soft tissue and bone).

In addition, the total atomic absorption cross section σ_a is comprised of several energy-dependent factors [Buzug, 2008],

$$\sigma_a(Z,E) = \sigma_{ray} + \sigma_{pho} + \sigma_{com} + \sigma_{pai}, \tag{2.27}$$

i.e. given by the sum of the cross sections for:

- Rayleigh scattering (σ_{ray}): Elastic scattering at bound electrons of an atom.
- Photoelectric absorption (σ_{pho}): An electron bound to an inner shell of the atom is expelled and the photon is absorbed.
- Compton scattering (σ_{com}): Inelastic, incoherent scattering at quasi-free electrons. The scattered photon continues to travel through the medium with lowered energy.
- Pair production (σ_{pai}): Only observed for photon energies above 1 MeV and therefore negligible for x-ray imaging.

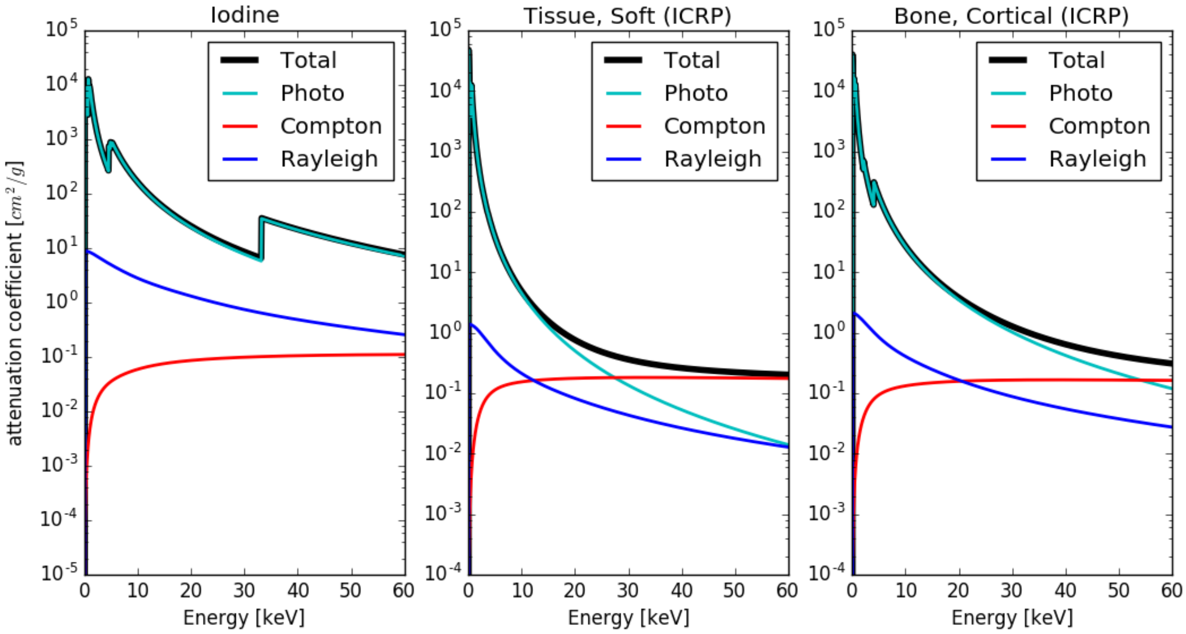

Figure 2.3.: Energy dependency of the attenuation coefficient. The different contributions to the linear attenuation coefficient show characteristic energy dependencies and also depend on the respective material (from left to right): Iodine with the characteristic absorption edge at 33.2 keV, soft tissue, and cortical bone. Data obtained from `xraylib` [Schoonjans et al., 2011].

For diagnostic x-ray imaging, the two most important processes are photoelectric absorption and Compton scattering, of which the latter becomes dominant for energies above $\sim$ 30 keV for soft tissue and above $\sim$ 50 keV for bone. The energy dependence of the different contributions to the total attenuation cross section is shown in figure 2.3 (b) for soft tissue and (c) for cortical bone.

Phase-shift cross section

The phase-shift is directly related to the electron density of the medium [Als-Nielsen and McMorrow, 2011],

$$\delta = \frac{r_e}{2\pi}\lambda^2\rho_e, \tag{2.28}$$

where $\rho_e = N_i \cdot Z$ is the electron density.

Other than for the attenuation, the phase-shift is only dependent on one process, namely Rayleigh scattering, i.e. elastic scattering from bound electrons. No energy change is involved in the scattering process, only a change in direction of the scattered x-rays, and the scattering is incoherent.

The energy dependency of the phase-shift cross section is $\sigma_{\text{phase}} \propto \frac{1}{E^2}$, hence decreasing less rapidly with increasing energy than the absorption cross section. This feature is especially beneficial for phase-contrast imaging over absorption-based imaging with respect to the possibility of dose reduction, as the image contrast decreases less rapidly with increasing x-ray energy.

The following section will present phase-sensitive imaging methods, with the main focus on grating-based phase-contrast imaging, as this technique was applied for experiments presented in this work.

2.2. Grating-based x-ray phase-contrast and dark-field imaging

Due to the very small refraction angle for x-rays, a direct measurement using standard x-ray detectors is not possible. Different approaches have been exploited throughout the last decades to make the phase shift measurable. These phase-contrast imaging (PCI) methods differ both in the measurement setup and in what they measure, as highlighted in table 2.1, where the principle ideas for each of the methods are briefly explained. For a more detailed description, please refer to the given references and references therein.

Method	Measured quantity	Description	Literature
crystal interferometer (CI)	Φ	The interferometer consists of three crystal blades. The first crystal splits the incoming x-ray beam in two parts, the second one changes their direction so they meet again and interfere at the position of the third crystal, which acts as analyzer. The sample is introduced into one of the two beams between the 2nd and 3rd crystal. Crystal interferometry is considered the most sensitive phase-contrast imaging method. A CI is very sensitive to vibrations, no transfer to medical applications has been made until today.	[Bonse and Hart, 1965, Momose, 1995]
Crystal analyzer-based imaging (ABI)/ diffraction-enhanced imaging (DEI)	$\frac{\partial\Phi}{\partial x}$	A single crystal acts as analyzer of sample-induced changes, usually applied with a laminar synchrotron beam. The crystal is tilted, creating a rocking curve on the detector, from which image signals (absorption, differential phase, small-angle scattering) can be extracted. ABI was successfully demonstrated for several medical applications.	[Davis et al., 1995, Chapman et al., 1997, Arfelli et al., 2000]

grating-based imaging (GBI)	$\frac{\partial\Phi}{\partial x}$	Two optical gratings are introduced in the x-ray beam. The first grating creates a intensity pattern, distortions of which through the introduction of a sample are analyzed with a second grating. The introduction of a third grating allows for the application with a laboratory source. Absorption, differential phase and small-angle scattering signals can be extracted from the phase-stepping curve. GBI has proven beneficial for several medical applications.	[Momose et al., 2003, Weitkamp et al., 2005, Pfeiffer et al., 2006, Pfeiffer et al., 2008, Schleede et al., 2013]
edge-illumination (EI) / Coded-aperture-based imaging	$\frac{\partial\Phi}{\partial x}$	The beam is shaped by a slit so that only half of the detector pixel is illuminated during the reference image. When introducing a sample into the beam, the intensity in the pixel will decrease or increase due to the refraction and subsequent beam deflection (similar to ABI, without a crystal). The laboratory adaptation is achieved by using so-called coded-aperture masks which create an array of separate 'beamlets'. EI has been investigated for medical applications.	[Olivo et al., 2001, Olivo and Speller, 2007, Olivo et al., 2013]
propagation-based imaging (PBI) / In-line holography	$\frac{\partial^2\Phi}{\partial x^2}$	For a sufficiently coherent source, phase effects can be observed even without optical elements in the beam by increasing the distance between sample and detector to allow free-space propagation of the x-ray wavefront (Fresnel diffraction). Intensity modulations at object interfaces produce an edge-enhanced image. PBI was explored in the mammography with synchrotron radiation study.	[Snigirev et al., 1995, Cloetens et al., 1999, Paganin et al., 2002, Arfelli et al., 1998]

Table 2.1.: Phase-sensitive x-ray imaging methods.

Out of the presented techniques, grating-based imaging is probably the most researched and most promising method for making phase- and dark-field information available, with several medical applications being investigated [Yaroshenko et al., 2015, Scherer et al., 2015, Eggl et al., 2015a].

As the GBI method was the one applied in this work, a detailed description of the principles and the signal extraction is presented in the following.

2.2.1. Talbot grating interferometry

A Talbot interferometer (also called x-ray grating interferometer (XGI), or shearing interferometer) uses two optical gratings in order to access the phase information of the x-ray wavefront. These optical gratings consist of periodically arranged thin bars that act absorbing or phase-shifting on x-rays [Weitkamp et al., 2006], with periods in the order of usually a few µm in order to resolve the small refraction angles and thus lateral shifts that are to be detected.

The first of the two gratings, usually named phase grating (G1), imprints a periodic spatial modulation to the wavefront amplitude or phase, and is therefore often referred to as beam splitter grating. The principle of x-ray grating interferometry then relies on the so-called Talbot self-imaging effect of optical gratings [Talbot, 1836]. First discovered for visible light, periodic structures under coherent illumination will repeat themselves after a certain distance, the Talbot distance, depending on the periodicity of the pattern p_1 and the wavelength of the illumination λ,

$$d_T = \frac{2p_1^2}{\lambda}. \tag{2.29}$$

The effect is also true for wavelengths in the x-ray regime when the x-ray wavefront is modulated by an optical grating, which can either be absorbing or phase shifting. Figure 2.4 shows the Talbot carpet, i.e. the wave propagation after passing through an optical grating with the imprinted intensity fringes, for the three most common types of gratings (absorption, $\pi/2$- and π-shifting phase gratings). In grating-based imaging, usually a phase grating is chosen for this wavefront modulation, as it has negligible absorption, while an absorption grating would cause a loss of about 50% in intensity. The height of the grating bars is adjusted to reach the desired phase shift for the appropriate x-ray wavelength.

Along the beam, at certain fractional Talbot distances, the intensity fringe contrast will reach maxima and minima (cf. fig. 2.4, maxima indicate by dashed lines), which are given by [Weitkamp et al., 2006]

$$d_n = \frac{1}{\eta^2}\frac{np_1^2}{2\lambda}, \tag{2.30}$$

where p_1 is the period of the beam splitter grating G1, and $n = 0, 1, 2, ...$ is the so-called Talbot order. Fringes from a phase grating will show maximum contrast at odd Talbot orders (or fractional Talbot distances), i.e. $n = 1, 3, 5, ...$, while those from an amplitude grating reach their maximum contrast at even Talbot orders. The factor η depends on the optical properties of G1,

$$\eta = \begin{cases} 1, & \text{if G1 is a } \frac{\pi}{2}\text{-shifting phase grating or an amplitude grating,} \\ 2, & \text{if G1 is a } \pi\text{-shifting phase grating.} \end{cases} \tag{2.31}$$

Since the modulations imprinted by G1 are spatially too small to be resolved by a regular detector, a second grating, usually named analyzer grating (G2), is placed in front of the detector, with an inter-grating distance of one of the fractional Talbot distances with maximum fringe contrast. This grating necessarily is an absorption grating and will

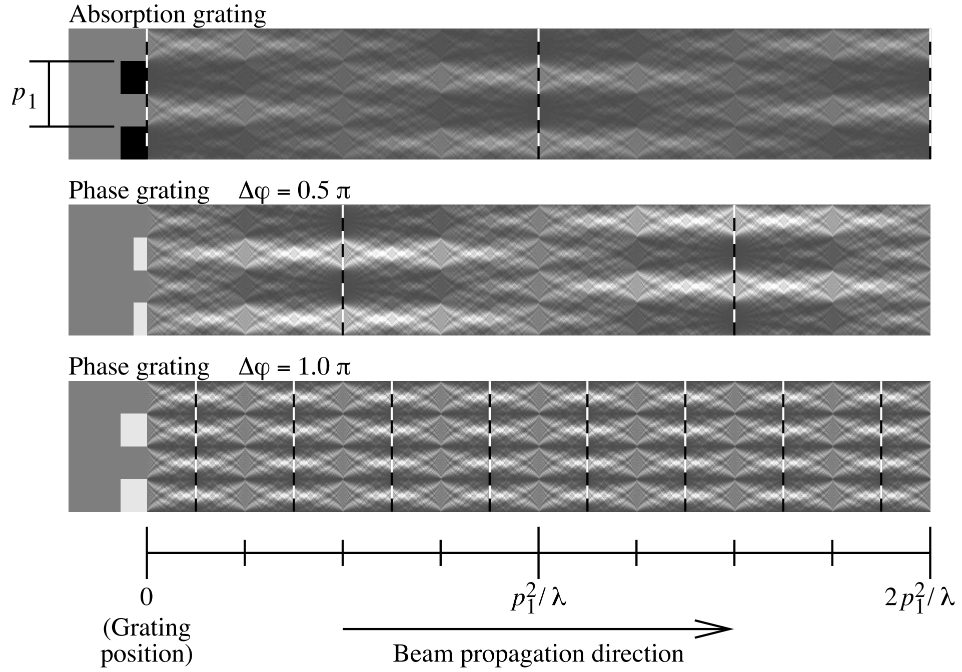

Figure 2.4.: Talbot carpets of the three most common types of gratings. A grating of period p_1 is illuminated by a coherent, plane wave, causing fringe modulations of the wavefront downstream of the grating. Dashed lines indicate so-called fractional Talbot distances with maximum contrast of the fringes. **Top:** amplitude grating with fully absorbing grating bars. **Middle:** $\pi/2$-shifting phase grating. **Bottom:** π-shifting phase grating. Figure adopted from [Weitkamp et al., 2006].

transform fringe positions into intensity values, therefore the grating bars are required to have a height large enough to fully absorb the x-ray beam. The period of the analyzer grating p_2 needs to be equal to the period of the fringes imprinted by G1, and therefore [Weitkamp et al., 2006]

$$p_2 = \begin{cases} p_1, & \text{if G1 is a } \frac{\pi}{2}\text{-shifting phase grating or an amplitude grating,} \\ \frac{p_1}{2}, & \text{if G1 is a } \pi\text{-shifting phase grating.} \end{cases} \tag{2.32}$$

In the case of the grating interferometer being illuminated by a spherical wave from a source at a distance L from G1 instead of a plane wave, the Talbot distances are shifted to [Weitkamp et al., 2006]

$$D_n = \frac{L d_n}{L - d_n} = \frac{L}{2\eta^2 \lambda L/(n p_1^2) - 1}, \tag{2.33}$$

where d_n is the Talbot distance for the plane wave. The fringe spacing at a Talbot distance D_n then is magnified by a factor

$$M = \frac{L + D_n}{L} = \frac{L}{L - d_n} = 1 + \frac{D_n}{L} = \frac{D_n}{d_n}, \tag{2.34}$$

with d_n and D_n denoting the Talbot distances for a plane wave and a spherical wave, respectively. Consequently, the period of the analyzer grating p_2 needs to be adjusted

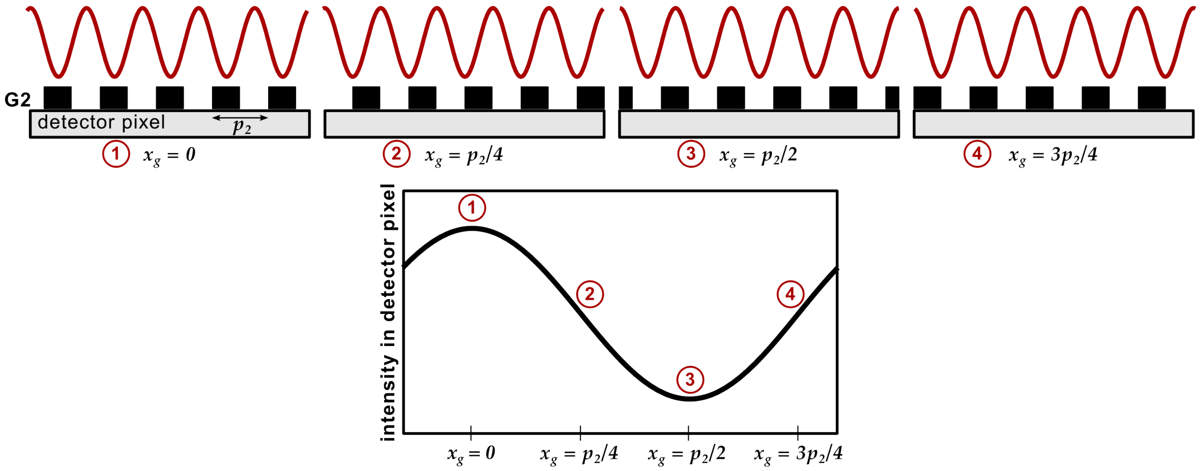

Figure 2.5.: Phase stepping. An x-ray wavefront propagates towards G2 and the detector. During the phase stepping, G2 is shifted laterally, which is pictured schematically for four different positions. The sinusoidal intensity pattern imprinted by G1 matches the period of the absorber grating. As the bars are moved, the intensity recorded in the detector pixel varies: while the grating bars are aligned with the minima of the wave (position (1), $x_g = 0$), the measured intensity will take its maximum and vice versa (position (3), $x_g = p_2/2$). In between (positions (2) and (4)), the intensity will take intermediate values following a sinusoidal curve, the so-called phase-stepping curve.

to the magnification,

$$p_2 = \frac{Mp_1}{\eta} = \frac{p_1}{\eta} \cdot \left(1 + \frac{D_n}{L}\right), \tag{2.35}$$

with $\eta = 1$ for a phase shift of $\pi/2$ and $\eta = 2$ for a phase shift of π.

The commonly applied procedure for analyzing the intensity modulation introduced by the grating interferometer and for extracting image signals, is called phase stepping, and will be subject of the next section.

2.2.2. Phase stepping and signal extraction

During the phase stepping scan, the analyzer grating[1] is shifted laterally by fractions of a grating period. As the grating period is matched to the modulations of the wavefront imprinted by G1, a change in intensity can be observed at the detector, even though the detector pixels are (usually) much larger than a grating period. This procedure is illustrated in figure 2.5, showing schematically how the intensity on the detector changes from maximum intensity for an alignment of the grating bars with the minima of the wavefront to a minimum value when the grating bars are aligned with the wavefront maxima.

During the movement of the grating over one full grating period, the intensity measured in the detector pixel will follow a sinusoidal curve, usually named phase-stepping curve.

---

[1] It is also possible to step G1, but G2 was chosen for the explanation here as it was the phase stepping grating for the experiments performed at the MuCLS.

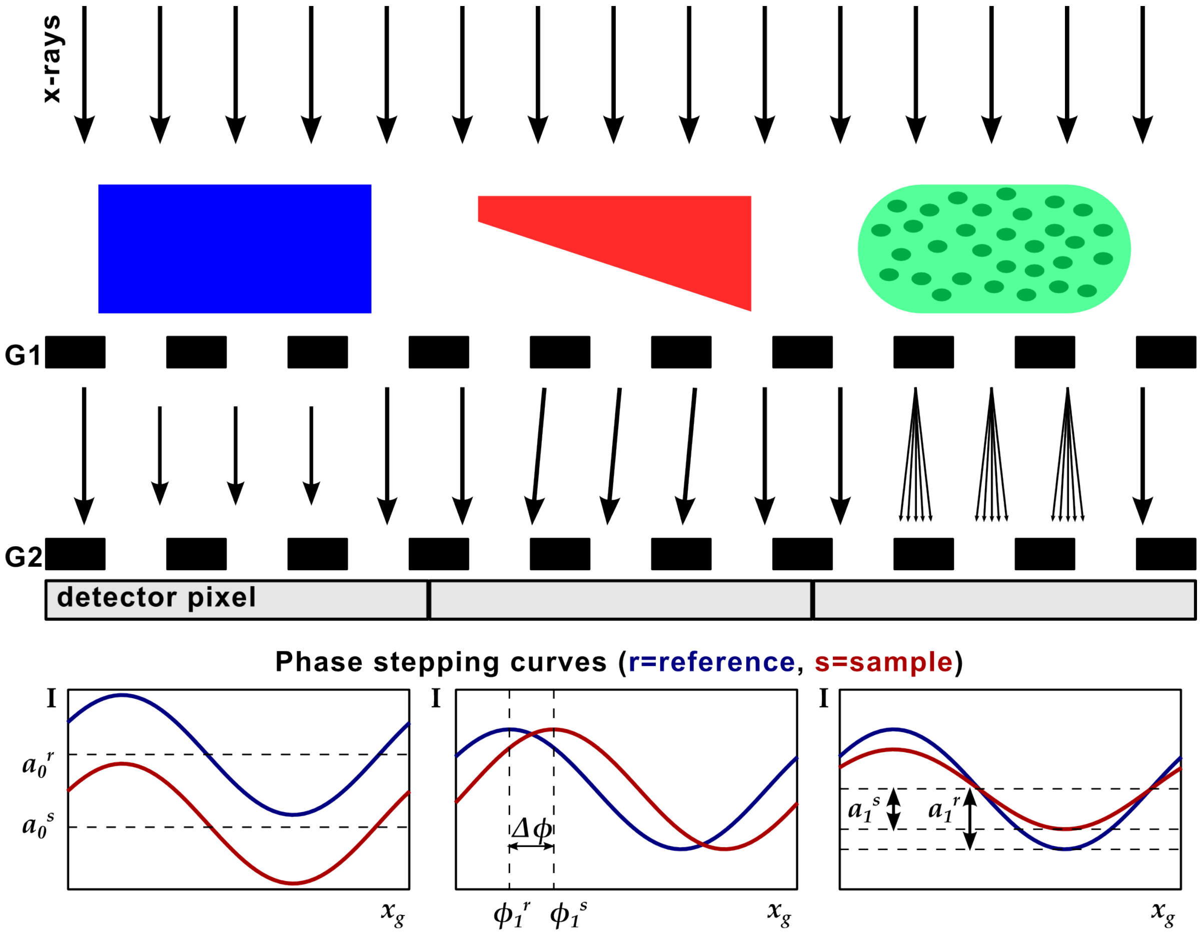

Figure 2.6.: Properties and retrieval of the three different contrast modalities from phase stepping. Three different idealized samples are placed in a grating interferometer setup (from left to right): a purely absorbing (blue rectangle), a purely refracting (red wedge) and a purely scattering (green rounded rectangle) sample. Placement up- or downstream of the phase grating G1 is possible (downstream pictured). The analyzer grating G2 is shifted laterally to produce phase stepping curves. The distinct features for each idealized sample have different effects on the phase stepping curves compared to the reference curve without the sample in place.

When a sample is then introduced into the beam (downstream or upstream of G1), the stepping curve will be altered compared to the reference stepping curve without the sample. This change, strongly dependent on the type of sample introduced in the beam, can be analyzed in order to obtain three complimentary image contrast signals: absorption, differential phase, and dark-field (or small-angle scattering). The principle is displayed in figure 2.6 for three samples that are (from left to right) purely absorbing, purely phase-shifting and purely scattering, in order to illustrate the effect of each of these properties on the phase stepping curve.

- Absorbing sample: the intensity of the interference pattern is decreased, thus lowering the mean amplitude of the phase-stepping curve.
- Phase-shifting sample: the interference pattern is shifted laterally, thus inducing a phase-shift to the phase-stepping curve.
- Scattering sample: the amplitude of the interference pattern is decreased due to a

loss in coherence through small-angle scattering, thus decreasing the amplitude of the phase-stepping curve.

Quantitatively, the changes can be analyzed by approximating the phase-stepping curve, i.e. the intensity modulation in each detector pixel $I(x, y, x_g)$, as a Fourier series (first order) [Pfeiffer et al., 2006, Pfeiffer et al., 2008]

$$
\begin{aligned}
I(x, y, x_g) &= \sum_i a_i(x, y) \cos(ikx_g + \phi_i(x, y)) && (2.36)\\
&\approx a_0(x, y) + a_1(x, y) \cos(kx_g + \phi_1(x, y)), && (2.37)
\end{aligned}
$$

where a_i are the amplitude coefficients, ϕ_i the corresponding phase coefficients, and $k = 2\pi/p_2$.

By performing one phase-stepping scan with the sample in the beam (sample scan, in the following denoted by superscript s) and one without the sample (reference scan, denoted by superscript r), three contrast signals can be extracted (we shall now consider a sample that may be absorbing, phase-shifting and scattering) [Pfeiffer et al., 2008]:

- **Absorption:** The normalized average transmission of the sample in each detector pixel is given by the ratio

  $$T(x, y) = \frac{a_0^s(x, y)}{a_0^r(x, y)}. \tag{2.38}$$

  Importantly, the transmission $T(x, y)$ measured with the grating interferometer is identical to what would be measured with a conventional x-ray radiography setup,

  $$T(x, y) = e^{-\int \mu(x,y,z)\mathrm{d}z}. \tag{2.39}$$

  Within this work, in accordance with clinical practice, not the transmission T but the absorption image A will be given,

  $$A(x, y) = 1 - T(x, y). \tag{2.40}$$

- **Differential phase-contrast:** Through refraction in the sample, the stepping curve is shifted laterally, and the phase shift of the stepping curve in each pixel is given by

  $$\Delta\phi(x, y) = \phi_1^s(x, y) - \phi_1^r(x, y), \tag{2.41}$$

  and is related to the refraction angle introduced by the sample α and the first derivative of the phase shift of the x-ray wavefront $\frac{\partial\Phi}{\partial x}$ through

  $$\frac{\partial\Phi(x, y)}{\partial x} = \frac{2\pi}{\lambda}\alpha = \frac{p_2}{d\lambda}\Delta\phi(x, y). \tag{2.42}$$

  The phase shift of the wavefront Φ is the projection of the refractive index decrement δ,

  $$\Phi(x, y) = \int \delta(x, y, z)\mathrm{d}z. \tag{2.43}$$

- **Dark-field:** The dark-field contrast is a measure of the local scattering power within the sample, that causes a loss in coherence and therefore a decrease in the so-called visibility of the phase-stepping curve,

  $$V^r(x,y) = \frac{I_{\max} - I_{\min}}{I_{\max} + I_{\min}} = \frac{a_1^r(x,y)}{a_0^r(x,y)}. \tag{2.44}$$

  The local scattering power is given by the ratio of the visibilities with and without sample in the beam,

  $$V(x,y) = \frac{V^s(x,y)}{V^r(x,y)} = \frac{a_1^s(x,y)}{a_1^r(x,y)} \frac{a_0^r(x,y)}{a_0^s(x,y)}, \tag{2.45}$$

  and the dark-field image then is defined as

  $$D(x,y) = 1 - V(x,y), \tag{2.46}$$

  i.e. for samples that have a homogeneous structure and therefore negligible scattering power, the dark-field signal $D = 0$, for a strongly scattering sample $0 < D < 1$, and for the extreme case of a total loss in visibility, $D = 1$.

  It is important to note that the dark-field signal is sensitive to scattering from structures that are smaller than the actual pixel size, hence providing sub-pixel information.

  Furthermore, the dark-field signal depends strongly on the relative orientation of scattering structures to the grating structures, which is utilized in advanced imaging methods like directional dark-field imaging/x-ray vector radiography [Jensen et al., 2010, Malecki et al., 2013] and x-ray tensor tomography [Malecki et al., 2014].

One of the most significant advantages of grating-based imaging is that the three image signals provide complimentary information on the sample, while being perfectly registered. In addition, the technique is not only applicable at highly coherent sources like synchrotrons, but also adaptable to laboratory x-ray tubes, as to be discussed in the following.

2.2.3. Adaptation for laboratory sources

A sufficient amount of longitudinal and especially spatial coherence of the x-ray beam is required for the occurrence of the Talbot effect and therefore for Talbot interferometry to work. One figure that is often used to compare the quality of different experimental setups and that is dependent on the beam coherence is the interferometer visibility V that is measured without the sample in the beam,

$$V^r(x,y) = \frac{I_{\max} - I_{\min}}{I_{\max} + I_{\min}} = \frac{a_1^r(x,y)}{a_0^r(x,y)}. \tag{2.47}$$

An extended source size and polychromatic beam, as common for conventional laboratory x-ray tube sources, do not offer enough coherence for the application of a Talbot interferometer. However, if a third grating is added to the interferometer (Talbot-Lau interferometer), a grating interferometer can even be set up at conventional, low brilliance sources, still yielding the same image contrast signals [Pfeiffer et al., 2006, Pfeiffer et al., 2008]. The additional grating, the source grating (G0), is an absorption grating, and acts to separate the beam into an array of individually coherent, but mutually incoherent line sources (making use of the fact that basically no spatial coherence is required in the direction parallel the grating lines). In order for the line sources to contribute constructively to the interference pattern, the period of the source grating p_0 needs to fulfill the condition $p_0 = p_2 \frac{L}{d}$, where L and d are the distances G0-G1 and G1-G2, respectively [Pfeiffer et al., 2006].

Theoretical considerations and practical implementation show that the MuCLS offers sufficient coherence for a Talbot interferometer in the first Talbot order to be feasible. A detailed discussion and calculation is presented in chapter 4.1.1.

2.3. Computed Tomography

Computed Tomography (CT) provides three-dimensional insights into the imaged object without requiring invasive or destructive techniques. The introduction of CT in the clinics in the 1960s and 1970s has revolutionized the field of diagnostic radiology by providing the examiners with a whole new imaging perspective.

From a technical point of view, CT requires a large set of radiographic projection images to be taken of the object from different angles. Using dedicated reconstruction algorithms, a 3D volume of the object can be reconstructed from these projections.

In clinical practice, state-of-the-art CT systems (e.g. Philips iCT, Siemens Somatom) are capable of acquiring a full-body CT dataset in the timescale of few seconds, yielding a voxel size of approximately 500 µm. On the other hand, dedicated micro- and nano-CT-systems (like for example the commercially available Zeiss Xradia Versa XRM) push the resolution down to a few or even below 1 µm, while the scan time increases to several hours. One of the main technical differences of patient vs. research CT systems is the rotation: clinical CT systems have a gantry that rotates the x-ray source and the detector around the patient, while for micro-CT systems, the source and detector are fixed and the sample is mounted on a rotation stage.

The following sections will outline the most important principles of CT reconstruction, explaining the most commonly known Filtered Backprojection (FBP) algorithm. Necessary adaptations for the tomographic reconstruction of phase-contrast data will be covered. The possibilities of using iterative reconstruction algorithms will briefly be discussed, but the full theoretical description of those would exceed the main focus of this work.

This work will use a parallel-beam geometry to explain the the reconstruction algorithm. Clinical CT systems apply a cone-beam geometry, which will require geometrical adaptations in the reconstruction algorithm.

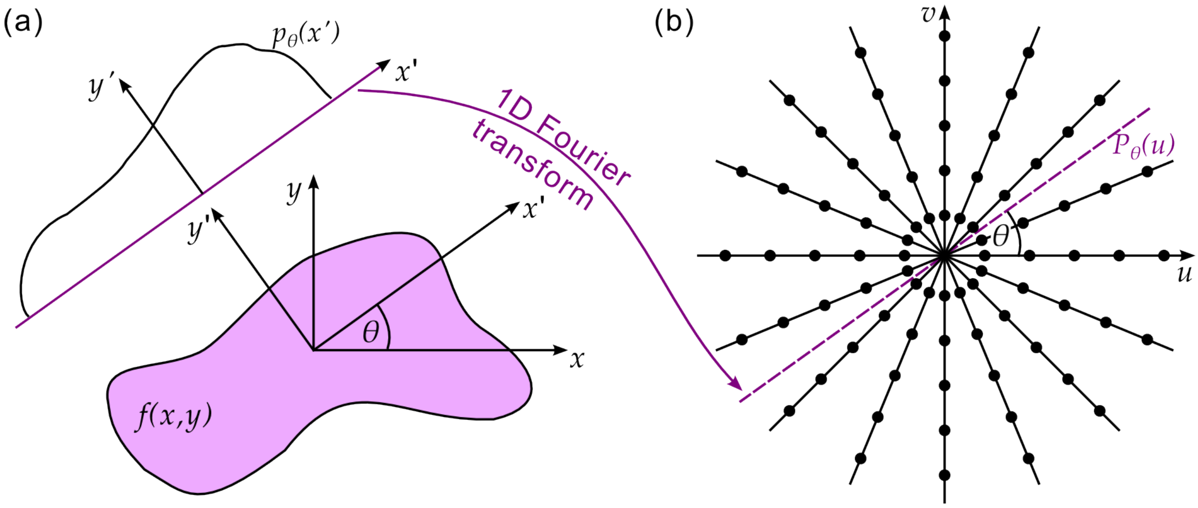

Figure 2.7.: The Fourier Slice Theorem. (a) An object f(x,y) is penetrated by x-rays under an angle θ. The projection $p_\theta(x')$ is given by the line integrals in the rotated coordinate system (x', y'). (b) The Fourier Slice Theorem states that the 1D Fourier Transform of the projection $p_\theta(x')$ equals a slice of the 2D Fourier transform of the object function $\mathcal{F}f(x, y) = P_\theta(u, v)$ under an angle θ. In addition, (b) shows the unequal angular sampling in Fourier space with higher sampling for lower than for higher frequencies.

2.3.1. Fourier Slice Theorem

As mentioned, during the CT data acquisition, the object (or gantry) is rotated by 360°[2], taking a projection image at each given angle increment. For a given projection angle θ, as illustrated in figure 2.7, the projection image is given by the line integral of the object function $f(x, y)$ [Kak and Slaney, 1988],

$$p_\theta(x') = \int f(x', y')\mathrm{d}y', \tag{2.48}$$

expressed in the rotated coordinate system (x', y'). The set of line integrals p_θ under all angles θ is called the Radon transform of the object function $f(x, y)$. The problem under question in CT is to find the inverse Radon transform, i.e. the object function for a measured set of projections.

The central theorem of CT reconstruction towards the solution to the inverse Radon transform is the Fourier Slice Theorem: it relates the 1D Fourier transform of the projection with the 2D Fourier transform of the object function, as will be shown mathematically in the following [Kak and Slaney, 1988] and illustrated in figure 2.7.

Let us consider the Fourier transform of the projection under the simplest case of $\theta = 0$,

$$P_\theta(u) = \mathcal{F}\{p_\theta(x)\} = \int_{-\infty}^{\infty} p_\theta(x)e^{-i2\pi ux}\mathrm{d}x. \tag{2.49}$$

The 2D Fourier Transform of the object function is defined as

$$F(u, v) = \mathcal{F}\{f(x, y)\} = \int_{-\infty}^{\infty}\int_{-\infty}^{\infty} f(x, y)e^{-i2\pi(ux+vy)}\mathrm{d}x\mathrm{d}y. \tag{2.50}$$

---

[2] In principle, a sampling over 180° is also sufficient.

Now we will look at the Fourier Transform along the line $v = 0$ and the integral simplifies to

$$F(u,0) = \int_{-\infty}^{\infty}\int_{-\infty}^{\infty} f(x,y)e^{-i2\pi ux}\mathrm{d}x\mathrm{d}y. \tag{2.51}$$

This expression can be split into two parts as the exponential factor no longer depends on y:

$$F(u,0) = \int_{-\infty}^{\infty}\left[\int_{-\infty}^{\infty} f(x,y)\mathrm{d}y\right] e^{-i2\pi ux}\mathrm{d}x. \tag{2.52}$$

From comparison with equation 2.48 it is obvious that the integral within the brackets equals the projection under the angle $\theta = 0$, hence when substituting equation 2.48 into 2.52, we get

$$F(u,0) = \int_{-\infty}^{\infty} p_{\theta=0}(x)e^{-i2\pi ux}\mathrm{d}x, \tag{2.53}$$

which is equal to equation 2.49. This result is valid for any orientation of the coordinate system.

In words, the 1D Fourier transform of a projection under the angle θ equals the slice of the 2D Fourier transform of the object function under the same angle theta (Fourier Slice Theorem).

Therefore, by measuring a large enough number of projections and computing their 1D Fourier transforms, in principle the object function can be recovered by performing an inverse 2D Fourier transform. However, two issues arise when doing so, which are visualized in figure 2.7 (b): first, the data points obtained from the 1D Fourier transforms are distributed on radial lines, i.e. on a polar grid instead of a rectangular one, hence requiring an interpolation. Second, the sampling becomes sparser with increasing distance from the center, leading to an image quality degradation due to lower sampling for high frequencies.

Requirements for angular sampling

In order to estimate the number of projections to achieve sufficient angular sampling, the distance between two radial lines at the maximum frequency r_{max} in Fourier space needs to be considered [Dierolf, 2015]. The distance must be smaller than the side length Δu of a pixel in reciprocal space, thus the maximum angular step is $\Delta\theta = \Delta u / r_{\mathrm{max}} = \pi / N_{\mathrm{proj}}$, with N_{proj} being the number of equally-spaced projections over an angular range of π. When substituting $r_{\mathrm{max}} = \Delta u \cdot N_{\mathrm{px}}/2$ for an image width of N_{px} pixels, a common rule of thumb for the required number of projections is obtained [Kak and Slaney, 1988],

$$N_{\mathrm{proj}} \approx \frac{\pi}{2} N_{\mathrm{px}}. \tag{2.54}$$

2.3.2. Filtered Backprojection

The issues arising from the unequal sampling in Fourier space are solved by the Filtered Backprojection (FBP) algorithm, where a weighting in the frequency domain is used before backprojecting the data, i.e. smearing each filtered projection over the image plane. This section will present the mathematical derivation of the introduction of a weighting factor in the frequency domain, based on [Kak and Slaney, 1988]. Considering the Fourier Slice Theorem, the object function can be expressed as the inverse 2D Fourier transform,

$$f(x,y) = \int_{-\infty}^{\infty}\int_{-\infty}^{\infty} F(u,v)e^{i2\pi(ux+vy)\mathrm{d}u\mathrm{d}v}. \tag{2.55}$$

When transferring from the rectangular grid (u,v) to a polar coordinate system (r,θ) with

$$\begin{aligned} u &= r\cos\theta \text{ and} && (2.56)\\ v &= r\sin\theta, && (2.57)\end{aligned}$$

the differentials also have to be substituted,

$$\mathrm{d}u\mathrm{d}v = r\mathrm{d}r\mathrm{d}\theta, \tag{2.58}$$

where r is the Jacobian. Equation. 2.55 can now be rewritten in polar coordinates,

$$f(x,y) = \int_0^{2\pi}\int_0^{\infty} F(r,\theta)e^{i2\pi r(x\cos\theta+y\sin\theta)}r\mathrm{d}r\mathrm{d}\theta. \tag{2.59}$$

The integral can be split into two parts, the intervals $\theta = [0,\pi]$ and $\theta = [\pi, 2\pi]$:

$$\begin{aligned} f(x,y) &= \int_0^{\pi}\int_0^{\infty} F(r,\theta)e^{i2\pi r(x\cos\theta+y\sin\theta)}r\mathrm{d}r\mathrm{d}\theta && (2.60)\\ &+ \int_0^{\pi}\int_0^{\infty} F(r,\theta+\pi)e^{i2\pi r(x\cos(\theta+\pi)+y\sin(\theta+\pi))}r\mathrm{d}r\mathrm{d}\theta. && (2.61)\end{aligned}$$

Using the shift property of the Fourier transform,

$$F(r,\theta+\pi) = F(-r,\theta), \tag{2.62}$$

we can rewrite equation 2.61 as

$$f(x,y) = \int_0^{\pi}\left[\int_{-\infty}^{\infty} F(r,\theta)|r|e^{i2\pi r(x\cos\theta+y\sin\theta)}\mathrm{d}r\right]\mathrm{d}\theta. \tag{2.63}$$

With $F(r,\theta) = P_\theta(r)$, the Fourier transform of the projection under the angle θ, the expression becomes

$$f(x,y) = \int_0^{\pi}\underbrace{\left[\int_0^{\infty} P_\theta(r)|r|e^{i2\pi r(x\cos\theta+y\sin\theta)}\mathrm{d}r\right]}_{\text{filtered projection}}\mathrm{d}\theta, \tag{2.64}$$

i.e. the backprojecting of each filtered projection. The filtering corresponds to a multiplication of the Fourier transformed projection with a filter function $H(r) = |r|$ in Fourier space.

Other filter functions than the linear ramp filter $|r|$, like for example the Ram-Lak filter [Ramachandran and Lakshminarayanan, 1971], Shepp-Logan filter, Hamming filter, a cosine filter, or others are also commonly used, depending on the desired effect. In general, there is always a tradeoff between reducing noise and sharpening of edges.

The most commonly known computed implementation of the FBP algorithm is the Feldkamp algorithm [Feldkamp et al., 1984].

2.3.3. CT reconstruction for trimodal data

The FBP algorithm can also be applied to the trimodal image data obtained in grating-based imaging.

In case of the absorption data, the the linear attenuation coefficient μ of the sample can be reconstructed, with the projection function

$$p_\theta(x') = e^{-\int \mu(x',y')\mathrm{d}y'}. \tag{2.65}$$

For dark-field data, the CT reconstruction can be performed without adaptations of the algorithm, using e.g. a Ram-Lak filter [Bech et al., 2009]. In a quantitative reconstruction, the linear diffusion coefficient ϵ can be retrieved,

$$p_\theta(x') = -\frac{p_2^2}{2\pi^2 d^2}\ln V_\theta(x') = \int \epsilon(x',z')\mathrm{d}z'. \tag{2.66}$$

Due to the differential nature of the phase-contrast data obtained in grating-based imaging, an adaptation to the FBP algorithm is necessary. The projection function now is the partial derivative of the object function, the refraction angle α:

$$\alpha_\theta(x') = \frac{p_2}{2\pi d}\phi_\theta(x') = \frac{\lambda}{2\pi}\frac{\partial\Phi_\theta(x')}{\partial x'} = -\int \frac{\partial\delta(x',y')}{\partial x'}\mathrm{d}y', \tag{2.67}$$

where ϕ is the measured differential phase signal, Φ is the actual phase front and δ is the refractive index decrement. This can be used as an input to the FBP algorithm, however, the standard filter function has to be replaced by a Hilbert filter [Pfeiffer et al., 2007b],

$$H(r) = \frac{1}{2\pi} i\,\mathrm{sgn}(r), \tag{2.68}$$

where $\mathrm{sgn}(r)$ is the signum function. It is important to note that the multiplication with the Hilbert filter in Fourier space corresponds to an integration of the differential projections in real space, i.e. the reconstruction will yield the actual phase signal.

2.3.4. Advanced reconstruction techniques

While the FBP algorithm is easily implemented and computationally fast, it is rather limited with respect to a possible reduction of required number of projections (and, subsequently, dose) and noise, while preserving small features. In addition, an equal spacing of the projections is required. Therefore, advanced iterative reconstruction schemes have been developed and employed in clinical practice and elsewhere throughout the last decades. They are capable of reducing noise while requiring far fewer projections, at the cost of increased computation power.

The basic principle of iterative reconstruction is to generate a first estimate for the reconstructed image (e.g. through FBP), forward project this image, compare it with the measured projections, update the estimate based on the discrepancies and the constraints imposed by the chosen algorithm, and repeat these steps until convergence.

Best known algorithm types are the algebraic reconstruction technique (ART) [Gordon et al., 1970], the simultaneous iterative reconstruction technique (SIRT) [Gilbert, 1972], and the simultaneous algebraic reconstruction technique (SART) [Andersen and Kak, 1984]. Most advanced are statistical iterative reconstruction (SIR) algorithms and these types of algorithms have been adapted in clinical CT systems [Beister et al., 2012].

Not only can iterative reconstruction algorithms reduce noise and allow for lower dosages to be applied, for example they can also be used to remove or reduce metal artifacts in absorption images or bone artifacts in phase-contrast images [Hahn et al., 2015].

3. The MuCLS

The Munich Compact Light Source (MuCLS) is a compact synchrotron source based on inverse Compton scattering. The performance of the MuCLS lies between that of a conventional x-ray tube source and a large-scale synchrotron. This chapter will first explain some figures of merit that are commonly used to compare different x-ray sources. The working principles of different x-ray sources, with x-ray tubes and synchrotron sources being the most common ones, will be presented. The majority of this chapter is dedicated to the MuCLS, explaining the physical background of the x-ray generation, and then highlighting the most important aspects of the technical realization and the operation of the MuCLS.

3.1. X-ray source technology

3.1.1. Figures of merit

Several figures of merit exist that are used to compare the performance of different x-ray sources. Some of the most important parameters of an x-ray source are the photon flux, the brilliance and the coherence. Depending on the chosen imaging technique, there may be different requirements on these parameters based on which the type of x-ray source best suited to the task can be chosen.

Brilliance

Besides the photon flux, the spectral brightness or brilliance is an important measure, providing the photon flux per unit area and per unit solid angle within a relative spectral bandwidth (BW). It gives a measure of how monochromatic the x-ray beam is, how small the source size is and how collimated the beam is. The brilliance is defined as the flux Φ radiated from an area ΔA into a solid angle $\Delta\Omega$ within the spectral BW $\Delta\omega/\omega$ [Attwood, 2007],

$$B = \frac{\Phi}{\Delta A \cdot \Delta\Omega \cdot \Delta\omega/\omega}. \tag{3.1}$$

Usually, the flux Φ is expressed in photons per second and thus brilliance is given in the units [Willmott, 2011]

$$[B] = \frac{\text{photons/s}}{\text{mrad}^2 \cdot \text{mm}^2 \cdot 0.1\%\ \text{BW}}. \tag{3.2}$$

Figure 3.1 provides an overview how the brilliance of different types of x-ray sources steadily increased with the invention of new types of sources. The MuCLS, as a compact

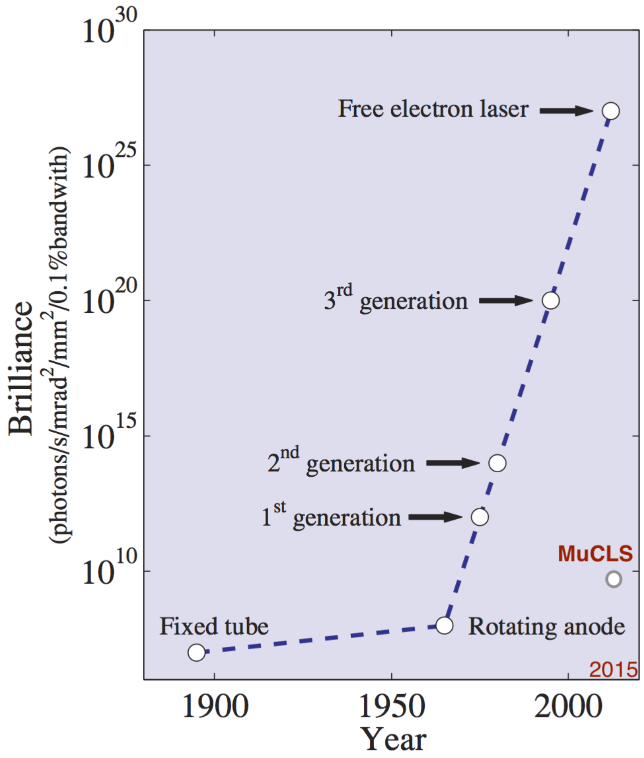

Figure 3.1.: The brilliance of different types of x-ray sources. Over time, the technology of x-ray sources and their brilliance have undergone a tremendous development. The MuCLS currently offers a brilliance that lies in between that of rotating anode x-ray tube sources and bending magnet radiation. Figure adapted from [Als-Nielsen and McMorrow, 2011].

synchrotron source, offers a brilliance that lies in between that of rotating anode x-ray tubes and bending magnets.

Emittance

The emittance of a beam is defined as the product of the linear source size with the beam divergence [Willmott, 2011],

$$\epsilon_x = \sigma_x \sigma'_x, \tag{3.3}$$

$$\epsilon_y = \sigma_y \sigma'_y, \tag{3.4}$$

where σ_x and σ_y are the standard deviations of the Gaussian beam profile and σ'_x and σ'_y are the corresponding angular divergences. A minimization of the emittance is desired as the brilliance scales inversely with the emittance. The fundamental lower limit to the emittance is given by Heisenberg's uncertainty principle [Willmott, 2011],

$$\epsilon_{\text{min}} = \frac{\lambda}{4\pi}. \tag{3.5}$$

Coherence

Various x-ray imaging techniques need the x-ray wavefront to propagate over long distances with minimal divergence or require for interference effects to take place, and therefore need x-ray waves with well-defined phase and amplitude variations. These properties are described by the term coherence. For example, conventional laboratory x-ray tube sources do not offer enough coherence for various x-ray imaging applications, like phase-contrast imaging (PCI), coherent diffraction imaging (CDI) or ptychography.

Real sources with a finite size are always partially coherent: they are not perfectly monochromatic and the beam does not propagate in a perfectly well defined direction [Als-Nielsen and McMorrow, 2011]. The spatial and temporal scales over which the radiation is well-defined in phase and amplitude are expressed through coherence lengths [Attwood, 2007].

- **Longitudinal coherence**: The longitudinal coherence length l_{coh} is defined along the direction of propagation of the wavefront and depends on the spectral bandwidth $\Delta\lambda$. It is defined as the distance it takes two waves with a difference in wavelength of $\Delta\lambda$ from being in phase to being exactly 180° out of phase:

  $$l_{\text{coh}} = \frac{\lambda^2}{2\Delta\lambda}. \tag{3.6}$$

  For example in interferometry or holography, where beams are split and recombined, it is essential that the difference in propagation length is smaller than the coherence length.
- **Spatial coherence**: The spatial (or transverse) coherence is defined perpendicular to the propagation direction and is related to the finite source size and angular divergence. Only a point source emitting a spherical wave will offer full coherence - how small the point source needs to be, can be deduced through Heisenberg's uncertainty principle,

  $$d \cdot \theta = \frac{\lambda}{2\pi}, \tag{3.7}$$

  where d is the source diameter and θ is the divergence half angle. Radiation from a source fulfilling this relation is called diffraction limited.

  The spatial coherence length $l_{\text{transverse}}$ is defined as

  $$l_{\text{transverse}} = \frac{\lambda L}{2\pi d}, \tag{3.8}$$

  with L the distance from the source.

  An example for a technique relying on the highest possible spatial coherence is scanning x-ray microscopy with diffraction limited focusing.

Coherence is an important subject in phase-sensitive x-ray imaging techniques, as they rely on propagation and interference effects. Coherence lengths greatly differ for the two most common types of x-ray sources: x-ray tubes and synchrotrons.

3.1.2. X-ray tube sources

The first widely available x-ray tube source was the so-called Coolidge tube, developed in 1912. Electrons are emitted from a glowing filament, accelerated towards a water-cooled metal anode, where x-rays are produced in two distinct processes. Electrons are decelerated (and eventually stopped) as they enter the metal, with the lost energy emitted as *bremsstrahlung*, generating a continuous x-ray spectrum. The maximum

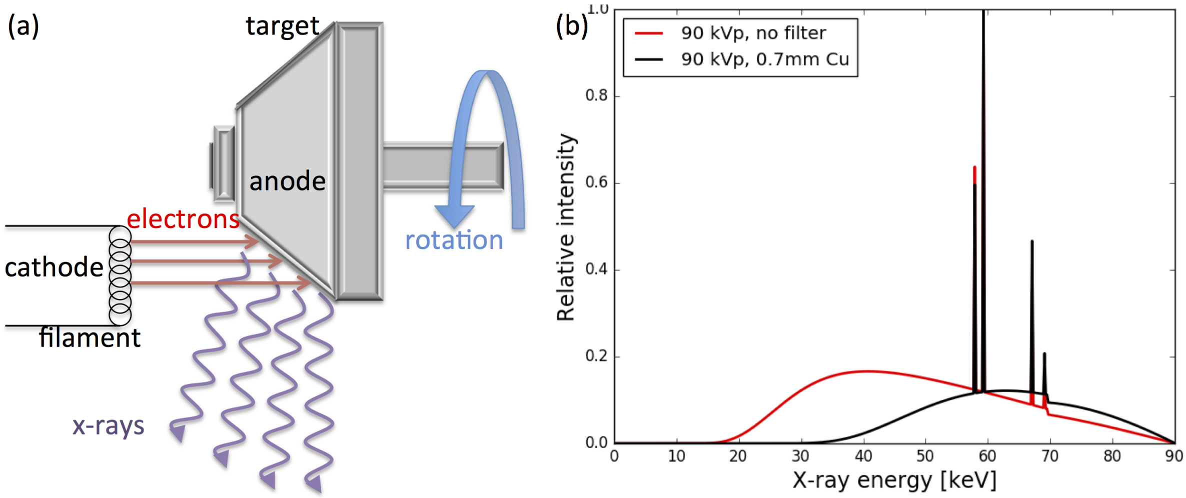

Figure 3.2.: X-ray tube source. (a) Schematic drawing of a rotating anode x-ray tube. Electrons are accelerated and hit the metal anode target, generating the continuous and characteristic x-ray spectrum. (b) A 90 kVp (90 kV peak acceleration voltage) x-ray spectrum for a tungsten anode, shown without filter (red) and filtered with 0.7 mm of copper (black). Spectra provided by Tobias Reusch, Philips AG, Germany [Reusch, 2016].

energy of the spectrum corresponds to the acceleration voltage applied to the x-ray tube. In addition to the continuous spectrum, an x-ray tube spectrum exhibits characteristic emission lines that arise from collisions of the impinging electrons with core electrons of the anode metal, removing them from the inner shells. The energy difference of the electron filling the vacancy from an outer shell is emitted as a photon with the energy of a characteristic line.

The next step in x-ray source development was the commercial availability of rotating anode x-ray tubes in the 1960s, which significantly increased the power output and brilliance compared to Coolidge tubes. The basic principle is the same as for the Coolidge tube, but the anode is rotated, allowing for a tremendous increase in heat dissipation and therefore output power. A schematic drawing of a rotating anode x-ray tube is shown in figure 3.2 (a) and a typical tube spectrum in figure 3.2 (b). Typically used materials for the anode are tungsten or molybdenum, differing in their characteristic lines. Rotating anode x-ray tubes offer a brilliance of approximately $10^8 - 10^9$ photons/s/(mm^2 mrad^2 0.1% BW).

3.1.3. Synchrotron sources

Synchrotron x-ray sources have had a tremendous impact on x-ray imaging, enabling the further development of techniques like crystallography that made it possible to resolve the structure of molecules. When the first synchrotrons were built in the 1950s and 1960s, they were intended as accelerators and synchrotron radiation was regarded as an unwanted energy loss of the electrons. In the 1960s, synchrotron radiation from bending magnets was started to be used for imaging (1st generation synchrotron facilities). The first facilities dedicated for synchrotron radiation were built in the 1980s (2nd generation). An immense gain in brilliance was made possible through designs that relied heavily on insertion devices (wigglers and undulators) as the main sources of radiation. The first facility of this 3rd generation was the European Synchrotron Radiation Facility (ESRF) (Grenoble, France) in 1994 with a brilliance of up to 10^{20} photons/(s mm^2 mrad^2 0.1% BW) [Willmott, 2011].

A modern 3rd generation synchrotron consists of an electron gun, a linear accelerator, a booster electron storage ring and the large electron storage ring with electron energies of several GeV. From this ring, many beamlines run off tangentially, either along the axes of insertion devices or tangentially at bending magnets [Willmott, 2011]. Before entering the experimental hutch, the x-ray beam can be monochromatized and/or focused.

In the following, the generation of synchrotron radiation in an undulator will be described, as it is the most relevant aspect with regard to compact synchrotrons like the MuCLS.

Undulators

Undulators, like wigglers, are insertion devices and are placed in straight sections of the storage ring. Magnet arrays manipulate the electrons' path to follow an oscillation while maintaining their average direction, producing synchrotron radiation caused by the oscillations.

Electrons moving at relativistic speeds along a circular arc will emit synchrotron radiation, directed in a narrow radiation cone in the same direction as the electron motion. The opening angle of the cone is $\theta \approx \frac{1}{\gamma}$, where γ is the Lorentz factor

$$\gamma = \frac{E_e}{mc^2}, \tag{3.9}$$

where E_e is the total electron energy and $mc^2 = 511$ keV is the rest energy of the electron.

An undulator, which is schematically shown in figure 3.3, coerces the electrons on an oscillatory path by magnet force. The excursions are of the order of γ^{-1} such that the emitted radiation cones overlap and interfere with each other. The amplitudes add up vectorially and the intensity is given by the square of the sum, peaking at those wavelengths with constructive interference[1] [Willmott, 2011].

An insertion device is characterized by the K-parameter, which is related to the maximum angular deviation $\phi_{\max}$ of the electron oscillations [Willmott, 2011],

$$K = \phi_{\max}\gamma, \tag{3.10}$$

or can be expressed in dependence on the maximum magnetic field B_0,

$$K = \frac{eB_0}{mck_u} = 0.934\lambda_u[\mathrm{cm}]B_0[\mathrm{T}], \tag{3.11}$$

where λ_u is the period of the oscillations in the undulator and $k_u = 2\pi/\lambda_u$. For a long undulator, $K \ll 1$.

---

[1] In contrast, a wiggler is characterized by excursions larger than the natural opening angle γ^{-1}, with the radiation cones not overlapping and thus the intensities adding up. A wiggler is characterized by incoherent superposition, an undulator by coherent interference.

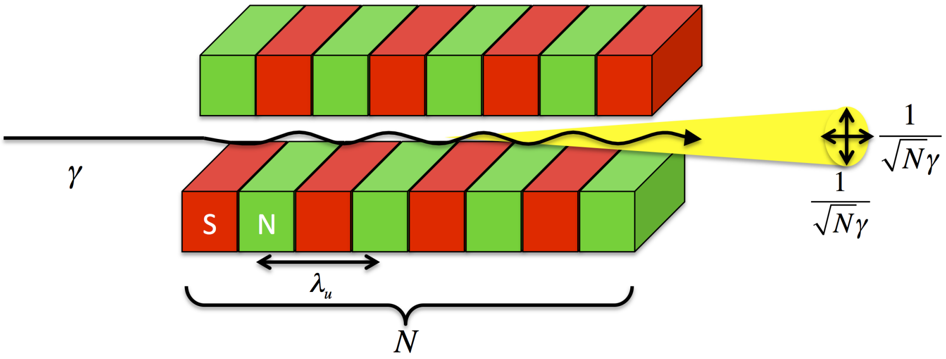

Figure 3.3.: Schematic diagram of an undulator. Alternating magnets force the electrons on an oscillating path and overlapping radiation cones are emitted. The opening angle of the resulting radiation added up from the single radiation cones from each oscillation is $1/(\sqrt{N}\gamma)$.

The opening angle of undulator radiation is approximately given by $\frac{1}{\sqrt{N}\gamma}$, where N is the number of periods of the magnets [Attwood, 2007]. The bandwidth of the undulator scales with N, $\Delta\lambda/\lambda = 1/N$.

Due to the overlapping and interfering radiation cones from each oscillation in an undulator, the undulator spectrum consists of a fundamental frequency plus a series of higher harmonics. The fundamental wavelength λ_1 of the undulator under an observation angle θ is given by [Attwood, 2007, Als-Nielsen and McMorrow, 2011]

$$\lambda_1 = \frac{\lambda_u}{2\gamma^2}\left(1 + \frac{K^2}{2} + \gamma^2\theta^2\right). \tag{3.12}$$

It follows that the undulator wavelength is contracted by $2\gamma^2$ on axis, but increased by a factor $(1 + \gamma^2\theta^2)$ off-axis and thus only near-axis radiation should be observed for narrow bandwidths. The fundamental wavelength λ_1 is tunable by adjusting the K-parameter, i.e. by changing the gap between the two sets of magnetic poles.

The on-axis undulator spectrum shows higher harmonics at odd multiples of the fundamental wavelength. Higher-order harmonics are more intense for a high-K than for a low-K undulator [Willmott, 2011].

3.1.4. Tabletop synchrotron sources

Synchrotron sources are by far the most brilliant x-ray sources and many imaging techniques require a monochromatic, highly brilliant and highly coherent beam. However, the large size and high cost of synchrotrons restrict them to large-scale research facilities and limit the accessibility. Therefore, research has not only been dedicated to making synchrotrons even more brilliant, but also to the development of brilliant laboratory-scale x-ray sources. Their brilliance lies between that of a rotating anode x-ray tube and a bending magnet. Mainly, three different paths are followed [Willmott, 2011]:

- **Inverse Compton sources**: the electromagnetic field of a laser beam causes electrons to wiggle and emit radiation with a spectrum similar to that produced by a long undulator. In the particle picture, this process is described as inverse Compton scattering. Several attempts to build an inverse Compton source have been started world wide: the Compact Light Source (CLS) [Loewen, 2003, Lyncean, 2017], ThomX [Variola, 2011, Variola et al., 2014], Compton source at AIST [Kuroda et al., 2011], Compton source at BNL ATF [Pogorelsky, 2016] and Tsinghua Thomson Scattering X-ray Source [Tang et al., 2009, Chi et al., 2017]. The designs differ, with these approaches based either on electron storage rings or on linacs. Most of these sources are still under development and functionality remains to be proven or has been demonstrated in first experiments, with the CLS being the only commercially available product [Eggl et al., 2016a].

- **Laser-wakefield accelerator**: the electromagnetic field of a laser pulse propagating through a dilute plasma will induce a locally high degree of charge separation and a subsequent strong potential gradient. This wakefield propagates trough the plasma and will accelerate electrons injected into it. The electrons will execute an oscillatory path, producing undulator-like synchrotron radiation (betatron radiation) [Willmott, 2011, Kneip et al., 2010, Tajima and Dawson, 1979, Wenz et al., 2015].
- **High-harmonic generation**: ultrashort laser pulses are used to tunnel-ionize atoms in a gas. The emitted electron will accelerate in the laser field and hereby gain energy, which can then be released as harmonics of the fundamental laser when the electron recombines with the ion. The emission of extreme UV or x-radiation is pulsed and perfectly synchronized to the driving laser [Kapteyn et al., 2005, Popmintchev et al., 2012].

The experiments presented in this work have been performed at the Munich Compact Light Source (MuCLS), the first commercial installation of the Compact Light Source based on inverse Compton scattering. This compact synchrotron source will be described in detail in the following section.

3.2. The MuCLS - a compact synchrotron

The Munich Compact Light Source (MuCLS) is a compact synchrotron based on inverse Compton scattering. The MuCLS was developed and manufactured by Lyncean Technologies Inc., USA [Lyncean, 2017]. X-rays are generated in the collision of relativistic electrons with laser photons. Due to the wave-particle dualism, the source can also be described as a laser undulator. The analogy of the two descriptions will be explained in what follows. Furthermore, the technical realization in a laser-electron storage ring will be described and properties of the generated x-ray beam will be derived.

3.2.1. Physics of an inverse Compton source

The following explanations are based on [Loewen, 2003, Loewen et al., 2015], if not stated otherwise.

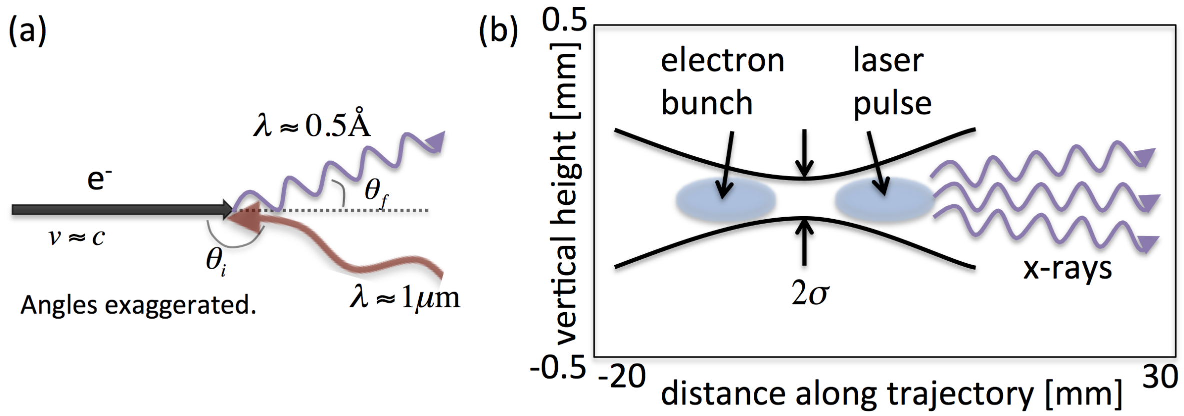

Figure 3.4.: (a) **Schematic representation of inverse Compton scattering.** A relativistic electron (e-) collides with an infrared laser photon. The photon is backscattered and receives energy from the electron so its energy now is in the x-ray regime. The incident collision angle is $\theta_i \approx \pi$ and the x-ray photon is preferably scattered into an opening angle $\theta_f \lesssim \frac{1}{\gamma}$.
(b) **Electron-photon beam-beam interaction.** An electron and a photon beam collide, producing a burst of x-ray photons. For simplicity, the beams are drawn with matched waists, i.e. equivalent waist size and focus depth.

Inverse Compton scattering

Inverse Compton scattering (sometimes also called Thomson backscattering)[2] can classically be viewed as the elastic collision of two particles, a relativistic electron and a laser photon, as shown in figure 3.4 (a). Following the conservation of the 4-momenta before and after scattering,

$$\left(\frac{E_e}{c}, \overrightarrow{p}\right) + \left(\frac{E_L}{c}, \hbar\overrightarrow{k}\right) = \left(\frac{E'_e}{c}, \overrightarrow{p}'\right) + \left(\frac{E_x}{c}, \hbar\overrightarrow{k}'\right), \tag{3.13}$$

where $\overrightarrow{p}$ and $\hbar\overrightarrow{k}$ are the momenta of the electron and the laser photon before the collision, respectively, and after collision with the prime. From squaring this relation, one can obtain an expression for the energy of the backscattered x-ray photon,

$$E_x = \frac{E_L(1-\beta\cos\theta_i)}{(1-\beta\cos\theta_f) + \frac{E_L}{E_e}(1-\cos(\theta_f-\theta_i))}, \tag{3.14}$$

with $\beta = \frac{v}{c}$ (v is the speed of the incident electron) and θ_i and θ_f the angles before and after collision as shown in figure 3.4 (a).

For head-on collision ($\theta_i = \pi$) and backscattering of the photon ($\theta_f = 0$), the relation simplifies to

$$E_x = \frac{E_e(1+\beta)E_L}{(1-\beta)E_e + 2E_L}. \tag{3.15}$$

---

[2] Thomson scattering is the low-energy limit of Compton scattering, i.e. when the laser energy is much lower than the electron rest energy. In the electron rest frame, the energies stays constant. In the laboratory frame though, due to the relativistic speed of the electron, the particles' kinetic energies are changed, with conservation of the 4-momenta.

When neglecting the recoil of the electron ($E_L \ll m_0c^2$), substituting $\gamma = \frac{1}{\sqrt{1-\beta^2}}$ and assuming $\beta \approx 1$, we get a rather simple expression for the on-axis x-ray energy:

$$E_x \approx \frac{E_L(1+\beta)^2 E_e}{E_e/\gamma^2} \approx 4\gamma^2 E_L. \tag{3.16}$$

The on-axis energy in dependence on the energy of the electron as calculated from equation 3.16 is plotted in figure 3.5 (a). The range of electron energies available for the CLS is 25-45 MeV, yielding maximum x-ray energies between 11-35 keV.

For a given incident collision angle (for simplicity, we will assume $\theta_i = \pi$), the x-ray energy can be calculated in dependence on the scattering angle θ_f,

$$E_x(\theta_f) = \frac{E_e(1+\beta)E_L}{E_e(1-\beta\cos\theta_f) + E_L(1-\cos(\pi-\theta_f))}. \tag{3.17}$$

Making a Taylor expansion for $\beta = \frac{1}{\sqrt{1-\frac{1}{\gamma^2}}} \approx 1 - \frac{1}{2\gamma^2}$ and the two cosines $\cos\theta = 1 - \frac{\theta^2}{2}$, we obtain for the off-axis x-ray energy

$$E_x \approx \frac{4\gamma^2 E_L}{1+\theta_f^2\gamma^2}, \tag{3.18}$$

having made the simplifications $\gamma^2 \gg 1$ and $\theta_f^2\gamma^2 \gg \theta_f^2/2$. In principle, based on the dependence in eq. 3.18, spectral filtering (i.e. monochromatization) of the x-ray beam can be accomplished by collimating the x-ray beam using an aperture[3]. The off-axis energy in dependence on the scattering angle θ_f is plotted in figure 3.5 (b) for the three x-ray energies most commonly used at the MuCLS (15, 25 and 35 keV). While the energy falls off rather quickly for scattering angles > 5 mrad, the x-ray energy stays almost constant within the collimation of ±2 mrad chosen for the CLS.

The angular intensity distribution for this case of head-on collision is given by the Klein-Nishina formula for scattering in the laboratory frame [Stepanek, 1998],

$$\frac{\mathrm{d}\sigma}{\sin\theta_f \mathrm{d}\theta_f} = \pi r_e^2 \frac{1-\beta^2}{(1-\beta\cos\theta_f)^2} R^2 \left(R + \frac{1}{R} - 1 + \left(\frac{\cos\theta_f - \beta}{1-\beta\cos\theta_f} \right)^2 \right), \tag{3.19}$$

where R is the ratio between the laser photon energy and the X-ray photon energy in the electron rest frame. R can be derived from equation 3.14 when setting $\beta = 0$ for the electron being at rest and further assuming $\theta_i = \pi$,

$$R = \frac{1}{1 + \frac{E_L^{\mathrm{ER}}}{mc^2}(1+\cos\theta_f)}, \tag{3.20}$$

where E_L^{ER} is the laser energy in the electron rest frame which can be approximated by $2\gamma E_L$. A polar plot of the angular intensity distribution $\frac{\mathrm{d}\sigma}{\sin\theta_f \mathrm{d}\theta_f}$ is displayed in figure 3.5 (d). The plot shows that the intensity falls off rapidly for scattering angles $\gtrsim$ 5 mrad, but within the ±2 mrad cutoff decreases by less than 10%.

---

[3] The x-ray spectrum is also dependent to a large extent on electron beam emittance. Equation 3.18 gives the case of a perfect electron beam with zero emittance.

The differential scattering cross-section for inverse Compton scattering with respect to the energy E_x can be expressed with the Klein-Nishina formula,

$$\frac{\mathrm{d}\sigma_{\mathrm{KN}}}{\mathrm{d}E_x} = \frac{\pi r_e^2}{2}\frac{1}{\gamma^2 E_L}\left[\frac{E_e^2}{4\gamma^2 E_L^2}\left(\frac{E_x}{E_e - E_x}\right)^2 - \frac{E_e}{\gamma^2 E_L}\frac{E_x}{E_e - E_x} + \frac{E_e - E_x}{E_e} + \frac{E_e}{E_e - E_x}\right], \tag{3.21}$$

having used $\frac{\mathrm{d}\sigma}{\mathrm{d}E_x} = \frac{\mathrm{d}\sigma}{\mathrm{d}\theta_f}\frac{\mathrm{d}\theta_f}{\mathrm{d}E_x}$.

The energy distribution for the x-ray beam scattered into the full angular range can be obtained from integrating the angular intensity distribution over the full angular range which yields the cross section in dependence on the x-ray energy [Sun and Wu, 2011]

$$\frac{\mathrm{d}\sigma}{\mathrm{d}E_x} = \frac{8\pi r_e^2}{X(\beta E_e - E_x)}\left[\left(\frac{1}{X} - \frac{1}{Y}\right)^2 + \frac{1}{X} - \frac{1}{Y} + \frac{1}{4}\left(\frac{X}{Y} + \frac{Y}{X}\right)\right], \tag{3.22}$$

where X and Y are Lorentz invariant quantities:

$$X = \frac{2\gamma E_x(1+\beta)}{mc^2}; \tag{3.23}$$

$$Y = X \cdot \frac{\beta E_e - E_x}{\beta E_e - E_l}. \tag{3.24}$$

A plot in figure 3.5 (c) visualizes the spectrum of inverse Compton scattering over the full angular range for the case of an unpolarized electron and a polarized laser photon and when neglecting the recoil effect according to equation 3.22. The high-energy cutoff is defined by the incident electron and photon energies E_e and E_l. In the case that an aperture is used, the energy spectrum has a low energy cutoff as well, defined by the maximum allowed angle. For the case of the CLS, where the beam is collimated to scattering angles ±2 mrad, only the part of the spectrum marked in magenta is sampled.

Please note that these theoretical calculations give the case of a perfect electron beam with zero emittance (i.e. a parallel electron beam pointing towards the center of the output aperture). For a realistic electron beam, the emittance of the electron beam will have a Gaussian distribution of angles, which smeares out the energy-angle correlation given by equation 3.18. This has the effect of the spectrum being broadened towards the low-energy tail, however, a real electron beam with non-zero emittance will have the (for imaging applications positive) effect of making the x-ray spectrum more uniform across an aperture, i.e. weakening the angle dependency of the energy shown in figure 3.5 (b).

Laser undulator

Alternatively, the interaction between the electron and the laser beam can be described in the wave picture. In this case, the electrons see the counter-propagating laser pulse as an electromagnetic field (cf. figure 3.4 (b)). This field acts on the electrons like the field of a permanent magnet undulator (described in section 3.1.3), causing the electrons to follow an oscillatory path and emit radiation.

The undulator parameter K can be expressed, like for the permanent magnet case, as

$$K = \gamma\phi_{\max} = \frac{e\lambda_u B_u}{2\pi m_0 c}, \tag{3.25}$$

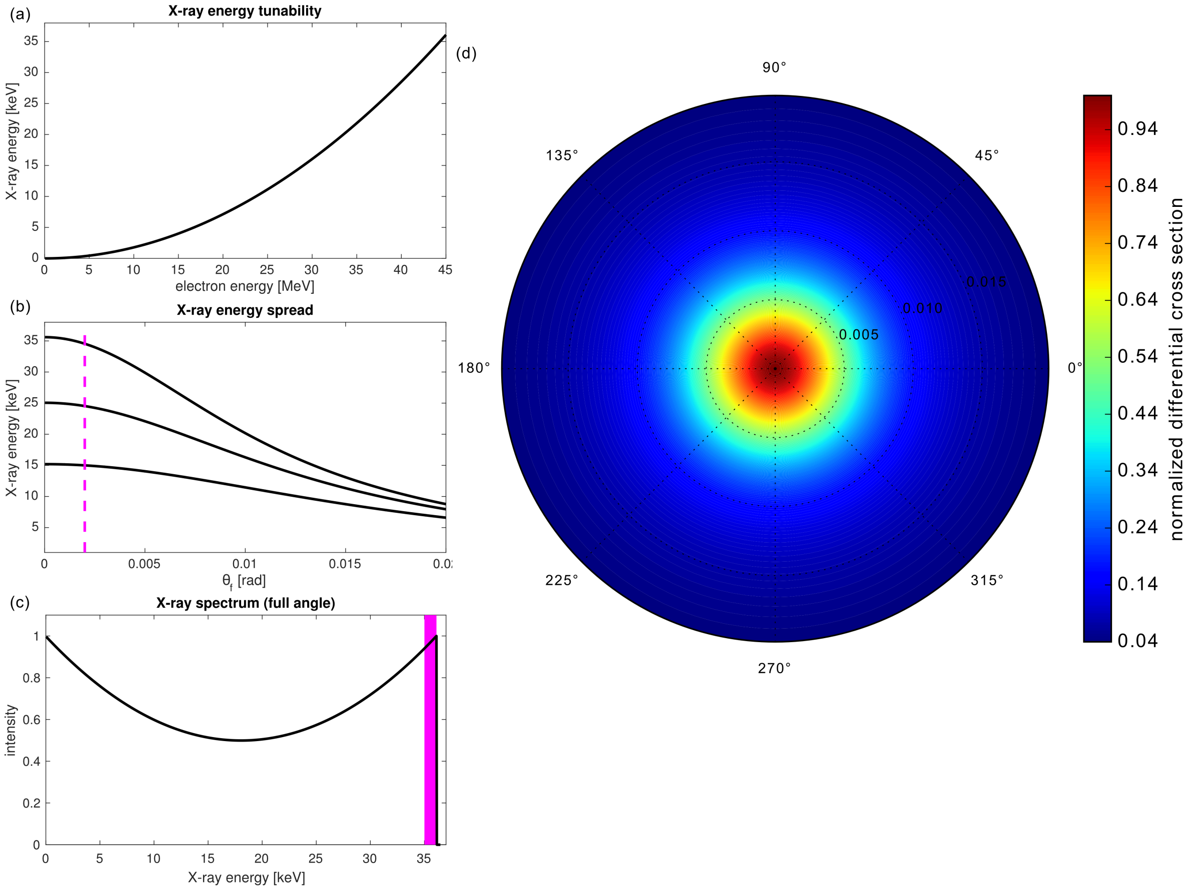

Figure 3.5.: Expected spectrum and differential cross sections of inverse Compton scattering as theoretically calculated. (a) The x-ray energy can be tuned by adjusting the electron energy. The possible electron energy range for the CLS is 25-45 MeV. (b) The x-ray energy decreases with increasing observation angle θ_f (cf. equation 3.18) (shown for head-on collision). The dashed lines indicate the ± 2 mrad cut-off of the CLS. The energy decrease off-axis is shown for the three most commonly used x-ray energies at the MuCLS (15, 25 and 35 keV). (a)-(b) adapted from [Schleede, 2013]. (c) The plotted curve shows the spectrum from an inverse Compton source at 45 MeV electron energy when the full angular range is sampled as calculated by equation 3.22 [Sun and Wu, 2011]. The magenta section shows the part of the spectrum which is used by the CLS in the 4 mrad collimation. (d) The differential cross-section $\frac{d\sigma}{\sin\theta_f d\theta_f}$ decreases with increasing observation angle θ_f (cf. equation 3.19). The CLS beam is collimated to 0.002 rad. Figure courtesy of Klaus Achterhold.

where $\phi_{\max}$ is the maximum angular deviation of the electron oscillation, and B_u is the peak magnetic field. The effective laser magnet field strength B_u seen by the electrons is given by

$$B_u = \frac{2}{c}\sqrt{2Z_0 I_0}, \tag{3.26}$$

where $Z_0 = \frac{1}{c\epsilon_0} = 377\,\Omega$ is the free space impedance and I_0 is the laser intensity. For a realistic value of $I_0 = 10^{12}\,\mathrm{W/cm}^2$, the effective magnetic field strength is $B_u \approx 20$ T. For a laser wavelength in the infrared (IR) range, this yields $K \approx 10^{-3}$, i.e. the laser pulse acts like a weak static undulator magnet with $N_u = 25\,\mathrm{ps} \cdot \frac{c}{\lambda_l/2} = 14000$ periods.

Looking at the undulator equation for off-axis radiation (3.12),

$$\lambda_1(\theta) = \frac{\lambda_u}{2\gamma^2}(1 + \frac{K^2}{2} + \gamma^2\theta^2), \tag{3.27}$$

and substituting $E = \frac{hc}{\lambda}$ and $\lambda_u = \frac{\lambda_L}{2}$ while neglecting the K-term ($K^2 \ll 1$ for a weak long undulator), we obtain

$$E_x = \frac{4\gamma^2 E_L}{1 + \gamma^2\theta^2}, \tag{3.28}$$

which is equivalent to equation 3.18 derived from the electron-photon scattering case.

The radiated power per electron from a weak undulator ($K \ll 1$) is given by

$$P = \frac{4\pi\epsilon_0}{3} r_e^2 c^3 \gamma^2 B_u^2 = \frac{32\pi}{3} r_e^2 \gamma^2 I_0. \tag{3.29}$$

For the laser undulator with a linearly polarized laser beam, the x-ray beam inherits the linear polarization, strongly peaked in the forward direction. A small amount of circular polarization is introduced in the enhancement cavity.

3.2.2. X-ray beam properties

Spectrum

The spectrum can be predicted for given undulator parameters (cf. eq. 3.22) and output aperture. For a real electron beam, the model needs to be extended by folding in the electron beam emittance and electron beam energy spread. The real spectrum will be broadened due to the Gaussian distribution of electron angles.

At a fixed observation angle θ_f, the finite interaction length of the laser pulse will broaden the spectral width of the radiated beam,

$$\frac{\Delta E}{E} \simeq \frac{1}{N} = \frac{1}{2\sigma_z/\lambda_L}, \tag{3.30}$$

where N is twice the number of wavelengths λ_L over the interaction length (i.e. laser pulse length) σ_z.

The angular spread for a small relative bandwidth $\frac{\Delta E_x}{E_x}$ around the peak energy is naturally collimated much better than the full $1/\gamma$ opening angle and falls within an

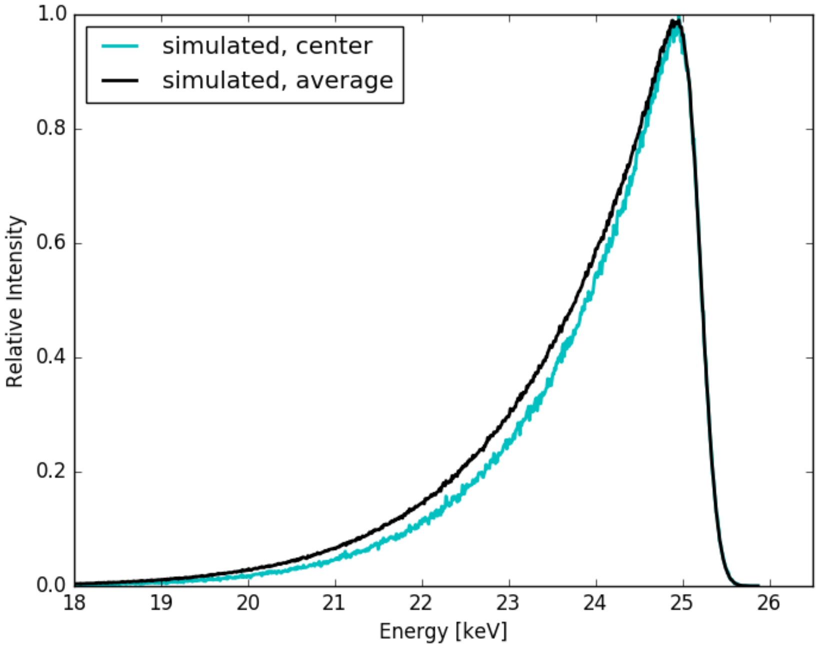

Figure 3.6.: Predicted MuCLS spectra from a Monte Carlo simulation. The simulation takes into account the physics of inverse Compton scattering, folding in the properties of a real electron beam (energy spread and emittance). The spectrum averaged across the whole aperture is slightly broader than the one in the center of the beam. Simulated spectra courtesy of Rod Loewen, Lyncean Technologies Inc. [Loewen, 2017].

angle[4]

$$\theta_{f\,\max} = \frac{1}{\gamma}\sqrt{\frac{\Delta E}{E}}. \tag{3.31}$$

The forward intensity is increased by a factor ~ 3 for small bandwidths, i.e. for a desired relative bandwidth of 1% around the peak energy, about 3% of the total power is confined within a forward cone of ~ 2 mrad.

For a given beam energy spread σ_E, the spectral width (eq. 3.30) will broaden as $\frac{\Delta E}{E} = 2\frac{\sigma_E}{E_e}$. The intrinsic angular spread will subsequently broaden, too, as follows from equation 3.31. For example, for a design energy spread of 0.3%, the intrinsic angular spread of the x-ray beam would be ~ 1 mrad.

The angular spread θ_e can be calculated from the normalized emittance $\epsilon^n = \gamma\sigma_r\theta_e$, where σ_r is the relative electron spot size given by the beta function. For a given spot size of 30 µm, $\epsilon^n = 5$ µm, and $\gamma \simeq 50$, the natural beam divergence is ~ 3.3 mrad. The full energy spread of the x-ray beam then would be $\sim 2.7\%$ (cf. eq. 3.18).

It is important to note that the x-ray beam inherits the same emittance as the electron beam. The majority of the flux from the laser undulator is confined in a total angle slightly larger than the average angular spread of the electron beam, $\theta_e = \frac{\epsilon^n}{\gamma\sigma_r}$.

The spectrum of the MuCLS can be simulated, taking into account the electron energy,

---

[4] This is consistent with the opening angle for undulator radiation given by $1/(\sqrt{N}/\gamma)$ [Attwood, 2007], since the relative bandwidth is given by $1/N$.

the electron beam energy spread, and the emittance of the electron beam, which will determine the peak x-ray energy, the upper slope of the spectrum, and the lower slope of the low-energy tail, respectively [Loewen, 2017]. Simulated spectra for the center of the beam and for an average across the full MuCLS aperture are shown in figure 3.6. The bandwidth slightly increases towards the edges of the aperture.

Flux

The total flux for the electron-photon beam-beam interaction, schematically displayed in figure 3.4 (b), is given by

$$\dot{N}_x = \mathcal{L}_0 \sigma_{\mathrm{Th}}, \tag{3.32}$$

where $\sigma_{\mathrm{Th}} = \frac{8\pi}{3} r_e^2 = 6.65 \cdot 10^{-29}\,\mathrm{m}^2$ is the Thomson cross section with $r_e = 2.82 \cdot 10^{-15}$ m, the classical electron radius. The luminosity $\mathcal{L}_0$ for two Gaussian beams with matched waists is defined as

$$\mathcal{L}_0 = \frac{N_e N_L f_c}{4\pi\sigma_r^2} = \frac{N_e N_L f_c}{2\pi\sqrt{\sigma_{ex}^2 + \sigma_{Lx}^2}\sqrt{\sigma_{ey}^2 + \sigma_{Ly}^2}}. \tag{3.33}$$

Hence the flux depends mainly on the following parameters:

- **the number of electrons** N_e: The number of electrons per bunch is limited by beam dynamics, as most single-bunch instabilities scale with electron bunch charge. If the average ring current, dependent on the repetition rate, is high, wakefield effects may be induced. The higher the bunch charge, the faster the emittance will grow and thus deteriorate the x-ray beam quality faster, or require more frequent electron beam refreshment. For the MuCLS design, a bunch charge of up to 600 pC appears feasible with the implementation of digital feedback systems, currently the typically stored charge is about 250 pC.

- **the number of laser photons** N_L: The number of laser photons, or equivalently the laser pulse energy, is limited by the input power of the optical cavity, the mirror performance and the cavity gain. The resonantly stored power in the enhancement cavity is given by the product of laser power and cavity gain. Until the laser upgrade, the stored power was about 100-140 kW with a gain of $\sim$ 6000 and was increased by a factor of more than 2 after the upgrade in March 2017 (cf. section 3.4). The feasibility of storing a power of more than 600 kW has successfully been demonstrated [Carstens et al., 2014].

- **the collision repetition rate** f_c: A high collision repetition rate of $\sim$ 65 MHz is realized through the laser-electron storage ring design that was chosen instead of a linac-based system. The ring size cannot be made deliberately small as it needs to leave space for the injection area and the interaction point as well as the bends.

- **the transverse spot size** σ_r: At the interaction point, the transverse spot size of the electron beam is given by $\sigma_e^2 = \beta^* \epsilon$ and the laser beam spot size is defined as $\sigma_L^2 = z_R(\lambda_L/4\pi)$ (for further explanation, see boxes below). Note that the bunch lengths decrease with waist size, hence too small spot sizes could lead to a reduction of flux due to the hourglass effect (see below).

Gaussian laser beam

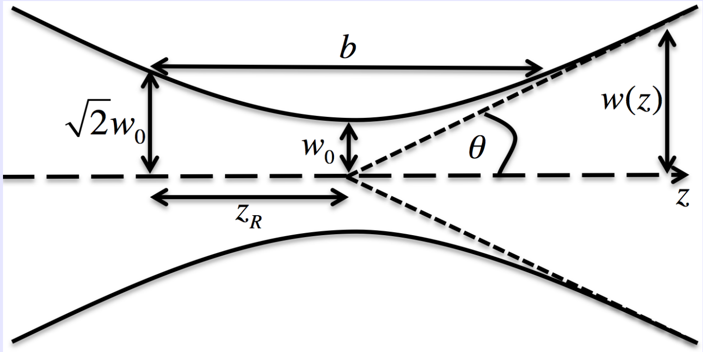

The Gaussian beamwidth as function of the distance z from the beam waist in beam direction is defined as

$$w(z) = w_0\sqrt{1 + (z/z_R)^2}, \tag{3.34}$$

where $w_0 = w(0)$ is the beam waist. The Rayleigh range $z_R = \pi w_0^2/\lambda$ is defined as distance from the waist to the place where the area of cross section has doubled, such that $w(z_R) = \sqrt{2}w_0$. It is determined by mirror curvatures and geometry. The confocal parameter b is defined as $b = 2z_R$.
The beam divergence is given by $\theta = \frac{\lambda}{\pi w_0}$ and the total angular spread is $\Theta = 2\theta$.

Electron beam size

The electron beam is assumed to have a Gaussian shape in transverse direction. The beta function, similarly to function for the waist of the Gaussian laser beam, is given by

$$\beta(z) = \beta^* + \frac{z^2}{\beta^*}, \tag{3.35}$$

assuming that the beta function takes its minimum β^* (depth of focus) at the interaction point, which is the equivalent of the Rayleigh range. The electron beam spot size σ_e as function of the location z along the beam trajectory is characterized by the beta function $\beta(z)$ and the beam emittance ϵ:

$$\sigma_e^2(z) = \beta(z)\epsilon. \tag{3.36}$$

Although not directly related to luminosity, the injection rate is an important parameter for x-ray beam quality as it helps to keep the electron beam emittance small. The re-injection rate is limited by the performance of the RF photocathode and the kicker magnet. The MuCLS currently uses a re-injection rate of 25 Hz, which is sufficient to provide stable intensity of the x-ray beam.

Two major geometrical effects can reduce the luminosity $\mathcal{L}_0$:

- **Crossing angle**: For Thomson backscattering, usually a scattering angle $(\pi+\theta_c)$ is chosen, where θ_c is a small crossing angle in order to avoid the backscattered x-rays from hitting the optical mirrors in the same spot as the laser beam, as distortion effects arising from the thinned mirror surface would compromise the stored laser power. Then, the projected source spot size $\sigma_x^\star$ increases like $\sigma_x^\star = \sqrt{\sigma_x^2 + (\sigma_z\theta_c)^2}$, i.e. the projected source size will become dominated by the angle instead of the focused waist σ_z when $\theta_c \sim \sigma_x/\sigma_z$. For the MuCLS, the critical angle is a few mrad.

The crossing angle should be chosen some factor larger than the far field divergence of the laser envelope, $\theta_0 = \frac{\lambda_0}{2\pi\sigma_r}$, with $\sigma_r = w_0/2$ the spot size for the Gaussian laser waist. For $\sigma_r = 30$ µm, a crossing angle larger than the laser divergence of 5 mrad would cause degradation in luminosity.

For the case of the MuCLS, a small crossing angle ($\sim 4 - 5$ mrad) was chosen in order to avoid hitting the center of the output optic with the laser beam, as this area is thinned for the x-ray beam output and would introduce distortion effects for the laser beam. The effect of this crossing angle is a $\sim 20 - 30\%$ reduction in luminosity.

- **Hourglass effect**: The waists of the two colliding beams vary depending on the distance from the interaction point (IP) (cf. equations 3.34 and 3.35). For beams not colliding at the IP, i.e. with their waists, the luminosity will be reduced by the factor

  $$R(u_r) = \frac{\mathcal{L}}{\mathcal{L}_0} = \sqrt{\pi} u_r e^{u_r^2}[1 - \mathrm{erf}(u_r)], \tag{3.37}$$

  where $u_r = \beta^*/\sigma_s = z_R/\sigma_z$. It follows that the bunch lengths should be comparable to or smaller than either β^* or z_R to maintain satisfactory colliding efficiency. For the MuCLS, $\beta^* \approx z_R \approx 1.5$ cm. These rather long possible bunch lengths are beneficial for electron beam stability and make the collision timing become less sensitive to jitter.

X-ray source size

The x-ray source size $\sigma_{\text{x-ray}}$ is given by the overlap product of electron and optical beams:

$$\sigma_{\text{x-ray}}^2 = \frac{1}{\frac{1}{\sigma_e^2} + \frac{1}{\sigma_L^2}} = \frac{\sigma_e^2\sigma_L^2}{\sigma_e^2 + \sigma_L^2}, \tag{3.38}$$

where σ_e and σ_L are the spot sizes of the electron and laser beams, respectively.

3.2.3. Technical realization – laser-electron storage ring

For the design of the MuCLS, a laser-electron storage ring setup [Huang and Ruth, 1998] was chosen: the laser pulse is stored in a high-finesse optical enhancement cavity and the electron bunch circulates in a miniature electron storage ring. The waists of the two beams are minimized at the interaction point (IP) and their revolution frequencies are matched to ensure collision upon each circulation of the electron bunch. The storage ring design for the electron beam has the advantage of a high repetition rate of the produced x-rays ($\sim$ 65 MHz), with the drawback that due to the rather long electron bunch length of several picoseconds no sub-ps phenomena can be imaged in time-resolved manner. Furthermore, the electron beam needs to be refreshed regularly in order to keep the

Performance parameters (as of 3/2017)	
Electron beam	
Electron energy	25-45 MeV
Ring circumference	4.6 m
Repetition rate	64.91 MHz (single bunch)
Bunch length	50 ps / 1.5 cm (rms)
Bunch charge	250 pC (max. 500 pC)
Re-injection rate	25 Hz
Focus spot size	45 μm×45 μm
Laser & Laser Cavity	
Laser wavelength	1064 nm
Cavity Length	9.2 m
Repetition rate	64.91 MHz (two pulses)
Pulse length	25-30 ps (FWHM)
Drive laser power	14 W
Stored laser power	up to 140 kW
Finesse, coupling	32000 with 69%
X-ray beam	
Energy range	11-35 keV
Source size	$<$ 45 μm×45 μm
Divergence	4 mrad
Energy bandwidth	3-5%
Brilliance (35 keV)	$0.6 \cdot 10^{10} \frac{\text{photons/s}}{\text{mrad}^2 \cdot \text{mm}^2 \cdot 0.1\% \text{ BW}}$
Flux (35 keV)	$1 \cdot 10^{10}$ photons/s
Flux scaling	$\propto E_x/E_{0x}$ ($E_{0x} =$ 35 keV)

Table 3.1.: Technical specifications for the MuCLS.

emittance and energy spread to a minimum, as these grow due to intra-beam scattering. In the following, the technical realization of the electron storage ring and the laser cavity will be described.

Table 3.1 shows a summary of the technical parameters of the MuCLS. The most important ones will be explained in more detail hereafter.

The information presented in the following is based on [Loewen et al., 2015, Loewen, 2003, Eggl et al., 2016a].

Electron beam

The electron beam system can be divided into three main parts: injector, transport and storage ring. An overview CAD drawing is shown in figure 3.7 (a). The most important features of these systems are described hereafter. For a more detailed description of accelerator physics, the reader is referred to e.g. [Wiedemann, 2007].

- **Injector**: The injector's task is to periodically supply an electron bunch at the desired energy. Electrons are produced by an RF photocathode source where UV pulses illuminate a Cu cathode to emit an electron bunch (a photograph is displayed in figure 3.7 (b)). The injector laser is a Nd:YLF laser with a wavelength of

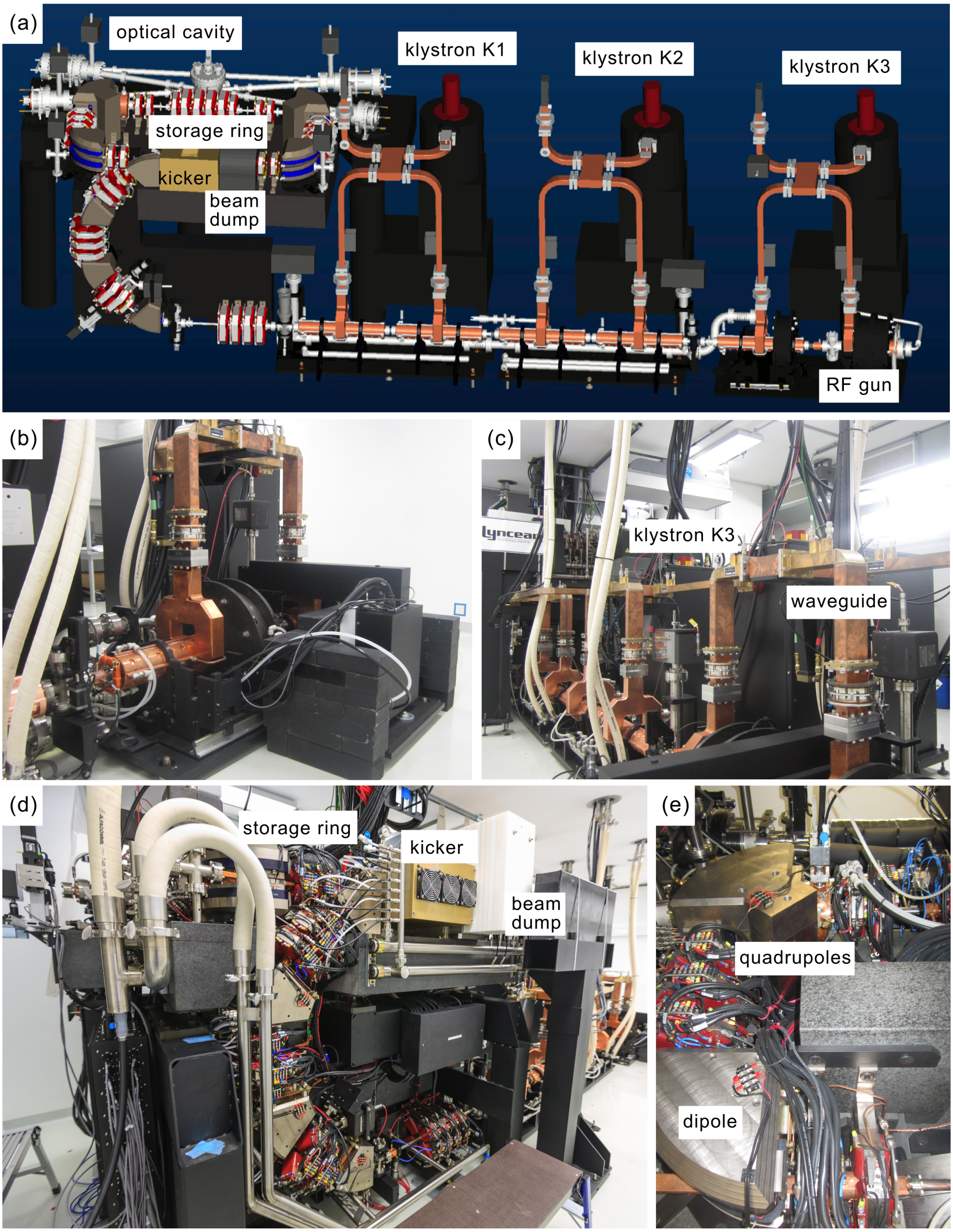

Figure 3.7.: The electron beam systems of the MuCLS. (a) CAD drawing of the MuCLS. To the right, the injector section is shown. To the left, the transport (bottom) and the electron storage ring with the laser cavity in the background (top) are displayed. Image courtesy of Lyncean Technologies, Inc. (b) Photograph of the RF photocathode and the first accelerator structure. (c) Photograph of the linac. Pictured are the klystrons, with the waveguides and the beam pipe in the foreground. (d) Photograph of the transport section. To the top, the kicker magnet and the beam dump are visible. To the very left, one can see the x-ray beam exit window, as well as collimators and diagnostics. (e) Photograph of half of the electron storage ring (part towards x-ray exit window). Dipole magnets in the bends and quadrupole magnets in between can be recognized.

1047 nm which is pulse-pumped at 25 Hz with a pulse energy of ∼ 120 µJ/pulse. The IR pulses of the laser are converted to UV (262 nm) using second harmonic generation in a regenerative amplifier (Regen). The pulse energy, and with it the charge of the extracted electron bunch, can be adjusted via the Regen diode gain. The emitted electron bunch is then accelerated in a linac section to the full desired energy, pictured in figure 3.7 (c). The linac consists of three pairs of radio-frequency (RF) cavities, where the electron bunch is accelerated. Three klystrons, powered by modulators, feed their energy to these accelerator structures through gas-filled waveguides.

RF Cavity

An RF cavity does not only have an accelerating effect on the electron bunch, but also a bunching one: the magnitude of the accelerating electric field in such a resonant cavity follows a sinusoidal curve over time. Therefore, slightly slower electrons which see the electric field at a later time (L), will receive a greater acceleration than faster particles that arrive earlier (E). Particles that arrive at the synchronous phase (S) will receive an intermediate acceleration. Hence particles with an imperfect energy will slightly be corrected such that the bunching is improved when passing through the RF cavity (phase focusing).

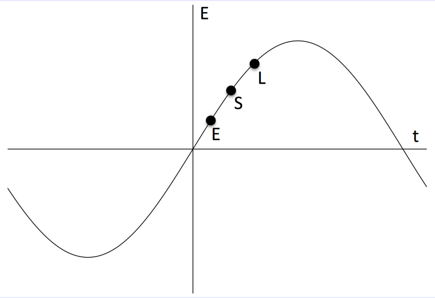

- **Transport**: The purpose of the transport section is to correctly condition the electrons bunch and inject the new electron bunch into the ring while discarding the old bunch. The transport section is pictured in figure 3.7 (d). When the electron bunch reaches the transport section, it is prepared for injection into the ring through focusing and bending magnets. Beam position monitors (BPMs)[5] and profile monitors are distributed along the transport line to measure energy spread and beam emittance. A septum magnet (Lambertson-style design) steers the electron bunch into the storage ring.
  One of the most crucial parts of the electron beam system then is the kicker magnet, as it aligns the electron bunch to the proper orbit in the storage ring. The kicker magnet, consisting of a series of pulsed electromagnets, has the important task of simultaneously injecting a new bunch into the ring and ejecting the old bunch out of the ring into the beam dump[6], with the requirement that the magnetic field needs to have vanished by the time the electron bunch has finished one round trip

---

[5] In the case of the MuCLS, the BPMs are passive RF cavities that measure and average the position of the electron bunch within the beam pipe.

[6] When the stored electron bunch is directed into the beam dump, the electrons are decelerated and various kinds of radiation may be emitted (neutrons, gamma rays, x-rays). Lead and polyethylene are used as shielding materials against radiation and neutrons.

in the storage ring (∼ 10 ns at 65 MHz revolution frequency). This design ensures that the electron bunch is refreshed regularly (at a rate of 25 Hz), hence keeping the emittance and energy spread low, without interrupting the continuous x-ray output.

- **Storage ring**: The storage ring is required to ensure stable circulation of the electron bunch, while maintaining the beam quality (especially emittance and energy spread), as the x-ray beam will inherit the emittance of the electron beam. The storage ring, with a total circumference of 4.6 m, consists of two 180° arcs and two longer straight sections, one of which is dedicated to the injection, while the other hosts the interaction point and is "shared" with the laser cavity. The design of the storage ring is symmetric with respect to the IP, one half of it is shown in figure 3.7 (e).
  After being injected into the ring, the electron bunch circulates stably for about 1 million turns. An RF cavity (L-band cavity) ensures that the beam stays tightly bunched as described above. Dipole magnets deflect the electron bunch around the bends and quadrupole magnets keep the bunch transversely focused. In addition, corrector magnets (often combined-function magnets with quadrupoles, to save space) correct the trajectory or orbit of the electron bunch. Before the interaction point (IP), i.e. the spot where the electron bunch is to collide with the laser pulse, the bunch is transversely focused to a small waist by a triplet of quadrupole magnets.

Laser cavity

The laser cavity is an optical resonator (passive optical cavity) and is designed in order to achieve low losses and high finesse and gain. The whole laser cavity is mounted on a thick granite table in order to keep vibrations to a minimum. A cw mode-locked laser (Nd:YAG, 1064 nm, repetition frequency 64.91 MHz, pulse width ∼ 25 ps, average power 5 W) is amplified by an assembly of four amplifiers. In the transport assembly, the laser beam is conditioned to match the cavity mode. Adjustable parameters are the offset and steering into the cavity, the astigmatism and the (longitudinal) waist of the beam. The laser is locked to the cavity (i.e. the laser central carrier frequency tracks the cavity resonant frequency) by modifying the path length to match the revolution frequency of the cavity. Frequency stabilization is achieved through Pound-Drever-Hall (PDH) locking [Drever et al., 1983].

The laser cavity is built in a bow-tie geometry, with one of the straight sections falling together with the electron storage ring, where the IP is located, as shown in figure 3.8. One of the mirrors is the input mirror, where the laser pulse is fed into the cavity, and the opposite one is the output mirror that has a thinned area which is transmissive for x-rays. The mirrors, together with the cavity length, fully determine the waist size and position and the mirror spot sizes, as well as the inherent sensitivity of the cavity. External coupling and cavity finesse are determined by mirror parameters of reflectivity, transmittivity and losses. The cavity length is approximately 9.2 m, thus two laser pulses are stored in the cavity to ensure a collision rate of 64.91 MHz (i.e. the circulation frequency of the electron bunch).

For a simplified case of a two-mirror cavity (Fabry-Perot-interferometer), the finesse

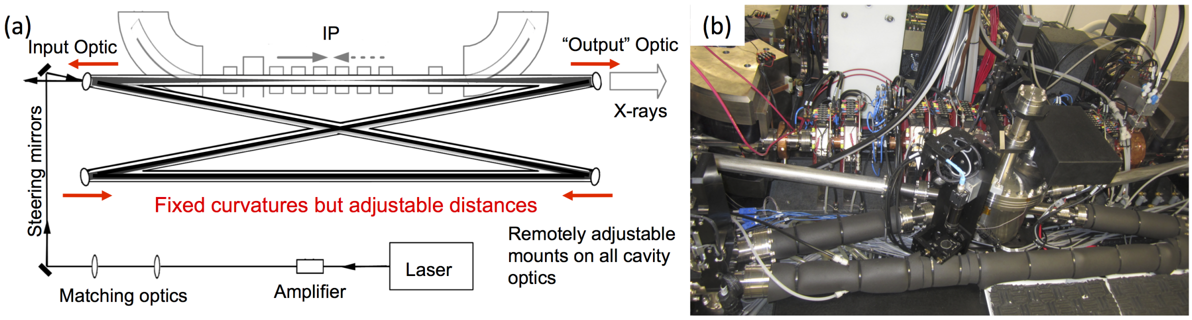

Figure 3.8.: The enhancement laser cavity. (a) Schematic drawing of the bow-tie laser cavity. The top left mirror serves to couple the laser beam into the cavity, the top right mirror serves in addition as output optic for the x-ray beam. The laser beam is focused to a small waist at the interaction point (IP). Image courtesy of Rod Loewen, Lyncean Technologies Inc. (b) Photograph of the MuCLS laser cavity.

can be calculated for given transmittivities T_i and losses L_i of the mirrors (where $R_i + T_i + L_i = 1$, with R the reflectivity). The bounce number b is defined from the round-trip power loss which is $\propto e^{-1/b}$ and can be approximated in the limit of small losses as

$$b = \frac{1}{T_1 + L_1 + T_2 + L_2}. \tag{3.39}$$

The cavity finesse $\mathcal{F}$ is defined as

$$\mathcal{F} = \frac{\pi \sqrt[4]{R_1 R_2}}{1 - \sqrt{R_1 R_2}} \simeq 2\pi b \simeq \frac{\mathrm{FSR}}{\Delta\nu_{\mathrm{cav}}}, \tag{3.40}$$

where $\Delta\nu_{\mathrm{cav}}$ is the cavity bandwidth and the free spectral range (FSR) is the axial-mode interval between resonances. The free spectral range is defined as $\mathrm{FSR} = \frac{c}{2L}$, with c the speed of light and L the mirror-to-mirror separation distance, i.e. the inverse of the time of one cavity round trip. The gain is defined as

$$\mathrm{gain} = \frac{U_0}{U_{\mathrm{inc}}} \simeq 4T_1 b^2, \tag{3.41}$$

where U_0 is the steady-state cavity pulse energy and U_{inc} is the incident pulse energy. The impedance match measures how well the incident field cancels the leakage field from the cavity in steady state,

$$\frac{E_{\mathrm{refl}}}{E_{\mathrm{inc}}} \simeq 1 - 2T_1 b, \tag{3.42}$$

with $(E_{\mathrm{refl}}/E_{\mathrm{inc}})^2$ gives the amount of power unable to couple into the cavity. If the input coupling equals the sum of all other losses in the cavity, $T_1 = L_1 + L_2 + T_2 = 1/2b$, i.e. for no net power reflection, the configuration is denoted as matched. In this case, the gain simplifies to gain $= 2b = 1/T_1$.

For example, to achieve a desired cavity enhancement of 10000, the total cavity losses should be below 200 ppm with a finesse of ~ 30000, as it is the case for the MuCLS.

A more detailed description of the physics of optical enhancement cavities is beyond the scope of this work and can be found for example in [Siegman, 1986] (especially Chapter 11).

Timing

Three phase-locked RF clocks determine the timing of all MuCLS subsystems: “S-band”, “L-band” and “65 MHz” references with frequencies of 2856 MHz, 1428 MHz and 64.91 MHz, respectively, with the L-band and 65 MHz being the 2nd and 44th subharmonics of the S-band reference. The 65 MHz reference is the repetition rate of the electron storage ring and the fundamental repetition rate of the injector laser and the optical cavity laser. The L-band reference sets the phase of the storage ring and is the frequency of the RF cavities of klystrons and the ring. By choosing the 65 MHz phase setpoint of the injector laser, one L-band bucket of the ring (there are $1428/64.91 = 22$ buckets) is chosen. The L-band reference of the ring has to be locked to the S-band reference of the RF photocathode gun. The kicker is synchronized through a fine-delay trigger.

Environment

The MuCLS is installed at the Munich School of Bioengineering (MSB) of the Technische Universität München (TUM) in Garching, Germany. The MuCLS is located inside a radiation shielding cave, which was built according to a patent from Forster Bau GmbH, Ingolstadt, Germany. The shielding walls have a sandwich-like construction, consisting of two 15 cm thick walls of heavy concrete (2.3-4.0 tons/m^3, depending on the location with respect to the bremsstrahlung emerging from the beam dump) and 50 cm of electric furnace slag in between (2.4 tons/m^3, concrete with a weight portion of 23% iron). From the radiation shielding cave, the x-rays travel through an evacuated beam pipe with Mylar windows to the experimental setups which are located in two different radiation shielding hutches, placed at a distance of approximately 2 m and 15 m from the interaction point, respectively. The total power consumption of the MuCLS is approximately 100 kW, of which the main part is required magnets and modulators, requiring chillers to compensate the waste heat [Eggl et al., 2016a].

Specifically designed chillers ensure that precise temperature setpoints are maintained for accelerating structures and the optical cavity. The precision of the chillers is ±0.05°C around the setpoint. A powerful air-conditioning system keeps the temperature in the radiation shielding enclosure constant. The air conditioning has to work under the constraint too keep noise and sudden airflow from fans to a minimum.

The MuCLS is protected from harm to the machine through its integrated protection system (IPS) which for example monitors temperatures and water flow and will perform a shutdown of relevant systems if one of the measured variables is out of the allowed range. In case of a power failure, the most sensitive system components are protected through uninterruptible power supplies (UPSs) to allow for a safe shutdown.

3.3. Operation of the MuCLS

This section will describe the most important aspects of the MuCLS operation. The electron beam and the laser cavity can basically be regarded as two separate systems which can be run independently from each other. In the process of x-ray tuning, the spatial and temporal match between the two beams is optimized in order to achieve maximum x-ray flux at minimal source sizes. Some challenges of the MuCLS operation will be discussed, including solutions that already have been or will be implemented.

3.3.1. Electron beam

- **Operation**: When starting up the MuCLS, the operators follow a specific workflow which shall be summarized briefly here.
    1. The chillers reach their temperature setpoints.
    2. Magnets and corrector magnet are conditioned and degaussed, respectively.
    3. The injector laser is locked to the S-band reference.
    4. If necessary, the RF photocathode is cleaned.
    5. The klystrons are ramped, leaving time for phases to reach their equilibrium. The phase of the klystron K1 is determined by performing a “Schottky Scan”, in order to find the optimum phase setting.
    6. One of the screens in the transport line bend is inserted in order to tune the electron beam by adjusting the phases of K2 and K3, and by optimizing the electron beam energy. A position feedback aligns the electron beam at the beginning of the transport line.
    7. The electron beam is first injected into the ring at reduced charge. After adjusting kicker settings and minimizing transients, the charge is ramped to the desired operating charge. The electron beam orbit in the ring is optimized using another feedback loop which acts on the corrector magnets.

  Figure 3.9 (a) shows a screenshot of the digital oscilloscope while electrons are stored in the ring. The traces are an important tool when optimizing the store of the electron beam. The yellow, bottommost trace shows the current stored in the ring. The step in the beginning of the trace is the time point of injection of a new bunch, i.e. increasing current. A large step signalizes that the beam is poorly stored and charge is lost while circulating in the ring. The three other traces indicate position errors of the electron bunch. The topmost trace (pink) shows the vertical position error and can be adjusted by changing the septum magnet settings. The second trace (green) shows the error in longitudinal position and is minimized by adjusting the phase of the L-band amplifier. The third trace (blue) indicates the horizontal position error, which can be corrected by adjusting the kicker magnet currents and timing.

  Another important tool in the operation of the electron beam is a plot of the history of several important parameters as shown in figure 3.9 (c). The chart displays the charges in the injector and the ring, the injection efficiency (ratio of charge in injector and in ring) and the gain of the Regen laser diode. The plot shows a typical day of operation. In the morning, the charge was low when preparing the electron beam for injection. During the day, the stored charge (light and dark blue lines) stayed constant, while the gain of the Regen (green) was increased by the Regen feedback in order to achieve this.
- **Feedback systems**: Several feedback systems are in place to ensure steady operating conditions. An *energy feedback* adjusts the modulator power such that the

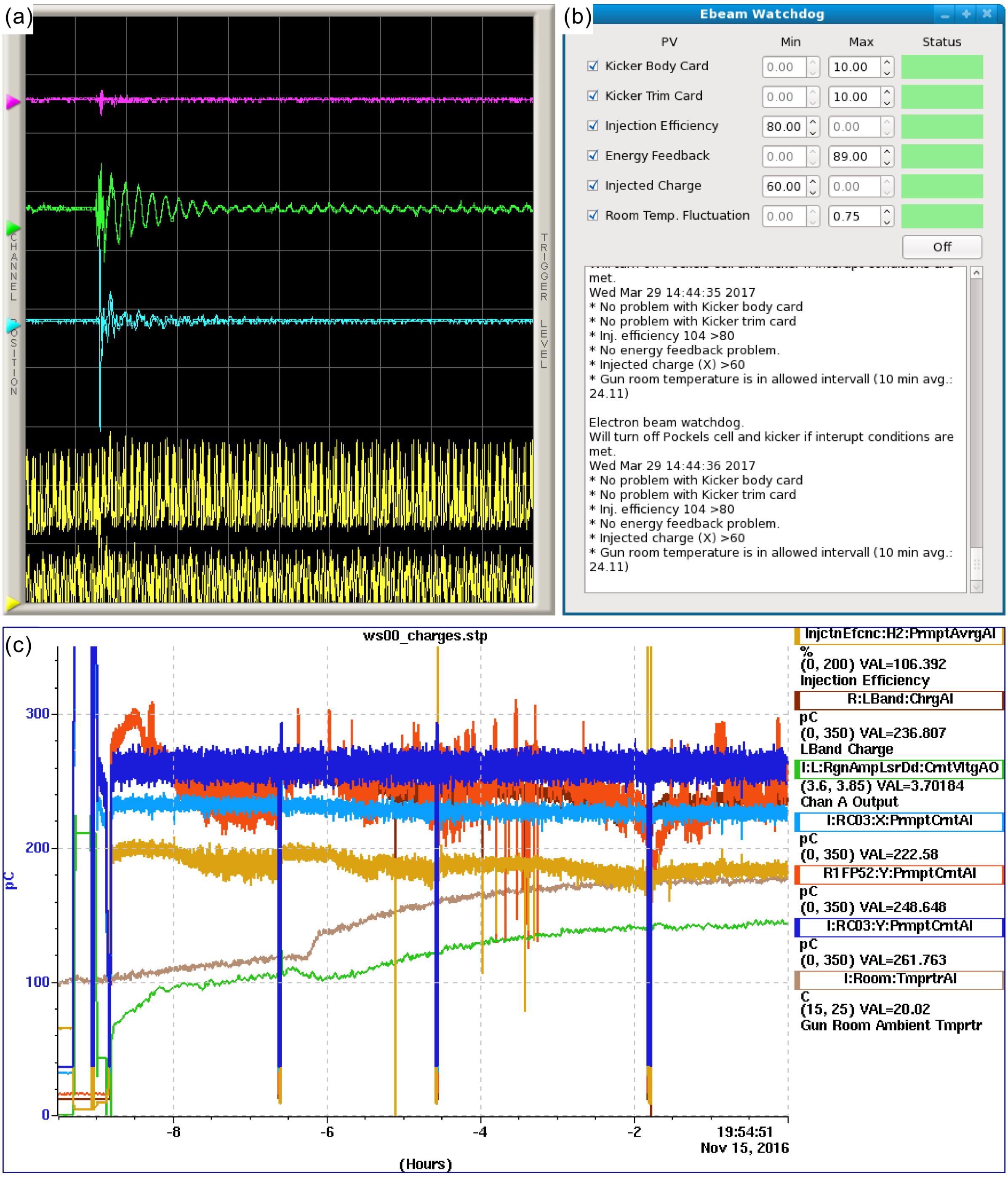

PV	Min	Max	Status
☑ Kicker Body Card	0.00	10.00	🟩
☑ Kicker Trim Card	0.00	10.00	🟩
☑ Injection Efficiency	80.00	0.00	🟩
☑ Energy Feedback	0.00	89.00	🟩
☑ Injected Charge	60.00	0.00	🟩
☑ Room Temp. Fluctuation	0.00	0.75	🟩

Off

```
met.
Wed Mar 29 14:44:35 2017
* No problem with Kicker body card
* No problem with Kicker trim card
* Inj. efficiency 104 >80
* No energy feedback problem.
* Injected charge (X) >60
* Gun room temperature is in allowed intervall (10 min avg.:
24.11)

Electron beam watchdog.
Will turn off Pockels cell and kicker if interupt conditions are
met.
Wed Mar 29 14:44:36 2017
* No problem with Kicker body card
* No problem with Kicker trim card
* Inj. efficiency 104 >80
* No energy feedback problem.
* Injected charge (X) >60
* Gun room temperature is in allowed intervall (10 min avg.:
24.11)
```

Figure 3.9.: Electron beam operation. (a) Screenshot of the oscilloscope for a stored electron beam. From top to bottom, the traces show: (pink) the vertical position error, (green) the error in longitudinal direction, (blue) the horizontal position error, (yellow) the current in the ring. (b) Screenshot of the watchdog GUI. All monitored parameters are within their allowed intervals. If one of the values exceeds the allowed interval, the electron beam will be turned off in order to prevent damage of the machine due to a poorly injected and stored beam. (c) Exemplary daily history for the electron beam. The chart shows the development of important parameters for the electron beam during a typical day of operation. The light and dark blue curves plot the charged in the injector. The brown trace displays the charge in the ring. The yellow trace shows the injection efficiency, i.e. the ratio between the charge in the injector and the ring (value not absolute). The green trace plots the gain of the Regen laser diode.

beam keeps the desired position on the beam position monitors in the transport line. The *Regen feedback* adjusts the gain of the Regen diode such that the charge stored in the ring is kept constant.

- **Watchdog**: A watchdog continuously checks on several parameters of the injection and store in the ring and also external facility parameters (e.g. temperature). If one of the monitored values is outside of the allowed interval, e.g. if the injection efficiency is too low or if there is a sudden change in ambient temperature, the electron beam will be shut down in order to avoid possible harm to the machine due to a degrading injection and store in the ring. A screenshot of the watchdog GUI is shown in figure 3.9 (b).

3.3.2. Laser cavity

- **Operation**: Like for the electron beam, the start up of the laser cavity follows a specific workflow, as summarized hereafter.

  1. A pellicle is used for low-finesse mode matching, with the goal to couple only the resonant mode TEM_{00} (eigenmode) into the cavity without higher order mode content.
  2. The laser is locked to the cavity (Pound-Drever-Hall (PDH) locking) using a fast piezo by scanning the frequency range of the laser, i.e. by adjusting distances. A CCD camera shows the reflection off the input optic (cf. fig. 3.10 (a,b)), and the input power is in addition measured with a sensor. When the laser is not locked to the cavity, the reflection is very bright (a), and should be as dark as possible (more power stored when less power is reflected) when the laser is locked (b).
  3. The cavity is then locked to the “65 MHz” reference in order to allow for timed collision with the electron beam.
  4. These tasks are observed with an oscilloscope, as shown in figure 3.10 (c).
  5. To achieve a good coupling to the enhancement cavity, steering and astigmatism settings are optimized. In addition, the carrier-envelope offset (CEO) phase[7] requires adjustment for achieving a good match to the cavity.

  A chart displaying the history of a typical day of optical cavity operation is shown in figure 3.10 (d). The history shows a day of stable operation that required little intervention by the operators.

- **Measuring cavity performance**: A ringdown measurement can be taken to assess cavity performance and to measure cavity losses and the coupling coefficient of the input beam. The cavity power is sampled using scatter from a mirror pickoff in the cavity. The laser is unlocked deliberately and the stored power in the cavity will fall off exponentially. An exponential decay can be fitted, with losses given

---

[7] The CEO phase is defined as the phase offset between the peak of the carrier wave of a pulsed wave and the peak of the pulse intensity envelope wave. The phase offset comes from the difference of phase and group velocities, and needs to be corrected by the operator when dispersion changes (e.g. due to temperature change or intensity change).

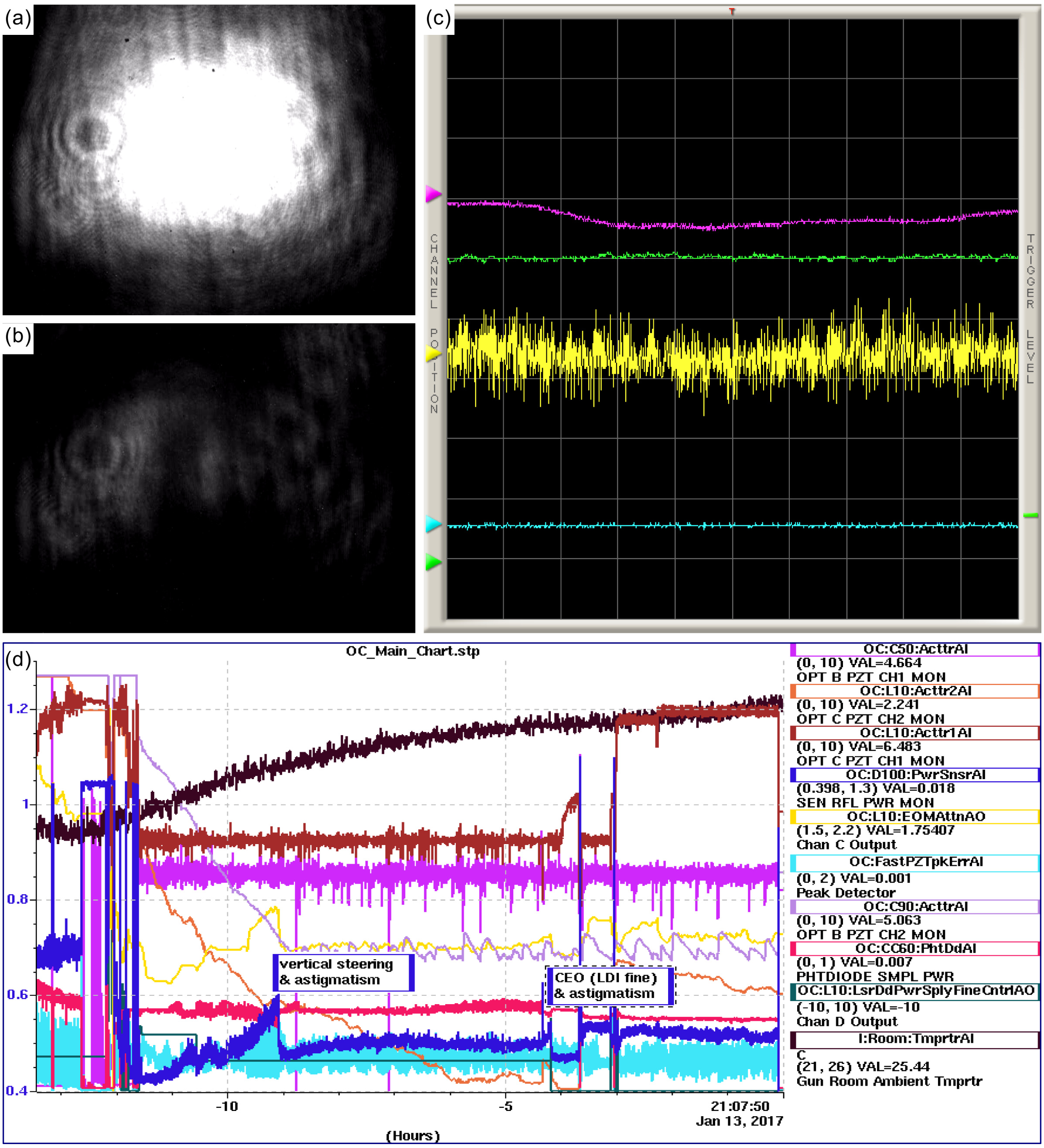

Figure 3.10.: Laser cavity operation. (a) CCD camera image of the laser reflected from the input optics. The full laser power is reflected from the input optic when the cavity is unlocked. (b) After the laser was locked to the cavity, a fraction of the laser power (coupling coefficient) is fed into the cavity, therefore less power is reflected from the optic and the camera image is darker. (c) Oscilloscope traces as observed during cavity operation while the laser is locked to the cavity and the cavity is locked to the reference. The pink trace shows the difference in frequency of the cavity from the 1428 MHz reference, it will flatten out once the cavity is locked to the reference. The yellow trace shows the error signal of the fast piezo and signalizes a good lock when slightly "bursting". The green trace is the cavity sample power, which is useful when trying to lock the laser to the cavity as it will show spikes as signs of locking. (d) Chart showing an exemplary day of cavity operation. The chart displays several values that are helpful for cavity operation and measure the performance of the optical cavity. The most important parameter is the power reflected from the input optics (dark blue), which (in this example) decreased from $\sim$ 10.5 W when unlocked to around 5.0 W when the laser is locked to the cavity. The yellow trace shows the gain of the PDH frequency feedback loop, which takes lower values when high power is stored in the cavity.

by $L = \frac{1}{\tau \cdot \mathrm{FSR}}$. When the reflected power (locked and unlocked) is known, one can solve for coupling:

$$\begin{aligned} P_{\mathrm{refl}} &= (P_{\mathrm{inc}} - P_0) + P_0 \left(\frac{E_{\mathrm{refl}}}{E_{\mathrm{inc}}}^2 \right) && (3.43) \\ &= (1 - c_0) P_{\mathrm{inc}} + c_0 P_{\mathrm{inc}} (1 - 2T_1 b)^2 && (3.44) \end{aligned}$$

An example for a ringdown fit which yielded $\sim$ 130 kW stored power in the cavity is presented in figure 3.11.

3.3.3. X-ray tuning

Once the electron beam is stored in the ring and the laser is locked to the cavity (and the cavity to the reference), the MuCLS should produce x-rays. The flux and the source sizes can then be tuned to their optimal values. For this procedure, a knife edge is inserted into the beam and the photon counting Pilatus detector is used to measured flux and source sizes (the latter through fitting an error function to the horizontal and vertical edges of the knife edge, as described in greater detail in chapter 5) and displayed in a chart on the operator interface, exemplarily shown in figure 3.12. At the beginning, the timing between laser beam and electron beam is checked: by varying the 65 MHz phase of the optical cavity, the operator can check for minimal source sizes (when timing is wrong, the two beams will not collide at their waists, which is visible through increased source sizes). After optimizing the timing, i.e. the longitudinal position of the collision, the transverse position needs to be optimized. The transverse overlap is changed by varying the position of the electron beam using corrector magnets. If the range of these magnets is not sufficient to find minimal source sizes and maximal flux, the position of the laser beam can be adjusted as well. After a move of the laser position, the position of the electron beam will be checked again. After a longer downtime of the machine or after an energy change, it may be necessary to repeat the procedure of scanning electron beam positions, finding a minimum at the end of the range, moving the laser beam, and scanning electron beam positions several times. With flux and source sizes optimized, the MuCLS is ready for an experiment to start.

3.3.4. Challenges of the operation

A complex system like the MuCLS relies on many different subsystems and their interaction. Some of the subsystems have, during the first two years of MuCLS operation, proven to cause some challenges for the operation. Some of these challenges have already been addressed, or are planned to be addressed in the future. The following overview presents the most common challenges of everyday operation, their effects on experiments and possible or already implemented solutions.

- **Kicker card failures**: The kicker magnet serves for the injection of a new electron bunch into the storage ring and to kick the old bunch out of the ring into the beam dump. Therefore, a high magnetic field needs to be built up for the time of injection and extraction, which has vanished by the next passing by of the electron bunch. This is managed by electronic boards (kicker cards), which may

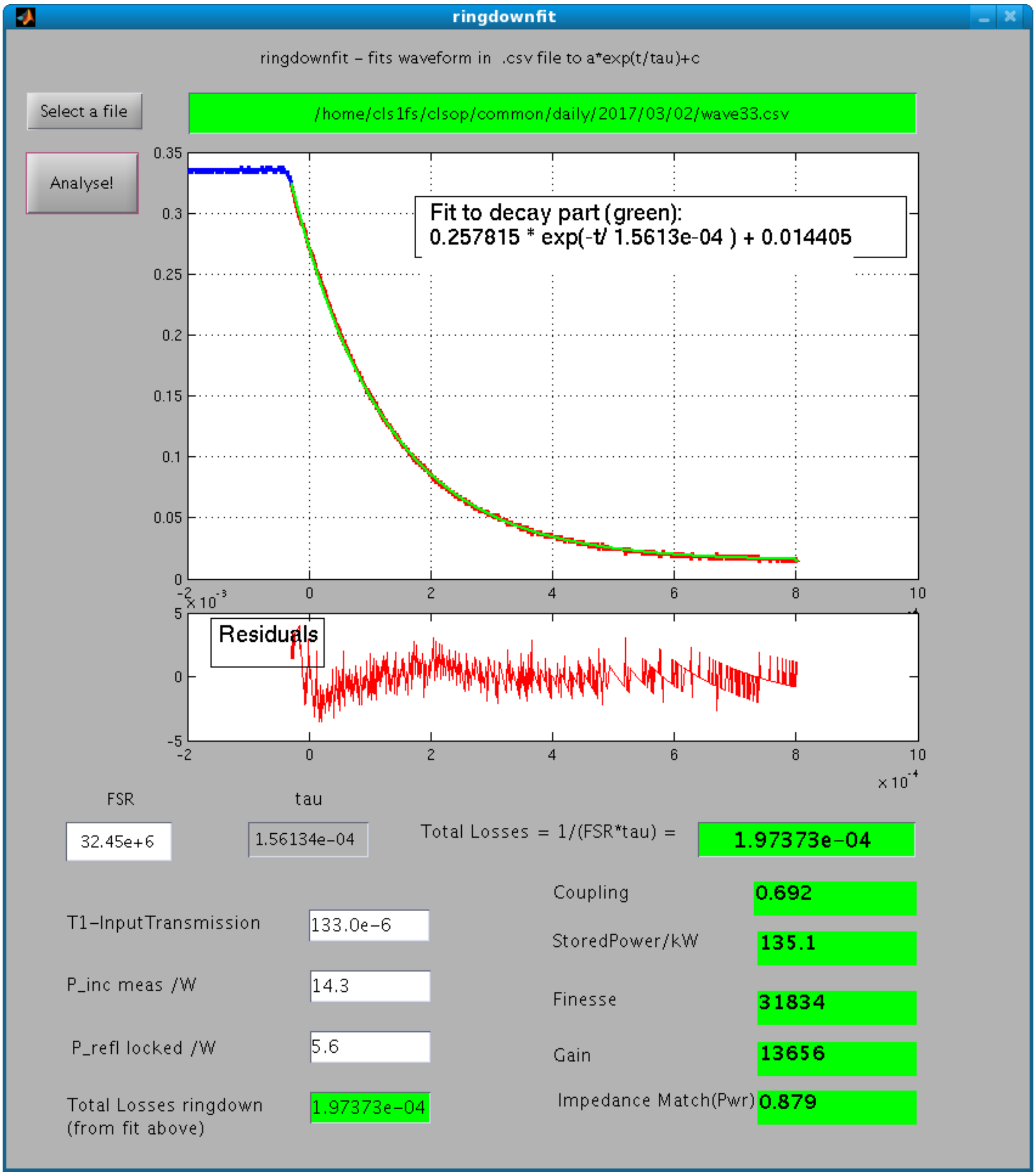

ringdownfit – fits waveform in .csv file to a*exp(t/tau)+c

/home/cls1fs/clsop/common/daily/2017/03/02/wave33.csv

Fit to decay part (green):
0.257815 * exp(-t/ 1.5613e-04) + 0.014405

FSR: 32.45e+6

tau: 1.56134e-04

Total Losses = 1/(FSR*tau) = 1.97373e-04

T1-InputTransmission: 133.0e-6

P_inc meas /W: 14.3

P_refl locked /W: 5.6

Total Losses ringdown (from fit above): 1.97373e-04

Coupling: 0.692

StoredPower/kW: 135.1

Finesse: 31834

Gain: 13656

Impedance Match(Pwr): 0.879

Figure 3.11.: Ringdown fit in order to assess power stored in cavity. When unlocking the laser, the stored power falls off exponentially. From an exponential fit to the decay, using a MATLAB GUI, the cavity losses and the coupling coefficient can be calculated.

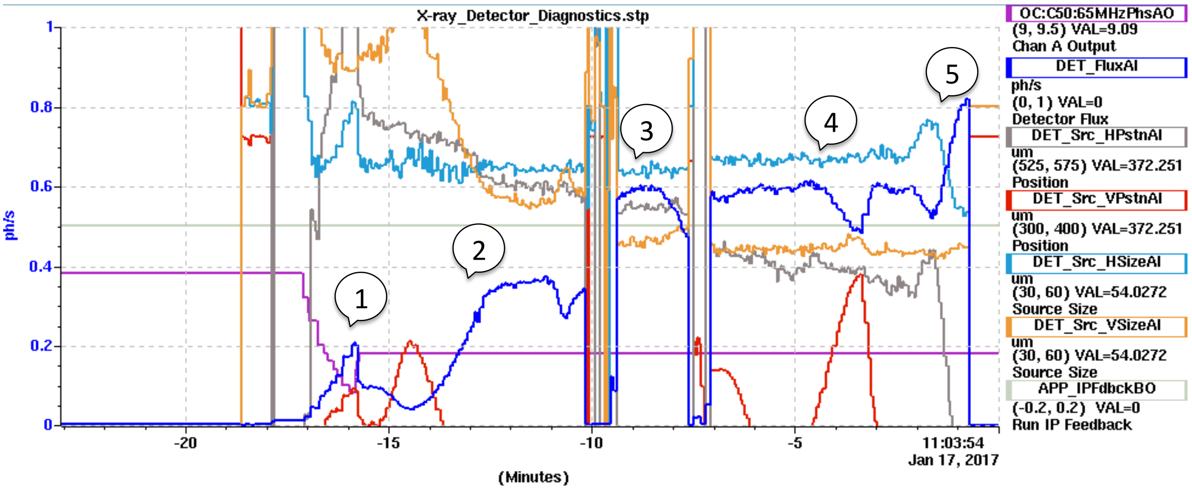

Figure 3.12.: Screenshot of an exemplary history of x-ray tuning. First, the timing is checked by varying the 65 MHz phase of the optical cavity (purple trace) to the value that minimizes the source sizes (1). Then, the position of the electron beam is varied (visible through movement of the vertical source position, red trace) (2), to find the best match for the waists of the electron beam and the laser beam, which will give maximum flux (dark blue) and minimal source sizes (light blue and orange). Once the magnets to move the electron beam reach the end of their range, the position of the laser beam is moved (3) (done twice in this example, visible through loss of x-ray beam as the lock to the cavity is lost). The vertical source position is now optimized (4). By adjusting the horizontal position of the electron beam, the optimal flux and minimal source sizes are achieved (5).

suffer from radiation damage. Radiation damage can accumulate over a longer time, or be caused by a bad injection or bad store in the ring. When a kicker card fails, injection into the ring is no longer possible and the card has to be replaced.
Issues for experiments: A kicker card failure will cause a significant delay in experiments. Before being able to identify and exchange the failed card, the operators have to wait for radiation levels caused by activation of materials in the vicinity of the beam dump to decay. Afterwards, the broken card needs to be identified by measurements of the current and then replaced. The whole procedure usually takes about 3 hours.
Solutions: A kicker diagnostic tool has been added in February 2017. It now allows for a failed card to be identified by software instead of individual test. This speeds up the exchanging procedure. In addition, the kicker diagnostics enable a software-based one-by-one check, which may help to identify failing cards which can be exchanged preventively before important experiments. Examples are displayed in figure 3.13.

- **RF gun charge decay**: The MuCLS suffered from rapidly decaying electron beam charge levels. The charge produced from the RF photocathode gun decreases due to *multipacting*, an effect caused by RF fields interacting with magnet fields to produce a resonant condition in which electrons accelerate between two surfaces and create a steady-state discharge. Multipacting is often accompanied by outgassing, and the gas will likely contaminate the cathode surface and affect

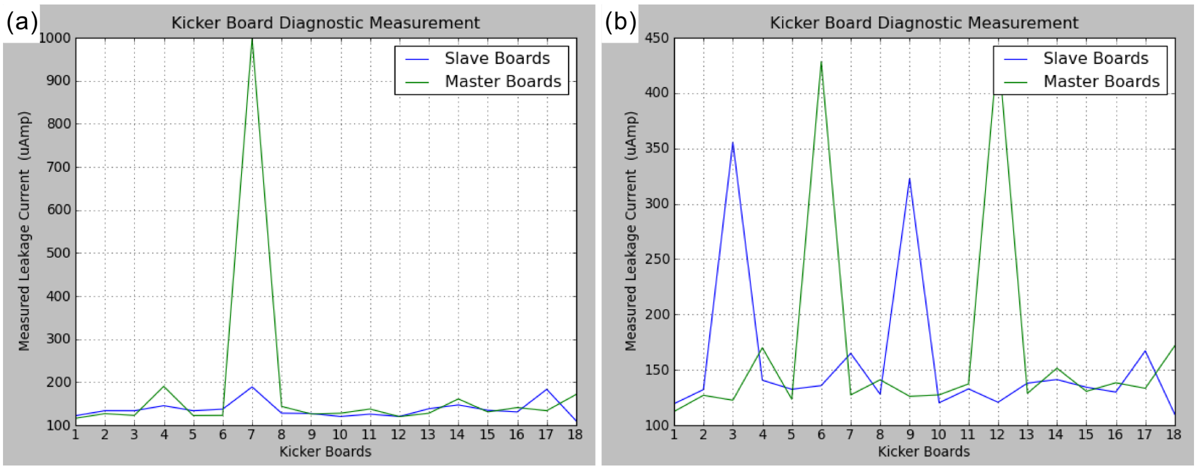

Figure 3.13.: The recently added kicker diagnostics feature. The diagnostic tool measures the leakage currents of each kicker card separately and helps to identify broken (a) or failing (b) cards, as these show increased leakage current.

the charge.
Issues for experiments: The decaying charge can be compensated by increasing the gain of the Regen diode. Once the maximum gain level is reached, the electron bunch charge stored in the ring will decrease, and subsequently an unwanted decay in x-ray flux is observed. An example for a day of operation with decaying charge is shown in figure 3.14.
Short-term solution: The cathode is “cleaned” with a focused laser beam. This procedure causes a downtime of approximately 1 hour, since klystrons have to be shut down and need time to re-stabilize. In addition, this task requires caution, as cleaning with too much laser intensity will cause unwanted dark current, i.e. current emitted by the cathode without being illuminated by the laser.
Long-term solution: Vacuum leaks in the RF gun lines due to microcracks were identified and the gun lines have subsequently been vacuum sealed in 10/2016. After charge levels started to decay again requiring more frequent cathode cleaning, the ion pump was exchanged in 2/2017 and the cathode water line was moved to the first structure. These treatments have reduced the required frequency of cathode cleaning for several weeks. An exchange of the photocathode is planned in the near future.

- **Optical cavity stability**: For a period of a few months in 2016, the optical cavity was very unstable. The lock of the laser to the cavity was lost several times per hour, as shown exemplarily in figure 3.15. While the lock to the cavity often recovers, the lock of the cavity to the reference has to be restored manually by an operator.
  Issues for experiments: Scans would frequently be interrupted, and an operator was required to be present during the time of the scan in order to maintain a running x-ray beam. A lost lock during e.g. phase-stepping scans will often cause leftover fringes in the images.
  Solution: Low-frequency noise in the cavity laser system (mostly injected by the

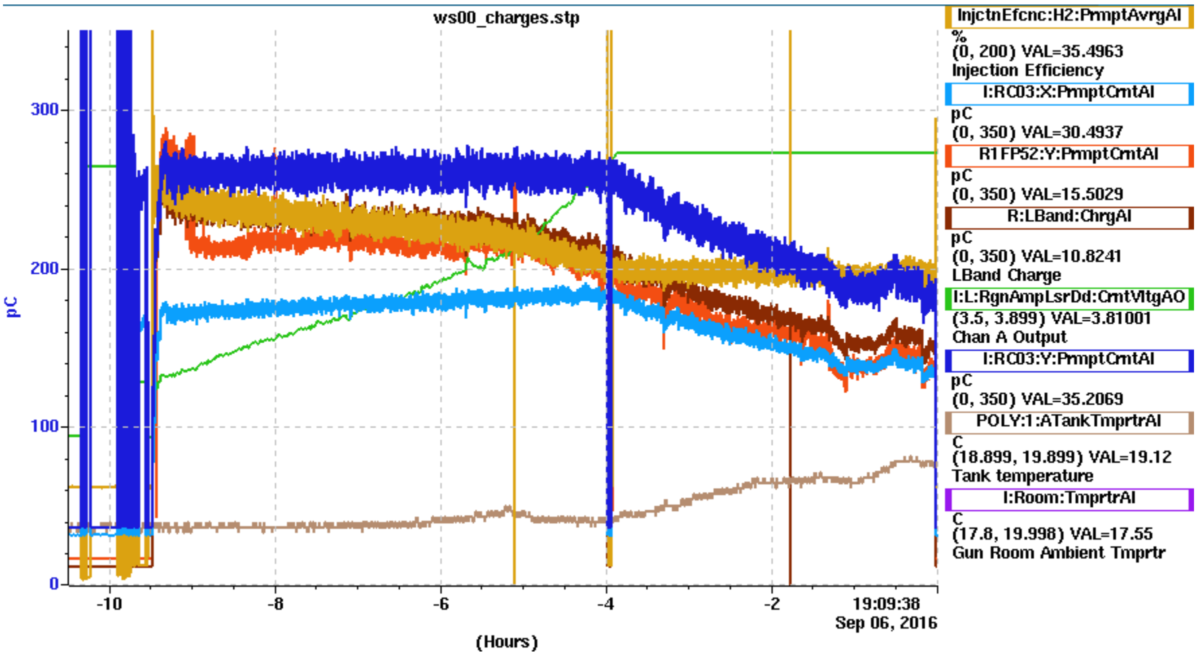

Figure 3.14.: Decaying charge issue. The daily history of the electron beam operation (recorded before vacuum sealing treatment) shows how the gain of the Regen laser diode was increased by the Regen feedback in order to maintain the desired charge level. Once the gain reached its maximum value, the charge starts to decay.

cooling water circuit) was identified as main cause for the frequent loss of the laser lock. Acoustic foam was added around the laser and amplifiers. The optical cavity feedback system was adjusted to suppress certain resonance frequencies. The cooling water circuit for the laser was moved.

- **Laser power decrease**: The output power of the cavity laser system (i.e. the power coupled into the cavity) decreases over time, due to a creeping misalignment of the laser.
  Issues for experiments: Reduced input power to the cavity means reduced x-ray flux.
  Short-term solution: The misalignment is corrected for the laser system power to be restored. This work needs to be performed by Lyncean Technologies Inc. in regular intervals.
  Long-term solution: After the laser amplifier upgrade in 3/2017, the problem of creeping misalignment should no longer persist.

- **Modulator interlocks**: The modulators may show interlocks from time to time, due to internal or communication problems. A modulator interlock causes an electron beam shut down.
  Issues for experiments: The experiment is interrupted until the interlock is cleared and the modulator has been re-ramped and reached equilibrium again.
  Short-term solution: Most interlocks can be cleared through software, or through powercycling the moculator. The latter involves entering the MuCLS enclosure.
  Long-term solution: The cause for the frequent interlocks is investigated in a joint

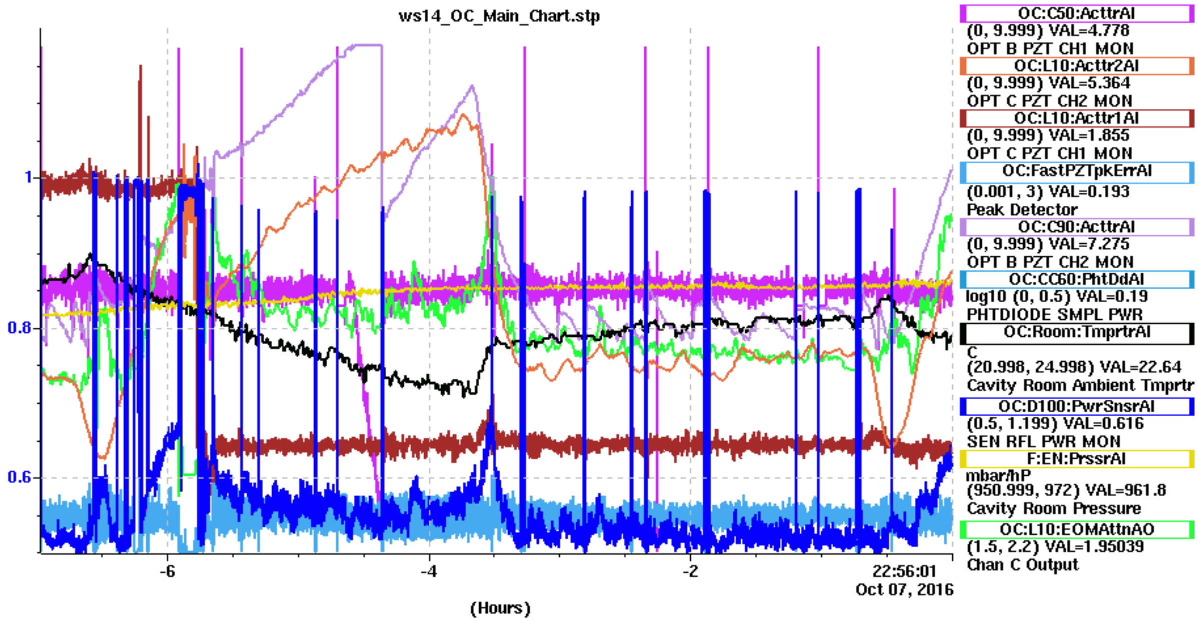

Figure 3.15.: Example for a day with low stability of the optical cavity. The dark blue curve displays the reflected power from the input optics. The frequent spikes in the trace signalize that the laser lost lock to the cavity (several times per hour on this occasion). Often, the laser will catch the lock again immediately without intervention, however, the lock to the reference has to be restored manually by an operator.

effort with the manufacturer of the modulators.

- **Temperature sensitivity**: Many components of the MuCLS are extremely temperature sensitive. The MuCLS performs best when in thermal equilibrium. *Issues for experiments:* Unstable environmental conditions make the x-ray beam unstable, and in the worst case can make operation impossible. *Solution:* An additional cooling unit was installed in the rack room in 6/2016. The programming of the facility air conditioning was improved such that unwanted temperature oscillations can be avoided.

3.4. Outlook

The Compact Light Source (CLS) technology has improved continuously ever since the first imaging experiments were performed [Bech et al., 2009]. Further advances in performance and added possibilities can be expected for the near future.

A laser upgrade (installed in 03/2017, first performance parameters presented in section 5.2.5) will increase the laser power fed into the optical cavity by a factor of 2, hence enabling a simultaneous increase in x-ray flux. The performance parameters of the MuCLS that have changed after the laser upgrade are presented in table 3.2. Additional feedback systems (e.g. a feedback for the CEO phase) are planned to be integrated into the system and should enable stable operation of the MuCLS for timescales > 8 hours without or with only little operator intervention.

In the near future, an x-ray beam position monitor (XBPM) system will be imple-

Performance parameters (as of 3/2017 after laser upgrade)	
Laser & Laser Cavity	
Drive laser power	30 W
Stored laser power	> 300 kW
Finesse, efficiency	32000 with 75-80%
X-ray beam	
Source size	< 50 µm×50 µm
Divergence	4 mrad
Energy bandwidth	5%
Brilliance	up to $0.8 \cdot 10^{10} \frac{\text{photons/s}}{\text{mrad}^2\cdot\text{mm}^2\cdot 0.1\%\ \text{BW}}$
Flux	up to $3.3 \cdot 10^{10}$ photons/s

Table 3.2.: Technical specifications for the MuCLS after the laser upgrade in March 2017.

mented which will provide live measurements of flux and source size and position during running experiments. Currently, with the source size and position measurement being based on a knife edge inserted into the beam and imaged with the Pilatus detector, the measurement can only be used during x-ray tuning but not while a different detector is used during an experiment. Correcting for drifts of the laser focus position to stabilize the source position, will also be helpful to keep the x-ray flux more constant. For the implementation of an XBPM, a small knife edge, which will only cover a very small fraction of the MuCLS beam and will therefore not impede the field of view for experiments, will be placed as close to the source as possible in order to reach a magnification of ~ 1 at the position of the XBPM approximately 3.6 m from the interaction point. The XBPM system will be composed of a thin LuAG scintillator (10 µm) coupled to a CCD camera with a pixel size of 5.5 µm (avA 1600-50gm, Basler AG, Germany) with a fiber-optic plate [Günther, 2017].

For an increased ease of operation, parts of the start-up routine could be automatized. Several tasks are rather time-consuming but do not actually require the manual intervention of an operator. The MuCLS operates best when at thermal equilibrium, therefore, these tasks could be performed automatically and leave time for the systems to reach thermal equilibrium before an operator starts his work.

A possible future upgrade would be to increase the output aperture of the MuCLS in order to provide a larger field of view (FOV). For instance, an output aperture with a diameter of 10 mm instead of the current 6 mm would increase the divergence of the beam from 4 mrad to 6.6 mrad and the FOV in the far hutch to about 11 cm in diameter. The increased FOV will increase the total flux. Of course, the increase in FOV also has some drawbacks. The flux density will not increase, and the flux and the energy will decrease towards the outer parts of the FOV. The latter can be beneficial for medical imaging, since the use of bow-tie filters that reduce the flux towards the outer parts of the field of view to account for decreasing sample thickness is very common in medical CT. The broader energy spectrum can be accounted for in the CT reconstruction. This increased output aperture would however not only require an exchange of the mirror, but will also require adjustments to the electron beam system, since the emittance of the electron beam is now optimized for the current aperture size.

Concerning K-edge imaging, a feature could be added to the system that allows to oscillate the x-ray energy between two close energies, e.g. below and above the iodine K-edge, without requiring a reconditioning of the magnets in order to perform K-edge subtraction (KES) imaging.

For the long-term future, further advances can be expected for the CLS technology. The energy range of currently 15-35 keV could be extended to 20-100 keV when using a green cavity laser (532 nm) instead of the currently used IR laser system. New magnet lattice designs and digital feedback systems will allow to design a low-emittance electron storage ring with the possibility to store a charge of > 800 pC. The brilliance is expected to increase by 2 orders of magnitude through an increase in flux and a reduction in source sizes.

4. Experimental setup & Methods Development

This chapter presents the experimental setup at the MuCLS at which the imaging experiments presented in this thesis were performed. Theoretical considerations concerning the chosen interferometer design are explained. The software package used for the processing of the mammography measurements is introduced.

At the MuCLS, two dedicated experimental hutches are available with different characteristics due to the divergence of the x-ray beam and therefore the different beam size, as shown in figure 4.1. The "front" hutch offers a beam size of 1.5-3.0 cm and is designed for micro tomography, high-resolution propagation-based phase-contrast imaging and micro-beam radiation therapy. The "far" hutch in a distance of ∼ 16 m from the source with a field of view of approximately 6.5 cm offers good conditions for radiographic and tomographic imaging of larger samples, and for grating interferometry.

Since the experiments presented in this work were only performed in the far hutch, the following presentation of the experimental setup will only cover the equipment in this experimental hutch.

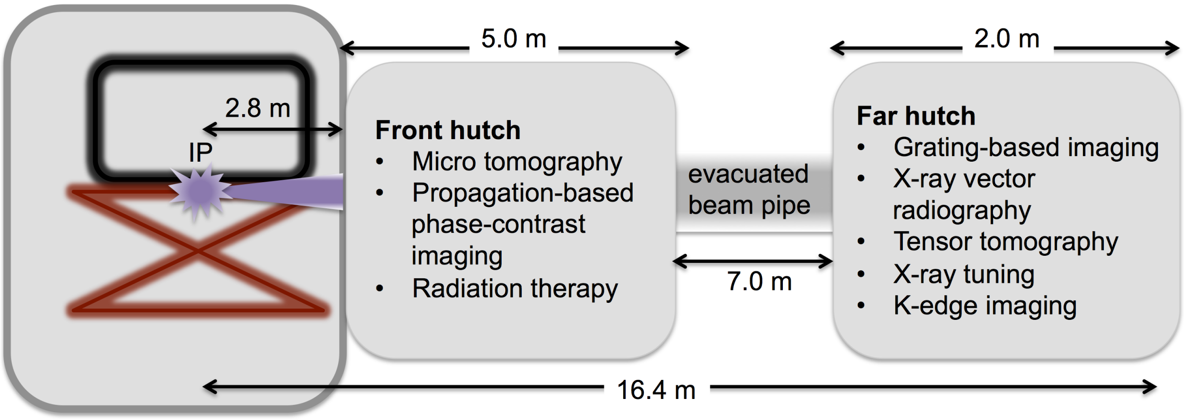

Figure 4.1.: Sketch of the experimental setups available at the MuCLS. The grating interferometer is installed in the hutch located about 16 m from the source.

4.1. Grating interferometer

The x-ray grating interferometer (XGI) at the MuCLS is operated in a Talbot configuration, i.e. with two gratings. The MuCLS source size is small enough to offer sufficient partial coherence to operate the XGI without a source grating which is needed for low-brilliance setups like for laboratory x-ray tube sources. The advantage is a more simple setup that is easier to align and furthermore, the full intensity of the source is preserved (while half of the intensity is absorbed when a source grating is present).

This section provides theoretical considerations about the choice of the interferometer setup and presents the existing setup at the MuCLS.

4.1.1. Theoretical considerations

For a partially coherent x-ray source like the MuCLS, that has a finite source size, the source blurring needs to be taken into account when choosing the setup of the XGI. [Weitkamp et al., 2006] presented an analysis of the source blurring and of coherence requirements from which the resulting visibility of a given interferometer setup can be estimated.

Longitudinal coherence

Concerning the longitudinal coherence of the x-ray source, i.e. the monochromaticity, [Weitkamp et al., 2005] provided a rule of thumb for the acceptable bandwidth of the x-ray source. Considering that the condition for the fractional Talbot distances d_n (in case of a $\pi/2$-shifting phase grating, cf. equation 2.30)

$$d_n = \frac{np_1^2}{4\lambda}, \tag{4.1}$$

with n the Talbot order and p_1 the period of the phase grating, is only met for the design wavelength, the contrast C of the fringe pattern varies sinusoidally with the wavelength: $C \propto \sin(\pi\lambda d/p_2^2)$. The half-width of the wavelength $\Delta\lambda$ between the two wavelengths to either side of the design wavelength λ_0 at which $C = 0$ can be taken as the effective energy range over which the interferometer operates efficiently:

$$\Delta\lambda = \frac{\lambda_0}{2n-1}. \tag{4.2}$$

Therefore, the higher the Talbot order n, the smaller the acceptable bandwidth $\Delta\lambda/\lambda_0$. For good contrast, an approximate condition for the required monochromaticity is [Weitkamp et al., 2006]

$$\frac{\lambda_0}{\Delta\lambda} \gtrsim n. \tag{4.3}$$

Considering the bandwidth of the MuCLS of less than 5% across the energy range, i.e. $\lambda_0/\Delta\lambda \gtrsim 20$ this condition is easily met for any generally used Talbot orders.

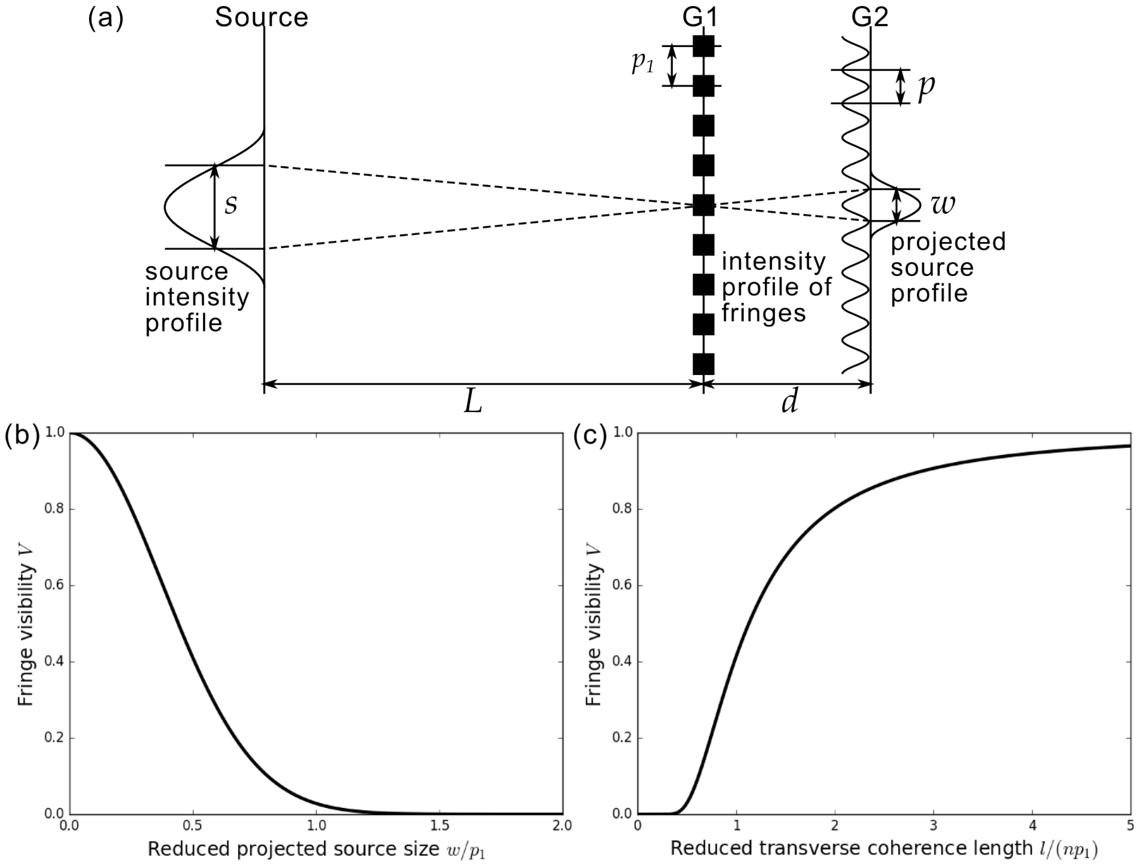

Figure 4.2.: Illustration of how the source blurring affects the interferometer visibility.
(a) Drawing of a two-grating-interferometer setup for partially coherent illumination (finite source size s). The phase grating G1 is placed a distance L downstream of the source and linear fringes of period p are created by each point in the source at a distance d from G1. The finite source size, i.e. the imperfect spatial coherence of the x-ray beam, causes a blurring of the fringes: the fringe intensity profile is convoluted with the projected source profile of width $w = s \cdot d/L$. For better visibility, the analyzer grating G2 is not drawn here.
Visibility of a sinusoidal fringe intensity profile as a function of (b) projected source size w (in units of the phase grating period p_1) and (c) reduced transverse coherence length $l_c/(n \cdot p_1)$. Both plots show the case of a $\pi/2$ shifting phase grating.
Adapted from [Weitkamp et al., 2006].

Spatial coherence

Assuming a partially coherent x-ray source and a two-grating setup as sketched in figure 4.2, the effects of the finite source size on the fringe profile can be calculated [Weitkamp et al., 2006].

For a Gaussian intensity profile with a full width at half maximum (FWHM) s, and the interferometer located at a distance L from the source with an inter-grating distance d, it is assumed that the detector plane coincides with the analyzer grating and a quasi-plane wave is considered. When higher diffraction orders are neglected, the intensity profile of the fringes created by G1 is a sinusoidal curve and for completely coherent illumination is given by

$$I(x) = I_0(1 + \sin(2\pi x/p)), \tag{4.4}$$

where x is the the transverse coordinate perpendicular to the grating lines, I_0 is the intensity incident on G1 and p is the period of the fringes. However, when the illumination does not come from a point-like x-ray source but is only partially coherent, the intensity profile $I(x)$ from a point source is convoluted with the projected source profile and therefore blurred. For a Gaussian source profile, this is a convolution with a Gaussian of the width of the so-called projected source size

$$w = s \cdot d/L, \tag{4.5}$$

where both s and w are the FWHM of the Gaussians.

This blurring causes a reduction of the visibility $V = \frac{I_{\max}-I_{\min}}{I_{\max}+I_{\min}}$ of the fringe pattern with $I_{\max}$ and $I_{\min}$ being the maximum and minimum values of the sinusoidal intensity pattern, respectively. From analytical or numerical evaluation of the convolution of a sine with a Gaussian profile, the decrease of visibility with increasing projected source size w follows the relation [Weitkamp et al., 2006]

$$V = \exp(-(1.887\frac{w}{p_2})^2), \tag{4.6}$$

i.e. the visibility decrease as a function of increasing projected source size has a Gaussian shape (cf. figure 4.2 (b)). In terms of the maximum allowed projected source size for a given minimum visibility V_0, this can be rearranged to

$$w \leq 0.53\sqrt{\ln V_0}. \tag{4.7}$$

The projected source size can be expressed in terms of the Talbot order n:

$$w = s\frac{d}{L} = s\frac{np_1^2}{2\lambda L}. \tag{4.8}$$

The spatial (transverse) coherence length l_c is defined as

$$l_c = \frac{\lambda L}{s}. \tag{4.9}$$

Together with the expression for the projected source size, this yields

$$\frac{w}{p_2} = \frac{np_2}{2l_c}, \tag{4.10}$$

and with equation 4.6, the visibility can be expressed in terms of the coherence length (cf. figure 4.2 (c)),

$$V = \exp(-(0.94\frac{np_2}{l_c})^2). \tag{4.11}$$

Spatial coherence at the MuCLS

For the far hutch at the MuCLS, the distance from source to detector is approximately 16.4 m. Therefore, depending on the inter-grating distance, $L \approx 16.1$ m and $d \approx 0.3$ m.

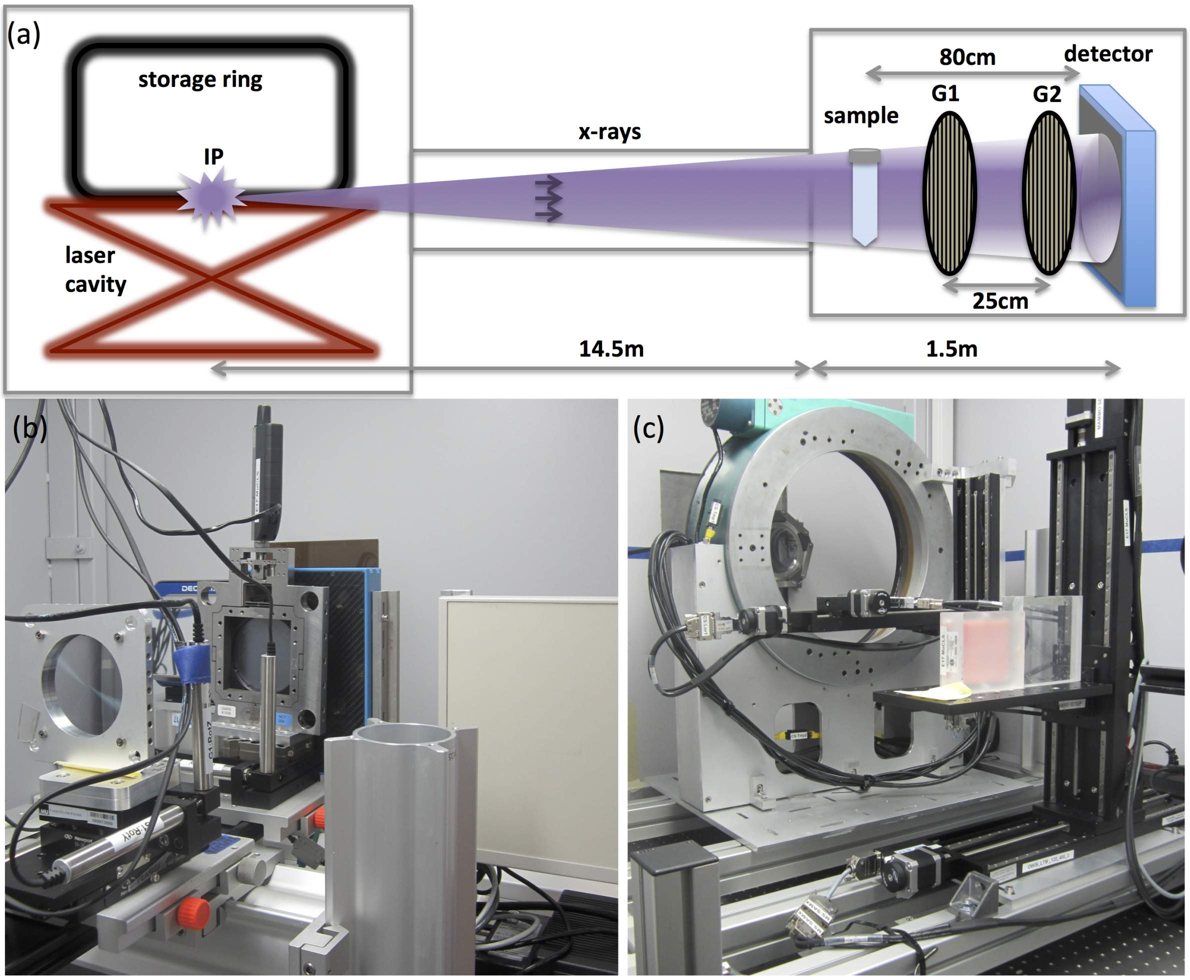

Figure 4.3.: The grating interferometer at the MuCLS. (a) Schematic drawing showing the distances of the most frequently used 25 keV configuration. (b) Photograph of the grating interferometer and the detectors available in the far hutch (from left to right: Pilatus 200K, Dexela 1512, PaxScan 2520D). (c) Photograph of the sample stages (one for translation only - mainly used for mammography and angiography - and one that offers rotation around the tomography axis and the optical axis to be used for x-ray vector radiography and tensor tomography) that are mounted on a separate stand so they are decoupled from the optical table.

With a source size of 45 µm (rms) and $s = 2.354 \cdot 45$ µm, this yields a projected source size of

$$w = s \cdot \frac{d}{L} = 1.97\,\mu\text{m}. \tag{4.12}$$

The x-ray wavelength $\lambda = \frac{hc}{E}$ is $\lambda_{25} = 0.50$ Å for 25 keV x-ray energy and $\lambda_{35} = 0.35$ Å for 35 keV, yielding the following transverse coherence lengths (eq. 4.9):

$$25\text{ keV:}\ \ l_c = 7.6\,\mu\text{m}, \tag{4.13}$$

$$35\text{ keV:}\ \ l_c = 5.3\,\mu\text{m}. \tag{4.14}$$

The expected visibility for a given analyzer grating period p_2 and Talbot order n can be calculated from these values using eq. 4.11 and is displayed for a few possible settings

Energy [keV]	p_2 [µm]	n	d [cm]	l_c [µm]	expected V
25	5.0	1	25	7.6	68%
25	5.0	3	75	7.4	3%
35	5.0	1	35	5.3	45%
25	3.4	1	12	7.6	84%
25	3.4	3	36	7.5	20%
35	3.4	1	17	5.4	70%
35	3.4	3	51	5.2	3%

Table 4.1.: Expected visibilities for a few selected analyzer grating periods and fractional Talbot distances.

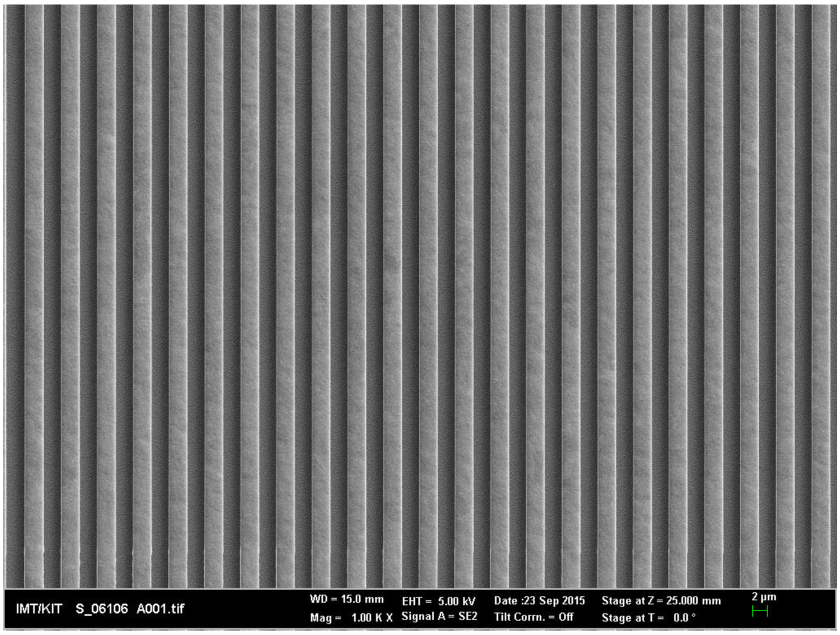

Figure 4.4.: Scanning electron microscope image of the analyzer grating G2 with a period of 5.0 µm. Image provided by Danays Kunka and Pascal Meyer, KIT.

in table 4.1. It is important to note that these estimated visibilities are only valid for perfect gratings, i.e. the visibility achieved at an experimental setup will always be lower.

The calculated visibilities show that a two-grating setup can be operated in the first fractional Talbot distance with sufficient visibility. For the third fractional Talbot distance, where the increased propagation distance would give the benefit of higher sensitivity of the interferometer, the expected visibilities are too low. For the best compromise between visibility and sensitivity, a 5.0 µm analyzer grating was chosen. For a setup with increased sensitivity, i.e. larger inter-grating distance, the introduction of a source grating will be necessary.

Grating	Design Energy	period	height	d	remarks
G1 ($\pi/2$)	25 keV	4.92 µm	4.39 µm Ni	25 cm	-
G1 ($\pi/2$)	35 keV	4.92 µm	6.15 µm Ni	35 cm	To achieve the desired period of 4.89 µm, the grating is tilted by ~ 12°.
G2	up to 35 keV	5.00 µm	~ 70 µm Au	-	-

Table 4.2.: Parameters of the gratings available at the MuCLS.

4.1.2. Grating interferometer at the MuCLS

As explained in the previous section, a two-grating setup (i.e. Talbot interferometer) in the first fractional Talbot distance was chosen for the MuCLS. A schematic sketch and a photograph of the setup are displayed in figure 4.3.

The gold bars of the analyzer grating G1 have a height of > 70 µm, which is sufficiently absorbing also for the highest available x-ray energy of 35 keV at the MuCLS. Two different phase gratings G2 to be used with this analyzer grating are available for the two most commonly used x-ray energies, 25 keV and 35 keV. The specifications of the gratings (period, height) are given in table 4.2. All gratings have a round active area with a diameter of 70 mm and thus are well matched to the available field of view.

The gratings were fabricated by the Karlsruhe Nano Micro Facility (KNMF) of the Karlsruhe Institute of Technology (KIT), Germany, applying the LIGA process [Bacher et al., 1995, Mohr et al., 2012]. Shortly summarized, a silicon wafer with a titanium layer is spin-coated with negative photoresist. With a mask generated from electron beam writing placed on the photoresist, the wafer is exposed to radiation (usually low-energy x-rays). The parts of the resist that were not exposed are removed during the development process, and the gaps between the unremoved resist are filled with a metal (usually Ni or Au) in a galvanic process. A scanning electron microscope of the grating structures of the analyzer grating is shown in figure 4.4.

The XGI at the MuCLS reaches a visibility of up to $\sim 50\%$ for 25 keV x-ray energy and $\sim 38\%$ for 35 keV. Exemplary stepping curves and visibility maps are shown in figures 4.5 (a) and (b) for 25 and 35 keV, respectively.

4.1.3. Stability of experimental setup

After initial installation, the grating interferometer setup at the MuCLS was very sensitive to external influences and vibrations. Therefore, as a first step, the rigid legs of the optical table were upgraded with passive isolation mounts. These damping mounts caused the optical table to tilt when sample stages were moving, influencing the grating interferometer and thus requiring an isolation of the sample stages from the optical table. Therefore, a decoupled mounting of the stages was added as shown in figure 4.3 (c). These measures were sufficient to significantly reduce the sensitivity of the grating interferometer to external influences. However, instabilities of the x-ray beam caused by the MuCLS itself (source position drifts and jumps, optical cavity dropouts) possibly

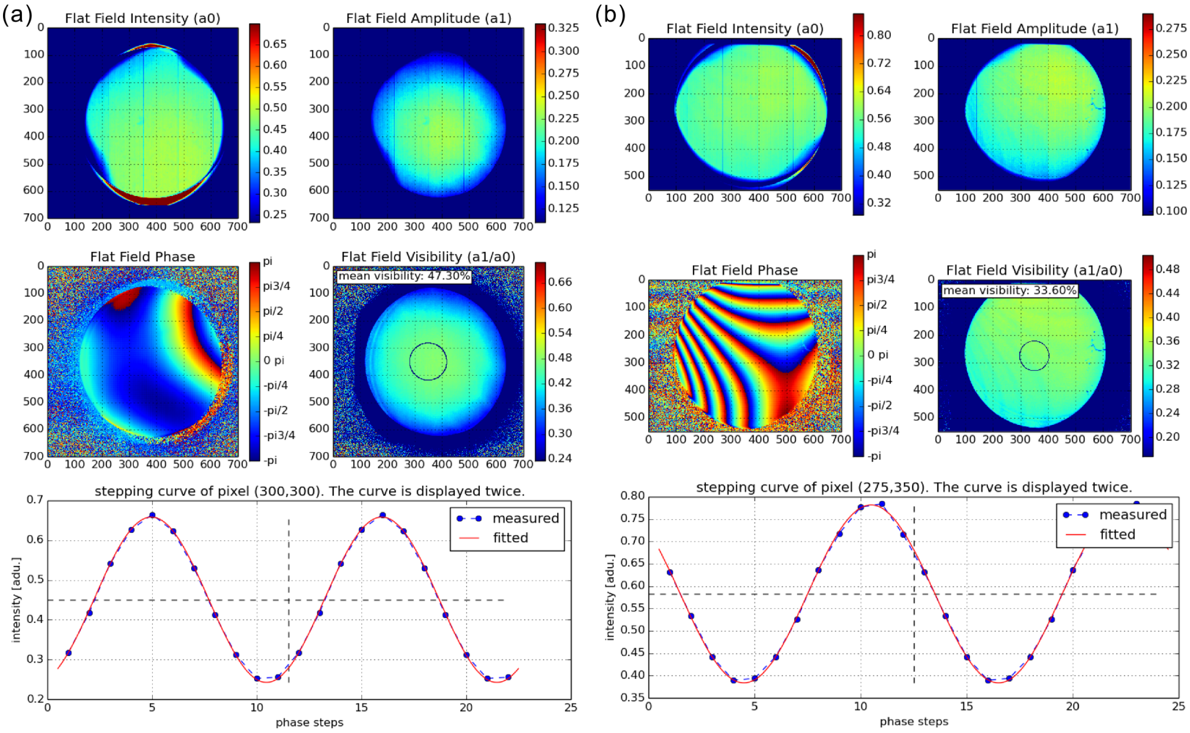

Figure 4.5.: Exemplary stepping curves. The two-grating interferometer at the MuCLS achieves visibilities of up to 50% for 25 keV (a) and up to 38% for 35 keV (b). Mean visibilities measured in the center of the beam were 47.3% an 33.6% in this example scan, respectively.

happening during a phase stepping scan still remain a challenge and require advanced postprocessing methods.

4.2. Detectors

Several x-ray detectors are available for imaging experiments in the far hutch at the MuCLS: three different flatpanel detectors and a single photon counting detector. Information on each detector is given in table 4.3, including information on the point spread functions as determined by [Cont, 2016] using an edge-fitting method. In addition, a scintillation counter is installed in the front hutch as a measure of x-ray flux during experiments, which is especially useful for dose estimation during e.g. mammography experiments (cf. chapter 8.2).

With the different characteristics of the detectors, each of them is best suited for different applications. The Pilatus detector offers the most advanced technology with single photon counting pixels with a 1 pixel wide box-like point-spread function (PSF) and a dark current free readout. It is perfectly suited for the x-ray beam characterization for measuring flux and source sizes using a knife edge fitting approach. However, concerning imaging applications, the quantum efficiency of the silicon sensor is rather low for energies above 20 keV (around 40% at 25 keV) and the pixel size is comparably large, especially since the MuCLS beamline barely adds any geometric magnification. In addition, the 17 pixel wide gap causes loss of information and might lead to diagnostic information being missed [Braig, 2015].

Manufacturer Model	Dectris Pilatus 200K	PerkinElmer Dexela 1512	Varian PaxScan 2520DX	Varian PaxScan 2520D
Type	single photon counting	CMOS	amorphous Silicon	amorphous Silicon
Sensor	1000 µm Si	150 µm Gd_2O_2S	208 µm Gd_2O_2S	600 µm CsI
Pixel pitch	172 µm	74.8 µm	127 µm	127 µm
Field of view	487 × 407 px 2 modules, 17 px gap	1536 × 1944 px	1536 × 1920 px	1536 × 1920 px
Eff. pixel size (H×V)	164.3 × 163.6 µm	71.1 × 71.1 µm	-	118.3 × 118.4 µm
PSF	1 × 1 px rectangular	0.95 × 0.95 px Gauss	1.19 × 1.15 px Gauss	1.09 × 1.12 px Gauss
max. frame rate	20 fps	26 fps	12.5 fps	12.5 fps
Application	x-ray tuning, beam characterization, CT	mammography, GBI, CT, K-edge imaging	GBI, CT, K-edge imaging	imaging, CT above 33 keV

Table 4.3.: Properties of the x-ray detectors available at the MuCLS (far hutch).

Please note that also a Pilatus 100K model (consisting of one 487 × 195 pixel module) has been used for some of the beam characterization and imaging experiments presented in this thesis. The most important difference between the 100K and the 200K model is, besides the different field of view, the maximum possible frame rate. While the 200K model offers a maximum frame rate of 20 Hz, the 100K model allows for image acquisition with frame rates up to 200 Hz.

While the previous laboratory phase-contrast mammography setup as presented in [Scherer, 2015] used the Varian PaxScan 2520DX detector with a Gd_2O_2S (Gadox) scintillator, this detector was replaced by a Dexela 1512 detector (also with a Gadox scintillator). Especially the lacking geometric magnification for the MuCLS setup required a detector with smaller pixel size in order to achieve a resolution comparable to clinical standards. In addition, the complementary metal-oxide-semiconductor (CMOS) technology of the Dexela is advantageous over the amorphous silicon technology of the PaxScan due to higher low dose dynamic quantum efficiency and faster possible readout speeds.

4.3. Software Development

For the mammography project at the MuCLS, mainly two software packages besides the standard `pyE17` package were used. The software package `MammoLib` that had been developed for a laboratory mammography setup with a rotating anode x-ray source [Scherer, 2015] was adapted and extended to fulfill the requirements imposed by the source characteristics of the MuCLS. Compared to a conventional x-ray source, the flux, source size and position show greater variation, hence requiring more advanced processing methods than the standard Fourier method.

Furthermore, a package `DoseCalc` for the air kerma and dose calculation at the MuCLS was developed.

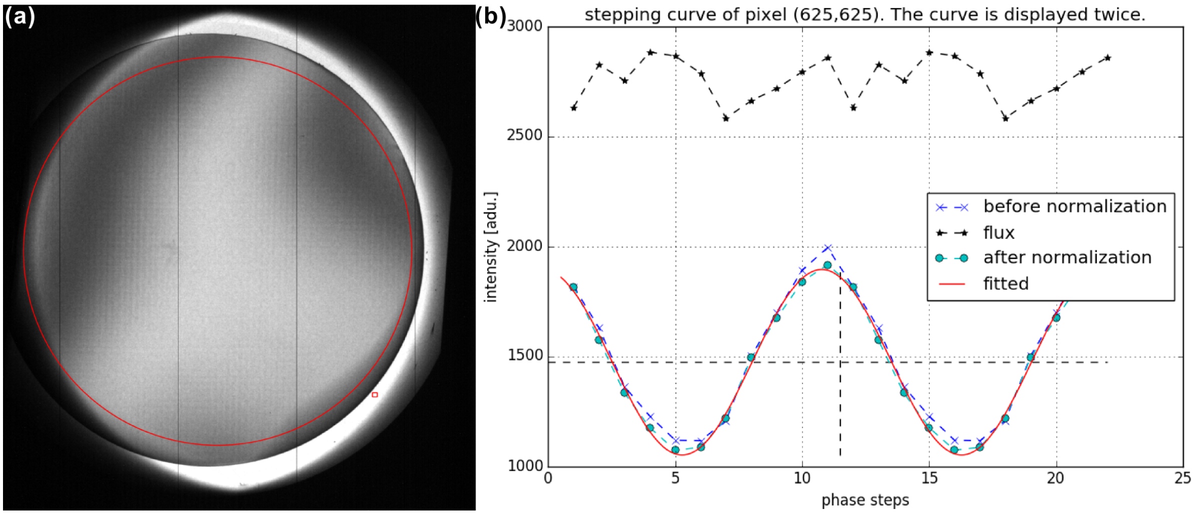

Figure 4.6.: Normalization of the phase stepping series. (a) Raw flat field image. A red rectangle marks the region of interest within the grating substrate that is used for normalization of the phase stepping curves. The red circle marks the mask that is applied to the image after normalization to keep only the active region for processing. (b) Exemplary phase stepping curve (displayed twice) before and after normalization. The normalization accounts for variations in flux.

4.3.1. MammoLib

`MammoLib` comprises functions for processing (retrieval of absorption, differential phase and dark-field signals), stitching and correction of projection data. Because the field of view available at the MuCLS (limited both by the beam size and the currently available grating size) is smaller than most breast samples, a scanning of the sample is required and thus postprocessing to obtain a stitched image, that has in addition been corrected for beam intensity fluctuations. The following steps are executed during the `mam_processing` routine (also illustrated in pseudo python code provided in listing 4.1):

1. Each recorded image is at first processed separately and the three image signals (AC, DPC and DFC) are retrieved using the function `mam.processing`, with the possibility to choose between the two basic functions `lsq_processing` and `em_processing` originating from the `ddfSetupProcessing` package (Guillaume Potdevin, 2012). While `lsq_processing` assumes a regular stepping curve and performs a least squares fit, `em_processing` can also handle irregular stepping curves using a more time-consuming expectation maximization method for the maximum likelihood estimator.
   Previous to the processing, each phase stepping series is normalized using a ROI outside of the grating area to account for flux variations and a mask is applied (fig. 4.6 (a)). Figure 4.6 (b) shows a stepping curve with and without normalization.
   In order to save measurement time, only two flat field images are acquired: one before and one after the sample scan that comprises up to 25 single images to cover the whole breast sample. To correct for possible phase drifts during the measurement, flat fields are interpolated using the function `interpolate_ff_linear` [Viermetz, 2015].

2. The scanning of the breast sample is performed in a zig-zag-move, in order to save scan time due to smaller motor movements. This requires resorting of the images before the stitching routine, which is done by the `mam.resort_fields` function.

3. Finally, the stitching routine is performed using the function `mam.correct_stitch`. A first guess for the correct overlap of the images is calculated from the motor movement and the effective pixel size. This initial choice can be refined previous to the stitching routine by choosing the best stitched picture from a series around the initial guess (best done for the absorption contrast) using the function `mam.find_overlap`. Then, the overlapping regions of all images are compared row-wise and column-wise and corrected for difference in absorption in absorption-contrast images and a phase drift in the differential phase-contrast images. Using a linear ramp for blending, the images (separately for each signal) are stitched together.

4. Further post-processing of the image can be performed using the `mam.filter_collection`.

5. The dose is calculated using the package `DoseCalc` (see below).

Listing 4.1: Python pseudo code illustrating the processing of mammography scans using the MammoLib and DoseCalc packages.

```
"""
Pseudo python script for phase-contrast mammography
@author: Elena Eggl
"""
import mammolib as mam
import dosecalc as dose
#--------------------------------------------------------------
# User input
sample_identifier = ’patient_I’
fields = [5,5] #number of recorded sample positions in each direction
processing = ’lsq’ #’lsq’ for least squares, ’em’ for expectation maximization
ROI = [920,930,840,850] #ROI for flux correction
mask =  [420,-80,-50] #round mask with 420 px diameter and offset=[-80,-50]
#calculate estimated overlaps using the effective pixel size
shifts = [35,38] #motor position shift during scan in mm
estimate_hor = shifts[0]/0.071
estimate_ver = shifts[1]/0.071
#--------------------------------------------------------------
# Processing
#--------------------------------------------------------------
#least squares or expectation maximization processing after normalization of the images, interpolation between the
```

```
   two flat fields recorded before and after the sample scan
   , returns arrays of processed but unstitched images
AC, DPC, DFC= mam.processing(sample_identifier, ROI, mask,
   processing, ff=interpolate, detector=’dexela’)
# Resort fields before stitching
AC, DPC, DFC = mam.resort_fields(AC, DPC, DFC, fields)
# Finding the correct overlap, stitching and correction
size_hor, size_ver = mam.find_overlap(AC, estimate_hor,
   estimate_ver, fields)
AC_stitched, DPC_stitched, DFC_stitched = mam.correct_stitch
   (AC, DPC, DFC, size_hor, size_ver, fields)
#-----------------------------------------------------------
# Calculate dose estimate
#-----------------------------------------------------------
pilatus_identifier = ’patient_I_pilatus’
ROI_pilatus=[240,260,130,150]
t = 4.5 #compressed breast thickness in cm
g = 0.5 #glandularity
MGD = dose.calculate_MGD(sample_identifier,
   pilatus_identifier, ROI_pilatus, t, g)
```

4.3.2. DoseCalc

The contents of the `DoseCalc` python package are described in chapter 8.2 and illustrated in listings 8.1 and A.1.

5. Characterization of the MuCLS

The MuCLS offers several unique properties. The x-ray beam is quasi-monochromatic and the energy is tunable in the range of 15 to 35 keV. Due to a divergence angle of 4 mrad, the beam size at the experimental stations is large compared to typical synchrotron beams. This chapter will present performance parameters of the MuCLS and their stability over short and long time scales. Measured spectra are discussed and compared to simulation results. Parts of the results presented in this chapter are based on the publication [Eggl et al., 2016a].

5.1. X-ray beam shape

5.1.1. Methods & Materials

The full x-ray beam of the MuCLS was acquired in the far experimental hutch (compare figure 4.1) using a PaxScan 2520D flat panel detector (Varian Medical Systems Inc., USA) with a CsI scintillator and a pixel size of 127 × 127 μm^2. The detector was located at a distance of 16.61 m from the interaction point. The divergence angles in horizontal and vertical direction were calculated by dividing the full width at half maximum (FWHM) of the respective beam profile by the distance from the interaction point.

5.1.2. Results

A detector image of the full x-ray beam is shown in figure 5.1. The beam shape is almost round, with a divergence of approximately 4 mrad, with the vertical dimension slightly larger. In a distance of 16.61 m from the interaction point, the beam size (FWHM) was 74.17 mm in the vertical dimension and 66.55 mm in the horizontal dimension, corresponding to divergences of 4.46 mrad and 4.01 mrad, respectively. Beam profiles show the uniform intensity of the beam. The structure visible in the image is caused by the structure of the detector sensor.

5.1.3. Discussion

The shape and size of the x-ray beam are defined by the geometry of the x-ray transmissive thinned area of the output mirror of the laser cavity. The exit mirror is slightly tilted with respect to the axis of the x-ray beam, causing the football-like shape of the transmitted x-ray beam. As the x-ray energy decreases with increasing observation angle (cf. equation 3.18), the spectrum of the x-ray beam will broaden with increasing beam size, i.e. there is a trade-off between beam size and monochromaticity. The chosen divergence angle of approximately 4 mrad is matched to the divergence angle of the

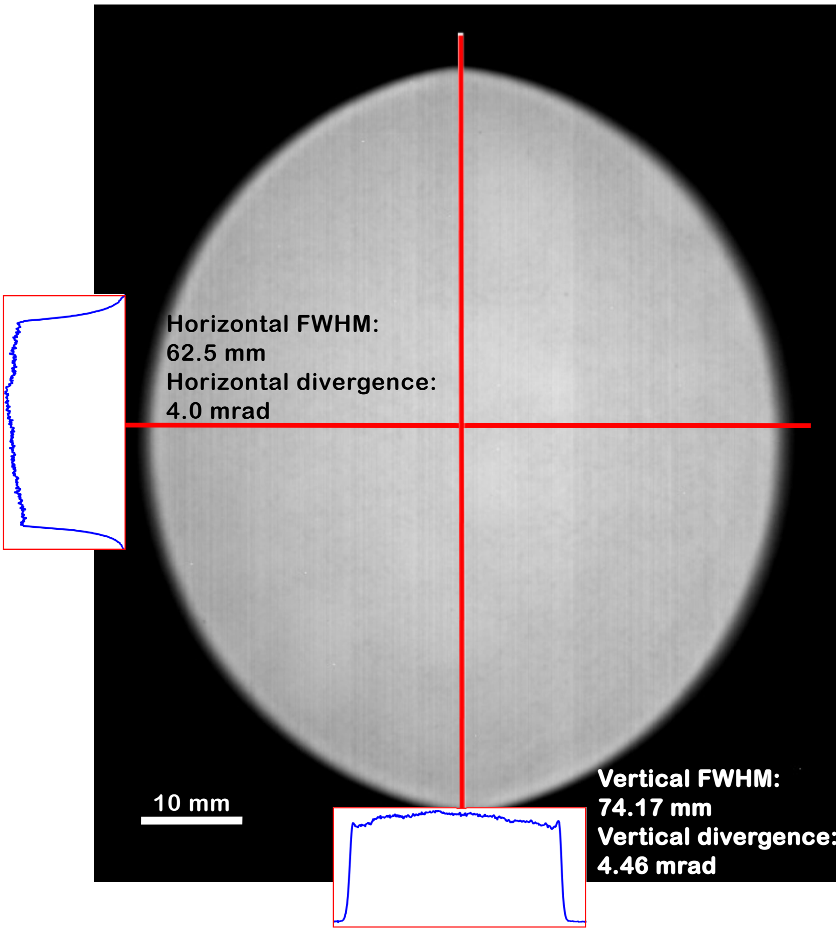

Figure 5.1.: Detector image of the x-ray beam in 16.6 m distance from the interaction point. The image was recorded with a Varian PaxScan detector with a CsI scintillator. The beam profiles show the divergence of approximately 4 mrad and the uniform intensity of the beam. The figure was previously published in [Eggl et al., 2016a].

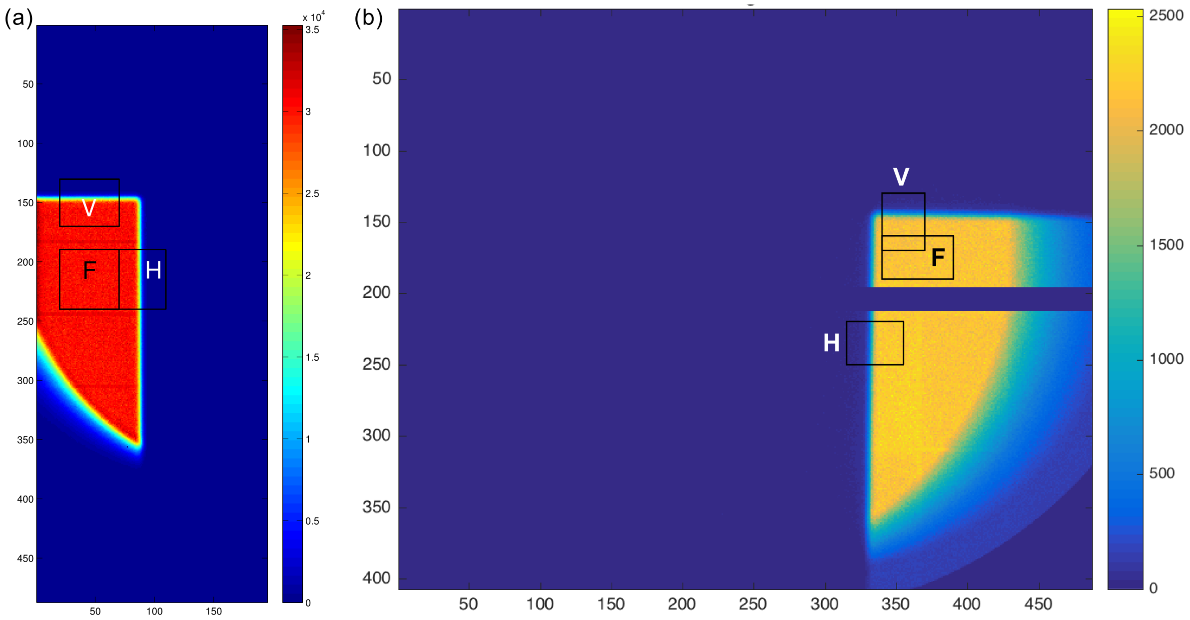

Figure 5.2.: Detector image during the stability analysis. Exemplary detector image taken with the Pilatus 100K detector (a) and the Pilatus 200K detector (b) for the stability analysis. The rectangles indicate the ROIs used for calculation of flux (F), horizontal (H) and vertical (V) parameters. (a) was previously published in [Eggl et al., 2016a].

electron beam and results in the best compromise between desirable large beam size and narrow bandwidth for our present applications. The beam profiles show that the beam intensity is highly uniform across the profile, and sharply falls to zero at the cutoff, as the intensity decrease with observation angle is very small in the chosen range (compare figure 3.5 (d)).

5.2. Source properties and stability

5.2.1. Methods & Materials

A knife-edge approach was chosen to simultaneously measure total flux, source size (horizontal and vertical) and source position (horizontal and vertical) and to examine the stability of these parameters over short and long time scales. A knife edge was placed closely behind the exit window of the x-ray beam and the magnified image of the knife edge was recorded with a Pilatus single photon counting detector (Dectris Ltd., Baden, Switzerland). The detector was located at a distance of approximately 16 meters from the interaction point, resulting in a magnification factor of ~ 9 for the knife edge. The Pilatus detector was equipped with a silicon sensor of 1000 µm thickness. The Pilatus detector is a single photon counting hybrid-pixel detector with a pixel size of 172×172 µm^2 and allows to calculate the photon flux at the detector position when the quantum efficiency of the detector sensor is taken into account.

The total flux was calculated from a region of interest (ROI) on the detector image (size $50 \times 50\,\mathrm{pixel}^2$, as shown exemplarily in figure 5.2, ROI 'F') and by multiplying the average photon count per pixel in ROI 'F' with the total number of pixels covered by

Test date	08/2014	04/2015 (1)	04/2015 (2)	04/2016	03/2017
Facility	Palo Alto	MSB	MSB	MSB	MSB
Operators	Lyncean Tech.	Lyncean Tech.	MuCLS Ops.	MuCLS Ops.	MuCLS Ops./ Lyncean Tech.
Energies [keV]	15/25/35	15/25/35	25	35	15/25/35
Stored charge [pC]	$\sim 500-600$	~ 400	~ 200	~ 260	~ 260
Stored power [kW]	$\sim 140-160$	~ 140	~ 140	~ 100	~ 300
Detector model	Pilatus 100K	Pilatus 100K	Pilatus 100K	Pilatus 200K	Pilatus 200K
IP-Knife edge [m]	1.505	1.470	1.470	1.603	1.603
Knife edge-detector [m]	13.795	14.440	14.440	14.888	14.812
Magnification	9.166	9.897	9.897	9.352	9.240
Air gap [m]	1.020	0.870	0.870	3.462	6.868
Beam pipe windows	Kapton	Mylar	Mylar	Mylar	Mylar
Windows [mm]	0.5	0.5	0.5	0.75	0.5

Table 5.1.: Conditions and parameters during the performance tests presented in chapter 5.2.

the full beam. This number was in addition corrected for the quantum efficiency of the detector sensor (taking only the photoelectric absorption coefficient of Si into account, as it was verified that the Compton effect can be neglected here) and for absorption in air and kapton/mylar windows in the beam path from exit window to detector.

The source sizes and positions were calculated from fitting error functions to the horizontal and vertical edges of the knife edge. The edge function was averaged over 50 pixel lines along the edges of the knife edge (cf. figure 5.2, ROIs 'H' and 'V'), having ensured that the edge was not tilted with respect to the pixels. The point spread function (1 pixel wide, box-shaped PSF) of the Pilatus detector was taken into account when fitting an error function

$$f(x) = a \cdot \operatorname{erf}\left(\frac{x-b}{\sqrt{2}c}\right) + d, \tag{5.1}$$

to the knife edge. The rms source size then is given by the standard deviation c, and b indicates the relative source position. The fit was performed with the `fit` function using a Levenberg-Marquardt algorithm implemented in Matlab.

For the calculation of the average values given in the tables below, the frames where the flux dropped to 0 were included for the average value of the flux and for the corresponding standard deviation, but they were not included for the mean values of source sizes and positions and the respective standard deviations.

Table 5.1 summarizes the parameters (facility, operators, distances, detector model) of all performance tests presented chapter 5.2.

5.2.2. Performance as assessed during Product Acceptance Test (08/2014)

The product acceptance test for the MuCLS was conducted at the facility of Lyncean Technologies Inc. in Palo Alto, California, USA. The flux, source sizes (horizontal and vertical) and source positions (horizontal and vertical) were measured as described above and their stability and on both short and long time scales were examined. For the short-term stability, 3000 frames with a frame rate of 5 Hz, i.e. corresponding to 10 min measurement time, were acquired for three x-ray energies (15, 25 and 35 keV) to measure flux and source sizes as described above. The time frame for an energy change in between these scans was 30 minutes. Selected results of these short-term stability scans, averaged over 10 minutes measurement time, are presented in table 5.2.

Energy	Quantity	Mean value	Std. deviation	Std. deviation [%]
15.2 keV	Total flux [ph/s]	$7.47 \cdot 10^9$	$1.63 \cdot 10^9$	21.8
	Hor. rms source size [µm]	53.3	0.4	0.8
	Ver. rms source size [µm]	49.7	0.4	0.7
	Hor. source position [µm]		2.6	
	Ver. source position [µm]		1.8	
25.0 keV	Total flux [ph/s]	$1.81 \cdot 10^{10}$	$0.06 \cdot 10^{10}$	3.1
	Hor. rms source size [µm]	49.7	0.3	0.6
	Ver. rms source size [µm]	47.5	0.4	0.8
	Hor. source position [µm]		0.7	
	Ver. source position [µm]		0.8	
35.0 keV	Total flux [ph/s]	$3.0 \cdot 10^{10}$	$0.09 \cdot 10^{10}$	3.0
	Hor. rms source size [µm]	49.6	0.3	0.6
	Ver. rms source size [µm]	49.6	0.4	0.9
	Hor. source position [µm]		0.9	
	Ver. source position [µm]		1.7	

Table 5.2.: Short-term stability analysis of flux, source sizes and source positions at peak x-ray energies of 15.2 keV, 24.8 keV and 35.0 keV 30 minutes after starting an energy change, recorded during the product acceptance test (8/2014). Values averaged over 10 minutes.

The analysis shows a mean total flux of $\sim 7.5 \cdot 10^9$ photons/s at 15 keV, $\sim 1.8 \cdot 10^{10}$ photons/s at 25 keV and $\sim 3.0 \cdot 10^{10}$ photons/s at 35 keV. The stability of the flux was good for the 25 and 35 keV runs (around 3% standard deviation), but not satisfactory at 15 keV (more than 20% standard deviation) due to the x-ray flux dropping to zero when the laser lost lock to the cavity. Overall, the stability during these fast time-scale was not satisfactory, with four out of nine short scans (three at each energy) showing drop-outs in flux and standard deviations of the flux above 20%.

To examine the long-term stability, 28800 frames with a frame rate of 1 Hz were recorded, corresponding to a total scan time of 8 hours. The results, acquired at an x-ray energy of 35 keV, are shown in table 5.3.

During this long scan, an average total flux of $\sim 2.3 \cdot 10^{10}$ photons/s was measured, however with a very high standard deviation of about 45%. As visible from the plot of the full scan shown in figure 5.3, the flux dropped to zero for three longer periods of time, plus on one short occasion. During the first two longer interruptions, the electron beam was stopped in order to clean the cathode after the intensity had started to decrease. During the third interruption, a failed kicker card was exchanged. During the short interruptions, the laser lost lock to the cavity.

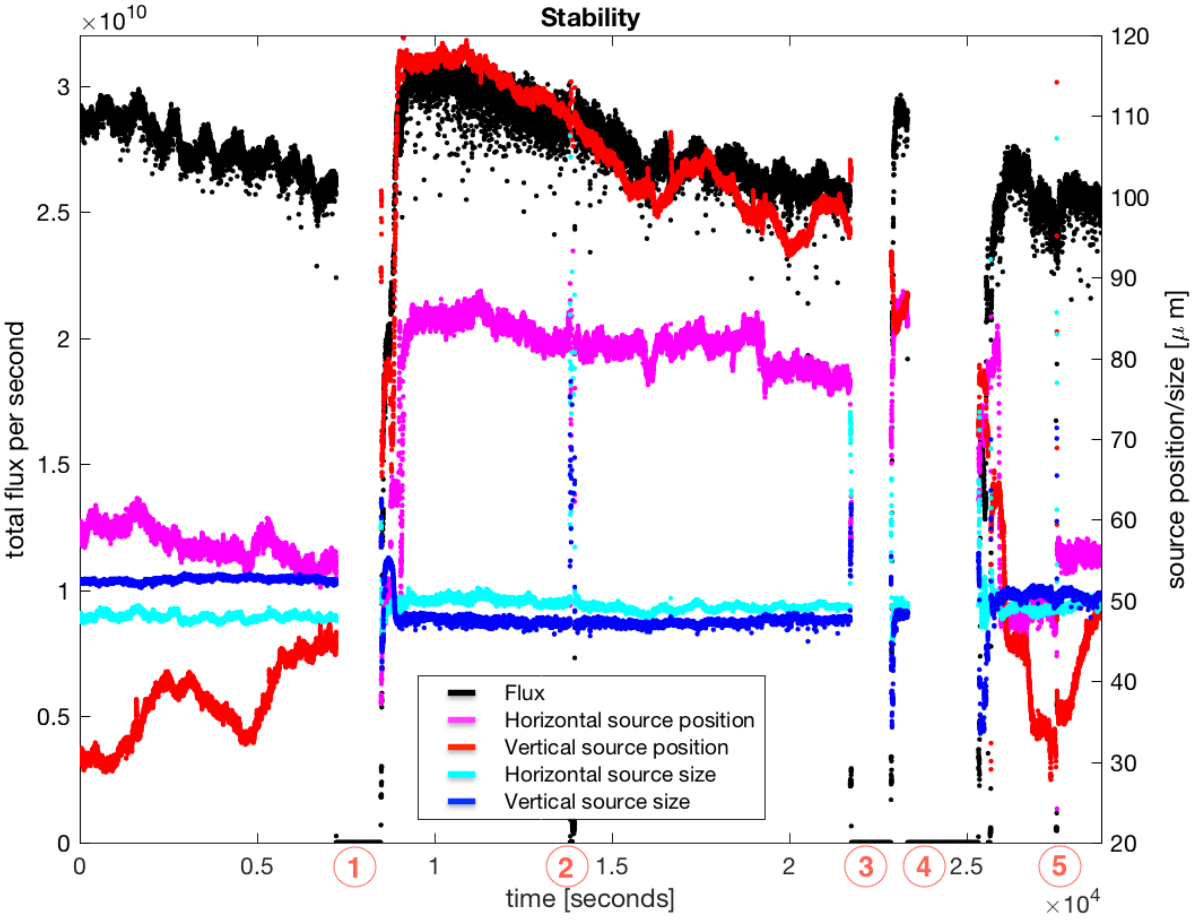

Figure 5.3.: Long-term stability as measured during the product acceptance test in August 2014 at 35 keV x-ray energy. The plot shows the time curves (28800 frames, 1 Hz) of the total flux, the source sizes and source positions. The total flux [ph/s] measured with the Pilatus detector was corrected for detector efficiency and absorption in air and kapton using the measured spectrum at 35 keV x-ray energy. The plot shows a rather unstable x-ray beam, with three extended drop-outs of the x-ray flux (two of which were due to cathode cleaning (1,3), one due to a kicker card failure (4)) and two short drops in intensity which were caused by the laser losing lock to the cavity (2,5). Furthermore, the x-ray beam follows instabilities of the laser system, which can be seen from changes in source position that also affect the x-ray flux.

Energy	Quantity	Mean value	Std. deviation	Std. deviation [%]
35.0 keV	Total flux [ph/s]	$2.28 \cdot 10^{10}$	$1.03 \cdot 10^{10}$	45.1
	Hor. rms source size [µm]	49.1	1.8	3.6
	Ver. rms source size [µm]	49.4	2.9	5.8
	Hor. source position [µm]		13.7	
	Ver. source position [µm]		33.4	

Table 5.3.: Long-term stability analysis of flux, source sizes and source positions at a peak x-ray energies of 35.0 keV, recorded during the product acceptance test (8/2014). Values averaged over 3 hours.

5.2.3. Performance as assessed during Facility Acceptance Test (04/2015)

Before the installation of the MuCLS at the MSB facility, the laser system was replaced to yield higher stability of the x-ray beam. Both short- and long-term stability scans acquired during and shortly after the facility acceptance test in April 2015 show an improved stability of the x-ray beam parameters over those acquired at the Palo Alto facility. Exemplary results from the short stability scans are provided in table 5.4. These were acquired 90 minutes after an energy change and the values were averaged over 10 minutes.

Energy	Quantity	Mean value	Std. deviation	Std. deviation [%]
15.2 keV	Total flux [ph/s]	$4.78 \cdot 10^{9}$	$0.06 \cdot 10^{9}$	1.13
	Hor. rms source size [µm]	47.1	0.3	0.5
	Ver. rms source size [µm]	42.4	0.9	2.1
	Hor. source position [µm]		0.5	
	Ver. source position [µm]		1.0	
24.8 keV	Total flux [ph/s]	$1.23 \cdot 10^{10}$	$0.03 \cdot 10^{10}$	2.85
	Hor. rms source size [µm]	42.4	0.2	0.5
	Ver. rms source size [µm]	38.3	0.5	2.1
	Hor. source position [µm]		0.5	
	Ver. source position [µm]		0.9	
35.0 keV	Total flux [ph/s]	$1.92 \cdot 10^{10}$	$0.04 \cdot 10^{10}$	1.83
	Hor. rms source size [µm]	40.2	0.3	0.8
	Ver. rms source size [µm]	37.8	0.3	0.8
	Hor. source position [µm]		0.5	
	Ver. source position [µm]		0.3	

Table 5.4.: Short-term stability analysis of flux, source sizes and source positions at peak x-ray energies of 15.2 keV, 24.8 keV and 35.0 keV 90 minutes after starting an energy change, recorded during the facility acceptance test (4/2015). Values averaged over 10 minutes.

The results show lower flux at $\sim 4.4 \cdot 10^9$ photons/s at 15 keV, $\sim 1.1 \cdot 10^{10}$ photons/s at 25 keV and $\sim 1.8 \cdot 10^{10}$ photons/s at 35 keV. The source sizes have improved, with the largest source size measured at 15 keV and the smallest at 35 keV at approximately

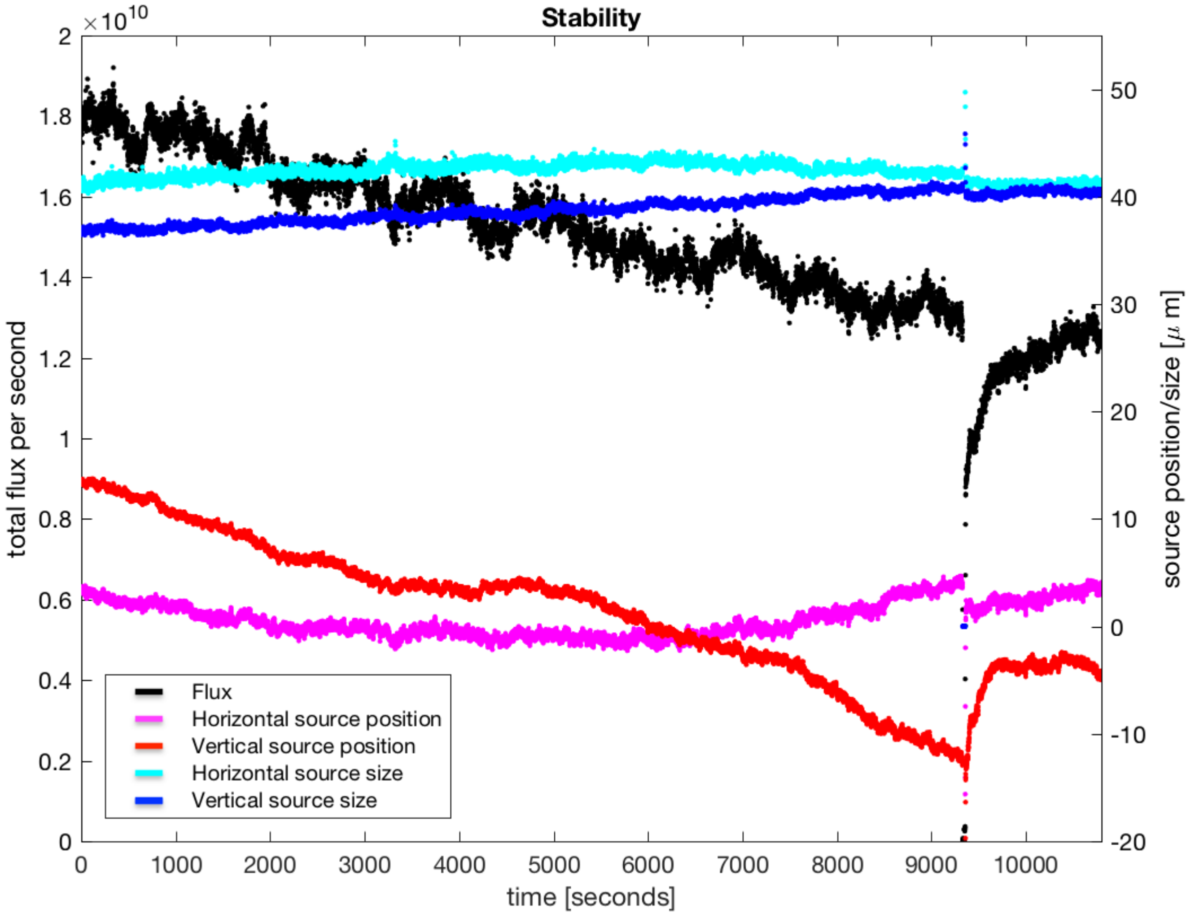

Figure 5.4.: Long-term stability as measured during the facility acceptance test in April 2015 at 35 keV x-ray energy. The plot shows the time curves (10800 frames, 1 Hz) of the total flux, the source sizes and source positions. The total flux [ph/s] measured with the Pilatus detector was corrected for detector efficiency and absorption in air and mylar using the measured spectrum at 35 keV x-ray energy. The flux decreased steadily during the scan, a short drop in intensity could be observed due to the cavity losing lock.

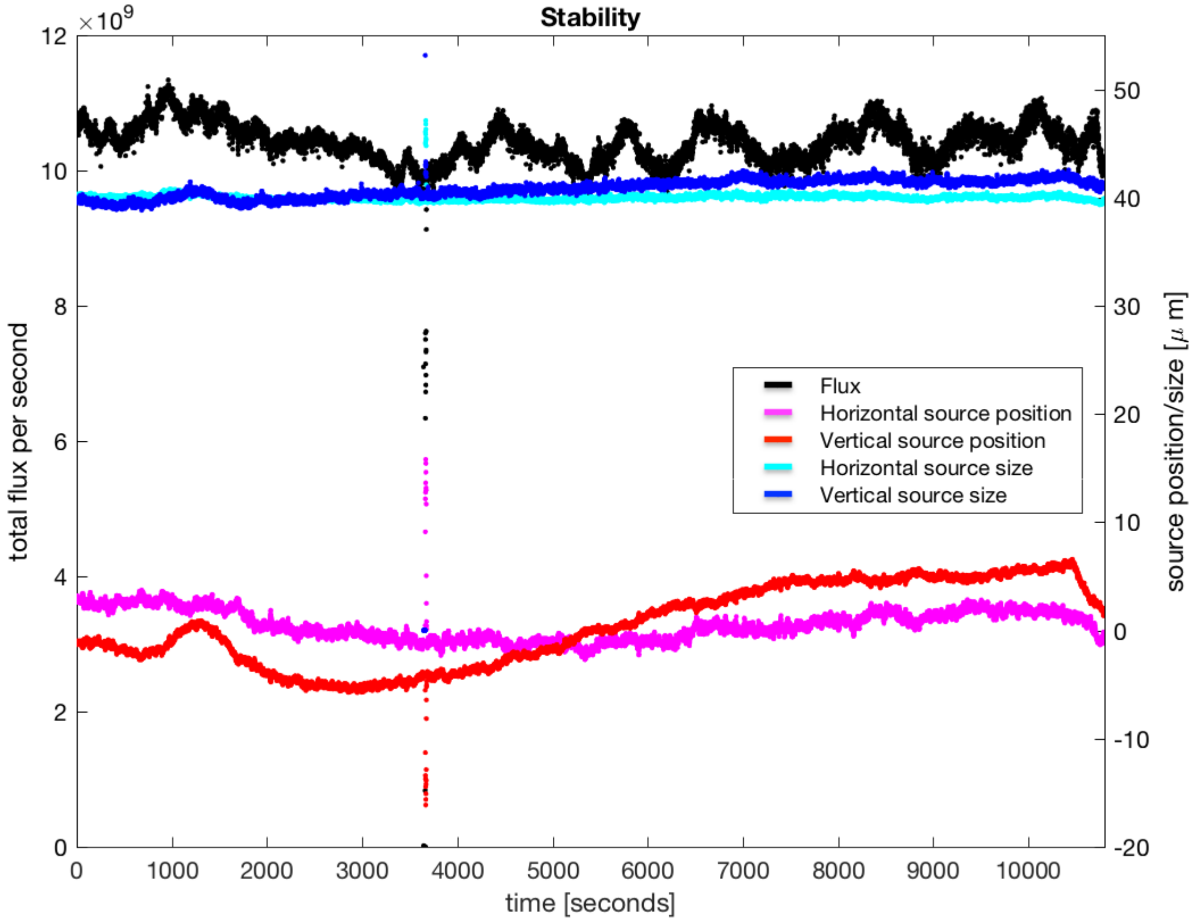

Figure 5.5.: Long-term stability as measured shortly after the facility acceptance test in April 2015 at 25 keV x-ray energy. The plot shows the time curves (10800 frames, 1 Hz) of the total flux, the source sizes and source positions. The total flux [ph/s] measured with the Pilatus detector was corrected for detector efficiency and absorption in air and mylar using the measured spectrum at 25 keV x-ray energy. The short drop in intensity was caused by the laser losing lock to the cavity, the lock was restored by the operators.

$40 \times 38\ \mu\mathrm{m}^2$. The stability improved significantly, with drop-outs of the x-ray beam (due to the laser losing lock to the cavity) only taking place in two out of nine scans (three at each energy). Also, the standard deviations of the flux have improved and were between 1-2% for the majority of the test scans. The standard deviations of source size and position are larger in the vertical than in the horizontal direction.

For the long-term stability, one three hour scan was acquired at 35 keV during the facility acceptance test (plot shown in figure 5.4 and one three hour scan at 25 keV shortly after the acceptance test (plot shown in figure 5.5). The flux, source sizes and positions were averaged over three hours and are shown in table 5.5.

Energy	Quantity	Mean value	Std. deviation	Std. deviation [%]
24.8 keV	Total flux [ph/s]	$1.04 \cdot 10^{10}$	$0.05 \cdot 10^{10}$	4.95
	Hor. rms source size [µm]	40.0	0.4	1.0
	Ver. rms source size [µm]	40.8	0.8	2.1
	Hor. source position [µm]		1.4	
	Ver. source position [µm]		3.8	
35.0 keV	Total flux [ph/s]	$1.49 \cdot 10^{10}$	$0.20 \cdot 10^{10}$	13.61
	Hor. rms source size [µm]	42.4	0.8	1.8
	Ver. rms source size [µm]	38.9	1.3	3.2
	Hor. source position [µm]		1.6	
	Ver. source position [µm]		6.6	

Table 5.5.: Long-term stability analysis of flux, source sizes and source positions at a peak x-ray energies of 24.8 keV and 35.0 keV, recorded in April 2015. Values averaged over 3 hours.

At 25 keV x-ray energy, the total integrated flux was mostly between $1.0 \cdot 10^{10}$ and $1.1 \cdot 10^{10}$ photons per second, with one short drop in flux about an hour into the run, yielding an average flux of $\sim 1 \cdot 10^{10}$ ph/s with a rms deviation of less than 5%. For the 35 keV x-ray energy run, the flux started at $1.8 \cdot 10^{10}$ photons/s and decreased steadily to about $1.2 \cdot 10^{10}$ photons/s with one short drop to zero, yielding an average flux of $1.49 \cdot 10^{10}$ photons/s with a standard deviation of 13.6%. The source sizes are similar to what has been observed during the short stability scans and they show good stability (1-3% standard deviation) even over a long period of time. The source positions show a standard deviation of a few micron.

5.2.4. Performance as assessed after extended maintenance (04/2016)

Extended maintenance work was performed on the MuCLS in April 2016, after which a shortened performance test was conducted. The performance was tested for short- and long-term stability, however only at a single energy (35.0 keV peak x-ray energy). During the measurements, the operators did not interact with the machine. The short time-scale stability of flux, source sizes and source positions was examined during 10 minute measurements with 5 Hz frame rate. Exemplary averaged results are given in table 5.6.

Energy	Quantity	Mean value	Std. deviation	Std. deviation [%]
35.0 keV	Total flux [ph/s]	$1.24 \cdot 10^{10}$	$0.03 \cdot 10^{10}$	2.5
	Hor. rms source size [µm]	39.0	0.5	1.2
	Ver. rms source size [µm]	36.4	0.2	0.6
	Hor. source position [µm]		0.4	
	Ver. source position [µm]		0.4	

Table 5.6.: Short-term stability analysis of flux, source sizes and source positions at a peak x-ray energy of 35.0 keV, recorded after the extended maintenance (4/2016). Values averaged over 10 minutes.

The three short scans that were performed showed very similiar results like the one presented in table 5.6, with a flux around $\sim 1.2 \cdot 10^{10}$ photons per second and source sizes around 39×37 µm^2. Very good stability was found during these scans, with standard deviations of 2.5% for the flux, less than 1.5% for the source size and less than 0.5 µm for the source positions.

For assessing the long-term stability, a three hour scan with a frame rate of 1 Hz was acquired. The average values for flux, source sizes and source positions are provided in table 5.7 and a plot of the values is shown in figure 5.6.

Energy	Quantity	Mean value	Std. deviation	Std. deviation [%]
35.0 keV	Total flux [ph/s]	$1.09 \cdot 10^{10}$	$0.20 \cdot 10^{10}$	18.0
	Hor. rms source size [µm]	42.6	1.2	2.8
	Ver. rms source size [µm]	40.1	1.4	3.4
	Hor. source position [µm]		3.5	
	Ver. source position [µm]		2.2	

Table 5.7.: Long-term stability analysis of flux, source sizes and source positions at a peak x-ray energy of 35.0 keV, recorded after the extended maintenance (4/2016). Values averaged over 3 hours.

The long scan revealed similar values for the flux, with a lower average value due to a decrease in flux during the last 45 minutes of the scan caused by changing environmental conditions (temperature drift in the MuCLS cave) which affected the injector laser and subsequently the injected charge, since this performance test was conducted without operator intervention. Shortly before the end of the run, a pressure wave caused the injector laser to lose lock and thus the no more electrons were injected. Before these events, the x-ray beam showed very good stability.

5.2.5. Performance as assessed after Laser Upgrade (03/2017)

In March 2017, an upgrade to the laser system of the MuCLS was installed. The amplifier system was replaced by a pre-amplifier and a power amplifier, increasing the input laser power from ~ 14 W to ~ 30 W and thus allowing to store a power of more than 300 kW in the enhancement cavity (compare tables 3.1 and 3.2). The performance was tested using the same approach as applied before, i.e. examining the short- and long-term stability of flux, source sizes and positions using the knife-edge method. Exemplary

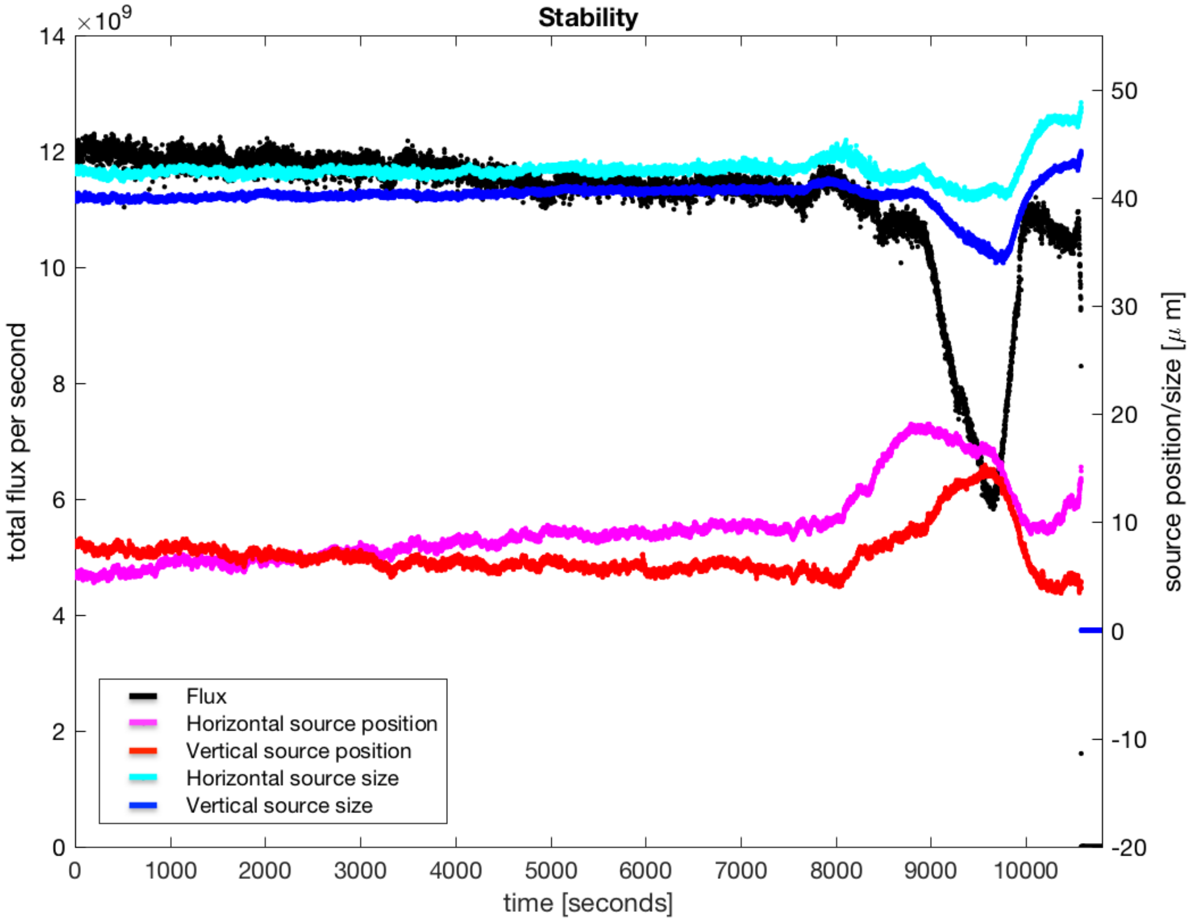

Figure 5.6.: Long-term stability as measured after the extended maintenance in April 2016 at 35 keV x-ray energy. The plot shows the time curves (10800 frames, 1 Hz) of the total flux, the source sizes and source positions. The total flux [ph/s] measured with the Pilatus detector was corrected for detector efficiency and absorption in air and mylar using the measured spectrum at 35 keV x-ray energy. The MuCLS was run without operator intervention. Therefore, the flux was strongly affected in the last part of the scan, where the facility temperature started to drift, which affected the injector laser system and resulted in reduced charge stored in the ring.

results for the short measurements, acquired at the three peak x-ray energies of 15.2, 25.0 and 35.0 keV are presented in table 5.8.

Energy	Quantity	Mean value	Std. deviation	Std. deviation [%]
15.2 keV	Total flux [ph/s]	$7.76 \cdot 10^9$	$0.16 \cdot 10^9$	2.04
	Hor. rms source size [µm]	51.20	0.26	0.5
	Ver. rms source size [µm]	46.42	0.34	0.74
	Hor. source position [µm]		0.93	
	Ver. source position [µm]		1.03	
25.0 keV	Total flux [ph/s]	$2.12 \cdot 10^{10}$	$0.05 \cdot 10^{10}$	2.52
	Hor. rms source size [µm]	47.82	0.39	0.81
	Ver. rms source size [µm]	46.06	0.39	0.85
	Hor. source position [µm]		0.91	
	Ver. source position [µm]		1.19	
35.0 keV	Total flux [ph/s]	$3.33 \cdot 10^{10}$	$0.04 \cdot 10^{10}$	1.31
	Hor. rms source size [µm]	43.30	0.48	1.11
	Ver. rms source size [µm]	39.28	0.22	0.56
	Hor. source position [µm]		0.82	
	Ver. source position [µm]		0.27	

Table 5.8.: Short-term stability analysis of flux, source sizes and source positions at peak x-ray energies of 15.2 keV, 24.8 keV and 35.0 keV 90 minutes after starting an energy change, recorded after the laser upgrade (3/2017). Values averaged over 10 minutes.

The analysis shows a significantly increased flux at all energies compared to the last tests performed at all energies in April 2015, even though the charge stored in the electron ring was lower (250 pC compared to 300-400 pC). Total fluxes of $\sim 7.8 \cdot 10^9$, $\sim 2.1 \cdot 10^{10}$ and $\sim 3.3 \cdot 10^{10}$ photons per second were reached at 15, 25 and 35 keV x-ray energy, respectively.

Due to the higher power in the cavity and a larger waist size of the laser beam at the interaction point, the source sizes increased slightly. Overall, the stability also improved, as also verified by two long-term stability tests performed at an x-ray energy of 25 keV. One run was performed for three hours without operator intervention, and the second one was performed over 5 hours with limited operator intervention. Results averaged over three and five hours, respectively, are summarized in table 5.9. Plots of all source parameters for the two long runs are displayed in figures 5.7 and 5.8 for 3 and 5 hours, respectively.

Figure 5.7 shows a steady decrease of flux, combined with a drift in source positions, caused by an alignment drift of the laser cavity (which remained uncorrected during this run without operator intervention). Figure 5.8 shows two drop-outs of the x-ray beam when such thermal drifts were corrected for by larger moves of the cavity, causing the laser to lose lock.

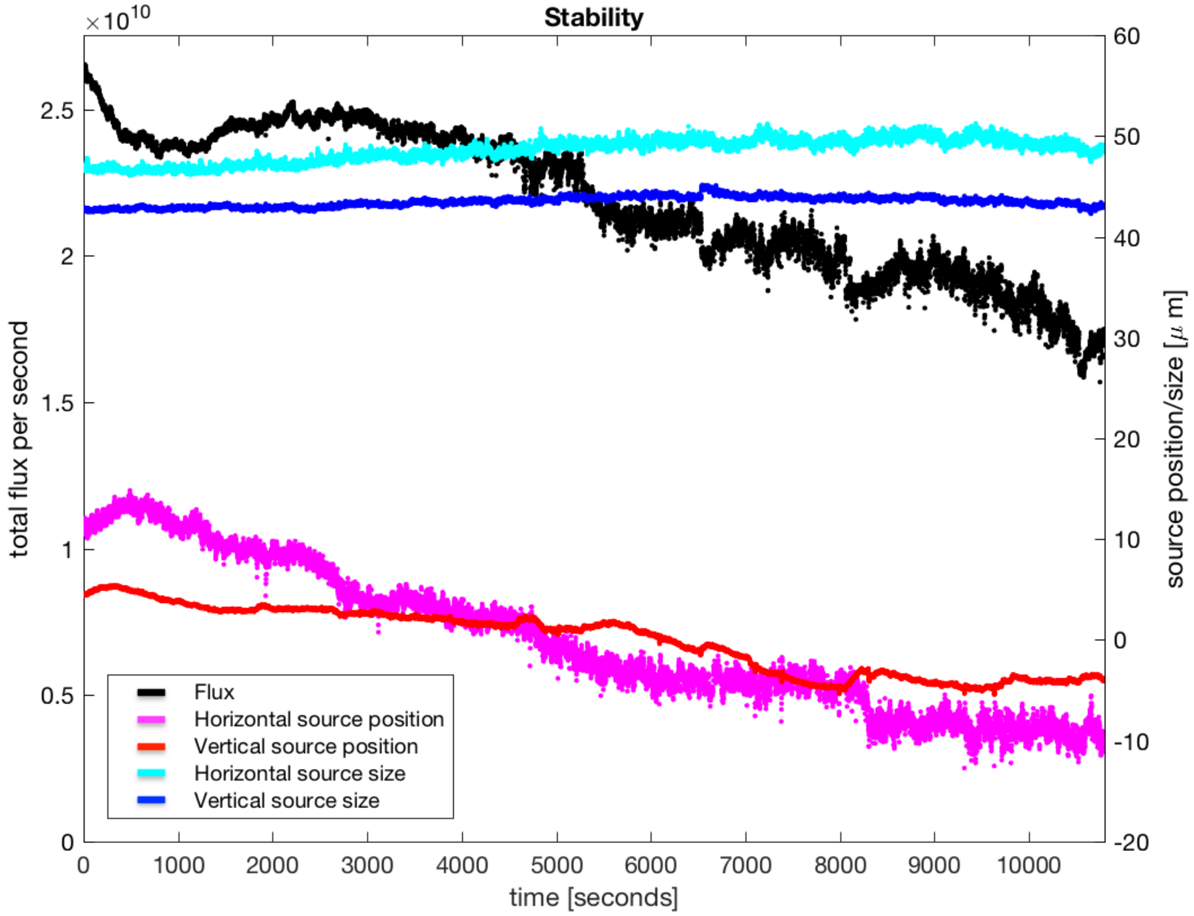

Figure 5.7.: Long-term stability as measured after the laser upgrade in March 2017 at 25 keV x-ray energy. The plot shows the time curves (10800 frames, 1 Hz) of the total flux, the source sizes and source positions. The total flux [ph/s] measured with the Pilatus detector was corrected for detector efficiency and absorption in air and mylar using the measured spectrum at 25 keV x-ray energy. The MuCLS was run without operator intervention. Therefore, the flux was strongly affected by a temperature drift of the optical cavity, as seen by the drift of the source positions.

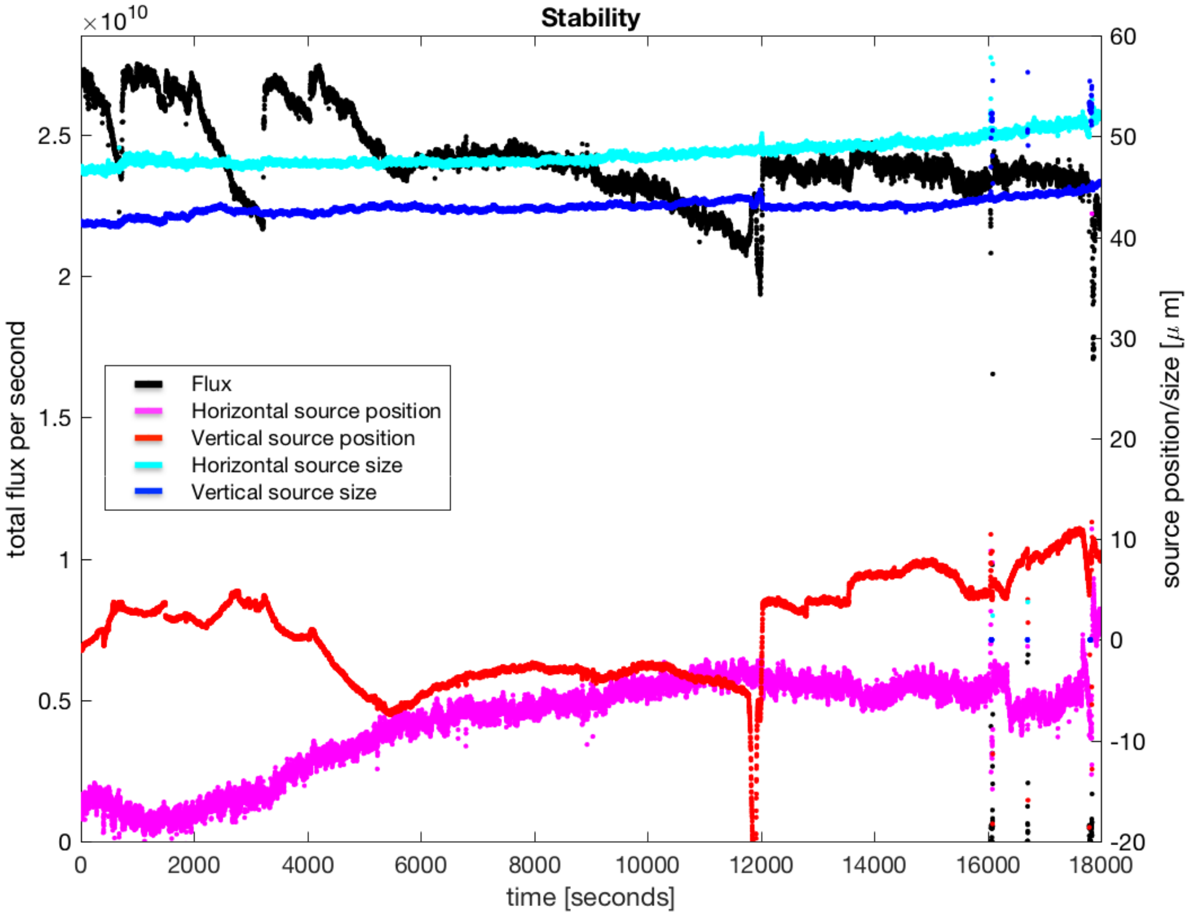

Figure 5.8.: Long-term stability as measured after the laser upgrade in March 2017 at 25 keV x-ray energy. The plot shows the time curves (18000 frames, 1 Hz) of the total flux, the source sizes and source positions. The total flux [ph/s] measured with the Pilatus detector was corrected for detector efficiency and absorption in air and mylar using the measured spectrum at 25 keV x-ray energy. The MuCLS was run with limited operator intervention. The x-ray beam was lost twice when a larger move on the laser cavity was performed.

Energy	Quantity	Mean value	Std. deviation	Std. deviation [%]
25.0 keV, 3h	Total flux [ph/s]	$2.19 \cdot 10^{10}$	$0.25 \cdot 10^{10}$	11.23
	Hor. rms source size [µm]	48.60	1.16	2.38
	Ver. rms source size [µm]	43.48	0.50	1.14
	Hor. source position [µm]		7.21	
	Ver. source position [µm]		3.22	
25.0 keV, 5h	Total flux [ph/s]	$2.40 \cdot 10^{10}$	$0.22 \cdot 10^{10}$	9.34
	Hor. rms source size [µm]	48.35	1.86	3.85
	Ver. rms source size [µm]	43.02	1.27	2.96
	Hor. source position [µm]		5.30	
	Ver. source position [µm]		5.24	

Table 5.9.: Long-term stability analysis of flux, source sizes and source positions at a peak x-ray energy of 25.0 keV recorded after the laser upgrade (3/2017). Values averaged over 3 hours and 5 hours, respectively.

Test date	08/2014	04/2015	04/2016	03/2017
Total flux [ph/s]	$3.00 \cdot 10^{10}$	$1.92 \cdot 10^{10}$	$1.24 \cdot 10^{10}$	$3.33 \cdot 10^{10}$
Source size [µm^2]	49.6×49.6	40.2×37.8	39.0×36.4	43.3×39.3
Brilliance $\left[\frac{\mathrm{ph}}{\mathrm{s\,mm^2\,mrad^2\,0.1\%\,BW}}\right]$	$7.72 \cdot 10^9$	$8.00 \cdot 10^9$	$5.53 \cdot 10^9$	$8.26 \cdot 10^9$

Table 5.10.: Brilliance for parameters measured during the tests as presented above at 35 keV calculated from equation 5.2.

5.2.6. Brilliance

The brilliance can be calculated from [Attwood, 2007],

$$B = \frac{\Phi \cdot 10^{-3}}{\Delta A \cdot \Delta\Omega \cdot \frac{\Delta E}{E}} \tag{5.2}$$

where Φ is the total x-ray flux per second, $\Delta A = \pi\sigma_x\sigma_y$ is the source area with $\sigma_{x,y}$ the source sizes, $\Delta\Omega \approx 4\pi\frac{\theta}{4}$ is the solid angle with θ the divergence angle, and $\Delta E/E$ is the bandwidth of the spectrum. The brilliance calculated from each set of performance parameters measured at 35 keV x-ray energy during the short-term stability scans in 08/2014, 04/2015, 04/2016 and 03/2017 is given in table 5.10. An angular spread of $\theta = 4$ mrad was used in the calculation for all measurements. A relative bandwidth of 4% for the measurements before the laser upgrade and a relative bandwidth of 6% after the laser upgrade at 35 keV was assumed.

5.2.7. Stability on very short time scales

Very high frame-rate scans were acquired using the Pilatus 100K detector. The measurements were acquired at the Lyncean Technologies facility in Palo Alto, USA. Therefore, the re-injection rate of the electron beam was 30 Hz instead of the 25 Hz used in Mu-

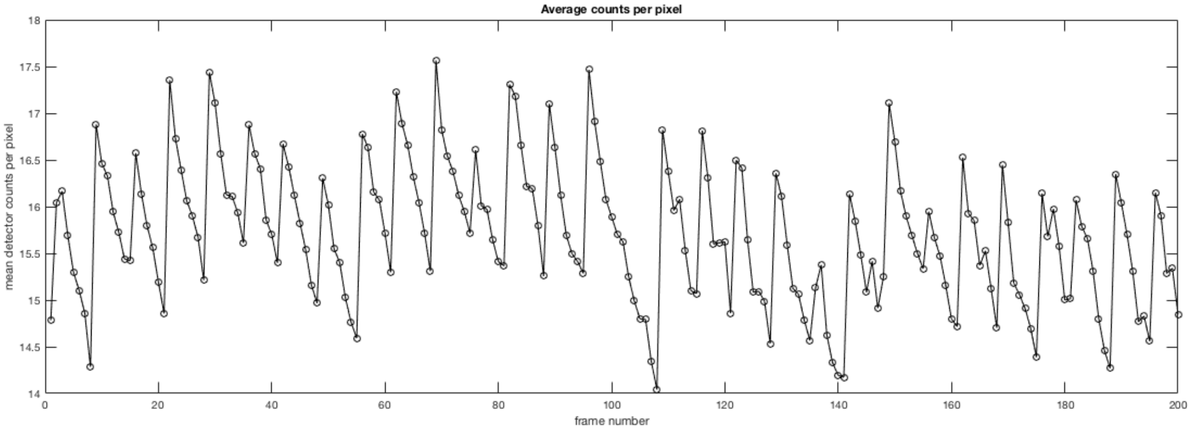

Figure 5.9.: Flux resolved with a high frame rate of 200 Hz. The plot of the mean detector counts per pixel shows how the flux decreases by about 10% during on injection cycle (corresponding to about 200 Hz/30 Hz = 6.67 frames).

nich[1]. Figure 5.9 shows the mean counts per detector pixel during 200 frames acquired with a frame rate of 200 Hz. The re-injection rate corresponds to 200 Hz/30 Hz ≈ 6.67 frames after which a new bunch is injected. The plot shows how the flux decreases by approximately 10% during 6-7 frames before it returns to the original value after the re-injection.

This effect, which will only be visible at very high frame rates above (for the Munich installation) 25 Hz, is very unlikely to have any negative effect on the image quality as usually performed experiments mostly used scan times of ∼ 1 second and therefore sample many re-injection cycles.

5.2.8. Discussion

The presented results show that the MuCLS produces stable flux over several hours and there is little variation in source size and position. This performance makes the source suitable for imaging experiments lasting several hours as demonstrated previously as well [Eggl et al., 2015b].

Since the product acceptance test conducted at the Lyncean Technologies facility in August 2014, the stability of the x-ray beam has seen great improvements due to the joint efforts of Lyncean Technologies and the MuCLS operators. The improvements in stability over the measurements in August 2014 and also over those in April 2015 were made at the expense of photon flux. The decrease in flux can be assigned to two main points. Firstly, before the MuCLS was installed in Munich, the laser amplifier system was exchanged in order to provide a more stable store of the laser beam in the cavity, while losing some input power to the cavity. To some degree, this could be compensated by achieving very low losses through improved cleanliness of the cavity optics and improved vacuum. The second aspect for increased stability is reduced electron bunch charge stored in the ring, which makes operation more stable and less prone to hardware issues such as kicker card failures.

---

[1] The re-injection rate is chosen as half of the power line frequency, which is 60 Hz in the USA and 50 Hz in Europe.

The combination of increased cavity stability, reduced electron bunch charge (which reduces the emittance of the electron beam) has had a positive effect on the x-ray source sizes which have decreased from $\sim$ 49 µm in August 2014 to $\sim$ 40 µm in April 2016. The laser upgrade caused a slight increase in source sizes due to the larger laser beam waists at higher power.

The upgraded laser amplifier installed in March 2017 more than doubled the power stored in the enhancement cavity to above 300 kW. This increased the flux to values above those reached in August 2014, yet at much lower electron bunch charge. Due to the increase in stored power, the time for the laser cavity to reach thermal equilibrium has been prolonged significantly, however the stability once equilibrated even has improved as shown by the small standard deviations in the short- and long-term stability measurements in March 2017.

The presented results for the x-ray flux and source size, i.e. decreasing flux and increasing source sizes with decreasing x-ray energy, confirm what can be expected from luminosity calculations that take into account the aperture window. When decreasing the electron energy (and hence the x-ray energy), the spot size at the interaction point (IP) will increase. In addition, the divergence at the IP will increase, such that less flux will be emitted through the output window due to the changed anglular distribution. This effect causes the flux to scale approximately with the energy. Low energies (especially for 15 keV) are affected in addition by the increasing absorption of the output window which is made of 200 µm thick silicon. From a combination of these effects, for otherwise equal conditions, the flux at 15 keV will be approximately 30% of the flux at 35 keV [Loewen, 2017]. Comparison of the values acquired at 15 and 35 keV during the tests in 2014, 2015 and 2017 shows that the flux at 15 keV is reduced even further ($\sim$25% of the 35 keV value).

5.3. Spectra

5.3.1. Methods & Materials

X-ray spectra were measured using an energy-dispersive Amptek X-123 detector. As an attenuator, 39 mm of PMMA were inserted for the 15 keV measurement and 78 mm of PMMA were inserted for the 25 keV and the 35 keV measurements. The energy channels were calibrated via the K_α and K_β lines from the fluorescence of a Cu plate. The measured spectra were corrected for the efficiency of the 500 µm thick Si sensor of the Amptek detector as well as the transmission through PMMA and the air gap between the IP and the detector. The bandwidth (BW) was calculated as the FWHM of the spectrum divided by the peak energy.

MuCLS spectra were simulated using the spectrum of inverse Compton scattering (compare equation 3.22) for a 4 mrad aperture, folding in the electron beam energy spread and emittance. The simulation is based on a Monte Carlo model and written in LabView [Loewen, 2017].

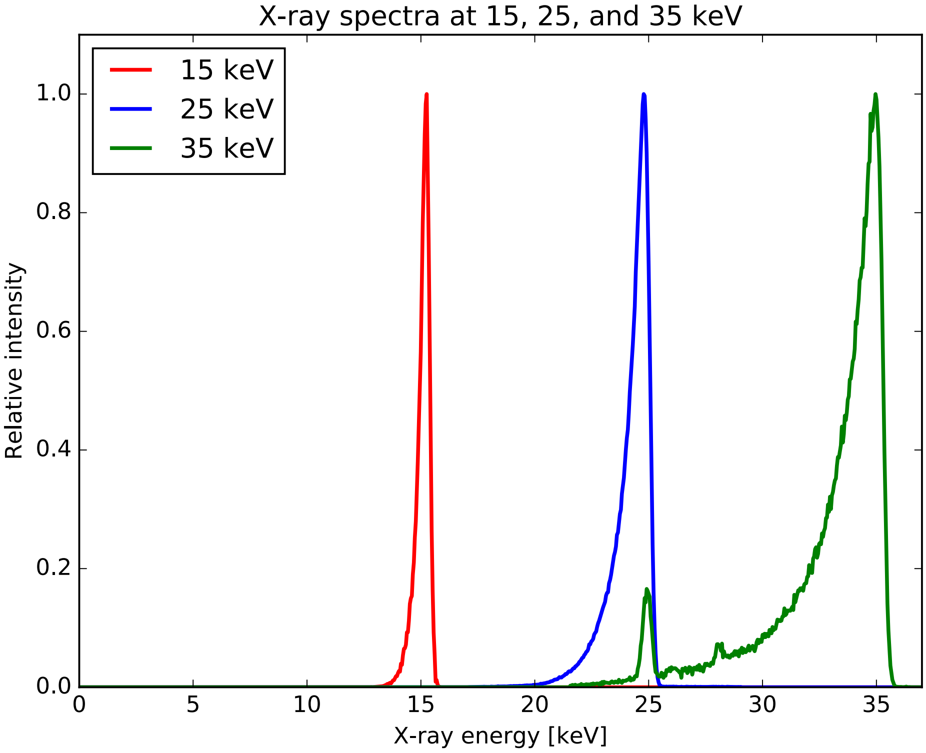

Figure 5.10.: Measured spectra at peak energies of 15.2 keV, 24.8 keV and 35.0 keV. The figure was previously published in [Eggl et al., 2016a].

Peak energy [keV]	FWHM [keV]	bandwidth $\frac{\Delta E}{E}$ [%]
15.26	0.46	2.99
24.78	0.89	3.60
34.96	1.50	4.29

Table 5.11.: Peak energies and bandwidths of the measured spectra shown in figure 5.10.

5.3.2. Results

Spectra acquired for three different x-ray energies are presented in figure 5.10. Displayed are data for peak energies of 15.2 keV, 24.8 keV, and 35.0 keV, normalized to their maximum value. In principle, the peak energy of the x-ray spectrum produced by the MuCLS is freely tunable between 15 and 35 keV by adjusting the electron energy according to equation 3.16. The small peaks visible for the 35.0 keV spectrum at $\sim$ 25 keV and $\sim$ 28 keV originate from the Sn-K_α and -K_β fluorescence lines of the solder of the thermoelectric cooler of the Amptek X-123 detector, respectively.

All spectra show narrow peaks. The FWHM and BWs for the three measured spectra are given in table 5.11, showing the quasi-monochromaticity of the source with a BW $\frac{\Delta E}{E}$ of a few percent over the full energy range.

Figure 5.11 (a) provides a comparison of spectra acquired when running the nominal 25 keV configuration at four different times. The spectrum measured in May 2016 shows a significantly increased FWHM (1.77 keV) and BW (7.2%) over the spectrum acquired

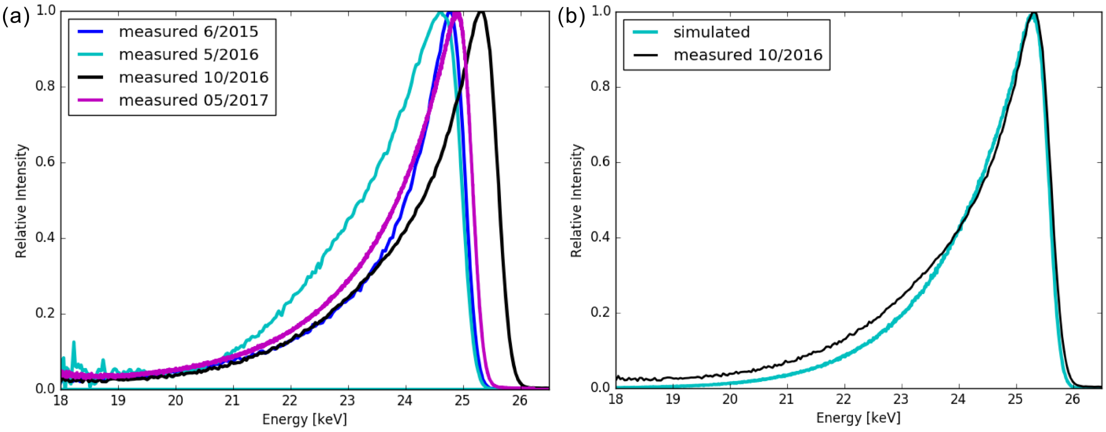

Figure 5.11.: Comparison of different 25 keV MuCLS spectra. (a) The plot presents four spectra acquired with the nominal 25 keV configuration at different time points, showing how the quality of the electron beam can affect the width and peak of the spectrum. (b) The plot compares a measured spectrum with a simulated one, showing very good agreement. Simulated spectrum provided by Rod Loewen, Lyncean Technologies Inc. [Loewen, 2017].

in June 2015. The spectrum from October 2016 has a bandwidth of 5.3% (FWHM), however with the peak x-ray energy shifted to 25.3 keV. In the spectrum measured in May 2017 after the installation of the laser amplifier upgrade in March 2017, the peak x-ray energy decreased to a value of 24.9 keV which is more similar to previously measured values with a bandwidth of 5.1% (FWHM).

The comparison of the measured with the simulated spectrum presented in figure 5.11 (b) shows very good agreement between the spectra for the high-energy tail. The low-energy tails agree also to a large extent, with some differences in the slope. The simulated spectrum follows an exponential decay to zero intensity, other than the measured one.

5.3.3. Discussion

The measured spectra show the narrow bandwidth of the MuCLS x-ray beam. From figure 5.10 it is visible that the peak in the spectra is broadened to both sides. The peak x-ray energy is determined by the electron beam energy. The high-energy tail is broadened by the electron energy spread $\Delta E_e/E_e$ and caused by distributions in electron energies and laser photon energies and follows an error function. The broadening of the low-energy tail is caused by the electron energy spread for the upper part, while the lower slope mainly has its origin in the electron beam divergence $\Delta\theta_e$ (i.e. electron beam emittance) and will follow an exponential decrease [Loewen, 2003].

The CLS spectrum widens with increasing x-ray energy, as the angular distribution of the electron beam changes with increasing energy, making the radiation cone of the x-ray beam smaller such that a larger part of the overall spectrum is collected within the aperture (determined by equation 3.18 folded with the Gaussian distribution of electron beam angles). The measured spectra do not fully follow the theoretically predicted exponential decrease towards lower energies, which is mostly caused by the upscaling of low energy channels of the energy dispersive detector when correcting for the attenuation in the PMMA absorber. Therefore, this effect is likely not physical but caused by measurement uncertainties.

The comparison of spectra acquired at different time points presented in figure 5.11 (a) shows how the quality of the electron beam store may affect the x-ray spectrum. While the spectrum measured in June 2015 shows a very good store of the electron beam with low emittance, the spectrum from May 2016 was acquired while the performance of the L-band amplifier was slowly degrading (resulting in a failure of the amplifier in August 2016). As the L-band amplifier powers the RF cavity which ensures that the electrons stay tightly bunched, the degrading power resulted in an increased emittance (i.e. longer electron bunches, larger distribution of angles) and thus the broadened spectrum. The bandwidth has decreased to the original values again after the amplifier replacement as shown by the spectra measured in October 2016 and May 2017. In addition, even small deviations from the optimal operating point in the tune diagram of the electron storage ring may cause a beam emittance growth that leads to a broadened spectrum.

The spectrum measured in October 2016 exhibits an increased peak x-ray energy at 25.3 keV, which has been caused by small changes to the magnet configuration and therefore energy in the ring. The spectrum measured in May 2017 confirms previously measured peak x-ray energies around 24.9 keV.

When comparing the measured spectra to a simulation [Loewen, 2017], the agreement for the high-energy tail is better than for the low-energy tail. It is difficult to quantify to what degree the difference is due to the real spectrum and how much influence measurement errors have. Measurement errors could come from the energy-dispersive detector itself, and in addition can be a result of the applied corrections for the PMMA attenuator and the detector efficiency. Most likely, the low-energy tail of the measured spectrum is slightly overestimated due to the upscaling performed during the correction, while theory predicts an exponential decay of the intensity.

5.4. Summary and Conclusion

Data on the performance of the MuCLS was presented for different time points before and after the installation in Munich in April 2015. The presented results show that the stability of the machine has improved significantly since the first tests in August 2014, at the expense of a reduced flux, and the additional benefit of reduced source sizes.

The flux of $> 10^{10}$ photons per second and the good stability with an rms variation of less than 5% of the flux and 1-2% of source sizes over three hours provide suitable conditions also for time-consuming x-ray imaging experiments, such as grating-based tomographic imaging or high-resolution micro-CT. Compared to previously published x-ray imaging studies [Eggl et al., 2015b] acquired at a CLS prototype at the Lyncean Technologies facility in Palo Alto, USA, scans can be acquired significantly faster thanks to the flux having increased by about a factor of > 5 in the meantime.

Previous studies [Achterhold et al., 2013, Eggl et al., 2015b] have demonstrated that the quasi-monochromatic beam with a bandwidth of a few percent provided by the CLS is suitable for quantitative absorption imaging, allows to overcome beam hardening artifacts, and enables a quantitative reconstruction of attenuation coefficient and refractive index decrement that is consistent with literature values.

Very recently, an upgrade on the laser system has been installed. First tests showed a significantly enhanced x-ray flux at equivalent or improved stability. In the near future, the stability of the MuCLS is expected to improve by implementation of even more sophisticated feedback systems, like for example digital feedback systems currently under development at SLAC, Menlo Park, USA.

Overall, the presented evidence shows the Compact Light Source technology has evolved far enough to provide suitable conditions for x-ray imaging with a quasi-monochromatic beam produced by a laboratory-scale device.

6. Mono-Energy Coronary Angiography

Coronary angiography is an important clinical application for the diagnosis of coronary heart disease. The information and figures presented in sections 6.1-6.4 have previously been published in [Eggl et al., 2017b].

6.1. Motivation

One of the clinical applications that could benefit significantly from a mono-energetic x-ray beam as provided by the MuCLS is coronary angiography, as it relies on contrast media application. A mono-energetic x-ray beam could thoroughly exploit the sudden increase of the absorption coefficient of a contrast medium at its K-edge.

Coronary angiography is an invaluable tool for the diagnosis of coronary disease[1]. Complications are frequently associated with the high amount of iodine-based contrast media that are injected during the catheterization procedure. Especially for patients presenting with pre-existing renal insufficiency, there is a high risk to suffer from renal failure due to nephrotoxic effects of iodine-based contrast agents, resulting in severe renal dysfunction and a high risk of subsequent dialysis treatment [Adams et al., 1973, McCullough et al., 1997, Gruberg et al., 2000, Tavakol et al., 2012]. In addition, several patients show allergic reactions following iodine injection, with the life-threatening risk of anaphylaxis [Tavakol et al., 2012]. A high amount of iodine can also induce hyperthyroidism by influencing the endocrine function of the thyroid gland [Thomsen et al., 2004]. The number of patients harmed by these adverse effects can be lowered if a good diagnostic image quality is achieved with a reduced amount of contrast media being injected.

Research efforts have furthermore been made to examine the use of gadolinium-based contrast media for coronary angiography as an alternative to iodine-based contrast agents. Gadolinium is a frequently used contrast agent for Magnetic Resonance Imaging (MRI) and is also successfully used for cardiovascular MRI [Cheng et al., 2007]. Even though there are some drawbacks related to the use of gadolinium for x-ray coronary angiography, such as a reduced image quality due to the lower possible concentration, several studies have shown the feasibility of applying gadolinium for patients with e.g. severe iodine allergy [Spinosa et al., 1999, Parodi and Ferreira, 2000, Ose et al., 2005, Sayin et al., 2007, Kälsch et al., 2008, Juneman et al., 2012]. Implementing a compact synchrotron source with an x-ray energy tuned directly above the gadolinium absorption edge could help to improve the image quality in the future while limits with respect to contrast agent concentration are adhered to.

---

[1] Coronary disease (also coronary heart disease or coronary artery disease) is the most common cardiovascular disease. The inner diameter of coronary arteries narrows due to calcium and fatty depositions (plaque) on the artery walls (atherosclerosis), obstructing the blood flow. Blood clots can suddenly block the blood supply to the heart. This can cause myocardial infarction.

Here we analyze the quantitative effect of quasi-mono-energetic x-ray spectra on the contrast-to-noise-ratio (CNR) of coronary angiography. We used virtual projection images calculated for a segmented human coronary artery from real patient data for a comparison of typically used clinical x-ray spectra with compact synchrotron spectra. For an iodine-based contrast agent, we compare a conventional x-ray tube spectrum at 60 kVp (peak kilovoltage) with a quasi-mono-energetic spectrum at 35 keV. A 90 kVp conventional x-ray tube spectrum and a 55 keV quasi-mono-energetic spectrum are examined for the application of gadolinium-based contrast media. Finally, we present experimental coronary angiography data acquired at the MuCLS of a porcine heart using iodine-based contrast media at an x-ray energy of 35 keV.

6.2. Simulation

6.2.1. Methods & Materials

Simulation

X-ray projection images were simulated using a spectral forward projector. According to the Lambert-Beer law, the projection image is given by

$$\hat{y}_i = b_i e^{-\int_{L_i} \mu(x,y,z)\mathrm{d}l}, \tag{6.1}$$

where $\hat{y}_i$ and b_i are the mean number of photons recorded by the detector with and without the sample in place, respectively, and i is an index running over all detector pixels. The line integrals over the spatially varying attenuation coefficient $\mu(x,y,z)$ can be replaced by sums and thus $\hat{y}_i$ can be rewritten as

$$\hat{y}_i = b_i e^{-\sum_{j=1}^{N} a_{ij}\mu_j}, \tag{6.2}$$

where a_{ij} is a geometric factor describing how much μ_j contributes to the line integral $\int_{L_i} \mu \, \mathrm{d}l$. For a polychromatic x-ray beam, this forward projector needs to be extended to include the x-ray spectrum consisting of K energy bins:

$$\hat{y}_i = \sum_{k=1}^{K} b_{ik} \exp\left(-\sum_{j=1}^{N} a_{ij}\mu_{jk}\right) = \sum_{k=1}^{K} r_{ik}, \tag{6.3}$$

where b_{ik} is the average number of photons per energy bin k in the flatfield and μ_{jk} is the attenuation coefficient in voxel j for the energy bin k. For simplification, a perfect flatfield is assumed, i.e. $b_i = b \; \forall i$.

The forward model yields the average number of photons behind the object, $\hat{y}_i$. We then calculated the detector projection image d_i for an ideal energy-integrating detector with a 700 µm CsI scintillator:

$$d_i = \sum_{k=1}^{K} P_{\mathrm{Poisson}}\{r_{ik} \cdot \kappa_k\} \cdot g_k, \tag{6.4}$$

where K is the number of energy bins, r_{ik} is the number of photons per energy bin behind the sample, and κ_k is the detector quantum efficiency in energy bin k. The detector

Contrast Agent	Iodine	Gadolinium
K-edge energy	33.17 keV	50.24 keV
X-ray tube	60 kVp, Tungsten 0.7 mm Cu filter	90 kVp, Tungsten 0.7 mm Cu filter
MuCLS	35.0 keV peak energy 4 % FWHM	55.0 keV peak energy 4% FWHM
Contrast media concentrations	high: 75 mg/ml low: 50 mg/ml	high: 75 mg/ml low: 50 mg/ml
Photons in Flatfield (x-ray tube / MuCLS)	4230 / 3000	15000 / 15000
Detector sensor	700 µm CsI	700 µm CsI
QE of detector sensor (x-ray tube / MuCLS)	98.3% / 99.5%	88.2% / 97.27%
Muscle tissue depth	3 cm	10 cm

Table 6.1.: Simulation parameters.

signal $r_{ik} \cdot \kappa_k$ is assumed to be Poisson distributed. This signal is then multiplied by the detector gain g_k for photons in the energy bin k, with the gain being proportional to the photon energy, $g_k \propto E_k$.

Simulated projections of coronary artery and CNR analysis

A coronary artery was segmented from a CT scan of a human patient. Projection images of the coronary artery embedded in muscle tissue were calculated with the simulation as described above for different spectra and for different contrast agent substances and concentrations within the artery.

The two contrast agents we evaluated were iodine and gadolinium. The parameters for all simulations that were performed are summarized in table 6.1. We used attenuation coefficients as provided by NIST [Hubbell and Seltzer, 1995]. The conventional x-ray tube spectra were simulated based on [Tucker et al., 1991] for typical clinical settings of acceleration voltage and filtration for a tungsten anode [Reusch, 2016]. The CLS spectrum at an energy of 35 keV was measured by an energy-dispersive detector (Amptek X-123, Amptek Inc., USA). For the gadolinium simulation, the measured MuCLS spectrum was rescaled. The CLS and x-ray tube spectra are shown together with the mass-energy attenuation coefficients of iodine and gadolinium in figures 6.1 (a) and 6.2 (a), respectively. The number of photons in the flatfield was chosen such that the absorbed dose was equal for x-ray tube and CLS spectrum for each contrast agent, and such that the number of transmitted photons was equal for the 60 kVp and the 90 kVp x-ray tube spectra.

In order to account for statistical variations due to Poisson noise, the simulation was performed 10 times for each setting of spectrum and contrast agent substance and concentration to be studied. The standard deviation due to the statistical variation is given with the results. Several regions of interest (ROIs) at different positions in the coronary vascular tree were selected for evaluation of the CNR in order to investigate the contrast between vessel and muscle tissue. The used ROIs are highlighted in figures 6.1 and 6.2

and their size was 8 × 8 and 4 × 4 pixel for thicker and thinner vessels, respectively.

The CNR was calculated according to the definition

$$\mathrm{CNR} = \frac{\overline{S_1} - \overline{S_2}}{\sigma_{\mathrm{BG}}}, \tag{6.5}$$

where $\overline{S_1}$ and $\overline{S_2}$ are the average signals in two ROIs which should be compared, and σ_{BG} is the standard deviation within a larger ROI located in the background region.

6.2.2. Results

Simulated angiography images for iodine-based contrast media

X-ray projection images of a human coronary artery filled with iodine-based contrast media were simulated for a conventional x-ray tube spectrum at 60 kVp (cf. fig. 6.1 (b)) and a compact synchrotron source spectrum at 35 keV (fig. 6.1 (c)). Visual comparison of the two images shows better visibility of small vessels for the quasi-mono-energetic image (c). The coronary artery tree is clearly visible with the right coronary artery (ROI 1) and the left coronary artery with its main branch, the left anterior descending artery (5). In addition, a small arterial branch arising from the aorta can be visualized (2). The analysis of the CNR presented in table 6.2 supports this impression. Except for ROI 6 located in the aorta, where the CNR is lower for the MuCLS spectrum due to photon starvation, the quasi-mono-energetic spectrum yields CNR values which lie 17%-22% above those for the conventional x-ray tube spectrum. When lowering the iodine concentration by 1/3, the advantage of the MuCLS spectrum increases to 24%-28%. The CNR values of the quasi-mono-energetic spectrum at lower iodine concentration are comparable with those of the conventional spectrum at a 50% higher iodine concentration.

ROI	60 kVp	35 keV	gain	60 kVp	35 keV	gain
	75 mg/ml iodine			50 mg/ml iodine		
1	8.51 ± 0.49	9.96 ± 0.36	17%	5.80 ± 0.32	7.18 ± 0.26	24%
2	3.24 ± 0.34	3.79 ± 0.19	17%	2.26 ± 0.20	2.83 ± 0.23	25%
3	6.33 ± 0.34	7.67 ± 0.38	21%	4.22 ± 0.21	5.41 ± 0.12	28%
4	7.49 ± 0.44	9.10 ± 0.47	22%	5.14 ± 0.21	6.54 ± 0.27	27%
5	6.42 ± 0.35	7.81 ± 0.22	22%	4.43 ± 0.17	5.49 ± 0.23	24%
6	39.54 ± 1.85	29.13 ± 1.07	-26%	34.40 ± 1.17	27.62 ± 0.61	-20%

Table 6.2.: CNR analysis for simulated projections for an iodine-based contrast medium. CNR calculated from simulated projections for two different concentrations of iodine-based contrast media. The standard deviation from the statistical variation of the simulation is given with the mean value of the CNR of the 10 simulation runs.

6.2.3. Simulated angiography images for gadolinium-based contrast media

Simulated x-ray projection images obtained for gadolinium-based contrast agent with a 90 kVp conventional x-ray tube spectrum and a 55 keV CLS spectrum are displayed

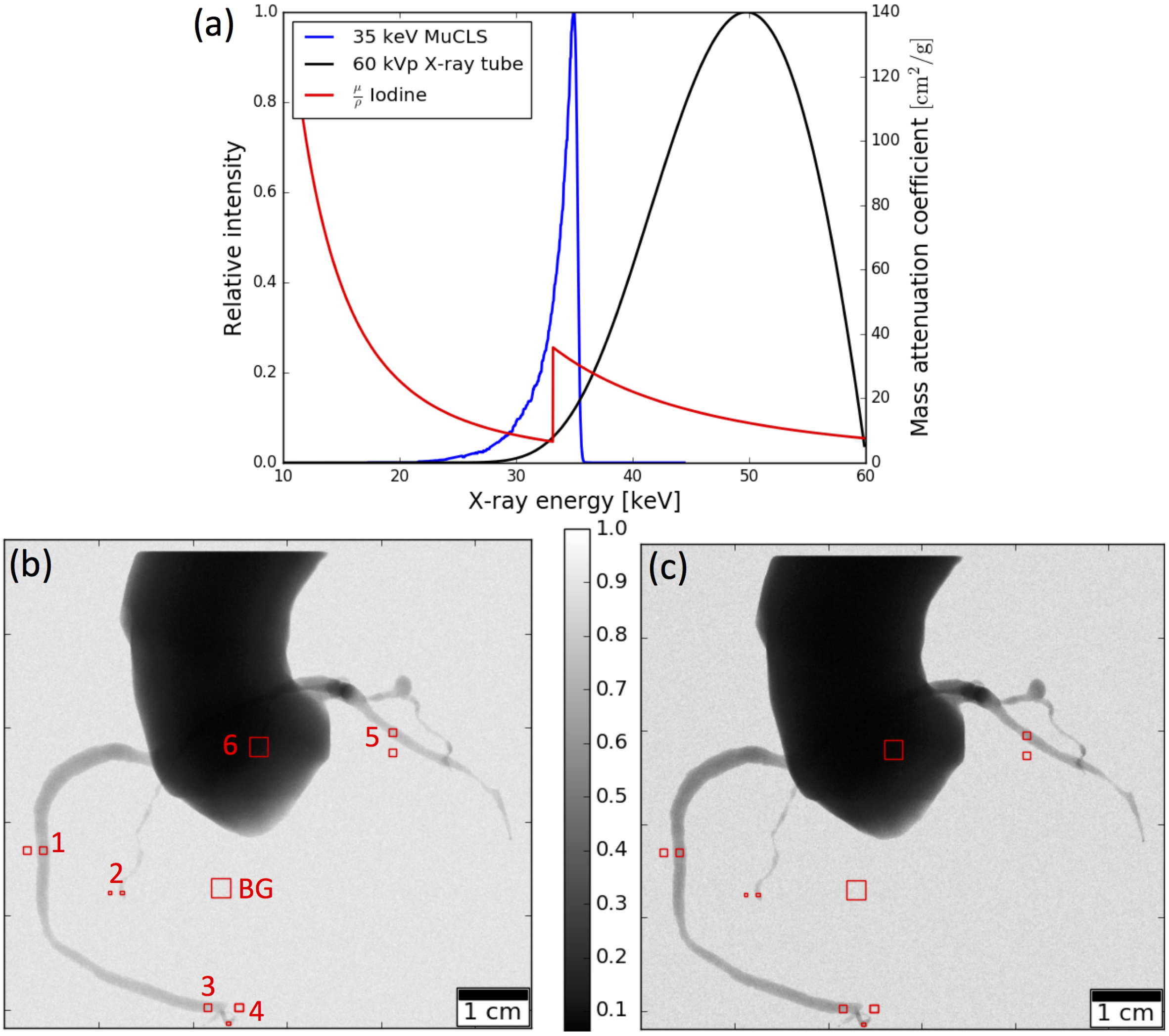

Figure 6.1.: Comparison of simulated data for MuCLS and x-ray tube spectra for an iodine-based contrast medium. (a) Measured MuCLS spectrum at 35 keV peak energy, x-ray tube spectrum at 60 kVp and mass attenuation coefficient of iodine. (b) Simulated iodine-based angiography image for the 60 kVp x-ray tube spectrum. (c) Simulated iodine-based angiography image for the 35 keV MuCLS spectrum. This figure was previously published in [Eggl et al., 2017b].

in figures 6.2 (b) and (c), respectively. The CLS spectrum provides a superior perceptability of the smaller vessels. The quantitative evaluation of the CNR is presented in table 6.3. The CNR achieved with a quasi-mono-energetic MuCLS spectrum is 41%-62% higher than with an x-ray tube spectrum in ROIs 1-5, and 12% higher in the aorta-ROI (6). For a reduced gadolinium concentration, the improvement with a mono-energetic spectrum even increases for most ROIs and is 30%-51% higher compared to a conventional spectrum. As in the previous section, CNR values achieved with the MuCLS spectrum at lower gadolinium concentration are similar to those from the conventional spectrum at a 50% higher concentration.

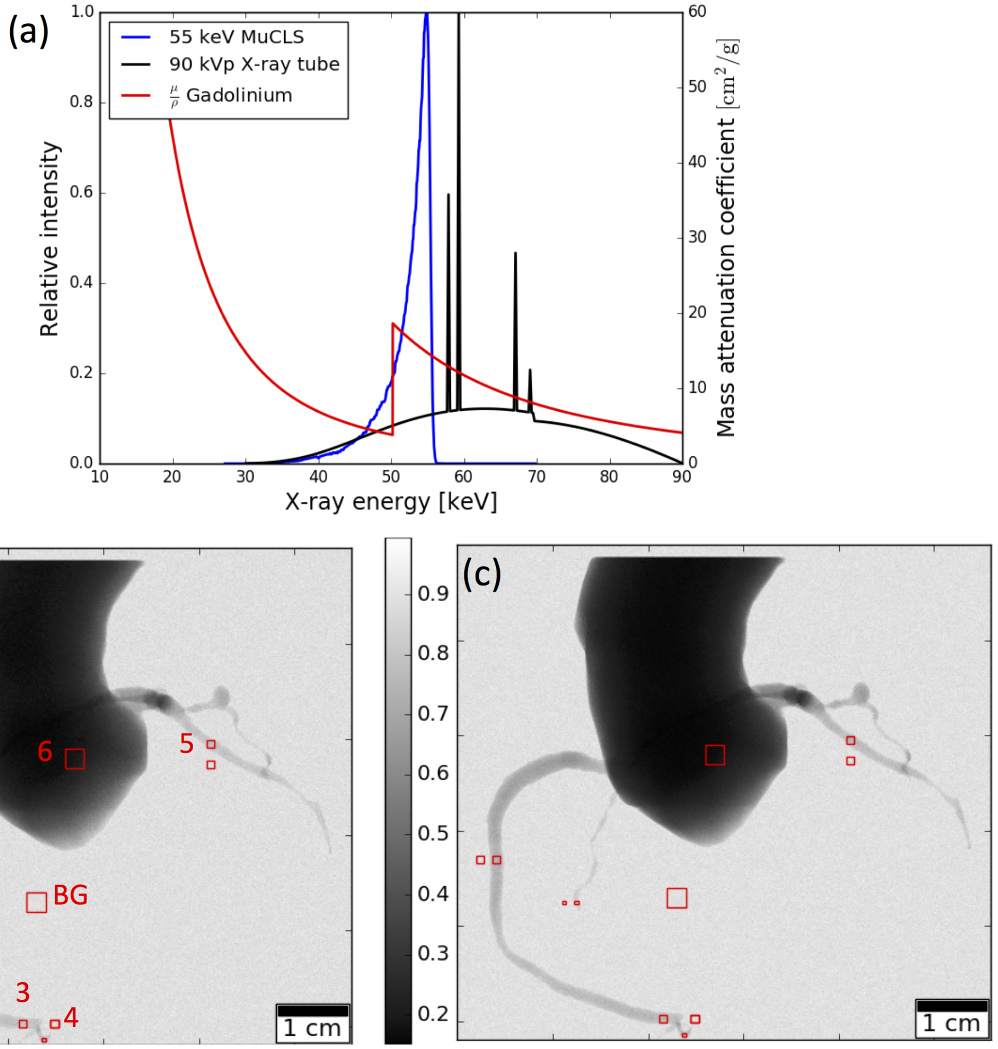

Figure 6.2.: Comparison of simulated data for MuCLS and x-ray tube spectra for a gadolinium-based contrast medium. (a) MuCLS spectrum rescaled at 55.8 keV peak energy, x-ray tube spectrum at 90 kVp and mass attenuation coefficient of gadolinium. (b) Simulated gadolinium-based angiography image for the 90 kVp x-ray tube spectrum. (c) Simulated gadolinium-based angiography image for the 55 keV MuCLS spectrum. This figure was previously published in [Eggl et al., 2017b].

6.3. Experimental demonstration at the MuCLS

6.3.1. Methods & Materials

The MuCLS was tuned to 35.0 keV x-ray peak energy, with a flux of approximately $1.1 \cdot 10^6$ photons/(s mm^2) at the sample position. A spectrum of the x-ray beam acquired with an Amptek X-123 detector is shown in figure 6.1 (a). An excised porcine heart was placed in a waterbath (photograph shown in figure 6.3 (a)) and iodine-based contrast agent (Solutrast 370, Bracco Imaging Deutschland GmbH) was injected into the coronary artery. A flatpanel detector (Varian PaxScan 2520DX, Varian Medical Systems Inc., USA), equipped with a Gd_2O_2S scintillator, with a pixel size of 127 µm was placed at 16.5

ROI	90 kVp	55 keV	gain	90 kVp	55 keV	gain
	75 mg/ml gadolinium			50 mg/ml gadolinium		
1	5.27 ± 0.18	7.42 ± 0.32	41%	3.55 ± 0.17	5.01 ± 0.13	41%
2	1.78 ± 0.41	2.87 ± 0.28	62%	1.27 ± 0.30	1.65 ± 0.22	30%
3	3.91 ± 0.15	5.57 ± 0.20	43%	2.40 ± 0.17	3.62 ± 0.18	51%
4	4.75 ± 0.15	6.75 ± 0.27	42%	3.04 ± 0.21	4.53 ± 0.29	49%
5	3.93 ± 0.17	5.69 ± 0.31	45%	2.64 ± 0.20	3.77 ± 0.16	43%
6	30.19 ± 0.95	33.83 ± 0.89	12%	24.93 ± 0.55	29.45 ± 0.87	18%

Table 6.3.: CNR analysis for simulated projections for a gadolinium-based contrast medium. CNR calculated from simulated projections for two different concentrations of gadolinium-based contrast media. The standard deviation from the statistical variation of the simulation is given with the mean value of the CNR of the 10 simulation runs.

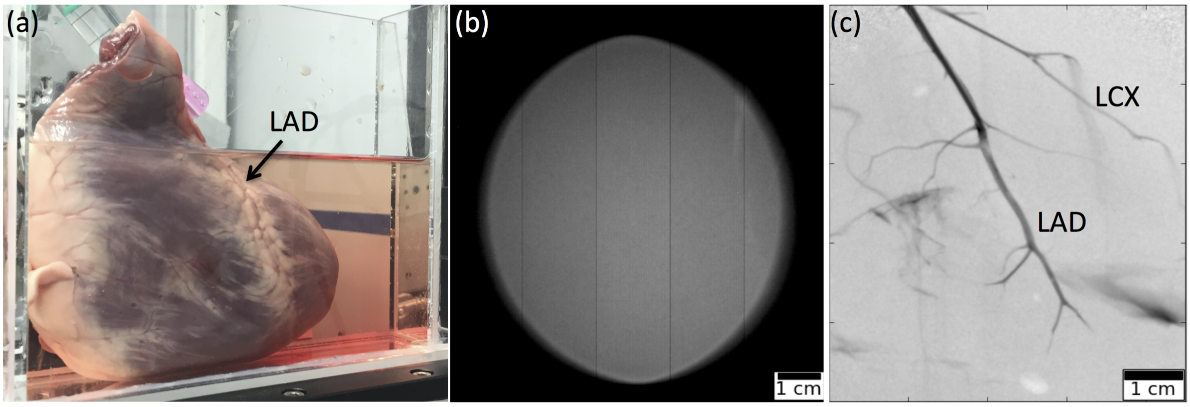

Figure 6.3.: Experimental demonstration of coronary angiography at the MuCLS. (a) Photograph of the sample in waterbath. (b) Empty image of full MuCLS beam. (c) Quasi-mono-energetic angiography image of a porcine heart acquired at the MuCLS, with iodine-based contrast agent injected into the left coronary artery. Visible are the left anterior descending artery (LAD) and the left circumflex artery (LCX). This figure was previously published in [Eggl et al., 2017b].

m from the x-ray source point. The sample-detector distance was 80 cm, corresponding to an effective pixel size of 121 µm. An image was acquired with an exposure time of 1 second and flatfield-corrected.

6.3.2. Results

The quasi-mono-energetic angiography image of a porcine heart acquired at the MuCLS is presented in figure 6.3 (c). The left anterior descending (LAD) artery and the left circumflex (LCX) artery arising from the left main coronary artery (not shown) are imaged with an excellent delineation even of the small side branches. Although the image quality is compromised by some contrast agent spread outside of the vessels, even small vessels are easily recognized. The background of the image is flat due to the waterbath in which the specimen was placed.

6.4. Discussion, Conclusion and Outlook

By numerical simulations and experimental images, we showed that a quasi-mono-energetic spectrum produced by an inverse Compton x-ray source is beneficial for coronary angiography. The feasibility of mono-energy coronary angiography at the MuCLS was experimentally demonstrated. In the future, the experimental approach can be extended to dual-energy K-edge subtraction (KES) angiography, where the beam energy is oscillated rapidly between above and below the edge. Technically, this energy change could either be realized through the electron beam energy or the laser wavelength (eq. 3.16). If the electron beam energy should be altered, the energy of the injected and stored electron beam could be oscillated at the few Hz timescale using laminated magnets. Alternatively, laser beams of two different wavelengths could be stored in the same optical cavity.

A simulation based on a polychromatic forward model allowed for a quantitative analysis of the CNR achieved for a segmented coronary artery for such a mono-energetic spectrum in comparison with a conventional x-ray tube spectrum. A quasi-mono-energetic spectrum tuned directly above the K-edge of iodine yielded higher CNR than a conventional x-ray tube spectrum at 60 kVp as typically used for coronary angiography. A mono-energetic spectrum would allow for a reduction of the iodine concentration by approximately 20%-30% at almost equal CNR, which can facilitate the administration of the contrast agent for the patients. However, due to penetration issues and dose constraints, a 35 keV MuCLS spectrum is mainly restricted to small-animal imaging. The application of the MuCLS for coronary angiography could profit from a better suited detector, e.g. a single photon counting detector. A flatpanel detector with CsI sensor was chosen for the simulation as it is widely used for clinical coronary angiography.

For contrast media based on gadolinium, the CNR values are in general lower than for iodine, on the one hand due to the higher sample thickness and on the other hand due to the lower absorption coefficient of gadolinium. Importantly, the improvement of the CNR achieved with a compact synchrotron source tuned directly above the K-edge compared to a conventional spectrum at 90 kVp is even higher than for the iodine case. An increase in CNR of over 40% was observed for the MuCLS spectrum. Gadolinium is a well established contrast agent in magnetic resonance imaging and has also been investigated for x-ray imaging. Since the allowed dosage of gadolinium is limited [Kälsch et al., 2008], the possibility of reducing the gadolinium concentration by $1/3$ at equal CNR for a quasi-mono-energetic spectrum compared to an x-ray tube spectrum motivates the implementation of compact synchrotron sources. Especially patients with severe iodine allergy or chronic renal insufficiency could profit from using gadolinium-based contrast agent in combination with a CLS for coronary angiography.

While the MuCLS is limited to a maximum x-ray energy of 35 keV, the field of compact synchrotron sources is strongly under research [Eggl et al., 2016a, Variola, 2011, Kuroda et al., 2011] and an extension to higher x-ray energies above 50 keV appears feasible. Higher electron and laser photon energies will require an adaptation of electron storage ring and laser cavity design. Furthermore, while, apart from the energy range, the current beam size and the flux are not yet compatible with requirements for patient studies, we believe that the expected evolution in compact light source technology will enable in-vivo application in the future.

In conclusion, we showed that the compact synchrotron source technology offers great potential in the field of coronary angiography by reducing the amount of required contrast media concentration. Quasi-mono-energetic x-ray beams from compact sources pave the way for investigating contrast media with higher atomic number as patients will benefit from dose and contrast media reduction.

A possible extension of the presented method is iodine-filter K-edge subtraction (KES) imaging [Umetani et al., 1993, Takeda et al., 1994]. A feasibility study of iodine-filter KES imaging at the MuCLS can be found in [Kulpe, 2017].

7. Grating-based phase-contrast and dark-field CT

This chapter highlights the possibilities of grating-based phase-contrast and dark-field CT imaging with a quasi-monochromatic x-ray beam, especially in the context of pre-clinical small-animal imaging. Chapters 7.1 - 7.3 have previously been published in [Eggl et al., 2015b].

7.1. Motivation

With the introduction of grating interferometry [Momose et al., 2003, Weitkamp et al., 2005, Pfeiffer et al., 2006], the field of x-ray phase-contrast imaging has seen great advances in the past decade. In comparison with conventional attenuation-contrast imaging, the phase-contrast modality greatly improves soft-tissue contrast, which can, for example, be used for better tumor visualization [Pfeiffer et al., 2007b]. With the development of the Talbot-Lau interferometer, grating-based phase-contrast imaging has become feasible not only with synchrotron sources, but also with standard x-ray tube sources [Pfeiffer et al., 2006, Pfeiffer et al., 2008]. On the downside, the visibility is degraded due to the broad polychromatic spectrum of the x-ray tube sources, thus compromising the image quality. Brilliant and highly monochromatic synchrotron sources yield superior results for high-resolution and high-sensitivity measurements [Weitkamp et al., 2005, Pfeiffer et al., 2007b, Momose et al., 2006, David et al., 2007, Momose et al., 2009, Zhu et al., 2010, Hoshino et al., 2012, Zanette et al., 2012, Pinzer et al., 2012, Sun et al., 2013].

However, limited availability, high cost and small fields of view make synchrotron sources incompatible with clinical applications or pre-clinical research on e.g. small-animal disease models in close vicinity to biomedical labs with small-animal infrastructure. Offering a monochromatic beam as well as higher brilliance and coherence than x-ray tube sources, compact synchrotron sources can be classified between tube sources and synchrotron sources. These features are achieved with the Munich Compact Light Source (MuCLS), a compact synchrotron based on inverse Compton scattering [Huang and Ruth, 1998], which has a size that is compatible with conventional labs, making it an interesting candidate for clinical and materials science applications of phase-contrast imaging. The produced x-ray beam is intrinsically monochromatic and coherent and offers a field of view suitable for imaging of macroscopic samples, providing suitable conditions for grating-based x-ray imaging of biomedical or material samples.

First studies employing a grating interferometer at a CLS yielded promising results for phase-contrast and dark-field projection images [Bech et al., 2009, Bech et al., 2012, Schleede et al., 2012, Schleede et al., 2013]. Quantitative attenuation-based CT demonstrated the capability of the CLS to overcome beam hardening issues and to provide precise density values [Achterhold et al., 2013].

Here we show the first grating-based computed tomography scans obtained with a CLS. Since tomographic imaging with a grating interferometer at a monochromatic source simultaneously yields quantitative information on linear attenuation coefficient, refractive index decrement and linear diffusion coefficient, it allows to discriminate substances that cannot be distinguished solely by their attenuation coefficient and yields increased soft-tissue contrast for biomedical samples. These performance gains are demonstrated in this study. We present a quantitative analysis of a fluid phantom and a tomography scan of a biomedical sample. Moreover, we show that the image quality of the phase signal can strongly be improved by applying an iterative reconstruction algorithm that reduces stripe issues and noise.

In addition, the further development of grating-based multimodal tomography after the installation of the CLS in Munich, is demonstrated in the CT images of two additional biomedical specimens (two infant birds) acquired at the MuCLS.

7.2. Separation of materials in a fluid phantom

7.2.1. Methods & Materials

Grating Interferometer

The tomographies were recorded with a Talbot grating interferometer which was located 16 m from the interaction point of the CLS prototype. The interferometer consisted of a Ni phase grating with a period of 5.3 µm and a phase shift of $\pi/2$ (design energy 23 keV) and an Au analyzer grating with a period of 5.4 µm. The inter-grating distance was 278 mm (first fractional Talbot distance). The Compact Light Source prototype located in Palo Alto, CA, USA, was tuned to a peak x-ray energy of $E_{\text{peak}} = 21$ keV ($\lambda_{\text{peak}} = 0.59\,\text{Å}$), with a full energy spread of $\Delta E/E_{\text{peak}} \simeq 3\,\%$.

Fluid phantom scan

The phantom consisted of seven polyethylene tubes filled with chemically well defined fluid and salt combinations of known weight fractions, w_i. A photograph of the phantom is shown in figure 7.1 (a) and the chemical composition of the seven fluids is given in table 7.1. The theoretical values for the mass attenuation coefficient $(\mu/\rho)_s$ and the refractive index decrement δ_s can be calculated [Herzen et al., 2009, Tapfer et al., 2012]:

$$\left(\frac{\mu}{\rho}\right)_s = \sum_i \left(\frac{\mu}{\rho}\right)_i w_i, \tag{7.1}$$

$$\delta_s = \frac{r_e \lambda^2}{2\pi} \cdot \rho_s \sum_i \frac{N_A Z_i}{A_i} w_i, \tag{7.2}$$

where λ is the x-ray wavelength, r_e is the classical electron radius, N_A is the Avogadro atomic number, A_i is the atomic mass of the constituent, and Z_i is the total number of electrons of the constituent. All tabulated data was obtained from the program XCOM

Sample	Solution [wt.%]	Density ρ_s [g/cm^3]
1	H_2O (demineralized)	0.997
2	$C_3H_8O_3$	1.260
3	$C_3H_8O_3$(75%) + C_2H_6O(25%)	1.110
4	$C_3H_8O_3$(50%) + C_2H_6O(50%)	0.982
5	H_2O(95%) + NaCl(5%)	1.033
6	H_2O(90%) + NaCl(10%)	1.069
7	C_2H_6O(98.75%) + NaCl(1.25%)	0.800

Table 7.1.: Measured density of the fluids in the fluid phantom. The density was measured employing the buoyancy of a gauged glass structure. Data has previously been published in [Tapfer et al., 2012].

(NIST, Gaithersburg, USA[1]). The linear attenuation coefficient is calculated using the density of the samples (cf. table 7.1).
200 projections over 360° were recorded. For each projection, a phase stepping scan of five steps over one grating period was performed, with an exposure time of 5 s per image. Flat field images were acquired before, after and in the middle of the tomography scan. The scan was acquired with a PILATUS 100K detector (Dectris Ltd., Switzerland) with a pixel size of 172 × 172 µm^2. The visibility was 37%.

Reconstruction

Multimodal projections of the samples were calculated using standard Fourier processing [Pfeiffer et al., 2006]. The tomography reconstruction was done using Filtered Backprojection (FBP) with a Ram-Lak filter for the attenuation projections and a Hilbert filter for differential phase projections.

7.2.2. Results

Figures 7.1 (b), (c) display reconstructed slices of the linear attenuation coefficient and the refractive index decrement of the fluid phantom, a photograph of which is shown in figure 7.1 (a). The images show an average of 10 slices for an improved signal-to-noise ratio. The reconstruction of the refractive index decrement has some streak artifacts, which are caused by strong phase shifts at plastic-air interfaces, but these could be avoided by placing the sample in a water bath during image acquisition or by using iterative reconstruction schemes [Hahn et al., 2015]. The fluids cannot be distinguished from visual inspection of solely the attenuation-contrast image or the phase-contrast image by themselves, because the gray values do not exhibit enough contrast. Fluids that show a strong contrast in their phase have similar gray values in the attenuation image and vice versa.

To identify the different fluids, a quantitative analysis is necessary. For this purpose, the mean value of a $10 \times 10\,\text{pixel}^2$ region of interest (ROI) and its respective standard deviation were calculated for each fluid sample and for each of the two imaging modalities.

---

[1] http://physics.nist.gov/PhysRefData/Xcom/Text/intro.html

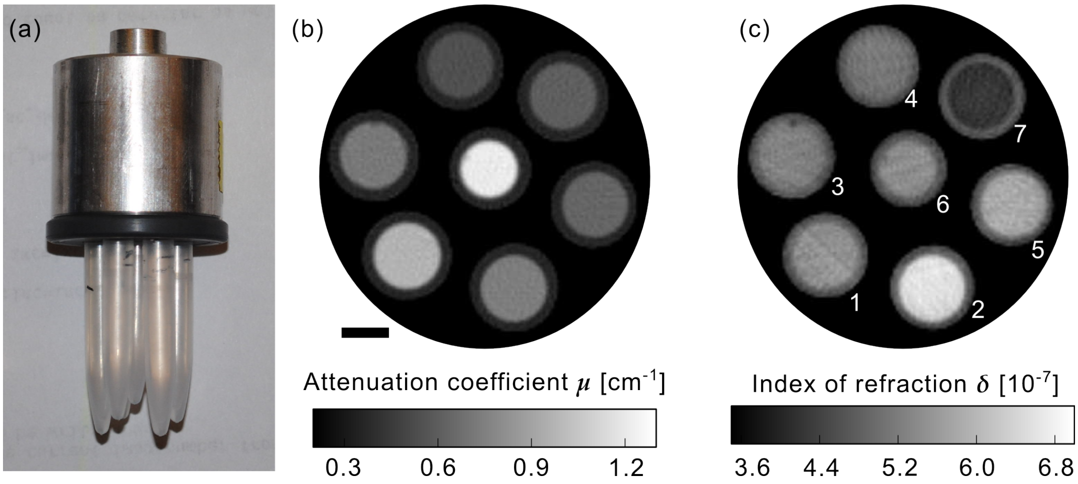

Figure 7.1.: Reconstructed absorption coefficient and refractive index decrement for the fluid phantom. (a) Photograph of the fluid phantom. It consists of seven polyethylene rods containing seven different, chemically well defined fluids (see table 7.1). (b)-(c) Average of ten reconstructed slices of the linear attenuation coefficient μ (b) and the refractive index decrement δ (c). Fluids with similar attenuation coefficient show strong contrast in the phase image and vice versa. The scalebar corresponds to 3 mm. The white numbers in (c) correspond to the fluid sample number used in tables 7.2 and 7.1. This figure was previously published in [Eggl et al., 2015b].

The results are given in table 7.2 and compared with values calculated using equations 7.1 and 7.2. The measured and the calculated values show very good agreement. The mismatch for the attenuation values is less than 1% and within the error margin of the measured values. For the refractive index decrement, the maximum mismatch between measured and calculated values is 5%. The higher deviation from calculated values for the refractive index decrement could be caused by the mentioned streak artifacts.

The quantitative analysis is further illustrated in the scatter plot shown in figure 7.2. The scatter plot displays μ and δ values from every pixel within the chosen ROIs. The calculated theoretical μ and δ values are displayed as large black triangles. It is well visible from the scatter plot that substances with overlapping attenuation values can be separated by their refractive index and vice versa. This indicates that quantitative multi-modal imaging of attenuation and phase is most helpful to distinguish materials with similar attenuation coefficient or similar refractive index decrement.

7.3. CT of an infant mouse

7.3.1. Methods & Materials

Image acquisition

An infant mouse was fixated in formalin in a falcon tube. The grating interferometer set up at the CLS prototype in Palo Alto, CA, USA, was as for the fluid phantom CT scan described in section 7.2.1. The tomography consisted of 361 projections over 180.5°. For

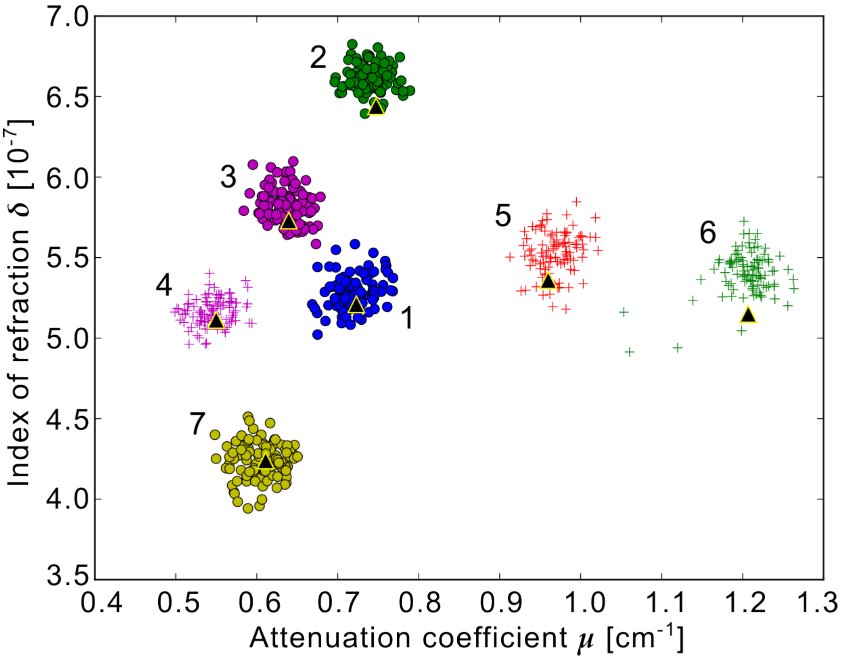

Figure 7.2.: The scatter plot displays the attenuation coefficient and refractive index decrement for all pixels in the $10 \times 10\,\text{pixel}^2$ ROIs in the fluid phantom reconstructions (cf. figure 7.1, (b) and (c)). Black triangles are the calculated values. Most substances show an overlap in either attenuation or phase signal alone, but all substances can clearly be distinguished using the combined information from both attenuation and phase. The different data clusters are labeled by numbers as used in tables 7.2 and 7.1. This figure was previously published in [Eggl et al., 2015b].

Sample	μ_m [0.1 cm^{-1}]	μ_c [0.1 cm^{-1}]	δ_m [10^{-7}]	δ_c [10^{-7}]
1	7.19 ± 0.23	7.23	5.28 ± 0.10	5.21
2	7.40 ± 0.19	7.47	6.62 ± 0.08	6.44
3	6.36 ± 0.20	6.40	5.82 ± 0.10	5.73
4	5.45 ± 0.22	5.50	5.16 ± 0.08	5.12
5	9.69 ± 0.22	9.60	5.53 ± 0.13	5.36
6	12.05 ± 0.32	12.07	5.40 ± 0.13	5.15
7	6.06 ± 0.24	6.11	4.24 ± 0.11	4.24

Table 7.2.: Measured and calculated linear attenuation coefficient μ and refractive index decrement δ for the different substances in the phantom. The subscripts m and c denote measured and calculated values, respectively. The error margin for the measured values was calculated from the standard deviation of the respective region of interest.

each projection, a phase stepping scan over one grating period was recorded, with an exposure time of 8 s per image. The number of phase steps was six, however, the last image was omitted during processing since it was identical to the first one. Flat field images were recorded before, after and in the middle of the tomography scan, yielding a mean visibility of 42%. A Mar CCD detector (Rayonix, USA) with a nominal resolution of 79.59 µm was used.

Data processing

Multimodal projections of the samples were calculated using standard Fourier processing [Pfeiffer et al., 2006] and reconstructed using a standard FBP algorithm. In addition, an iterative reconstruction scheme [Hahn et al., 2015] was used for the phase-contrast images of the mouse, in order to reduce stripe artifacts and noise in the reconstruction. Attenuation, differential phase and dark-field values in each pixel and the respective uncertainties are acquired from an analytical weighted least squares minimization, in accordance with the Fourier processing routine. The uncertainties are propagated from the initial Poisson counting statistics in each pixel, $\sigma_I = \sqrt{I}$. Reconstruction was performed through the optimization of penalized weighted least squares, using 25 iterations and a Huber regularization with a weighting factor of $\lambda = 10^{-5}$ and $\gamma = 0.01$ [Hahn et al., 2015].

Dose estimate for mouse scan

From flat-field images taken with the PILATUS 100K detector, an average flux of $9.76 \cdot 10^5$ photons $\mathrm{mm}^{-2}\mathrm{s}^{-1}$ at the sample position has been estimated, where the efficiency of the detector as well as the attenuation of the two gratings and the surrounding air has been taken into account. The absorbed dose for the whole sample (mouse and formalin fixation) was calculated as 5.94 mGy per projection (5 phase steps with 8 seconds exposure time), assuming the average density of the sample to be ρ_{water}. This gives an absorbed dose of 2.14 Gy for the full tomography scan. This first grating-based multimodal CT scan was not dose-optimized and the dose can be significantly decreased, for example by reducing the support thickness of the grating structures and by reducing the exposure time and number of projections.

7.3.2. Results

Reconstruction results for a biological sample (a fixated infant mouse, ex-vivo) are presented in figures 7.3 and 7.4. The figures display sagittal and axial views of the three imaging modalities: attenuation contrast (a), phase contrast (b and c) and dark-field contrast (d). In contrast to the phase-contrast image (b) which was reconstructed with a standard FBP algorithm, the image (c) was reconstructed with an iterative reconstruction scheme [Hahn et al., 2015]. The phase-contrast image processed with a standard FBP algorithm (b) displays strong streak artifacts caused by the bones. Comparison of the two images shows that the iterative reconstruction strongly reduces stripe artifacts and noise compared to the FBP reconstruction. Moreover, artifacts stemming from structures inducing a high phase shift, such as the soft tissue - bone interface, are

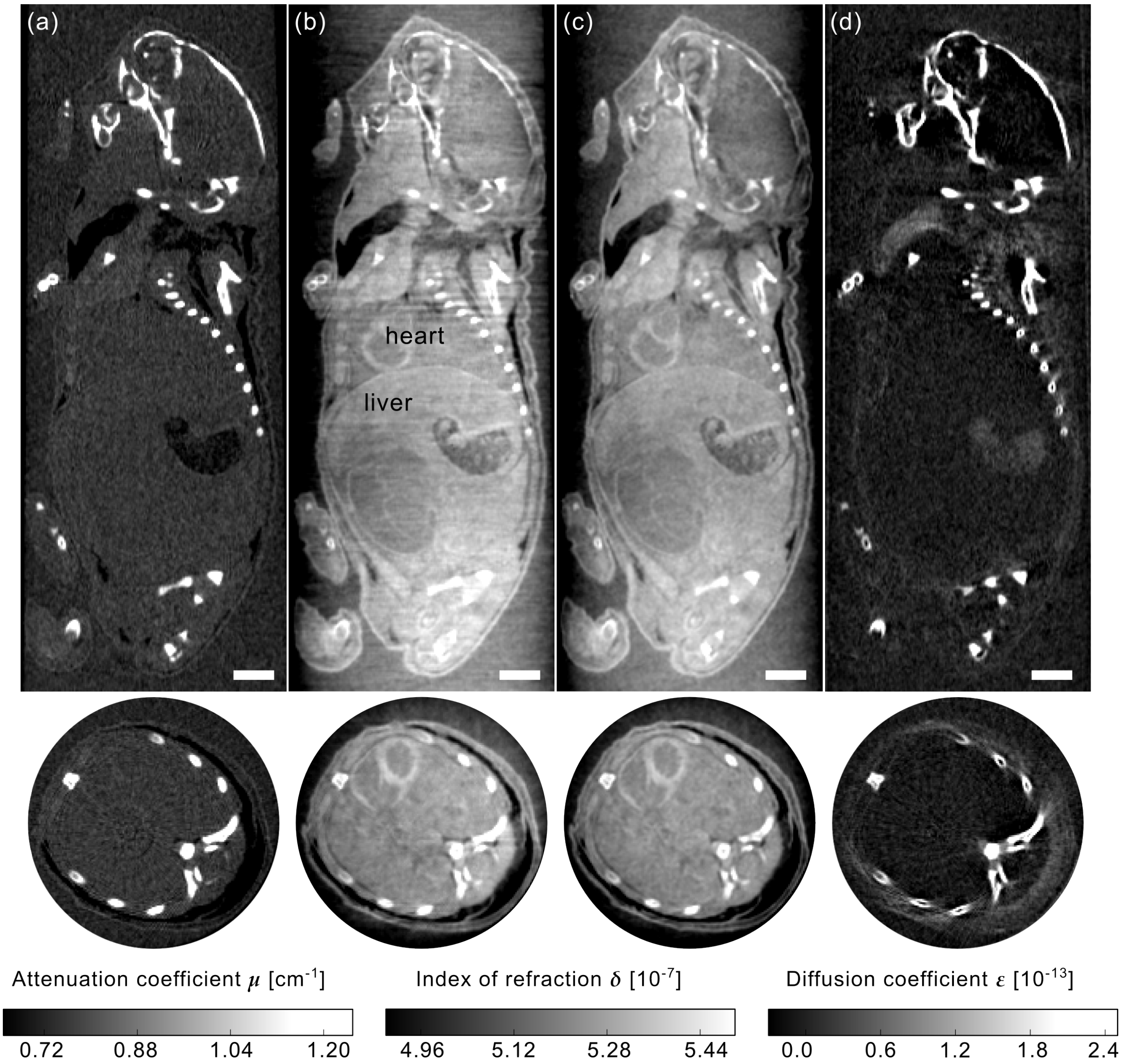

Figure 7.3.: Reconstructed slices of a grating-based, multimodal CT scan of a biological sample (a formalin fixated infant mouse). Shown are sagittal (top row) and axial (bottom row) slices. The reconstruction yields quantitative values of linear attenuation coefficient μ (a), refractive index decrement δ (b, c) and linear diffusion coefficient ϵ (d). For the phase image (c), an iterative reconstruction scheme [Hahn et al., 2015] was used instead of conventional FBP reconstruction in order to reduce stripe artifacts and noise. The scalebars correspond to 2 mm. This figure was previously published in [Eggl et al., 2015b].

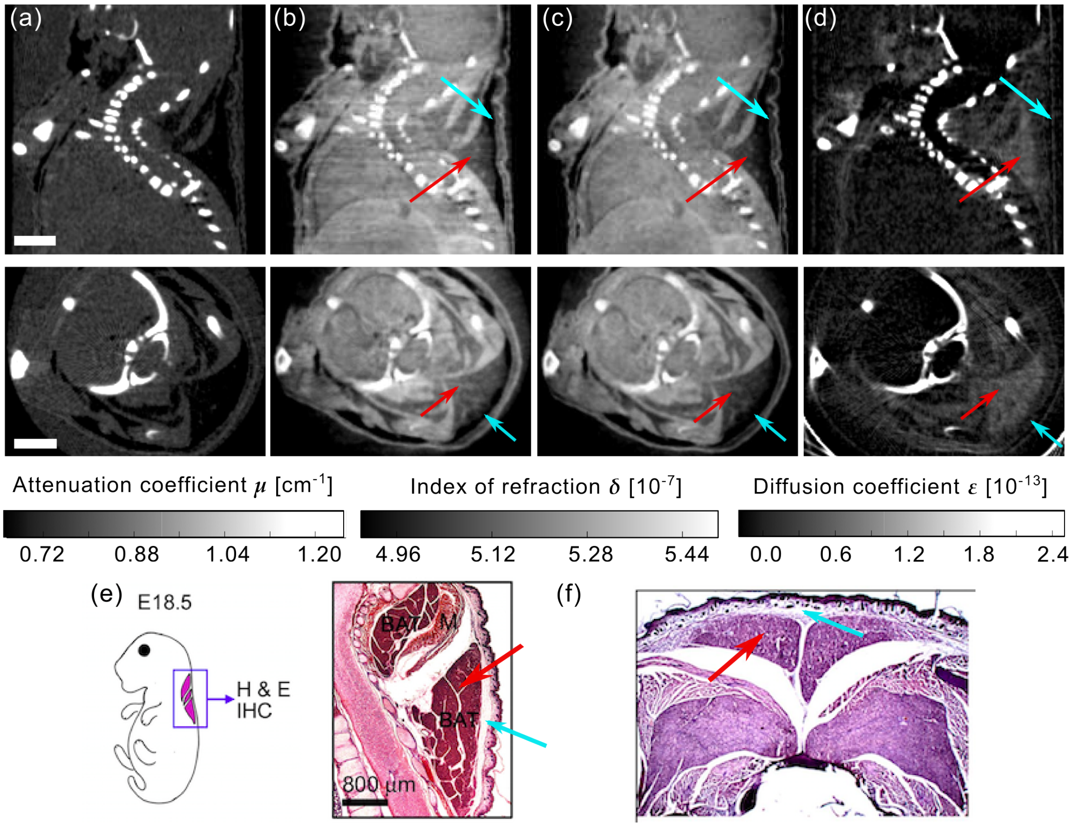

Figure 7.4.: Further reconstructed slices of a grating-based, multimodal CT scan of a biological sample (a formalin fixated infant mouse), in analogy to figure 7.3. The top row shows sagittal, the bottom row axial slices. The images demonstrate that brown adipose tissue (red arrows) is visible and can be discriminated from white adipose tissue (blue arrows) in phase-contrast (b,c) and dark-field contrast (d), but not in absorption contrast (a). The scalebars correspond to 2 mm. Histological slices presented in images (e) and (f) support this claim. Image (e) shows a sagittal section of the cervical/thoracic area stained with H&E of a mouse embryo (adapted from [Lee et al., 2013]). Image (f) shows an axial section of the interscapular area stained with H&E of a mouse embryo (adapted from [Zhou et al., 2014]). Red arrows indicate brown adipose tissue, while blue arrows indicate white adipose tissue. This figure was previously published in [Eggl et al., 2015b].

removed well by the iterative algorithm. The image quality benefits significantly from the use of the iterative reconstruction technique.

The conventional attenuation contrast image (a) in figure 7.3 gives good image contrast for bone structures. However, barely any information on the internal organs located in the mouse's abdomen can be drawn from this image. It is clearly visible that the phase-contrast images (b,c) provide superior soft-tissue contrast compared to the attenuation contrast image (a). Several internal organs such as the heart and the liver and structures within the organs can be recognized in the phase-contrast images, but not in the attenuation image, in the sagittal as well as in the axial images. The dark-field image (c) displays strong scattering at the bones and at air-filled organs.

With the slices chosen in figure 7.4, we would like to point out that, with phase contrast and dark-field contrast, brown adipose tissue and white adipose tissue are visible and can be discriminated. Comparing the phase-contrast and dark-field contrast images (b-d) to histology images stained with hematoxylin-eosin (H&E) 7.4 (e) and (f) (adapted from [Lee et al., 2013] and [Zhou et al., 2014], respectively), the brown and white adipose tissue in the interscapular region can clearly be identified, which is indicated with red and blue arrows, respectively. While their attenuation is to similar to allow the discrimination between brown and white adipose tissue, they have a different refractive index decrement. Scattering takes places for brown, but not for white adipose tissue.

7.4. CT of an infant bird

7.4.1. Methods & Materials

Data acquisition

Two infant birds (*passer domesticus*) were fixated in a 10% formaldehyde solution in falcon tubes. The MuCLS was tuned to an x-ray energy of 25 keV and the XGI was set up as described in chapter 4.1.2, i.e. with grating periods of $p_1 = 4.92$ µm for the phase grating and $p_2 = 5.00$ µm for the analyzer grating and an inter-grating distance of about 25 cm, as sketched in figure 4.3.

A CT scan was acquired for each bird, performing 5 phase steps with 1 second exposure time at each angular position. The interferometer visibility was $\sim 50\%$. The falcon tube was placed in a water bath in order to avoid phase wrapping artifacts.

Bird 1 was imaged using a PaxScan 2520 DX detector with a Gadox scintillator (Varian Medical Systems Inc., USA) with an effective pixel size of $\sim$ 118 µm, acquiring 350 angular projections. The tomography scan was acquired without a typewriter correction.

For bird 2, a Dexela 1512 detector with a Gadox scintillator (PerkinElmer Inc., USA) with an effective pixel size of $\sim$ 69 µm was used for the measurements. 650 projections were acquired over an angular range of 360°, applying a random typewriter correction (i.e. moving the sample small random steps perpendicular to the optical axis in order to reduce ring artifacts in the reconstruction).

For both tomography scans, a reference stepping curve was acquired every 20 angles.

Data processing and reconstruction

The absorption, differential phase-contrast and dark-field signals for each projection were retrieved (cf. chapter 2.2) using a least squares algorithm and a flux correction as described in chapter 4.3.1 and shown in figure 4.6. A statistical iterative reconstruction (SIR) algorithm was applied to reconstruct the three dimensional volume for all three image signals. A Huber regularization was used ($\lambda = 5 \cdot 10^{-2}, \gamma = 10^{-3}$, applying 3 momentum accelerated OSSPS iterations for absorption and dark-field, and 10 NLCG iterations for phase contrast). For bird 1, in addition a reconstruction with previous masking of the lungs was conducted. In this case, the reconstruction of the dark-field contrast volume was performed in two steps with 10 momentum accelerated OSSPS iterations each (first step with $\lambda = 10, \gamma = 10^{-2}$, second with $\lambda = 10^{-1}, \gamma = 10^{-2}$).

7.4.2. Results

Trimodal grating-based tomographies were acquired of two infant birds fixated in formaldehyde solution. Figure 7.5 shows coronal and sagittal slices of bird 1, acquired with an effective pixel size of 118 µm. The conventional absorption-contrast images (a,d) show good contrast for strongly absorbing structures (bones) and air-filled structures (lungs, air sacs), but have inherently low soft-tissue contrast. The phase-contrast images (b,e) show significantly increased soft-tissue contrast, making several features visible that cannot be recognized in the absorption image, such as structures within the eye and the abdomen, like the stomach and the intestines and pancreas. The dark-field contrast image offers good contrast for strongly scattering structures, like bones and air-soft tissue interfaces. The quality of the phase-contrast and dark-field contrast images is compromised by strong scattering in the lungs of the bird, which destroys the visibility in the projection images and therefore leads to strong stripe artifacts in the reconstruction.

A possible correction for streak artifacts is presented in figure 7.6. In the phase contrast and dark-field contrast projections, the lungs were masked out previous to the reconstruction. In addition, a ramp correction was applied to the projections. The reconstruction with the applied mask requires stronger regularization in order to successfully remove stripe artifacts, especially for the dark-field contrast, and causes a degeneration of image quality with respect to sharpness, making edges appear more blurred compared to the reconstruction in figure 7.5.

Figure 7.7 displays absorption-contrast (a,d,g), phase-contrast (b,e,h) and dark-field contrast (c,f,i) images of a second bird. The top row shows coronal, the middle row sagittal and the bottom row axial slices. Bird 2 has been measured after having been fixated in formaldehyde solution for a longer time than bird 1, presumably the lungs and air sacs have filled with liquid in the meantime and barely any scattering at all is visible from the lungs (c,f). Otherwise, the images show similar features as those of bird 1. Internal organs and structures within the eyes are only resolved in the phase-contrast image. Furthermore, the quills of the wing feathers are very well visible in the phase-contrast and somewhat less in the dark-field contrast image, but can barely be recognized in the absorption-contrast image. The image quality in the phase-contrast reconstruction is compromised by streak artifacts originating from air bubbles at the falcon tube-water interface, which are smoothed out but not fully removed by the iterative reconstruction

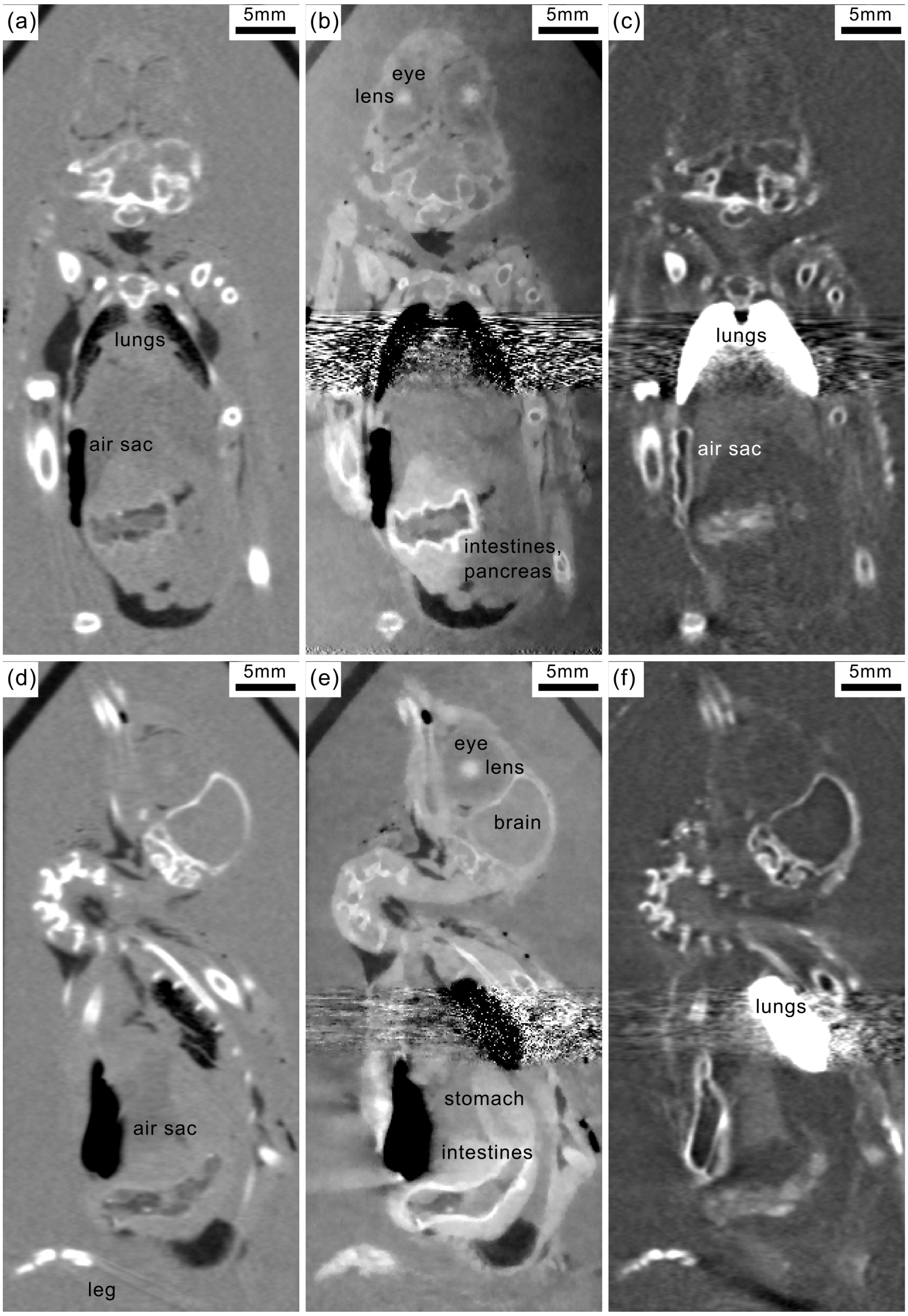

Figure 7.5.: Trimodal tomographic reconstruction of an infant bird (1). The top row shows coronal slices, the bottom row sagittal slices. From left to right, the multimodal contrast modalities are displayed: absorption contrast (a,d), phase contrast (b,e) and dark-field contrast (c,f). The phase contrast modality shows significantly enhanced soft tissue contrast and reveals tissue features that are invisible in the conventional absorption image, such as internal organs in the abdomen of the bird and even different tissues within the eyes. The phase-contrast and the dark-field contrast images are compromised due to the strong scattering in the lungs of the bird, causing a complete loss of visibility and therefore extreme artifacts in this region. The effective pixel size of the recorded images was 118 µm.

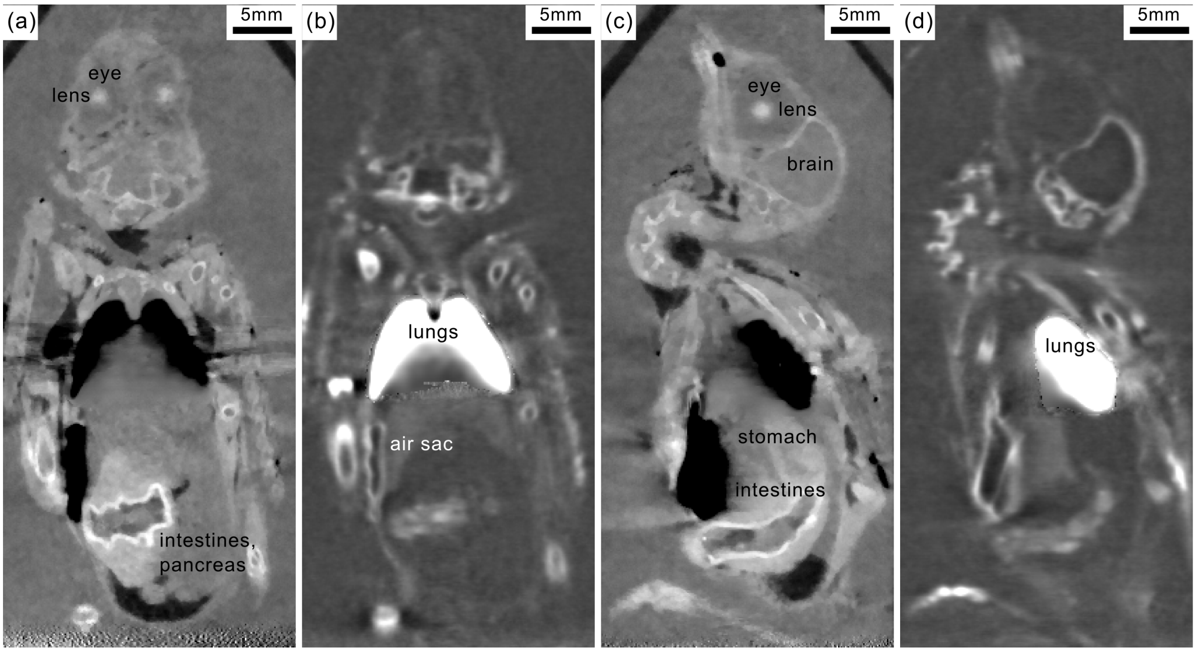

Figure 7.6.: Trimodal tomographic reconstruction of an infant bird (1) with masking of the lungs. Shown are coronal (a,b) and sagittal (d,e) slices for phase-contrast and dark-field contrast, respectively. The strongly scattering lungs which cause streak artifacts as visible in figure 7.5 were masked out before the reconstruction and a ramp correction was applied for the phase contrast image. The reconstruction with masking requires a different regularization, leading to stronger blurring and less image sharpness compared to figure 7.5, but streak artifacts are successfully removed.

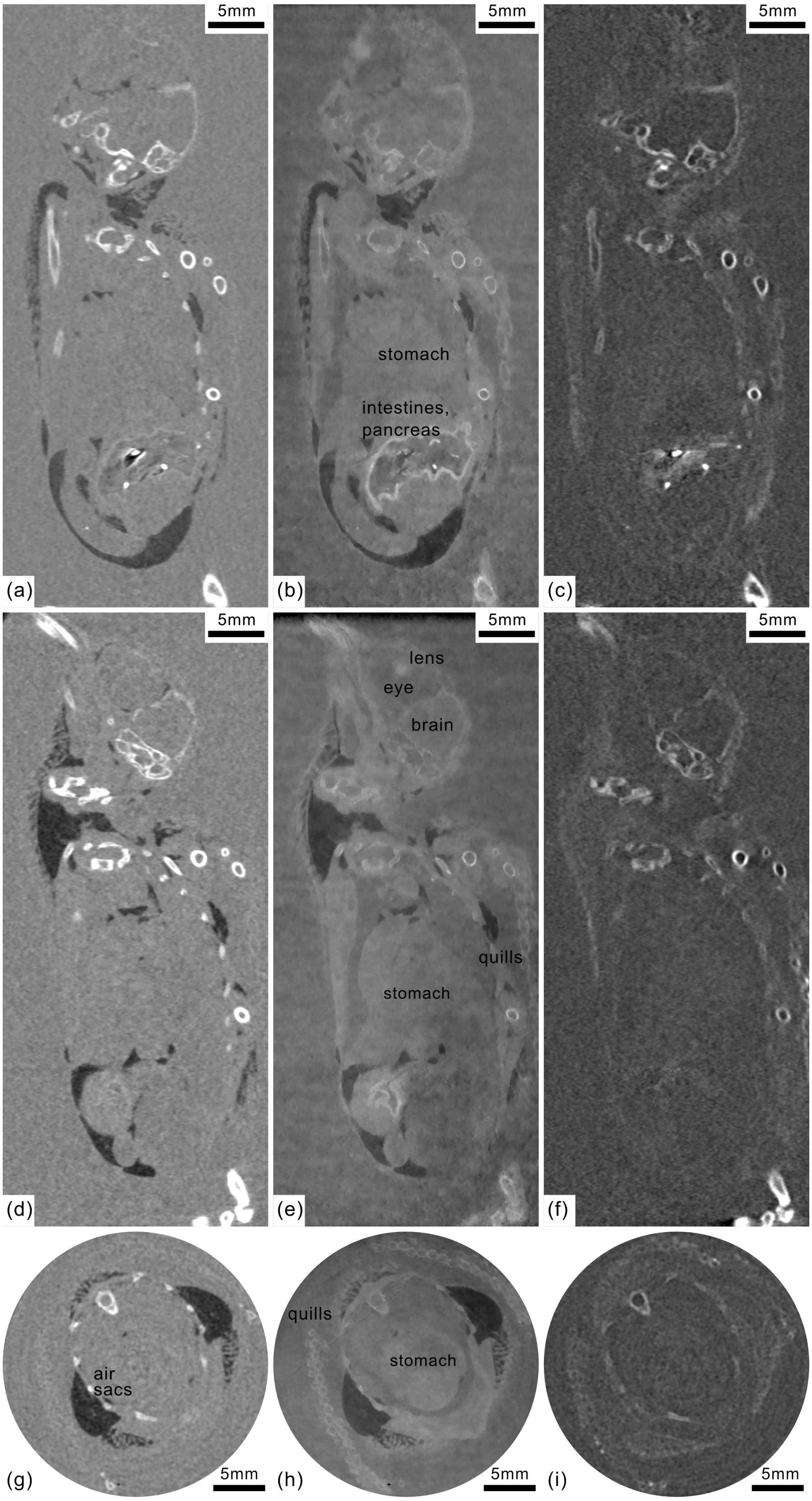

Figure 7.7.: Trimodal tomographic reconstruction of an infant bird (2). The top row shows coronal slices, the middle row sagittal slices, and the bottom row displays axial slices. From left to right, the multimodal contrast modalities are displayed: absorption contrast (a,d,g), phase contrast (b,e,h) and dark-field contrast (c,f,i). The effective pixel size of the recorded images was 69 µm.

scheme.

7.5. Summary and Conclusion

With multimodal tomography measurements of a fluid phantom at a compact synchrotron source, we showed that a combined analysis of both attenuation and phase provides a significant gain in information on different materials in the sample. Different fluids, which cannot be distinguished using solely the information obtained from either attenuation- or phase-contrast, can clearly be differentiated making use of the combined information.

Quantitative values of the linear attenuation coefficient and the refractive index decrement match very well with calculated theoretical values. We assume that the remaining small discrepancy from calculated values for the refractive index decrement could be further reduced using an iterative reconstruction algorithm to remove present stripe artifacts. Importantly, the measurement and calculation procedure is by far more accurate with the monochromatic beam of a CLS compared to measuring with a polychromatic x-ray tube source [Herzen et al., 2009, Tapfer et al., 2012, Nielsen et al., 2012]. The quantitative analysis in a scatterplot is facilitated because attenuation-contrast and phase-contrast images recorded with a grating interferometer are intrinsically perfectly registered.

Furthermore, we demonstrate the applicability of monochromatic grating-based tomography for biomedical samples. We presented the first multimodal computed tomography acquired at a CLS. For a fixated infant mouse, quantitative values for the linear attenuation coefficient, the refractive index decrement and the linear diffusion coefficient were reconstructed. Results show that especially the reconstruction of the refractive index decrement yields superior soft tissue contrast compared to the conventional attenuation image. We showed that employing an iterative reconstruction algorithm instead of FBP even improves the phase reconstruction and successfully removes stripe artifacts and noise.

The dose which was estimated to 2.14 Gy is significantly higher than the dose that is suggested for subsequent in vivo scans of mice which should be below 500 mGy [Rodt et al., 2011], but below the $LD_{50/30}$ dose [2] of 5-9 Gy [Figueroa et al., 2008]. In the future, the dose could strongly be reduced, by optimizing the gratings, by reducing scan time (shorter exposure times, fewer projections), and by using a more efficient detector.

Two multimodal grating-based tomography scans acquired at the MuCLS of two infant birds further demonstrate the superior soft-tissue contrast that is achieved in the phase contrast images and even enhanced by the monochromatic x-ray beam. Not only internal organs in the abdomen can be resolved in the reconstructed phase-contrast images, even structures within the eyes of the birds become visible. Feather quills that are invisible in the absorption contrast slices can easily be identified in phase and dark-field contrast slices. The possible masking previous to the reconstruction of structures with complete visibility loss was demonstrated, with the trade-off of a loss in image acuteness.

In addition, these two datasets acquired at the MuCLS show improved image quality over the mouse tomography acquired at the prototype, due to smaller source sizes and

---

[2] The $LD_{50/30}$ dose is defined as the dose which is lethal for 50% of the mice within 30 days.

better interferometer visibility as the x-ray energy was more closely matched to the design energy of the interferometer. The scan time could be reduced drastically, decreasing the exposure time per phase step from 8 seconds (mouse tomography) to 1 second.

In summary, the results show that a compact synchrotron source based on inverse Compton scattering is capable of providing high image quality and enabling a quantitative analysis of both biomedical and materials science specimens. While being compact enough to fit into a standard laboratory, these compact synchrotron sources have the potential to close the gap between conventional laboratory x-ray tube sources and large-scale synchrotron sources.

8. Grating-based phase-contrast and dark-field mammography

Mammography is an invaluable tool for the early detection of breast cancer. Here we investigate how advanced x-ray imaging methods can further improve the diagnostic content of mammography and possibly serve as a second-level examination in the case of inconclusive diagnosis. Chapter 8.2 presents a summary on the topic of dose calculation and explains the method applied for measurements at the MuCLS. The feasibility of grating-based multimodal breast tomosynthesis is demonstrated in chapter 8.3, the contents have been published in [Eggl et al., 2016b]. In chapter 8.4, we present dose-compatible quasi-monochromatic mammography images acquired at the MuCLS. Both conventional absorption and grating-based multimodal images are compared to clinical state-of-the-art digital mammography images. The results have been submitted as [Eggl et al., 2017a].

8.1. Motivation

Breast cancer still is the second most frequent type of cancer caused death for women worldwide [Siegel et al., 2012], even though extensive screening programs have been established over the last decades. The most widely established screening approach is mammography, a radiographic x-ray imaging technique, which especially relies on the detection of microcalcifications and tumor nodules to identify cancerous lesions. Mammography is an invaluable clinical tool for the early detection of breast cancer. However, the inherently low contrast in absorption x-ray imaging for soft tissue compromises the diagnostic performance, especially in the case of dense breasts. The radiation sensitivity of breast tissue limits the allowed dose [Perry et al., 2008]. Recent literature reports a sensitivity[1] between 69% and 94% and a specificity[2] between 78% and 95% for digital mammography, depending on patient age and breast density [Stout et al., 2014]. The positive predictive value[3] is between 7% and 13% in screening examinations [Venkatesan et al., 2009]. These numbers explain why the field of mammography is vastly under research and a non-invasive second-level examination besides ultrasonography is needed to clarify questionable or suspicious findings and avoid unnecessary invasive procedures such as biopsies.

---

[1] The sensitivity is defined as the ratio between the number of true positives and the number of ill patients.

[2] The specificity is defined as the ratio between the number of true negatives and the number of healthy patients.

[3] The positive predictive value is defined as the ratio between the number of true positives and the number of positive test results.

To improve the soft-tissue contrast, the possibility of x-ray phase-contrast and dark-field imaging has been investigated in various studies over the last decade. Different approaches have been studied, including propagation-based phase-contrast [Arfelli et al., 2000, Castelli et al., 2011], analyzer-based phase-contrast and dark-field imaging [Bravin et al., 2007, Keyrilainen et al., 2010], as well as grating-based (or aperture-based) phase-contrast and dark-field imaging [Stampanoni et al., 2011, Anton et al., 2013, Olivo et al., 2013, Scherer et al., 2014, Hauser et al., 2014, Grandl et al., 2015]. Grating-based imaging appears as the most promising approach as it is feasible not only with synchrotron but also with standard x-ray tube sources [Pfeiffer et al., 2006] and simultaneously provides attenuation, differential phase and dark-field signals [Pfeiffer et al., 2006, Pfeiffer et al., 2008]. The latter is related to small-angle scattering and has been shown to improve the visibility of microcalcifications [Michel et al., 2013] and could even help to distinguish between different types of calcifications [Scherer et al., 2016]. In addition, improved detectability of tumor lesions in the phase-contrast image was shown in the studies and proved the technique as a promising approach for breast cancer diagnosis, providing increased diagnostic content. However, initial investigations of this technique were performed with applied radiation doses far above radiological guidelines. Only recently, dose-compatible phase-contrast mammography images were presented [Scherer et al., 2015]. In addition, the feasibility of installing a grating-interferometer into a conventional digital mammography unit was successfully demonstrated [Roessl et al., 2014, Koehler et al., 2015]. Challenges are the low sensitivity of the interferometer due to the limited distance between the gratings, and dose compatibility.

Another strongly investigated topic is mammography with monochromatic radiation. The x-ray energy can be optimized for the best ratio of contrast to dose, thus eliminating the x-ray photons that do not give sufficient contrast (above the ideal energy) or those that deposit too much dose (below the ideal energy). A large clinical study at the SYRMEP beamline of the synchrotron Elettra (Trieste, Italy) has aimed at the patient group with inconclusive diagnosis after mammography and ultrasonography. The combination of absorption contrast and edge-enhancement resulting from phase shifts and subsequent free-space propagation enabled higher relative visibilities of abnormalities and the number of true-negative findings could significantly be increased, while the dose level was lower or comparable to conventional mammography [Castelli et al., 2011, Longo et al., 2014, Olivo and Castelli, 2014]. However, mammography with synchrotron radiation has the disadvantages of limited availability, remoteness with respect to clinics, and high costs.

In order to combine the advantages and avoid some disadvantages of the two approaches, we suggest to perform grating-based multimodal mammography at a compact synchrotron source based on inverse Compton scattering [Huang and Ruth, 1998]. Compact synchrotron sources have been suggested and theoretically investigated previously for pre-clinical imaging because of their profitable narrow bandwidth [Keyrilainen et al., 2010, Oliva et al., 2009]. With a footprint small enough to fit into a standard-sized laboratory, their performance is superior to that of classical x-ray tube sources in terms of monochromaticity, brilliance, source size and coherence. The beam size is significantly larger than at synchrotron sources, which is particularly beneficial for imaging larger biomedical samples, as in breast imaging. Previous studies exploring grating-based phase-contrast and dark-field imaging at an inverse Compton compact x-ray source have proven the suitability of such sources for pre-clinical research, e.g. on lung emphysema diagnosis [Schleede et al., 2013] and their suitability for breast imaging has been evaluated in simulation studies [Oliva et al., 2009]. Offering a quasi-monochromatic x-ray beam that is tunable in energy and partially coherent, a compact synchrotron like the MuCLS allows to obtain increased diagnostic content from grating-based phase-contrast and dark-field images while achieving equal image quality at lower dose compared to the aforementioned laboratory setups. In addition, monochromatic conventional absorption-based imaging, or propagation-based phase-contrast imaging as done at SYRMEP, is possible. Since the spatial and financial requirements of inverse Compton sources are relatively small compared to large-scale synchrotrons, the installation at medical centers appears feasible.

Two different new approaches for mammographic imaging are presented here. In chapter 8.3, we demonstrate the feasibility of phase-contrast and dark-field tomosynthesis at a CLS. We show that the phase-contrast and the dark-field images provide complementary information on real breast tissue. Furthermore, we show that tomosynthesis is capable of revealing necrotic breast tissue which was not visible in the projection image due to glandular tissue overlap, as verified by histopathology.

Furthermore, in chapter 8.4, we investigate the dose compatibility of mammographic imaging at the MuCLS. Both absorption-only and grating-based multimodal images of freshly dissected cancerous mastectomy specimens acquired at the MuCLS at lower or equal dose are compared to state-of-the-art clinical images. A dose study and analysis of the contrast-to-noise ratio on a well defined sample, a mammographic accreditation phantom, is conducted. In addition, we present a comparison of the spatial resolution for experimental and clinical images.

We believe that compact synchrotron sources like the MuCLS have great potential to bring benefits to clinical imaging, in particular for mammography, but also other fields, like coronary angiography [Eggl et al., 2017b] could profit from the monochromatic, tunable x-ray beam.

8.2. Dose calculation

Dosimetry is one of the key points in mammographic imaging due to the radiation-sensitivity of breast tissue. The challenge is to reach good diagnostic quality while not exceeding a given dose. Of course, the dose actually applied to the breast tissue cannot be measured, and therefore needs to be approximated. This task is usually performed by Monte Carlo simulations, providing conversion factors from measurable quantities (intensity of the x-ray beam) to dose to the breast.

8.2.1. Relevant dosimetric quantities

Air Kerma

The kerma (<u>k</u>inetic <u>e</u>nergy <u>r</u>eleased per unit <u>ma</u>ss) is defined as the sum of the kinetic energy of all charged particles liberated per unit mass [Schlegel and Bille, 1999]:

$$K = \frac{\mathrm{d}\overline{E_{\mathrm{tr}}}}{\mathrm{d}m} \tag{8.1}$$

where $d\overline{E_{\text{tr}}}$ is the mean kinetic energy transferred to charged particles from uncharged particles in a mass dm of a given material. The unit of kerma is

$$[K] = \frac{\mathrm{J}}{\mathrm{kg}} = \mathrm{Gy}. \tag{8.2}$$

Usually kerma is expressed in terms of the distribution $\Psi(E) = E \cdot \Phi(E)$ of the uncharged energy fluence with respect to energy.

$$K = \int E \cdot \Phi(E) \cdot \frac{\mu_{\text{tr}}(E)}{\rho} \mathrm{d}E \tag{8.3}$$

where $\frac{\mu_{\text{tr}}(E)}{\rho}$ is the mass energy transfer coefficient of the material for uncharged particles of energy E.

The total kerma is given by the sum of collisional kerma K_{coll} and radiative kerma K_{rad}:

- Collisional kerma produces secondary electrons that dissipate their energy as ionization and excitation.
- Radiative kerma includes the part of energy that is transferred to radiative photons (bremsstrahlung), annihilation radiation of positrons and fluorescent radiation.

The IAEA Code of Practice [IAEA, 2007] has recommended the use of air kerma as dosimetric measure for radiation in air, due to the difficulty to quantify the energy absorbed from radiation in air. The quantity of air kerma was adopted as primary standard for keV x-rays for dosimetric calibration instruments like ionization chambers. For air and for low x-ray energies, the fraction of the initial kinetic energy of the particles transferred to bremsstrahlung is very small ($K_{\text{rad}} \approx 0$) and therefore, the air kerma is usually expressed as [Schlegel and Bille, 1999]

$$K_{\text{air}} = \int \Phi(E) \cdot E \cdot \left(\frac{\mu_{\text{en}}(E)}{\rho}\right)_{\text{air}} \mathrm{d}E \tag{8.4}$$

where $\left(\frac{\mu_{\text{en}}(E)}{\rho}\right)_{\text{air}}$ is the mass energy absorption coefficient of air for uncharged particles of energy E, $[\frac{\mu_{\text{en}}(E)}{\rho}] = 1\frac{\mathrm{cm}^2}{\mathrm{g}} = 10^{-1}\frac{\mathrm{m}^2}{\mathrm{kg}}$.

Exposure

Exposure is a quantity used equivalently to air kerma. It is outdated to current nomenclature and units, but still present in US papers. The quantity exposure has specifically been designed for dosimetry with air-filled ionization chambers. It is only applicable for radiation from photons in air and then is equivalent to the collisional kerma. Exposure is defined as the electric charge freed by the radiation divided by the mass of the air [Schlegel and Bille, 1999]

$$X = \frac{\mathrm{d}Q}{\mathrm{d}m}, \tag{8.5}$$

where $\mathrm{d}Q$ is the amount of charge of ions that have been created in the air element of mass $\mathrm{d}m$ through secondary electrons from photon radiation, when the secondary electrons are fully decelerated in air. The unit of exposure is Roentgen and a simple conversion between exposure and air kerma is possible: 1 R = 8.7 mGy or 1 Gy = 114 R.

8.2.2. Measurement of dosimetric quantities

In clinical practice, usually radiation detectors are used to determine radiation dose quantities such as air kerma (common for imaging) or, mainly in the case of radiation therapy, absorbed dose to water. One of the most common devices are ionization chambers. They consist of a gas-filled volume between two electrodes connected to a HV supply. Ionizing radiation creates ion pairs in the gas and the positive and negative ions are then attracted by the electrodes. The emerging current can be measured by an electrometer and a certain detector specific calibration factor (e.g. Gy/C) is applied to relate the measured signal to a radiation dose value [Schlegel and Bille, 1999].

8.2.3. Mammographic dosimetry

Only recently, [Dance and Sechopoulos, 2016] published a comprehensive review on dosimetry in breast imaging, which is briefly summarized here.

Historically, breast dosimetry started with calculating the entrance surface dose. However, as dose decreases exponentially with increasing depth within the breast, the surface dose is a poor measure of the dose applied to the radiation-sensitive glandular tissue. These tissues have the highest risk of carcinogenesis. Therefore, [Karlsson et al., 1976] proposed the mean dose to the glandular tissues as better measure of risk. Nowadays, the mean glandular dose (MGD) is the basis for most, if not all, national and international breast dosimetry protocols.

[Young and Oduko, 2016] analyzed the glandular dose received by women attending the UK breast-screening program in 2010-2012. They found an average MGD of 1.8 mGy for mediolateral-oblique (MLO) images and 1.6 mGy for cranio-caudal (CC) images. The average MGD per two-view examination was 3.0 mGy for digital radiography (4 mGy for film-screen mammography).

The applied dose is related to a lifetime risk of radiation induced breast cancer. A 50 year old woman who receives a MGD to both breasts of 3 mGy would have a lifetime risk of 3 in 100.000 for radiation induced breast cancer [Yaffe and Mainprize, 2011]. This means the risk for an individual breast exposure is small. However, the detection of breast calcification decreases with decreasing dose [Warren et al., 2012] and it is important that while keeping dose to a minimum, sufficient clinical image quality is ensured.

As MGD cannot be measured directly, conversion factor are necessary to relate MGD to measurable dosimetric quantities, like air kerma or exposure. These conversion factors are generally derived by Monte Carlo simulations of how radiation is deposited in the breast trough scattering and absorption and depend strongly on x-ray energy as well as breast size and composition. Most widely used are conversion factors as published by [Dance, 1990, Dance et al., 2000] in the UK and [Wu et al., 1991, Wu et al., 1994] in the USA.

8.2.4. Choice of conversion model for the MuCLS

All commonly used models for conversion from air kerma or exposure to MGD use simplified geometrical models of the human breast, where a circular or elliptical shape of varying thickness consists of an outer skin layer (thickness 4-5 mm) and an inner breast tissue volume, in which glandular and adipose tissue is homogeneously distributed with varying volume proportions. The most common assumption is a 50% glandular/ 50% adipose distribution of tissue but this number has a major effect on the calculated dose. Most Monte Carlo calculations use measurements of adipose and glandular tissue density and attenuation coefficients as published by [Hammerstein et al., 1979].

Model developed by Dance et al.

Most commonly used in Europe is the model developed by [Dance, 1990, Dance et al., 1999, Dance et al., 2000]. Here, the mean glandular dose is related to the incident air kerma K (cf. section 8.2.1) by the use of three conversion factors:

$$\mathrm{MGD} = K \cdot gcs, \tag{8.6}$$

where g is a conversion factor for a breast of 50% glandularity tabulated according to breast thickness and specified half value layer (HVL) of aluminum for the given x-ray spectrum [Dance, 1990]. The factors c and s correct for breast composition (glandularity) and x-ray spectrum, respectively, and are tabulated in [Dance et al., 2000].

Concerning the applicability for the mammographic imaging at MuCLS, the choice of factors g and s makes the use of this model difficult to use. Naturally, the MuCLS spectrum is not tabulated and therefore the choice of the s-factor would rather be an educated guess without the availability of a Monte Carlo simulation. The HVL for the MuCLS spectrum can be calculated, but is higher than most given HVL values in Dance's tables and therefore misses for a range of breast thicknesses. Therefore, without Monte Carlo code being available to compute correct conversion factor for the MuCLS spectrum, the Dance dosimetry protocol is not the best choice for the MuCLS as it is associated with too many uncertainties when the effect of the spectrum on the conversion factors is unknown.

Model developed by Wu et al.

In the USA, the MGD is usually calculated applying the model developed by [Wu et al., 1991, Wu et al., 1994]. Here, MGD is obtained by multiplying the exposure by a factor DgN (normalized average glandular dose). Wu et al. provide tabulated values of DgN for different x-ray spectra. Therefore, due to the same reasons as for Dance's model, this model is not suitable for the MuCLS either.

Model developed by Boone et al.

[Boone, 1999, Boone, 2002] extended Wu's model by including a larger range of breast thicknesses and breast glandularities. More importantly, Boone et al. provide monoenergetic DgN values, thus allowing for the glandular dose to be computed for any arbitrary x-ray spectrum, hence offering the best applicability for the MuCLS.

They used a SIERRA Monte Carlo code to compute dose deposition within the human breast which was assumed as semi-circular in cranio-caudal projection with a skin layer of 4 mm. For breast thicknesses from 2 to 9 cm (1 cm increments) and glandularities of 0%, 50% and 100%, normalized glandular dose fit equations DgN(E) are provided

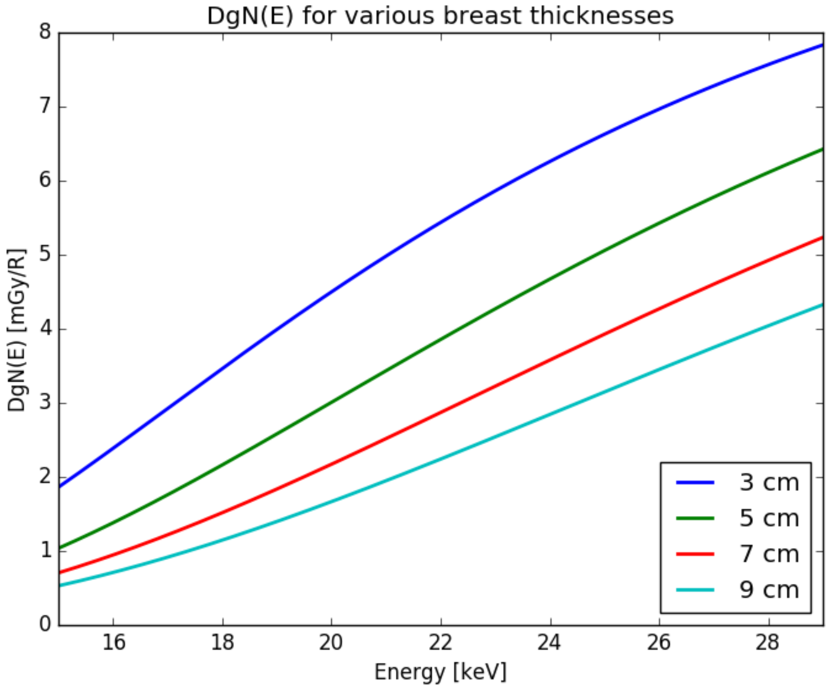

Figure 8.1.: The monochromatic normalized glandular dose DgN(E) over the energy range relevant for mammography at the MuCLS, computed for 50% glandularity and various breast thicknesses between 3 cm and 9 cm.

in the energy range between 8-50 keV, given in the unit of dose (mGy) per exposure (R). [Boone, 2002] found an excellent agreement for DgN values with those published by [Wu et al., 1991]. The normalized glandular dose depending on energy is exemplarily shown in figure 8.1 for various thicknesses over the energy range relevant for the MuCLS calculations.

With the provided fit equations, the (polyenergetic) mean glandular dose can be calculated for any given spectrum, knowing the photon flux per energy bin [Boone, 2002],

$$\mathrm{MGD} = \frac{\sum_{E=E_{\mathrm{min}}}^{E_{\mathrm{max}}} \Phi(E)\vartheta(E)\mathrm{DgN}(E,t,g)}{\sum_{E=E_{\mathrm{min}}}^{E_{\mathrm{max}}} \Phi(E)\vartheta(E)}, \tag{8.7}$$

where $\Phi(E)$ is the flux in energy bin E and $\mathrm{DgN}(E,t,g)$ is the monochromatic normalized glandular dose coefficient as provided for breast thickness t and glandularity g and depending on energy bin E. A fit equation for the exposure $\vartheta(E)$ is also provided by [Boone, 2002], however, this equation is incorrect [Nosratieh et al., 2015].

As a workaround, equation 8.7 was adapted by replacing $\vartheta(E)$ with the more common unit $K(E)$ and the corresponding conversion factor:

$$\mathrm{MGD[mGy]} = \sum_{E=E_{\mathrm{min}}}^{E_{\mathrm{max}}} K(E)\,[\mathrm{mGy}] \cdot \kappa \left[\frac{\mathrm{R}}{\mathrm{mGy}}\right] \cdot \mathrm{DgN}(E,t,g) \left[\frac{\mathrm{mGy}}{\mathrm{R}}\right] \tag{8.8}$$

where $K(E)$ is the air kerma per energy bin E, $\kappa = 0.114$ R/mGy is the air kerma/-exposure conversion factor and $\mathrm{DgN}(E,t,g)$ is the normalized glandular dose coefficient as provided for breast thickness t and glandularity g and depending energy bin E.

DgN values for intermediate densities can be calculated by weighing the DgN coefficients for 0%, 50%, and 100% by the volume glandular fraction V_g [Nosratieh et al., 2015]:

$$V_g = \left[\frac{(1-f_g)}{f_g} \frac{\rho_g}{\rho_a} + 1 \right]^{-1}, \tag{8.9}$$

where f_g is the weight fraction of glandular tissue, ρ_g is the density of 100% glandular tissue and ρ_a is the density of 100% adipose tissue ($\rho_g = 1.04$g cm^{-3} and $\rho_a = 0.93$g cm^{-3} from [Hammerstein et al., 1979]).

DgN values for intermediate breast thicknesses can simply be interpolated. There are no tabulated values for breast thicknesses larger than 9 cm, but these large breast thicknesses were not experienced in the experiments carried out at the MuCLS.

Model by Arfelli et al.

[Arfelli et al., 1998] proposed a model for mammographic imaging with synchrotron radiation that requires the knowledge of energy-dependent attenuation coefficients of adipose and glandular breast tissue. For a breast with an outer skin layer of thickness t_s (usually assumed to be 0.5 cm), the glandular dose D_g deposited in a depth x can be calculated as

$$D_g(x) = \Phi \cdot E_x \cdot \frac{\mu_{\mathrm{en},g}}{\rho_g} \cdot \exp\left[-\mu_a t_s - \mu_m (x - t_s)\right]. \tag{8.10}$$

Then the MGD applied to a breast of thickness t is given by

$$\mathrm{MGD} = \frac{1}{t - 2t_s} \int_{t_s}^{t-t_s} D_g(x) \mathrm{d}x. \tag{8.11}$$

In the case an outer skin layer is absent, the integral can simply be solved analytically,

$$\mathrm{MGD} = E_x \cdot \Phi \cdot \frac{\mu_{\mathrm{en},g}}{\rho_g} \cdot \frac{1}{t} \cdot \frac{1}{\mu_m} \cdot \left(1 - \mathrm{e}^{-t \cdot \mu_m}\right), \tag{8.12}$$

where E_x denotes the energy of the x-ray photons, Φ the x-ray flux (number of photons per mm^2 per second), and t the thickness of the breast. For the glandular tissue mass attenuation coefficient $\mu_{\mathrm{en},g}$, the glandular tissue density ρ_g, and the glandular-adipose mixture attenuation coefficient μ_m, [Dance et al., 1999] published tabulated values, for 20 keV x-ray energy based on a first publication by [Hammerstein et al., 1979].

This approach was chosen in [Schleede et al., 2012] and [Eggl et al., 2016b], where the CLS peak x-ray energy was 21 keV, thus the mean energy being relatively close to the 20 keV for which tabulated values exist. In addition, the approach by Arfelli et al. is the only one where the absence of a skin layer can be accounted for. Due to the limited access to tabulated values for the 25 keV peak energy used at the MuCLS and also because the approach is not clinically applied, the calculation as proposed by [Arfelli et al., 1998] was not chosen for MuCLS mammographic imaging.

Advanced breast models - heterogeneous glandular distributions

All commonly used dosimetry methods are based on Monte Carlo calculations assuming a homogeneous distribution of glandular and adipose tissue throughout the breast and a surrounding skin layer of 4-5 mm thickness. With the introduction of breast CT, three dimensional data sets of human breasts became available, thus allowing for a realistic model of the distribution of glandular tissue to be gained. It appears that far less glandular tissue is located close to the surface of the breast. As radiation exposure decays exponentially throughout the breast, homogeneous glandular distributions as previously assumed have been found to substantially overestimate the dose to the glandular tissue.

[Hernandez et al., 2015] have calculated updated normalized glandular dose coefficients (DgN) with Monte Carlo simulation based on heterogeneous glandular distributions obtained from a large number of breast CT data sets. They found an 25-35% over-estimation of mean glandular dose when comparing Monte Carlo simulations with heterogeneous to homogeneous glandular distributions.

Even though first DgN coefficients based on heterogeneous glandular distributions have recently become available [Hernandez et al., 2015], these have not yet been refined to be incorporated into clinical dosimetry protocols. In order to allow for comparability with clinical dosimetry numbers as e.g. provided by clinical mammography units, this work will apply established glandular dose coefficients.

8.2.5. Dose calculation at the MuCLS

This section describes the procedure that is performed for dose calculation at the MuCLS. The data is processed using the corresponding software package `DoseCalc`, as explained hereafter and illustrated in listing 8.1. The full software code is provided in listing A.1 in the Appendix.

- A scan of the empty MuCLS beam (no gratings, no sample) is acquired with the Pilatus detector on the same day of the sample measurements. During this scan, the scintibloc counts are logged simultaneously. To ensure sufficient statistics, e.g. 10 frames with 1 second exposure time are acquired.

- It has been verified that the scintibloc shows a linear behavior in the intensity range that is of interest [Cont, 2016].

- The flux measured with the Pilatus detector, a single photon detector, is used to calculate the air kerma, taking into account the MuCLS spectrum (`dose.calculate_air_kerma`).
  - For the Pilatus scan, a ROI in the center of the x-ray beam is selected (indicated with `pilatus_roi` in listing 8.1). The number of photon counts per pixel is calculated for the ROI, averaging over the given number of frames from the Pilatus scan.
  - The MuCLS spectrum at 25 keV – either measured using an energy-dispersive detector (compare section 5.3) or simulated [Loewen, 2017] – is corrected (for efficiency of the energy-dispersive detector and attenuation in PMMA and air for the measured spectrum, for attenuation in the silicon output window and air in case of the simulated spectrum) to resemble the spectrum at the sample/Pilatus position.

- The quantum efficiency (QE) of the Pilatus detector (i.e. photoelectric absorption in 1000 µm Si) and the absorption in the air gap between the sample position and the Pilatus (80 cm) are calculated. The fraction of transmitted intensity T through a material of absorption coefficient $\frac{\mu}{\rho}$ of thickness d and density ρ can be calculated for a given spectrum,

  $$T = \frac{\sum_{E=E_{\mathrm{min}}}^{E_{\mathrm{max}}} S(E) \cdot \exp\left(-\frac{\mu}{\rho} \cdot \rho \cdot d\right)}{\sum_{E=E_{\mathrm{min}}}^{E_{\mathrm{max}}} S(E)}, \tag{8.13}$$

  where $S(E)$ is the normalized intensity of the spectrum in energy bin E. Absorption coefficients for the different materials are taken from the python package `xraylib` [Schoonjans et al., 2011] that uses the XCOM database [Berger et al., 2010].

- The corrected total flux Φ at the sample position is obtained from the Pilatus counts per pixel:

  $$\Phi = \frac{\frac{\text{Pilatus counts}}{\text{pixel frame}}}{\mathrm{QE}_{\mathrm{Pilatus}} \cdot T_{\mathrm{Air}} \cdot \xi} = \frac{\text{Photon fluence}}{\mathrm{mm}^2\,\text{frame}}, \tag{8.14}$$

  where $\mathrm{QE}_{\mathrm{Pilatus}} = 1 - T_{\mathrm{Si}}$ is the quantum efficiency of the Pilatus calculated from the photoelectric absorption in 1000 µm air and T_{Air} is the transmission through 80 cm of air between sample and detector. ξ is a correction factor taking into account the pixel size of the Pilatus detector (0.172 mm^2) and the magnification factor at the sample position to obtain the photon fluence per mm^2 per frame at the sample position.

- The corrected flux is multiplied with the normalized spectrum, to obtain a corrected flux $\Phi(E)$ per energy bin.

- The MuCLS spectrum and the corrected flux are used to calculate the air kerma per energy bin:

  $$K_{\mathrm{MuCLS}}(E) = \left(\frac{\mu_{\mathrm{en}}}{\rho}(E)\right)_{\mathrm{air}} \cdot E \cdot \Phi(E), \tag{8.15}$$

  where $\left(\frac{\mu_{\mathrm{en}}}{\rho}\right)_{\mathrm{air}}$ is the mass energy attenuation coefficient of air, for which we the most recently published values were used [Buhr et al., 2012].
  To convert from $\frac{\mathrm{cm}^2\,\mathrm{keV}}{\mathrm{mm}^2\,\mathrm{g}}$ to $\frac{\mathrm{J}}{\mathrm{kg}}$ = mGy, a factor of $100 \cdot 1000 \cdot 1.602 \cdot 10^{-16} \cdot 1000$ is needed.

- The air kerma at the sample position per frame is calculated for the sample scan using the ratio of the average number of scintibloc counts during the whole sample scan N_{sample} (mean of all phase steps and stitched fields) and the pilatus scan N_{Pilatus}. The (average) air kerma per frame during the sample scan can then be calculated without having to know the exposure times:

  $$K_{\mathrm{sample}}(E) = K_{\mathrm{MuCLS}}(E) \cdot \frac{N_{\mathrm{sample}}}{N_{\mathrm{Pilatus}}}, \tag{8.16}$$

  where $K_{\mathrm{MuCLS}}(E)$ is the air kerma per energy bin calculated according to equation 8.15 for the Pilatus scan.

- Knowing the air kerma per frame during the sample scan, the number of phase steps N_{steps} (for absorption-only measurements, $N_{\mathrm{steps}} = 1$), the thickness t and the glandularity g of the sample, the mean glandular dose (MGD) can be calculated using Boone's polychromatic normalized glandular dose coefficients $\mathrm{DgN}(E)$ (`dose.DgN`) and again taking into account the MuCLS spectrum, using the function `dose.calculate_MGD`:

  $$\mathrm{MGD} = N_{\mathrm{steps}} \cdot \sum_{E=E_{\mathrm{min}}}^{E_{\mathrm{max}}} K_{\mathrm{sample}}(E)\,[\mathrm{mGy}] \cdot \mathrm{DgN}(E,t,g) \left[\frac{\mathrm{mGy}}{\mathrm{R}}\right] \cdot 0.114 \left[\frac{\mathrm{R}}{\mathrm{mGy}}\right]. \tag{8.17}$$

  For the case of breast thicknesses or glandularities that have intermediate values between those tabulated by [Boone, 2002], interpolated MGD values are provided by the function `dose.interpolate_ normalized_glandular_dose`.
  Note that the number of stitched fields does not need to be taken into account because the coefficients DgN always give the dose for a full imaged breast (we assume for simplicity that no overlap during the stitching took place, i.e. each spot in the sample was only illuminated once) .

Listing 8.1: Python pseudo code illustrating the dose calculation using the DoseCalc package.

```
"""
Python pseudo code for dose calculation.
@author: Elena Eggl
"""
import DoseCalc as dose
import numpy as np
import os
#------------------------------------------------------------
def calculate_MGD(sample_identifier, pilatus_identifier, pilatus_roi, t, g)
    #calculate air kerma per energy bin from Pilatus scan
    #includes loading and correcting a MuCLS spectrum (’simulated’ or ’measured’), and calculating the flux at the samples position from the Pilatus scan taking into account the quantum efficiency, air absorption and geometric considerations
    energy, air_kerma = dose.calculate_air_kerma(pilatus_identifier, pilatus_roi, ’simulated’)
    #load the average number of scintibloc counts during the Pilatus scan
    scintibloc_counts_pilatus = np.mean(np.loadtxt(pilatus_identifier + ’_scintibloc.txt’))
    #load the average number of scintibloc counts during the sample scan, averaging over all fields that will be stitched together
    nb_fields = len(os.listdir(patient_I))-2 #get the number of fields for stitching, subtract 2 flat fields
```

```
    scintibloc_counts = ()
    for i in range(nb_fields):
    scintibloc_counts = np.append(scintibloc_counts, np.
   loadtxt(sample_identifier[i] + '_scintibloc.txt'))
    nb_steps = len(os.listdir(sample_identifier[1])) #number
    of steps during sample scans
    scintibloc_counts_sample = np.mean(scintibloc_counts)
    #calculate air kerma per energy bin during sample scan
    air_kerma_sample = scintibloc_counts_sample/
   scintibloc_counts_pilatus * air_kerma
    #calculate the MGD, summing over all energy bins
    #normalized_glandular_dose assesses the fit equations
   for DgN through dose.DgN(energy[j],t,g)
    MGD = dose.interpolate_normalized_glandular_dose(energy,
    air_kerma_sample, t, g) * nb_steps
    return MGD
#-----------------------------------------------------------
# calculate the MGD for patient I with 5 cm compressed
   breast thickness and a glandularity of 50%
MGD = calculate_MGD('patient_I', 'patient_I_pilatus',
   [240,260,130,150], 5.0, 0.5)
```

Limitations of dose estimation

Several measurement uncertainties are included in the dose calculation.

- As discussed in chapter 5.3, the spectra measured at the MuCLS varied over time and showed some discrepancy to the simulated spectrum for lower energies due to the upscaling of especially lower energies when correcting for the attenuator used during the spectrum measurement. To keep the error as small as possible, a simulated spectrum adapted to a spectrum measured shortly before the mammography experiments was used for the dose calculation (compare spectra shown in figure 5.11 (b)).

- The breast thickness and breast glandularity have a significant influence on the calculation of the MGD. The compressed breast thickness was determined when the breast was placed in the sample holder. For best comparability to clinical dose values, a glandularity of 50% was assumed for all specimens. This conforms with a statement in [Boone, 2002], that a specific woman's MGD can only have limited accuracy and general conditions (50% glandularity) should be used to compare benchmark values from different mammography systems.

- The photon flux is calculated using the single photon counting Pilatus detector. According to [Donath et al., 2013], the measured quantum efficiency for the Pilatus detector corresponds to theoretical values within the relative measurement uncertainty of 2%.

- The tabulated values of the absorption coefficients for air, silicon, PMMA, etc. contain measurement uncertainties themselves.

Validation of the air kerma calculation

For verification of the calculation of the air kerma from the MuCLS spectrum and photon flux calculated from the Pilatus detector, the measurements were validated with a calibrated ionization chamber (Soft X-ray Ionization Chamber 34013, PTW Freiburg GmbH, Germany). The ionization chamber is calibrated for air kerma, has a sensitive volume of $0.0053\,\mathrm{cm}^3$ and has a flat energy response in the range from 10 keV to 100 keV according to the manufacturer.

The ion chamber was placed in hutch 1, 7.9 m from the interaction point, surrounded by air (no backscatter, no phantom slab). The air kerma was recorded during 1.5 minutes and 1 second exposures were recorded with the Pilatus detector in the meantime. The air kerma was calculated from the Pilatus measurements according to equation 8.15, summing over all energies, and the difference in magnification compared to the ionization chamber and the air absorption were taken into account.

The charge measured at the ionization chamber needs to be multiplied with the calibration factor and corrected for air pressure, temperature or photon beam qualities in order to obtain the air kerma K [Schlegel and Bille, 1999, PTW Freiburg, 2016]:

$$K = M \cdot k_Q \cdot N_w, \tag{8.18}$$

where k_Q is the measured charge, N_w is the calibration factor (Gy/C) given by the manufacturer and M is the correction factor:

$$M = (M_{uncorr} - M_0) \cdot k_{TP} \cdot k_Q \cdot k_S \cdot k_{pol}, \tag{8.19}$$

where

- M_{uncorr} is the reading from the electrometer.
- M_0 is the reading without irradiation.
- k_{TP} corrects for air density: $k_{TP} = \frac{p_0 \cdot (273.2+T)}{p \cdot (273.2+T_0)}$. In our case, $k_{TP} = \frac{1013.25\,\mathrm{hPa} \cdot 298.2\,\mathrm{K}}{970.5\,\mathrm{hPa} \cdot 295.2\,\mathrm{K}} = 1.055$.
- k_Q corrects for beam quality: The manufacturer provides values of $k_Q = 1.000$ for a TW30 spectrum (30 kVp tungsten with 0.5 mm Al filtration) and $k_Q = 1.021$ for a TW50 spectrum (50 kVp tungsten with 1.0 mm Al filtration). For the 25 keV MuCLS spectrum, we assumed a correction factor of $k_Q \simeq 1.01$.
- The corrections for saturation efficiency k_S and polarity k_P are neglectable according to the manufacturer PTW of the used ionization chamber [PTW Freiburg, 2016].

The measurements showed that the calculated air kerma K_{MuCLS} agreed with the value measured by the ionization chamber within the measurement uncertainties of 10%.

Therefore we believe that, in combination with the well confirmed values for the monoenergetic glandular dose coefficients [Boone, 2002], an accurate dose estimate for mammographic imaging at the MuCLS can be given.

8.3. Grating-based multimodal tomosynthesis

The measurements presented in this section have been acquired at a prototype of the Compact Light Source in Palo Alto, CA, USA and have been published in [Eggl et al., 2016b].

8.3.1. Motivation

As mammography is a projection-based approach, overlapping glandular tissue especially in dense breasts can cause obscuration of tumor masses and lesions, but also an increase in false-positive diagnoses.

To counteract the problems imposed by glandular tissue overlap, both attenuation-based breast CT [Lindfors et al., 2008, Kalender et al., 2012] and tomosynthesis [Teerstra et al., 2010, Gennaro et al., 2010] have been studied. The 3D aspect provided by tomosynthesis has been shown to improve visibility and delineation of masses and to facilitate the distinction between superposition artifacts and real existing mass lesions, as well as allowing for a localization of the tumorous mass within the breast.

A relatively new approach is to combine the benefits phase-contrast imaging and tomosynthesis. Few studies have been published that explore the possibilities of phase-contrast tomosynthesis, using propagation-based [Hammonds et al., 2011, Guan et al., 2014], analyzer-based [Maksimenko et al., 2007, Sunaguchi et al., 2011] and grating-based [Li et al., 2014] phase-contrast tomosynthesis imaging.

Only recently, the first grating-based phase-contrast tomosynthesis results of a human ex-vivo breast sample have been presented[Schleede et al., 2014]. However, the images were acquired at a large-scale synchrotron source and therefore the clinical compatibility of the technique still needs to be proven. We now present images of the same specimen as investigated in [Schleede et al., 2014] measured at a Compact Light Source (CLS), a miniature synchrotron based on inverse Compton scattering [Huang and Ruth, 1998].

Here we demonstrate the feasibility of phase-contrast and dark-field tomosynthesis at a CLS. We show that the phase-contrast and the dark-field images provide complementary information on real breast tissue. Furthermore, we show that tomosynthesis is capable of revealing necrotic breast tissue which was not visible in the projection image due to glandular tissue overlap. These findings are verified with histology. We compare signal-to-noise ratio for absorption and phase-contrast images at the CLS to the previously acquired synchrotron images, showing that the superior potential of phase-contrast imaging to reveal tumor features is conserved for the lower-statistics images of the CLS.

8.3.2. Methods & Materials

Data acquisition

The CLS prototype located in Palo Alto, CA, USA, was operated at an energy of 21 keV ($\lambda_{\text{peak}} = 0.59$ Å). A Talbot grating interferometer was set up at a distance of 16 m from the interaction point. The $\pi/2$ phase grating (G1) had Ni bars with a height of 4.03 µm and a period of 5.3 µm. The analyzer grating (G2) was an Au absorption grating with a height of 55 µm and a period of 5.4 µm. The inter-grating distance was 278 mm, corresponding to the first fractional Talbot distance at 23 keV design energy. We used a photon counting Pilatus 100K detector (Dectris Ltd., Switzerland) with a pixel size of 172 µm and an active area of 195 × 487 pixel^2. The detector was equipped with a 450 µm silicon sensor. The mean visibility was 40%. The tomosynthesis scan covered an angular range of ±30°, over which 31 projections were recorded. For each projection, 5 phase steps with an exposure time of 4 seconds each were taken.

Data processing and reconstruction

From the raw data, the absorption contrast, differential phase-contrast and dark-field images were calculated using standard Fourier processing as described in [Pfeiffer et al., 2006]. To cover the full breast slice, eight projections were stitched together, resulting in a field of view of $372 \times 856\,\text{pixel}^2$. For stitching, linear ramps were used in overlapping regions and an additional linear ramp was subtracted from differential phase projections. The sinograms comprising 31 projections were reconstructed with a standard Filtered Backprojection (FBP) algorithm, using a Ram-Lak filter for attenuation and dark-field data and a Hilbert filter for the phase-contrast data [Pfeiffer et al., 2007b]. To find a plane within the tomosynthesis volume matching the histological sections, the data was manually aligned using the 3D visualization software VGStudio Max (Volume Graphics GmbH, Heidelberg, Germany).

Sample preparation and histology

The study was performed according to the Declaration of Helsinki and was approved by the local ethics committee. Written informed consent from the patient was obtained. The breast sample used for our study was a mastectomy specimen from a 66-year-old female patient containing an invasive ductal carcinoma. We used a representative sagitally oriented, 9 mm thick slice for the tomosynthesis examination. The sample was fixed in 4% neutral buffered formaldehyde solution. The sample has been used in a previous study [Schleede et al., 2014]. Histology was performed after the images had been acquired. The sample was embedded in paraffin and 5 µm thick slices were cut with a microtome and stained with hematoxylin-eosin (H&E).

CNR analysis

The contrast-to-noise-ratio (CNR) was calculated for several regions of interest (ROIs) as

$$\text{CNR} = \frac{M_1 - M_2}{\sigma_{\text{bg}}}, \tag{8.20}$$

where M_1 and M_2 denote mean tissue gray values and σ_{bg} is the noise level [Tapfer et al., 2013]. The noise level was calculated from a region outside the sample in the formalin-filled volume. A feature is lost in noise, if the CNR is less than 1. The chosen ROIs are indicated in fig. 8.6.

Mean glandular dose

The mean glandular dose (MGD) was calculated as described by [Arfelli et al., 1998] and in section 8.2.4 taking into account the absence of an outer skin layer (eq. 8.12).

For the glandular tissue attenuation coefficient $\mu_{\mathrm{en},g}$, the glandular tissue density ρ_g, and the glandular-adipose mixture attenuation coefficient μ_m we used the values calculated by [Dance et al., 1999] for 20 keV x-ray energy: $\mu_a = 0.512\,\mathrm{cm}^{-1}$, $\mu_g = 0.794\,\mathrm{cm}^{-1}$, $\mu_{\mathrm{en},g}/\rho_g = 0.509\,\mathrm{cm}^2/\mathrm{g}$ with $\rho_a = 0.93\,\mathrm{g/cm}^3$ and $\rho_g = 1.04\,\mathrm{g/cm}^3$. A 50% glandular and 50% adipose by weight breast tissue composition was assumed. With a thickness of the breast slice $t = 9$ mm, an x-ray flux $\Phi = 1.75 \cdot 10^6\,\frac{\mathrm{photons}}{\mathrm{mm^2 s}}$, and 31 projections, 5 phase steps per projection and 4 seconds exposure time per phase step, a total mean glandular dose of 141 mGy was calculated.

8.3.3. Results

Multimodal tomosynthesis images of a mastectomy specimen containing an invasive ductal carcinoma (shown in fig. 8.2 (a)) were acquired at a Compact Light Source (CLS).

Projections

Figure 8.2 (b-d) displays the multimodal projection images acquired at 0°. Important sample features are marked by numbers 1-3. Comparison of the images demonstrates the complementarity of the three imaging modalities. In the absorption image (b), adipose (dark) (1) and glandular (bright) (2) can easily be discriminated. However, the glandular region appears completely homogeneous in attenuation contrast and shows no signs of the contained tumor. The differential phase-contrast image (c) enhances the borders of glandular and adipose regions and the dark-field contrast image (d) shows strong scattering at these borders. Both the phase-contrast and the dark-field image display substructures in the glandular region where the attenuation image appears homogeneous. Tumor characteristics such as fibrous structures (3) become visible. Some leftover fringes are present in the phase-contrast and the dark-field projections; they were caused by instabilities during the experiment.

Tomosynthesis reconstruction

The central slices of the multimodal tomosynthesis reconstruction are displayed in figure 8.3. The attenuation (a), phase-contrast (b), and dark-field (c) images again demonstrate the complementarity of the three imaging modalities, while attenuation and phase image allow for a better comparison after the phase image has been integrated during the reconstruction. As for the projection image, several important sample features are visible only in the phase-contrast and the dark-field image. While a large region, which also contains the carcinoma, appears homogeneous (2) in the attenuation image (a), fibrotic structures (3) can be identified in both the phase-contrast and the dark-field image.

To evaluate the benefit of the tomosynthesis approach especially for the modality of phase-contrast, several tomosynthesis slices (b-f) are compared to the projection image (a) in fig. 8.4. The images show a 37 mm × 29 mm region of interest containing the carcinoma. The images demonstrate the ability of tomosynthesis imaging to resolve structures that are projected on top of each other if only the radiographic image is taken into account. Fibrous structures are visible in the lower right part (red arrow) of the projection image (a). With the tomosynthesis reconstruction, they can be attributed

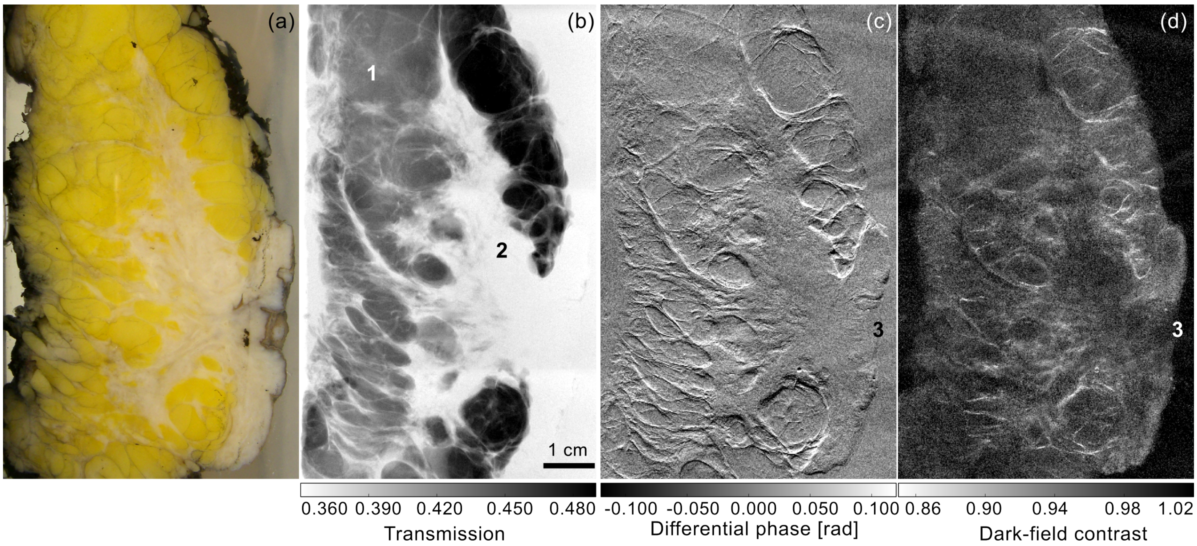

Figure 8.2.: Photograph and multimodal projection images of the breast specimen. The photograph (a) shows the mastectomy specimen. Images (b), (c), and (d) show multimodal x-ray projection images (transmission, differential phase-contrast and dark-field contrast, respectively) of the mastectomy sample resulting from stitching eight single images together. The transmission image (b) offers good contrast between fatty (dark) (1), glandular and tumorous (white) (2) tissue. However, fibrous structures (3) exist in the perimamillary region that can clearly be depicted in the phase-contrast (b) and the dark-field (d) image, but not in the transmission image. Even more importantly, the phase-contrast and dark-field images display substructures in certain regions, which appear homogeneous in the transmission image. The photograph has been published before in [Schleede et al., 2014]. This figure was previously published in [Eggl et al., 2016b].

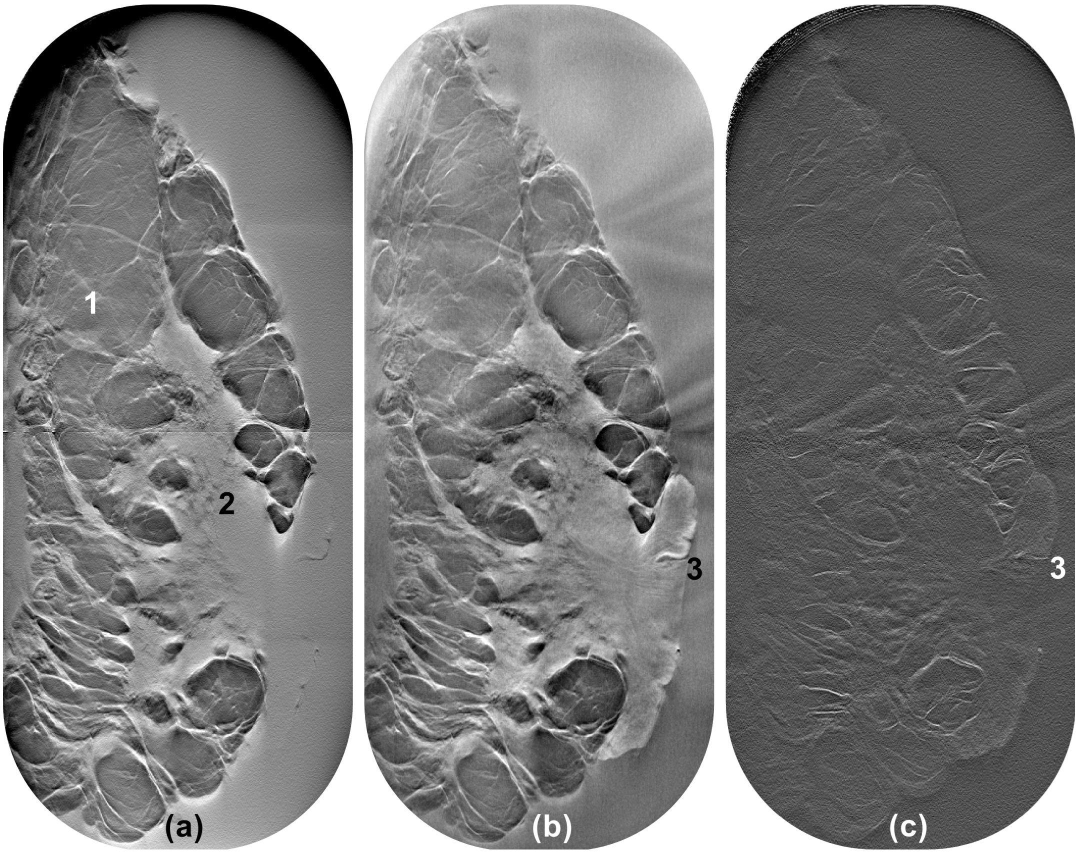

Figure 8.3.: Multimodal tomosynthesis reconstruction. The images show the central slice of the reconstructed tomosynthesis dataset from the absorption signal (a), the phase signal (b), and the dark-field signal (c). The images are scaled in order to show maximum detail visibility. This figure was previously published in [Eggl et al., 2016b].

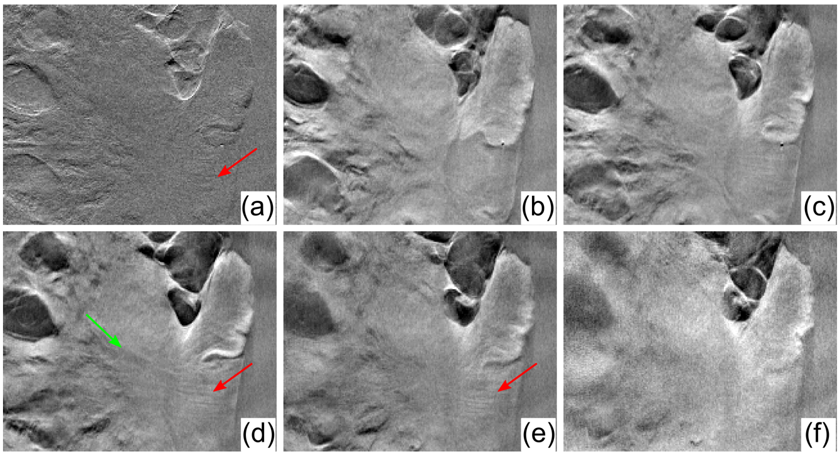

Figure 8.4.: Comparison of a differential phase-contrast projection with different phase-contrast tomosynthesis slices. The projection image (a) shows a 37×29 mm region of the breast, while images (b-f) show slices reconstructed from the tomosynthesis scan of the same region, with the slices being 2 mm apart from each other. This figure demonstrates how tomosynthesis can reveal features such as a parenchymal necrosis that are not visible in the projection image at all (green arrow, (d)) and help localize features such as fibrous structures within the specimen (red arrows, (d) and (e)). This figure was previously published in [Eggl et al., 2016b].

to a certain region within the sample, as they are only visible in images (d-e). Even more importantly, a parenchymal necrosis can only be distinguished in the tomosynthesis slice (d) (green arrow), it is invisible in the projection image and the other tomosynthesis slices.

Comparison of breast tomosynthesis results to histology

A correlation of the tomosynthesis results to histopathology is presented in figure 8.5. The multimodal tomosynthesis slices were manually reoriented to best match the histological slices (a-d). Prominent histological features are dermal fibrosis (1), parenchymal necrosis (2), a region containing tumorous tissue (3), and necrotic tissue with an adjacent tumor spread (4). All of these features exhibit greater contrast in the phase-contrast (f) and dark-field image (g) than in the attenuation image (e). Especially the parenchymal necrosis is invisible in the attenuation image due to the low contrast from soft-tissue attenuation.

Contrast-to-noise ratio analysis

A contrast-to-noise-ratio (CNR) analysis was performed for certain sample features that had been identified from histopathological results (cf. fig. 8.5) in order to quantitatively assess the benefit from phase-contrast versus conventional absorption tomosynthesis. Furthermore, we compare the CNR calculated for the CLS measurements with the benchmarking dataset acquired at a large-scale synchrotron (European Synchrotron Radiation Facility (ESRF), France) [Schleede et al., 2014]. Fig. 8.6 illustrates for both datasets (synchrotron data (a) and CLS data (b)) the regions of interest (ROIs) on which the analysis was performed: the red ROIs correspond to three different types of tissue

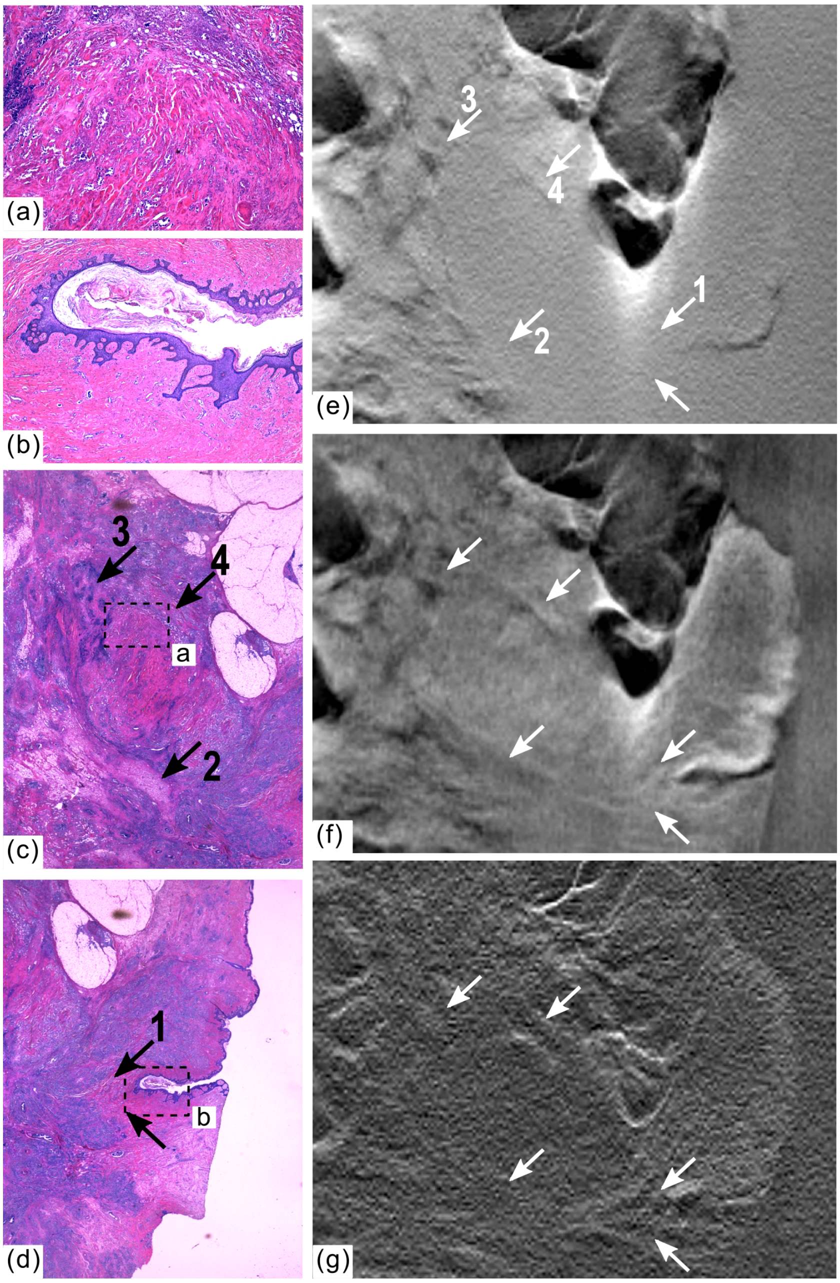

Figure 8.5.: Comparison of histology results to phase-contrast tomosynthesis imaging results. Arrows highlight important features in the images. The histological section stained with H&E (c) shows a parenchymal necrosis (2), a region containing tumorous tissue (3), and nodular necrotic tissue with an adjacent tumor extension (4). A zoom of the necrosis (4) is provided in (a). The second histological section also stained with H&E (d) contains a region with dermal fibrosis (1) of which a zoom is shown in (b). Images (e), (f), and (g) show the tomosynthesis slice in absorption contrast, phase-contrast and dark-field contrast, respectively, which has been found to best resemble the histology slices. The histology images have been published before in[Schleede et al., 2014]. This figure was previously published in [Eggl et al., 2016b] (adapted).

Setup	Tissue combination	$\mathrm{CNR}_{\mathrm{att}}$	$\mathrm{CNR}_{\mathrm{pc}}$
ESRF	fat - necrosis	5.2 ± 0.2	74 ± 3
ESRF	fat - fibrosis	5.4 ± 0.1	133 ± 3
ESRF	fibrosis - necrosis	0.209 ± 0.005	60 ± 1
CLS	fat - necrosis	9.6 ± 0.7	13 ± 1
CLS	fat - fibrosis	10.0 ± 0.7	18 ± 1
CLS	fibrosis - necrosis	0.43 ± 0.03	4.9 ± 0.3

Table 8.1.: Contrast-to-noise-ratio analysis. Shown is a comparison of the CNRs for attenuation ($\mathrm{CNR}_{\mathrm{att}}$) and phase contrast ($\mathrm{CNR}_{\mathrm{pc}}$) images for high-resolution synchrotron data (cf. [Schleede et al., 2014]) and lower statistics CLS data. This table was previously published in [Eggl et al., 2016b].

(fibrosis, necrosis, fat) and the turquoise ROI outside the sample was used to estimate the noise level. The CNR was calculated according to equation 8.20 and results are given in table 8.1.

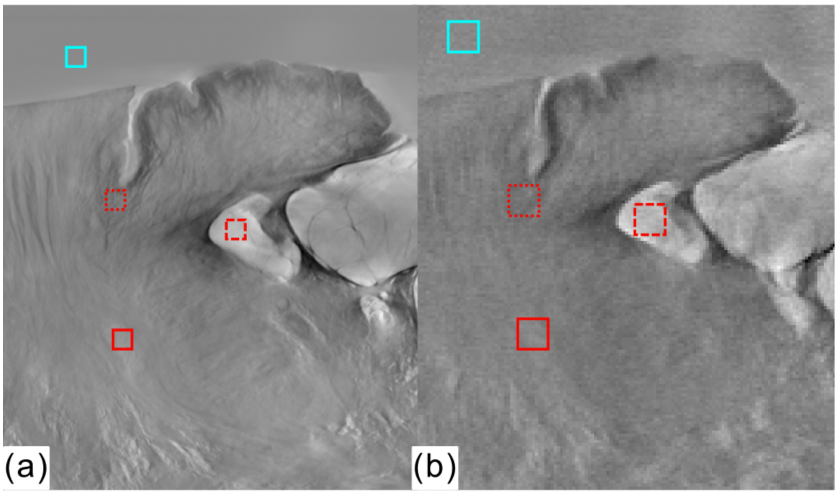

Figure 8.6.: Comparison of the CNR for different tissue types for the benchmark synchrotron data (a) and the lower-dose CLS data (b). The colored rectangles indicate the ROIs used to perform the CNR analysis. The turquoise rectangle was used to estimate the noise level from the background. The ROIs given by the red rectangles were chosen to represent the following tissue types: adipose tissue (dashed line), dermal fibrosis (dotted line), and parenchymal necrosis (solid line). The choice of the ROIs is validated with histology in figure 8.5. The rectangles cover an area of 0.81 mm^2 and 3.0 mm^2 in (a) and (b), respectively. This figure was previously published in [Eggl et al., 2016b].

All CNR values are higher for the phase-contrast than the attenuation-contrast tomosynthesis slice, demonstrating quantitatively that different tissue types can be depicted more clearly in the phase-contrast image. This is especially the case for the parenchymal necrosis with respect to to fibrosis, where the CNR is below 1 for the conventional absorption tomosynthesis images, but significantly larger than 1 for the phase images. The CNR analysis indicates that these features can only be distinguished in the phase-contrast tomosynthesis image, while they are lost in image noise in the attenuation-contrast image.

Overall, the benefit from the phase images is not as large for the CLS measurements, which were acquired with significantly lower dose and larger pixel sizes, as for the ESRF measurements. However, a direct comparison is not possible due to the differences in spatial resolution and experimental setup.

8.3.4. Discussion

We presented grating-based phase-contrast and dark-field tomosynthesis measurements of a human ex-vivo breast slice containing an invasive ductal carcinoma, for the first time acquired at a Compact Light Source (CLS) based on inverse Compton scattering. Our results imply that multimodal tomosynthesis breast imaging is a promising technique to overcome the two main limitations currently present for absorption-based, radiographic mammography: limited soft-tissue contrast and compromised visibility caused by superposition artifacts.

Concerning the limited soft-tissue contrast, the complementarity of the three image modalities acquired with grating-based x-ray imaging significantly improves the diagnostic value of the images. While the absorption image allows for an easy discrimination between glandular and adipose tissue, the phase-contrast and the dark-field image make small substructures associated with cancerous tissue visible: as validated with histopathology and a CNR analysis, we show that dermal fibrosis and parenchymal necrosis are depicted significantly better in the phase-contrast than the absorption image. The studied sample did not contain microcalcifications, however, previous studies [Stampanoni et al., 2011, Anton et al., 2013] demonstrated superior detection of microcalcifications in the dark-field image compared to the absorption image. As the three image modalities are supplied mutually in grating-based x-ray imaging, the benefits from each modality can be combined to provide an overall improved detectability of breast tumors.

Moreover, we showed the benefits arising from the possibility of in-depth analysis offered by tomosynthesis reconstruction. While the existence of fibrotic structures was already discernible in the phase-contrast projection, the tomosynthesis then allows allocating the feature within the studied volume, which is important for the planning of biopsies or surgeries. In the case of a parenchymal necrosis present in the studied specimen, the need for depth resolution in breast cancer becomes even more obvious: while the feature was obscured by tissue overlap in the projection image, it can be depicted in one of the tomosynthesis slices.

Compared to the synchrotron benchmarking results of the same breast specimen presented by [Schleede et al., 2014], the results in this study acquired at a compact synchrotron source based on inverse Compton scattering show more noise than the large-scale synchrotron results. This is also reflected in the comparison of the contrast-to-noise ratios, which show a smaller benefit from phase-contrast over absorption-contrast images for the CLS images. The main reason for this is the choice of an acquisition scheme with lower dose and therefore also a larger pixel size and lower statistics, intended as a first step towards dose-compatible phase-contrast tomosynthesis measurements. Therefore, a direct comparison of values cannot be made. Importantly, all CNRs for phase-contrast images are well above 1, indicating that diagnostic features are preserved also for this lower-dose measurement compared to synchrotron results.

The mean glandular dose applied in the multimodal tomosynthesis examination was calculated as ~ 141 mGy and thus was much larger than the dose applied in conventional mammography (3 mGy for two-view mammography [NCRP, 2004]). It is important to note that this value is not directly comparable to clinically applied doses, especially due to the absence of an outer skin layer and the very thin breast slice. The skin layer and the adipose parts of the breast act as radiation shielding layers to the radiation-sensitive tissue. In addition, we believe that potential improvements concerning acquisition and reconstruction of the data can bring the dose to a dose level compatible with clinical imaging. Regarding the used hardware, the applied dose could significantly be reduced by using a more efficient detector (increase in quantum efficiency from 32% to >90% by using a 1000 µm CdTe sensor instead of 450 µm Si), thinner grating wafers (250 µm instead of 500 µm) and placing the sample behind G1. These currently available technologies would reduce the dose by over 80%. When in addition the number of phase steps is decreased from 5 to 4, the applied dose would be brought down to 21 mGy.

For a reduction in dose and an improved image quality, also data processing and reconstruction routines should be considered and investigated in the future. Even though FBP reconstruction algorithms are commonly used for tomosynthesis reconstruction [Sechopoulos, 2013, Li et al., 2014], the development of dedicated tomosynthesis filter designs, or even more promising, of iterative reconstruction algorithms specifically for phase-contrast tomosynthesis could significantly improve the reconstruction.

Overall, the presented results demonstrate the benefits of multimodal tomosynthesis imaging over absorption-based mammography and also show the suitability of Compact Light Sources for a pre-clinical investigation of the technique. These findings encourage the investigation of dose-compatible acquisition and reconstruction schemes in future studies, as well as a study with a larger number of mastectomy samples with different cancer types. We are confident that further developments with respect to hardware, combined with advanced post-processing algorithms and dedicated reconstruction algorithms have the potential to further reduce the dose to compatible levels.

8.4. Dose-compatible mammography at the MuCLS

The measurements presented in this section were acquired at the MuCLS and have been submitted as [Eggl et al., 2017a].

8.4.1. Motivation

As demonstrated in the clinical study performed at the Elettra synchrotron [Longo et al., 2014], mammography with synchrotron radiation is capable of providing enhanced diagnostic content over standard clinical mammography. A compact synchrotron like the MuCLS can offer a quasi-monochromatic beam that is available in close vicinity to clinical settings, to offer a second level examination in case of inconclusive diagnosis after mammography and ultrasound.

We present both absorption-only and grating-based multimodal images of freshly dissected cancerous mastectomy specimens acquired at the MuCLS at lower or equal dose

Specimen	I	II	II	IV	Phantom
	Sample position for ex-vivo mammography				
Orientation	AP	AP	AP	CC	-
Compressed thickness [cm]	4.0	6.0	4.5	6.0	4.5
	Clinical acquisition parameters				
X-ray tube settings	27 kVp (W/Rh) 72 mAs	35 kVp (W/Ag) 92 mAs	30 kVp (W/Rh) 100 mAs	39 kVp (W/Ag) 23 mAs	28 kVp (W/Rh) 200 mAs
MGD civAC-Mx [mGy]	1.3	3.8	2.9	1.3	-
MGD cevAC-Mx [mGy]	0.9	2.2	1.4	1.1	2.0
	Acquisition parameters MuCLS				
Energy	25 keV	25 keV	25 keV	25 keV	25 keV
MGD mAC-Mx [mGy]	-	-	0.3	0.4	1.0-2.0
MGD mgb-Mx [mGy]	0.8	0.9	0.9	-	0.7-1.8
Stitching	4 × 4	5 × 5	5 × 5	4 × 4	2 × 2

Table 8.2.: Parameters and information for each specimen.

compared to state-of-the-art clinical images. Furthermore, a dose study and analysis of the contrast-to-noise ratio on a well defined sample, a mammographic accreditation phantom, is conducted. In addition, we present a comparison of the spatial resolution for experimental and clinical images. We believe that compact synchrotron sources like the MuCLS have great potential to bring benefits to clinical imaging, in particular for mammography, but also other fields, like coronary angiography [Eggl et al., 2017b], could profit from the monochromatic, tunable x-ray beam.

8.4.2. Methods & Materials

Table 8.2 summarizes the applied mean glandular doses for in-vivo and ex-vivo clinical mammography as well as monochromatic mammography and gives an overview of the acquisition parameters for each sample. The mean glandular dose (MGD) for the clinical images was provided automatically by the mammography station and is calculated based on the x-ray tube settings and the compressed sample thickness.

The MGD value for the clinical ex-vivo absorption-contrast mammography (cevAC-Mx) images was corrected when an incorrect sample thickness was assumed due to the shape of the sample holder. A correction factor was calculated based on the half value layer of Aluminum for the respective acquisition settings and the assumed and correct breast thickness, from tabulated values by [Dance, 1990, Dance et al., 2000].

Study protocol

The study was conducted in accordance with the Declaration of Helsinki and approved by the local ethics committee. The local ethics committee (Ethikkommission of the Ludwig-Maximilians-Universität, Munich, project number 24010, date of permission 26/08/2010,

Patient	Histological diagnosis	Max. tumor diameter
I	multicentric lobular invasive carcinoma, G2, and lobular carcinoma in situ	51 mm
II	recurrent, invasive carcinoma of no specific type (NST, formerly invasive ductal), G3	47 mm
III	invasive carcinoma of no specific type (NST, formerly invasive ductal), G2, and adjacent intraductal carcinoma (DCIS)	5 mm
IV	bifocal invasive carcinoma of no specific type (NST, formerly invasive ductal), G1, and intraductal carcinoma (DCIS)	25 mm

Table 8.3.: Tumor characteristics of patients I - IV as verified by histopathology.

amendment 30/05/2012) approved the study. Patients gave their written consent before participation after adequate explanation of the study protocol. Inclusion criteria were a histologically proven breast cancer in preoperative core biopsy with a recommendation for mastectomy according to gynecological guidelines or the patient's wish for mastectomy, as well as completed preoperative conventional breast diagnostics.

Preoperative diagnostics

Preoperative diagnostics included clinical breast examination, standard two-view digital mammography in cranio-caudal (CC) and mediolateral-oblique (MLO) projections (Hologic Selenia Dimensions, Bedford, USA) using a standard breast compression paddle and high resolution B-mode ultrasound (standard linear transducer 13.5 MHz, Siemens Acuson Antares, Siemens Healthcare, Germany). Additional MRI was performed in three cases by using a dedicated sensitivity-encoding-enabled bilateral breast coil with a 1.5- or 3.0-Tesla system.

Ex-vivo mammography

The mastectomy samples were intraoperatively marked with surgical sutures for 3D orientation. The samples were fixed within a metal-framed sample holder to afford adequate breast compression. The position was cranio-caudal, or anteroposterior in case a cranio-caudal position was impossible due to the shape of the dissected specimen. A digital ex-vivo mammography image was acquired at a clinical mammography unit (Hologic Selenia Dimensions) with a pixel size of 70×70 µm^2.

Mammography at the MuCLS

Maintaining the position of the breast specimen within the sample holder in order to ensure comparability, monochromatic mammography images were acquired at the MuCLS. A Talbot interferometer was set up approximately 16 m from the interaction point

of the MuCLS, as shown schematically in figure 4.3. The inter-grating distance was ~ 25 cm, the grating periods were $p_1 = 4.9$ µm for the phase grating (G1) and $p_2 = 5.0$ µm for the analyzer grating (G2) (for more information, see chapter 4.1.2. The signals were retrieved from phase stepping as described in [Pfeiffer et al., 2008] and in chapter 2.2. Conventional absorption-contrast images were acquired without the grating interferometer. A Dexela 1512 flatpanel detector (PerkinElmer Inc., USA) with a Gd_2O_2S scintillator was used, yielding an effective pixel size of 71×71 µm^2.
Stitching of several images was required to cover the whole samples, using linear ramps to blend the overlapping areas. Table 8.2 summarizes the acquisition parameters for each scan. The MuCLS x-ray energy was tuned to 25 keV for all samples. The interferometer visibility was approximately 45%-50% for all measurements.

Dose calculation

The MGD automatically registered by the clinical mammography unit is given in table 8.2 for each sample.
For the monochromatic mammography performed at the MuCLS, the MGD was calculated using monoenergetic normalized glandular dose coefficients DgN(E) (with E the x-ray energy) as tabulated by Boone et al. [Boone, 2002], taking into account the MuCLS spectrum [Eggl et al., 2016a] and summing over all energy bins E:

$$\mathrm{MGD} = \sum_E K(E)[\mathrm{mGy}] \cdot 0.114 \left[\frac{\mathrm{R}}{\mathrm{mGy}}\right] \cdot (\mathrm{DgN}(E) \left[\frac{\mathrm{mGy}}{\mathrm{R}}\right]. \tag{8.21}$$

The formula for the MGD was adapted from [Boone, 2002] to be used with air kerma K instead of the older unit exposure, as the fitted equation for exposure given by [Boone, 2002] is incorrect [Nosratieh et al., 2015]. The DgN(E) values were selected according to the compressed thickness of the dissected breasts, and assuming a 50%/50% distribution of glandular and adipose tissue. The air kerma for the MuCLS beam K per energy bin E can be calculated for known photon flux $\Phi(E)$ at the sample position and x-ray spectrum [Schlegel and Bille, 1999]:

$$K(E) = E \cdot \Phi(E) \cdot (\mu_{\mathrm{en}}/\rho)_{\mathrm{air}}(E), \tag{8.22}$$

where $(\mu_{\mathrm{en}}/\rho)_{\mathrm{air}}(E)$ is the mass energy attenuation coefficient of air [Buhr et al., 2012]. The photon flux was calculated from a single photon counting Pilatus 200K detector (Dectris Ltd., Switzerland), taking into account x-ray spectrum and the efficiency of the Si sensor of the detector [Donath et al., 2013]. The calculation of the air kerma was validated using a soft x-ray ionization chamber (Model 34013, PTW Freiburg GmbH, Germany) and values agreed within the measurement uncertainties of ±10%. A scintillation counter was calibrated to calculated air kerma prior to each sample measurement and the scintillation counts were logged for each measurement frame, thus yielding an exact measure of air kerma for each scan. A more elaborate description of the dose calculation is given in chapter 8.2.

mAC-Mx	monochromatic absorption-contrast mammography
mgbAC-Mx	monochromatic grating-based absorption-contrast mammography
mgbDPC-Mx	monochromatic grating-based differential phase-contrast mammography
mgbDFC-Mx	monochromatic grating-based dark-field-contrast mammography
cevAC-Mx	clinical ex-vivo absorption-contrast mammography
civAC-Mx	clinical in-vivo absorption-contrast mammography

Table 8.4.: Contrast modality abbreviations.

Image Analysis

The CNR was calculated according to the definition

$$\mathrm{CNR} = \frac{\overline{S_1} - \overline{S_2}}{\sigma_{\mathrm{BG}}}, \tag{8.23}$$

where $\overline{S_1}$ and $\overline{S_2}$ are the average signals in two regions of interest (ROIs) which should be compared, and σ_{BG} is the standard deviation within a larger ROI located in the background region.

The resolution of the images was determined by analyzing their power spectra [Modregger et al., 2007]. The images were Fourier transformed and a Gaussian filter was applied on the squared norm. The resolution of the images is then given by the maximal spatial frequency where the spectral power of the signal equals twice the spectral power of the noise baseline, taking into account the effective pixel size of clinical and experimental images.

8.4.3. Diagnostic benefits for freshly dissected mastectomy samples

Four freshly dissected mastectomy specimens were investigated with clinical ex-vivo absorption-contrast mammography (cevAC-Mx) and both conventional absorption and grating-based multimodal monochromatic experimental mammography. The tumor characteristics for each sample are summarized in table 8.3. The applied mean glandular dose (MGD) is given in table 8.2 for each sample and imaging modality. Abbreviations used for the different contrast modalities in the following are explained in table 8.4.

Improved delineation of tumor lesions in phase-contrast image

Patient I presented with a palpable mass in the right breast and skin retraction. Conventional clinical in-vivo absorption-contrast mammography (civAC-Mx) showed an asymmetry in the respective region (figure 8.7(e)). Ultrasound revealed inhomogeneities and several hypoechogenic lesions. Additional dynamic MRI showed an extensive infiltration with tumor branches extending close to the pectoralis muscle. Histopathology of the mastectomy specimen revealed a multicentric, invasive lobular carcinoma (G2) with extensive manifestations of a lobular carcinoma in situ.

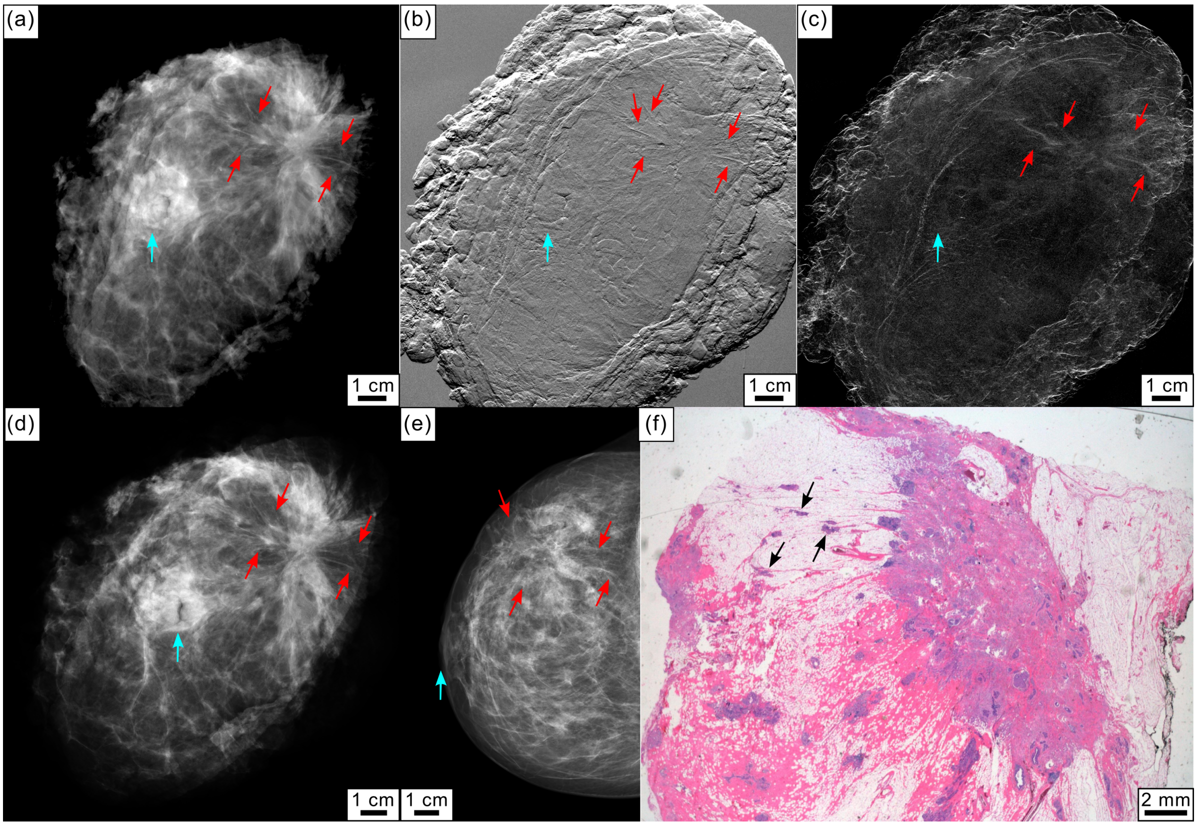

Figure 8.7.: Patient I (a) Monochromatic grating-based absorption-contrast (mgbAC-Mx), (b) differential phase-contrast (mgbDPC-Mx), and (c) dark-field contrast (mgbDFC-Mx) mammography. (d) Clinical ex-vivo absorption-contrast mammography (cevAC-Mx) in anteroposterior position. (e) Clinical in-vivo absorption-contrast mammography (civAC-Mx) of patient I in craniocaudal position. Tumorous lesions are indicated by red arrows, the mamilla is indicated by a light blue arrow. All images were scaled for maximum detail visibility. (f) Histopathology of the mastectomy sample showing the existence of tumorous lesions (black arrows).

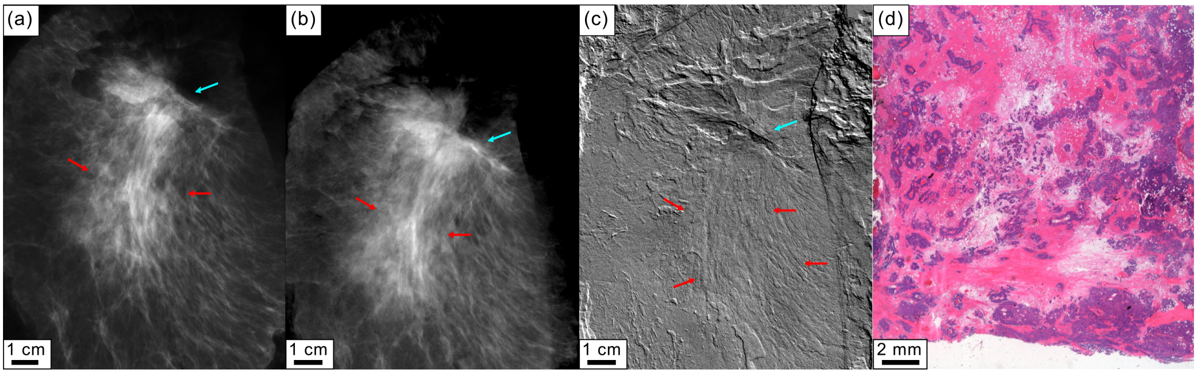

Figure 8.8.: Patient II (a) Clinical ex-vivo absorption-contrast mammography (cevAC-Mx). (b) Monochromatic grating-based absorption-contrast (mgbAC-Mx) and (c) monochromatic grating-based differential phase-contrast (mgbDPC-Mx) mammography. Red arrows indicate the tumorous region with spiculae visible especially in the mgbDPC-Mx (c). The cyan arrow points to the mamilla. All images were scaled for maximum detail visibility. (d) Histopathology of the mastectomy sample showing the scar tissue (pink) being infiltrated by tumor cells (purple).

Figures 8.7 (a)-(d) show monochromatic grating-based absorption-contrast mammography (mgbAC-Mx), differential phase-contrast mgbDPC-Mx, dark-field contrast mgbDFC-Mx and ex-vivo clinical absorption-contrast cevAC-Mx mammography images of the mastectomy specimen from patient I, measured in anteroposterior (AP) orientation. The mgbAC-Mx (a) provides improved delineation of tumor lesions (marked by red arrows) over the cevAC-Mx (d) and civAC-Mx (e) images. The mgbDPC-Mx (b) clearly shows fine tumor branches originating from the tumor and perfusing the surrounding tissue to both sides of the carcinoma. To a reduced extent, the tumor branches are also visible in mgbDFC-Mx (c). The histopathologic analysis in hematoxylin-eosin (H&E) staining proved the existence of the tumor spiculae originating from the main tumor (black arrows, (e)).

Patient II had a history of breast cancer. While aftercare mammography and ultrasound showed a slight, ill-defined density in the scar area but no circumscribed lesion, dynamic MRI of the right breast revealed an extensive carcinoma. Histology of the mastectomy sample showed nodular infiltrations of a poorly differentiated (G3) invasive breast cancer of no special type (NST).

Figures 8.8 (a)-(c) show cevAC-Mx, mgbAC-Mx, and mgbDPC-Mx measured in an AP orientation of the specimen. While the differentiation of tumor and scar tissue is difficult in the absorption-contrast images, the mgbDPC-Mx (c) depicts the tumor spiculae (red arrows) as verified by histopathology (d). The H&E stained histology image shows the infiltration of the scar tissue (pink) with tumorous cells (purple).

Detection of microcalcifications at reduced dose

In **Patient III**, civAC-Mx revealed a cluster of microcalcifications in the retromamillary area. Ultrasound found a hypoechoic lesion and MRI showed a corresponding suspicious mass with early contrast enhancement. Histology of the mastectomy sample revealed an invasive carcinoma of no special type (NST), G2, and an adjacent ductal carcinoma in situ (DCIS), with comedonecrosis and extensive microcalcifications.

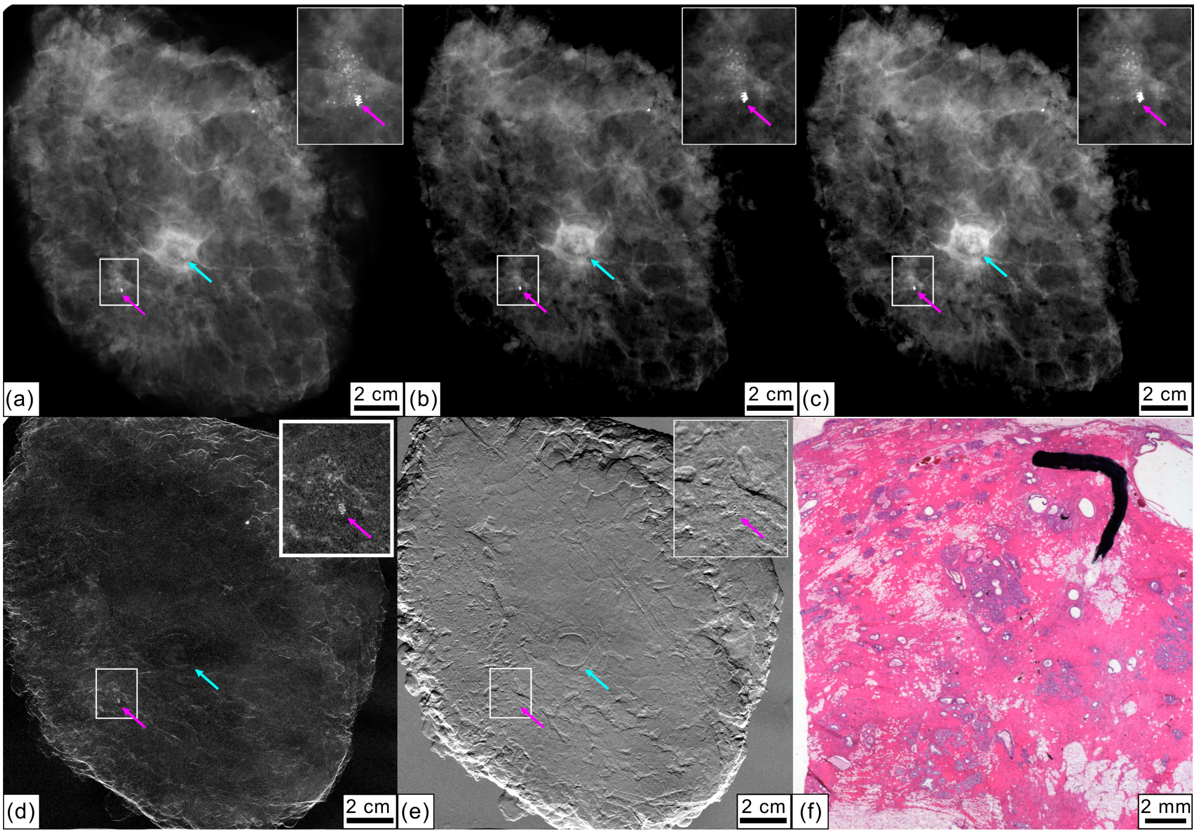

Figure 8.9.: Patient III (a) Clinical ex-vivo absorption-contrast mammography (cevAC-Mx). (b) Monochromatic absorption-contrast mammography (mAC-Mx). (c) Monochromatic grating-based absorption-contrast mammography (mgbAC-Mx), (d) dark-field mammography (mgbDFC-Mx) and (e) differential phase-contrast mammography (mgbDPC-Mx). Insets show a calcification cluster that had previously been marked. The clip marker is highlighted with a magenta arrow, a light blue arrow indicates the mamilla. All images were scaled for maximum detail visibility. (f) Histopathology of the mastectomy sample showing microcalcifications.

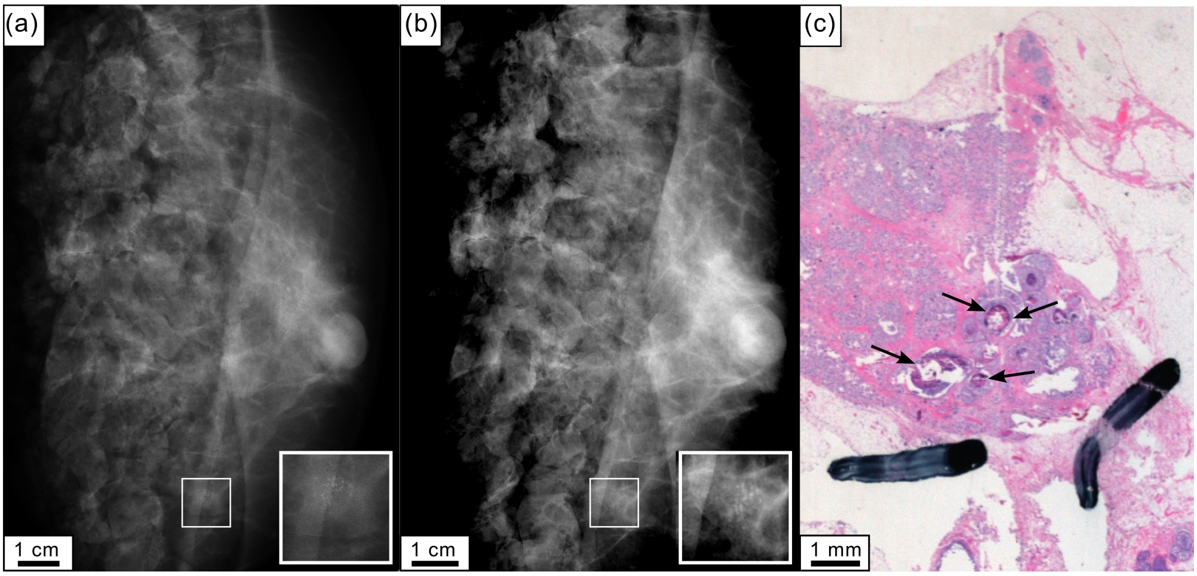

Figure 8.10.: Patient IV (a) Clinical mammography (cevAC-Mx). (b) Monochromatic absorption-contrast mammography (mAC-Mx). Insets show a calcification cluster. All images were scaled for maximum detail visibility. (c) Histopathology of the mastectomy specimen showing extensive microcalcifications (black arrows).

Figures 8.9 (a)-(e) display cevAC-Mx, mAC-Mx, mgbAC-Mx, mgbDPC-Mx and mgbDFC-Mx measured in AP orientation. A calcification cluster that had preoperatively been clip-marked (magenta arrows) is shown in magnification in the small insets. The mAC-Mx image (b) equally shows the extent of the microcalcification cluster compared to cevAC-Mx (a), at significantly lower dose (0.3 vs. 1.4 mGy). The existence of the microcalcification cluster was verified by histopathology (f). The invasive carcinoma revealed by histopathology could not clearly be identified by any of the imaging modalities, including civAC-Mx.

Patient IV was diagnosed with three microcalcification clusters in civAC-Mx, two of which were partially extracted in a biopsy. Histology of the mastectomy sample revealed a bifocal, well differentiated (G1) breast cancer of no special type (NST), with an extensive ductal carcinoma in situ (DCIS) and microcalcifications.

Figures 8.10 (a) and (b) present cevAC-Mx and mAC-Mx measured in a cranio-caudal (CC) position. Both images reveal a microcalcification cluster to equal extent, with significantly lower dose for the mAC-Mx (0.4 vs. 1.1 mGy). The histopathologic work-up (c) confirms the existence of microcalcifications. The bifocal carcinoma revealed by histopathology is obscured by the surgical margins of the mastectomy sample in images (a) and (b).

Resolution

A power spectrum analysis was performed for all absorption and dark-field images cevAC-Mx, mAC-Mx, mgbAC-Mx and mgbDFC-Mx (not for mgbDPC-Mx due to the differential nature of the signal) in order to compare their resolution [Modregger et al., 2007]. As illustrated in table 8.5, the resolution is mainly in the range between 3 and 4 linepairs (lp) per mm. The analysis shows that a higher resolution was achieved in the

Sample	cevAC-Mx [LP/mm]	mAC-Mx [LP/mm]	mgbAC-Mx [LP/mm]	mgbDFC-Mx [LP/mm]
Phantom	3.70 ± 0.26	3.81 ± 0.11	3.55 ± 0.26	3.90 ± 0.74
I	2.52 ± 0.68	2.77 ± 0.41	3.03 ± 0.77	3.87 ± 0.70
II	1.42 ± 0.17	-	3.44 ± 0.16	5.30 ± 0.53
III	3.23 ± 0.68	3.37 ± 0.61	3.49 ± 0.07	3.56 ± 0.61
VI	2.94 ± 1.43	3.49 ± 0.66	-	-

Table 8.5.: Resolution calculated from power spectrum analysis.

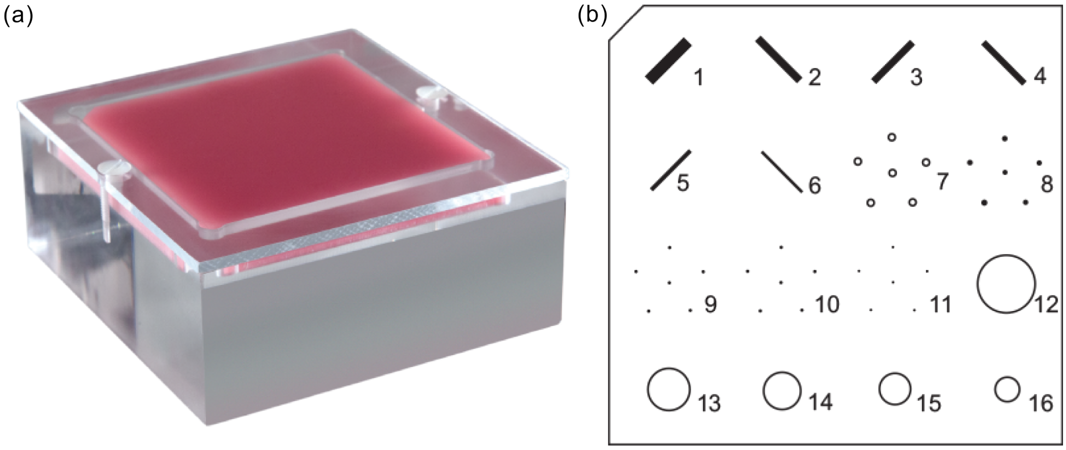

Figure 8.11.: The mammographic accreditation phantom (Gammex, Model 156) used for the dose study. (a) Photograph of the phantom. The phantom has a thickness of 4.5 cm, mimicing a compressed breast thickness of 4.2 cm. (b) Scheme displaying the distribution of the test objects. Six nylon fibers (fibrils), five groups of microcalcifications and five tumor masses are distributed across the phantom. Image source: `https://www.sunnuclear.com/solutions/diagnostic/mammography/156phantom`, accessed 2017/05/05.

mAC-, mgbAC- and mgbDFC-MX than in the cevAC-Mx for all investigated samples, at lower or equal dose of the monochromatic images.

8.4.4. Dose-study with a mammographic accreditation phantom

In order to quantitatively compare monochromatic MuCLS mammography with a clinical mammography unit, a contrast-to-noise-ratio (CNR) analysis was performed for a mammographic accreditation phantom (Gammex, Model 156). The phantom and the distribution of the test objects are pictured in figures 8.11 (a) and (b), respectively. The image of the accreditation phantom acquired by the conventional mammography system by automated exposure control is compared to both monochromatic absorption-contrast images and also grating-based trimodal images acquired at different mean glandular doses. A CNR analysis for different test objects is presented in table 8.6. A selection of images is shown in figure 8.12.

It is clearly visible that the absorption images cevAC-Mx (fig. 8.12 (a)), mAC-Mx (fig. 8.12 (b,c)), and mgbAC-Mx (fig. 8.12 (d)) fulfill the standard criteria of clinical

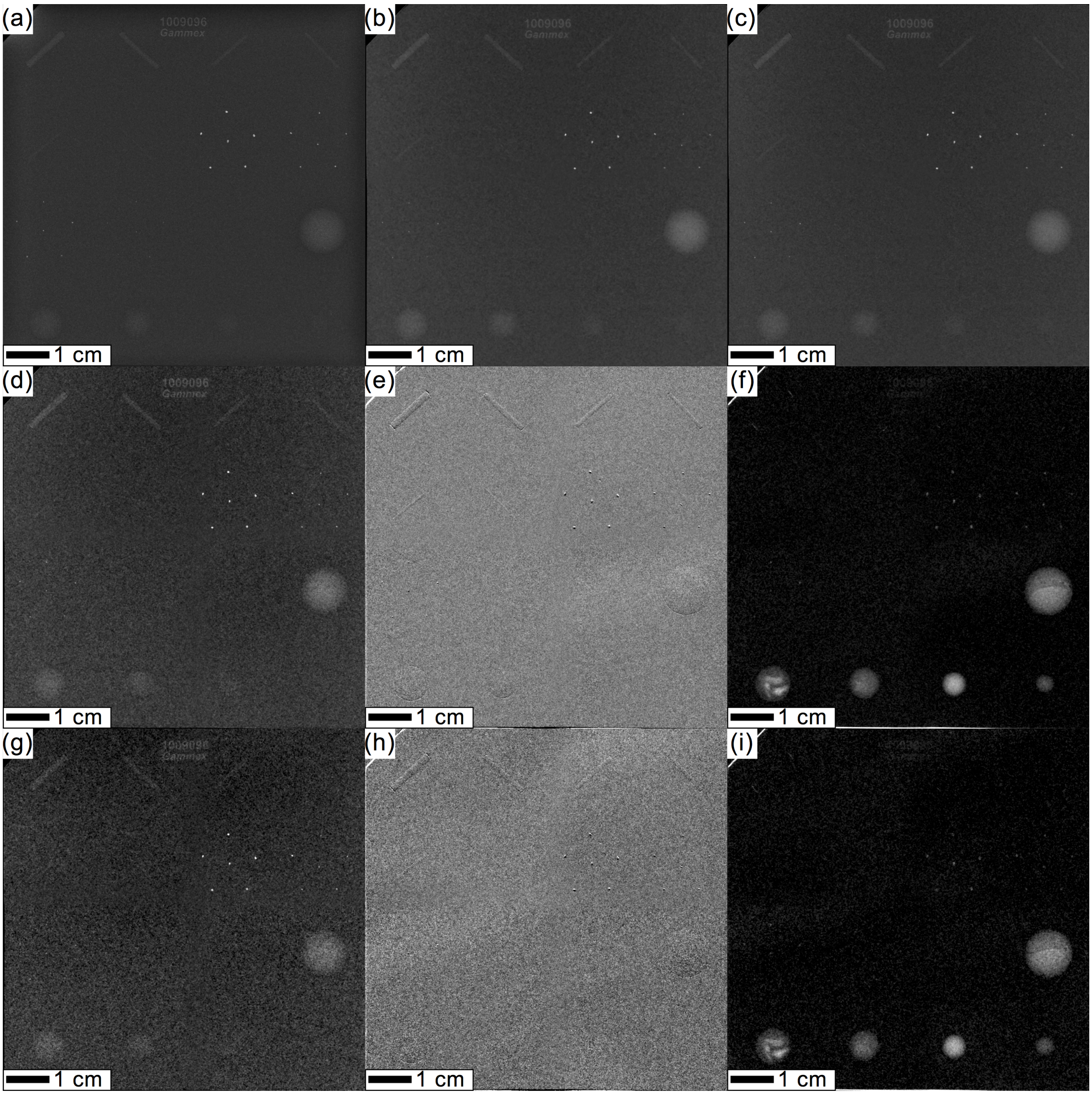

Figure 8.12.: Dose study for the mammographic accreditation phantom. ACR guidelines require for a minimum of four fibrils, three groups of microcalcifications, and three tumor masses to be resolved. (a) Clinical mammography cevAC-Mx acquired at 2.0 mGy mean glandular dose (MGD). (b-c) Monochromatic absorption-contrast mammography (mAC-Mx) acquired at 2.0 mGy MGD (b) and 1.6 mGy MGD (c). (d-f) Monochromatic grating-based absorption-contrast (mbgAC-Mx) (d), differential phase-contrast (mgbDPC-Mx) (e) and dark-field-contrast (mgbDFC-Mx) (f) mammography acquired at 1.8 mGy MGD. (g-i) mgbAC-Mx (g), mgbDPC-Mx (h), mgbDFC-Mx (i) acquired at 0.7 mGy MGD. All images were scaled for maximum detail visibility.

modality	MGD [mGy]	fibers 1	fibers 4	calcifications 1	calcifications 3	tumor masses 1	tumor masses 5
cevAC-Mx	2.0	2.51	1.99	36.84	13.89	5.92	0.53
mAC-Mx	1.0	3.16	0.11	30.86	11.94	8.64	1.50
mAC-Mx	1.6	3.51	1.61	38.47	15.60	10.70	2.73
mAC-Mx	2.0	4.71	1.39	44.11	16.85	12.19	2.67
mgbAC-Mx	1.8	4.46	0.15	25.32	13.25	7.14	0.89
mgbDFC-Mx	1.8	0.65	0.16	6.50	10.42	15.00	9.59
mgbAC-Mx	0.7	2.17	0.09	13.87	5.93	2.73	0.30
mgbDFC-Mx	0.7	1.25	2.55	3.59	7.77	11.84	5.58

Table 8.6.: CNR calculated for dose study with mammographic accreditation phantom.

image quality set by the ACR [Hendrick et al., 1999], which require a minimum of 4 fibrils, 3 groups of microcalcifications, and 3 tumor masses to be resolved. A quantitative analysis (tab. 8.6) demonstrates that the CNR in the mAC-Mx (b) image considerably exceeds the CNR in the cevAC-Mx (a) image at equal dose. The mAC-Mx (c) still slightly outperforms the cevAC-Mx image (a) at 20% reduced dose.

For the grating-based images, the mgbAC-Mx (fig. 8.12 (d)) image at slightly lower dose than the cevAC-Mx (a) provides a comparable CNR. Especially for the small tumor masses, the mgbDFC-Mx (f) CNR by far outperforms the clinical image (a), where the smallest tumor mass cannot be distinguished from the background (CNR<1). This is still the case when the dose is reduced to 35% of the clinical value (i). In addition, the mgbDPC-Mx (e), for which a quantitative analysis is not possible due to the differential nature of the signal, allows to depict all six tumor fibrils. The mgbDFC-Mx (f,i) reveals additional structures within the two largest tumor masses of the accreditation phantom.

Importantly, while the low-dose mgbAC-Mx (g) does not fulfill the ACR criteria, the combination with mgbDPC-Mx (h) and mgbDFC-Mx (i) meets or, in the case of the tumor masses, even exceeds the ACR criteria.

8.4.5. Discussion

We presented conventional absorption-contrast as well as grating-based multimodal mammography images of freshly dissected mastectomy samples acquired with a monochromatic x-ray beam at a compact synchrotron source. Comparison with clinical ex-vivo mammography images showed equal diagnostic quality at lower dose or superior diagnostic quality at equal dose of the monochromatic images. Tumorous lesions could be identified significantly better in the phase-contrast modality as verified by histopathology (Patients I, II). Microcalcification clusters were revealed to an equal extent as in the clinical mammography image, at a significantly reduced dose for the monochromatic images (Patients III, IV).

A power spectrum analysis showed that the monochromatic absorption-contrast and dark-field-contrast images (mAC-Mx, mgbAC-Mx, mgbDFC-Mx) could achieve better resolution than the clinical image (cevAC-Mx) at lower or equal dose, proving that the small source size of the MuCLS is beneficial for the resolution.

A dose study conducted with a mammographic accreditation phantom showed a superior CNR of various test objects at equal mean glandular dose and a higher or comparable CNR at 20% reduced dose for the monochromatic mammography images compared to the clinical one. The grating-based phase-contrast and dark-field image yield an enhanced diagnostic content for the fibers and tumor masses, respectively. The dark-field image outperforms the clinical image for the tumor masses even at a 65% lower dose.

The presented results demonstrate that mammography at a compact synchrotron source like the MuCLS has great potential to improve the diagnostic quality of mammography. The compact size and limited financial requirements compared to large-scale synchrotron source allow for envisioning the installation at hospitals in the future. Thus, the implementation of a compact synchrotron could enable a second-level examination in the case of inconclusive diagnosis (as performed at the SYRMEP beamline [Castelli et al., 2011, Longo et al., 2014, Olivo and Castelli, 2014]), in addition with the possibility to choose between conventional, but monochromatic absorption imaging and grating-based trimodal imaging.

The main limitation of our study was the different orientation (anteroposterior instead of cranio-caudal or mediolateral-oblique) for three of the four specimens compared to clinical in-vivo mammography. The different orientation was necessary in order to avoid artifacts originating from surgical resection margins. Therefore, the ex-vivo images are not fully comparable to in-vivo images concerning orientation and sample thickness.

The limited sizes of beam gratings required scanning of the samples, resulting in an increased scan time incompatible with clinical applications. Only recently, the feasibility of manufacturing stitched gratings in order to cover larger fields of view was demonstrated [Schröter et al., 2017]. The field of compact synchrotron sources is constantly developing [Eggl et al., 2016a, Variola, 2011, Kuroda et al., 2011] and considerable improvements and further developments of the technology with regard to increased stability, flux and beam size can be expected. In addition, other potential clinical applications will profit especially from an extension of the energy range.

Concerning the mean glandular dose applied in mammography, our results show that dose-compatible grating-based mammography is feasible at a monochromatic source. The used setup even has the potential for further dose reduction by thinning the grating wafers from the currently used 500 µm thick Si substrate down to 200 µm and by modifying the setup to allow positioning of the sample to behind the phase grating.

In conclusion, we believe that monochromatic x-rays provided by compact synchrotron sources like the MuCLS, the first commercially installed source of this type, can enable significant improvements in diagnostic x-ray imaging. Mammography could benefit from enhanced diagnostic image content and improved resolution at a reduced dose. In addition, as the x-ray energy of these sources is tunable, also other applications, like for instance coronary angiography [Eggl et al., 2017b], could benefit from the implementation of compact synchrotron sources in a clinical setting.

8.5. Summary and Conclusion

Two new approaches for mammographic imaging that can benefit from the x-ray beam properties of a compact synchrotron were investigated.

The feasibility of grating-based phase-contrast and dark-field tomosynthesis was studied. Tumor characteristics that were obscured in the projection images could be identified in the reconstructed slices, as verified by histopathology. In addition, a CNR analysis demonstrated quantitatively that the phase-contrast images provide a superior CNR to distinguish different tissue types. However, this feasibility study was performed with a mean glandular dose far above values recommended in radiological guidelines and a dose reduction to clinical compatible levels appears challenging for a combination of tomosynthesis and grating-based multimodal imaging.

The second investigated topic was the dose-compatibility of grating-based multimodal mammography with the monochromatic MuCLS beam, and a possible dose reduction at equal diagnostic quality for monochromatic absorption-contrast imaging. Having measured four freshly dissected breast specimens, we demonstrated increased diagnostic content for monochromatic grating-based phase-contrast images at slightly reduced dose compared to clinical images. The extent of microcalcification clusters could be identified equally at significantly reduced dose in monochromatic absorption-contrast mammography. A quantitative analysis of the CNR showed that monochromatic absorption-contrast mammography and grating-based dark-field mammography outperform the clinical image at equal or reduced dose.

These promising results highlight the potential of compact synchrotron sources like the MuCLS to serve as a second-level clinical examination, providing increased diagnostic quality and helping to clarify diagnoses in case of inconclusive clinical mammography results to possibly avoid invasive procedures. While this application has successfully been studied at the Elettra synchrotron, large-scale synchrotrons are difficult to integrate into clinical practice due to their remote locations and limited available beamtime. Compact synchrotron sources on the other hand could become available in close vicinity to clinical centers, thanks to their compact dimensions.

9. Summary, conclusions and outlook

The Munich Compact Light Source (MuCLS) is the first commercial installation of a compact synchrotron source based on inverse Compton scattering. This work presented, for the first time, an independent analysis of the x-ray beam characteristics of such a source. We analyzed source properties such as flux, source size and source position and their stability over short and longer periods of time. In addition, spectra measured at different energies were discussed [Eggl et al., 2016a]. The presented results show the evolution of the stability and performance of the MuCLS and prove the suitability of the MuCLS for various experiments, such as imaging or even radiation therapy.

With the quasi-monochromatic, tunable x-ray beam, high partial coherence, and high flux density (depending on the location with respect to the interaction point), the MuCLS offers beneficial conditions for a various applications, which would otherwise be limited to large-scale synchrotron sources or which can profit from significant improvements due to the unique characteristics of the CLS x-ray beam.

Several biomedical applications were studied in this work. They can be divided in three major topics: coronary angiography, grating-based multimodal tomography, and mammography.

For **coronary angiography**, we investigated beneficial effects of the possibility to tune the x-ray energy to be directly above the absorption edge of the contrast medium. Quantitative analysis in a simulation study showed that the amount of the applied contrast agent could be reduced by 20-40% while the contrast-to-noise-ratio (CNR) is kept constant [Eggl et al., 2017b]. Especially when this approach is extended to K-edge subtraction (KES) angiography, clinical imaging could benefit from the monochromaticity offered by a compact synchrotron source.

Concerning **grating-based multimodal tomographic imaging**, the monochromatic beam simplifies the quantitative evaluation of absorption coefficient and electron densities, and results show good agreement with literature values. In addition, the high partial coherence allows for a synchrotron-like configuration of the grating interferometer, without the need for a source grating. We presented multimodal tomographic reconstructions of small-animal specimens, proving the enhanced soft-tissue contrast, which even allows to distinguish between white and brown adipose tissue as demonstrated for an infant mouse [Eggl et al., 2015b].

A possible clinical application of compact synchrotrons sources, besides coronary angiography, is **mammography**. A pre-clinical study, which included four freshly dissected breast specimens, however showed the potential of compact synchrotron sources to serve as a second level examination in the case of inconclusive diagnosis after clinical mammography and ultrasound. We found enhanced diagnostic information in monochromatic grating-based differential phase-contrast images, while the applied dose was lower or equal compared to the mean glandular dose in state-of-the-art clinical mammography. Microcalcification clusters could be identified to an equal extent at significantly reduced dose in the monochromatic images. In a quantitative analysis performed with a well-defined sample, a mammographic accreditation phantom, the monochromatic absorption-contrast images more than equaled the clinical one with respect to CNR even at 20% reduced dose. The monochromatic grating-based dark-field images outperformed the clinical image in case of the tumor masses even at 65% reduced dose [Eggl et al., 2017a].

In addition, we investigated grating-based multimodal tomosynthesis with promising results: phase-contrast tomosynthesis slices were able to reveal tumor features that had been obscured by tissue overlap in the projection image. The application in a clinical setting appears challenging as the applied radiation dose was incompatible with radiological guidelines [Eggl et al., 2016b].

Especially the results obtained in the mammography study [Eggl et al., 2017a] appear promising for further investigation. Concerning the experimental setup, a possible next step would be to explore the possibilities of a grating interferometer with higher sensitivity. Increased sensitivity for differential phase and dark-field contrasts can be achieved by increasing the inter-grating distance e.g. from the (currently used) first to the third fractional Talbot distance. As demonstrated quantitatively in chapter 4, this step will require the introduction of a source grating, imposing additional challenges with respect to stability and flux.

In addition, the results obtained for monochromatic absorption-contrast mammography motivate the study of monochromatic absorption-based breast CT, which is already investigated at polychromatic conventional sources [Kalender et al., 2012], but could benefit from dose reduction and increased contrast due to the monochromatic x-ray beam.

Further applications of inverse Compton sources are micro-beam radiation therapy [Burger et al., 2017], high-resolution propagation-based phase-contrast imaging [Gradl et al., 2017], spectroscopy or high-resolution absorption-contrast tomography of stained biomedical samples. Moreover, the imaging of bone diseases with advanced imaging techniques like x-ray vector radiography appears promising, especially if the range of available x-ray energies can be extended in the future, as the monochromatic beam will help to avoid beam hardening artifacts and has beneficial effects on the interferometer visibility and thus image quality. Possible clinical applications are the diagnosis of osteoporosis as previously studied at a conventional x-ray tube source [Eggl et al., 2015a, Baum et al., 2015] or the detection of radiographically occult fractures [Jud et al., 2017].

For the MuCLS, with upgrades already realized – like the laser upgrade – or upgrades expected for the near future – like the installation of an x-ray beam position monitor (XBPM) and implementation of sophisticated digital feedback systems – the performance and stability of the MuCLS is expected to improve even more. The laser upgrade yields an increase in flux by more than a factor of 2, helping to significantly reduce exposure times and possibly improving cavity stability. The implementation of an XBPM-based source feedback will help to provide more stable imaging conditions. Dedicated digital feedback systems, and later even low-emittance storage rings, will facilitate the operation of the electron beam system and allow to store a higher charge in the electron ring, with beneficial effects both on flux and stability.

In the future, imaging and radiation therapy applications at the MuCLS will benefit from further developments of the compact synchrotron source technology. Increased stability and increased flux can be expected in the near future. In the mid-term, an extension of the energy range can be expected, increasing the number of possible applications in the clinical and materials science fields.

Overall, the studied applications show the large range of possibilities provided by compact synchrotron sources. Various clinical, biomedical and materials science applications can profit from the unique properties of these sources, while being compatible with spatial prerequisites at research institutes with close vicinity to small-animal facilities or at medical centers.

A. Appendix

A.1. The DoseCalc python package

Listing A.1: Python package: DoseCalc.

```
"""
dose calculation according to Boone (Medical Physics 29(5), 2002)
taking into account the MuCLS spectrum
@author: Elena Eggl
"""
import os, sys
import numpy as np
import pyE17
import matplotlib.pyplot as plt
import matplotlib.patches as patches
import mammolib as mam
import xraylib
from scipy.interpolate import interp1d

def flux_per_energy_bin(spectrum,flux):
    #Give the measured spectrum and the flux (per pixel or mm2) as measured with the Pilatus
    Spectrum_normalized=spectrum/np.sum(spectrum)
    return flux*Spectrum_normalized

def normalized_glandular_dose(energy,spectrum,total_flux,glandularity,thickness):
    #using exposure, as published by Boone 2002
    #According to Nosratieh (Phys Med Biol, 2015), the equation for calculating the exposure is wrong.
    flux=flux_per_energy_bin(spectrum,total_flux)
    exposure = -5.023290717769674E-06 + 1.810595449064631E-07*(flux**(0.5*np.log(flux)) + (0.00883865845981692 6/(flux**2)))
    norm_gland_dose = np.sum(flux*exposure*DgN_E(energy[flux_0!=0.],glandularity,thickness))/np.sum(flux*exposure)
    return norm_gland_dose

```

```
def normalized_glandular_dose_air_kerma(energy,air_kerma,glandularity,thickness):
    norm_gland_dose_kerma = np.sum(air_kerma*(DgN_E(energy,glandularity,thickness)*0.114))
    return norm_gland_dose_kerma

def DgN_E(energy,glandularity,compressed_thickness):
    #DgN fit equations as provided by Boone (Medical Physics 29(5), 2002)
    #Normalized glandular dose for glandularities of 0%, 50% and 100%, and breast thicknesses between 2cm and 9cm
    if glandularity==0.:
        if compressed_thickness==2.:
            DgN = np.exp(2.352457196063259 + ((164.8557218942891*np.log(energy))/energy**2) + (-707.7221984249481/energy**2))
            return DgN
        elif compressed_thickness==3.:
            DgN = np.exp(2.344321182069257 +(92.84217079678439/energy**1.5) + (-695.2155151287379/energy**2))
            return DgN
        elif compressed_thickness==4.:
            DgN = np.exp(3.369823461573904 + (-0.2201420852007887*np.log(energy)) + (-496.024868341179/energy**2))
            return DgN
        elif compressed_thickness==5.:
            DgN = np.exp(1.905764270203028 + (13.0301906474967*np.log(energy)/energy) + (-228.2929772583756/energy**1.5))
            return DgN
        elif compressed_thickness==6.:
            DgN = np.exp(4.431089727402091 + (-0.4579328540315146*np.log(energy)) + (-254.4810674204082*np.log(energy)/energy**2))
            return DgN
        elif compressed_thickness==7.:
            DgN = np.exp(3.411921621218032 + (-0.1161547260170639*energy**0.5) + (-250.4911807423938*np.log(energy)/energy**2))
            return DgN
        elif compressed_thickness==8.:
            DgN = np.exp(0.06582014537348851 + (33.80799856520028/energy**0.5) + (-134.7596910839139/energy))
```

```
            return DgN
        elif compressed_thickness==9.:
            DgN = np.exp(0.1070181313820536 + (33.27992230956326/energy**0.5) + (-135.5259464673136/energy))
            return DgN
    elif glandularity==0.5:
        if compressed_thickness==2.:
            DgN = np.exp(2.391926241342124 + (144.6136623109463*np.log(energy)/energy**2) + (-698.4084999454397/energy**2))
            return DgN
        elif compressed_thickness==3.:
            DgN = np.exp(2.144310706434551 + (2.756318009819883/energy**0.5) + (-502.7953879238766/energy**2))
            return DgN
        elif compressed_thickness==4.:
            DgN = np.exp(1.716433088631987 + (7.179067281599553/energy**0.5) + (-271.3718672962624*np.log(energy)/energy**2))
            return DgN
        elif compressed_thickness==5.:
            DgN = np.exp(3.456584050727194 + (-0.05152119626934488*(np.log(energy)**2)) + (-252.8149668441184*np.log(energy)/energy**2))
            return DgN
        elif compressed_thickness==6.:
            DgN = np.exp(0.1749925269960791 + (33.68685291846966/energy**0.5) + (-135.572672463385/energy))
            return DgN
        elif compressed_thickness==7.:
            DgN = 0.006479595866252293 + 9.690964247835408*(1 - np.exp(-(energy - 11.48130632636424*np.log(1 - 2**(-1/4.082789296534261)) - 27.77297517314492)/11.48130632636424))**4.082789296534261
            return DgN
        elif compressed_thickness==8.:
            DgN = 0.001514055822116926 + 9.302279326003922*(1 - np.exp(-(energy - 11.70783648570947*np.log(1 - 2**(-1/4.668923725610867)) - 28.67229051531071)/11.70783648570947))**4.668923725610867
            return DgN
```

```
        elif compressed_thickness==9.:
            DgN = -0.003052797289268421 + 8.883576151099609*(1 - np.exp(-(energy - 11.87561125641665*np.log(1 - 2**(-1/5.334505796775558)) - 29.40731202621383)/11.87561125641665))**5.334505796775558
        return DgN
    elif glandularity==1.:
        if compressed_thickness==2.:
            DgN = np.exp(2.437085448514773 + (134.6728278368162*np.log(energy)/energy**2) + (-715.8947925715821/energy**2))
            return DgN
        elif compressed_thickness==3.:
            DgN = np.exp(2.668096499935712 + (-0.0003399770257870519*energy**1.5) + (-502.8638304806826/energy**2))
            return DgN
        elif compressed_thickness==4.:
            DgN = np.exp(3.485845171898047 + (-0.1101976465725361*energy**0.5) + (-248.2673932801099*np.log(energy)/energy**2))
            return DgN
        elif compressed_thickness==5.:
            DgN = np.exp(0.2532306145360197 + (33.76671539417317/energy**0.5) + (-137.6610047762377/energy))
            return DgN
        elif compressed_thickness==6.:
            DgN = 0.002412258040503123 + 10.25838874740784*(1 - np.exp(-(energy - 11.65780112797468*np.log(1 - 2**(-1/4.59809016999979)) - 28.63408329980996)/11.65780112797468))**4.59809016999979
            return DgN
        elif compressed_thickness==7.:
            DgN = -0.003927061630471755 + 9.824895880330871*(1 - np.exp(-(energy - 11.85192102940326*np.log(1 - 2**(-1/5.679097586463206)) - 29.72001651040758)/11.85192102940326))**5.679097586463206
            return DgN
        elif compressed_thickness==8.:
            DgN = -0.0108403641005931 + 9.377528438584098*(1 - np.exp(-(energy - 11.97212002206073*np.log(1 - 2**(-1/7.30469546215369)) - 30.61741955987141)/11.97212002206073))**7.30469546215369
```

```
            return DgN
        elif compressed_thickness==9.:
            DgN = -0.01422564354864223 + 8.943319843739161*(1 - np.exp(-(energy - 12.19532893182253*np.log(1 - 2**(-1/8.65073238056524)) - 31.4182574085736)/12.19532893182253))**8.65073238056524
        return DgN

def interpolate_normalized_glandular_dose(e,air_kerma, glandularity,thickness):
    #Interpolates the values calculated according to Boone, in steps of 0.05 for glandularity, and 0.1 for thickness
    dose_array=np.zeros((3,7))
    for i in range(0,7):
        dose_array[0,i] = normalized_glandular_dose_air_kerma(e,air_kerma,0.,float(i+3))
        dose_array[1,i] = normalized_glandular_dose_air_kerma(e,air_kerma,0.5,float(i+3))
        dose_array[2,i] = normalized_glandular_dose_air_kerma(e,air_kerma,1.0,float(i+3))
    dose_array_interpolated_1=np.zeros((21,7))
    for i in range(0,7):
        g=[0.,0.5,1.0]
        glandularities = np.linspace(0.,1.,21)
        dose_array_interpolated_1[:,i] = np.interp(glandularities,g,dose_array[:,i])
    dose_array_interpolated_2=np.zeros((21,61))
    for i in range(0,21):
        t=[3.,4.,5.,6.,7.,8.,9.]
        thicknesses = np.linspace(3.,9.,61)
        dose_array_interpolated_2[i,:] = np.interp(thicknesses,t,dose_array_interpolated_1[i,:])
    return dose_array_interpolated_2[int(glandularity/0.05), int((thickness-3.0)*10)]

def calculate_air_kerma_measured_spectrum(path,ROI,type):
    #From flux on Pilatus detector in given ROI, calculate the air kerma per energy bin for the CLS spectrum.
    #Takes into account geometric considerations, attenuation in air, and the QDE of the Pilatus detector sensor.
    #Returns two arrays: one for the energy bins and the second for the air kerma per bin
```

```
    if type = 'measured':
        #25 keV Spectrum measured with Amptek at MuCLS in October 2015
        SpecEnergy, Spectrum = np.loadtxt('measured_spectrum.txt', unpack=True, usecols=[0,1])
    elif type = 'simulated':
        #simulated spectrum, provided by Rod Loewen, Lyncean Tech.
        SpecEnergy, Spectrum = np.loadtxt('simulated_spectrum.txt', unpack=True, usecols=[0,1])
        SpecEnergy /= 1000.
    #-----------------------------------------------------
    #mass energy attenuation coefficient in air (from Buhr et al. (2012))
    E_air = np.asarray((8.0, 9.0, 10.0, 12.5, 15.0, 17.47, 20.0, 22.5, 25.01, 27.51, 30.0), dtype=float)
    mu_en_rho_air_0 = np.asarray((9.163, 6.376, 4.595, 2.296, 1.289, 0.796, 0.5223, 0.3598, 0.2592, 0.1933, 0.1493), dtype=float)
    f=interp1d(E_air,mu_en_rho_air_0,kind='cubic')
    mu_en_rho_air = f(SpecEnergy)
    #absorption in air
    mu_air = [xraylib.CS_Total_CP("Air,␣Dry␣(near␣sea␣level)",E) for E in SpecEnergy]
    mu_air = np.asarray(mu_air,dtype=float)
    #photoelectric absorption and total absorption in Silicon
    mu_photo_si = [xraylib.CS_Photo_CP("Si",E) for E in SpecEnergy]
    mu_photo_si = np.asarray(mu_photo_si,dtype=float)
    mu_si = [xraylib.CS_Total_CP("Si",E) for E in SpecEnergy]
    mu_si = np.asarray(mu_si,dtype=float)
    #absoprtion in the PMMA
    mu_pmma = [xraylib.CS_Total_CP("Polymethyl␣Methacralate␣(Lucite,␣Perspex)", E) for E in SpecEnergy]
    mu_pmma = np.asarray(mu_pmma,dtype=float)
    #Constants for calculating transmission
    rho_si = 2.335 #in g/cm^-3
    rho_air = 0.0012 # in g/cm^-3
    rho_pmma = 1.18 #in g/cm^-3
    thickness_pilatus_sensor = 0.1 #cm
    thickness_amptek_sensor = 0.05 #cm
    thickness_air = 80 #cm   between sample and pilatus
    thickness_pmma = 10.0 #cm during Spectrum measurement
    pixel_size = 0.172 #mm
```

```
    distance_IP = 16415 #cm  between IP and pilatus
    total_air = 680 #cm between IP and Pilatus
    transmission_mylar = 0.98 #transmission through 2 mylar
windows
    #-----------------------------------------------------
    if type = ’measured’:
        # Weigh spectrum with Si attenuation and PMMA
absorber during spectrum measurement
        amptek_eff = 1.-np.exp(-mu_photo_si*rho_si*
thickness_amptek_sensor)
        Spectrum_weighted = Spectrum/(amptek_eff*np.exp(-
mu_pmma*rho_pmma*thickness_pmma))*np.exp(-mu_air*rho_air
*380)
    elif type = ’simulated’:
        #calculate spectrum at Pilatus position (correct for
 absorption in Si output mirror, air between IP and
Pilatus, and 4 Mylar windows)
        Spectrum_weighted = Spectrum*np.exp(-mu_si*rho_si
*0.02)*np.exp(-mu_air*rho_air*total_air)*(
transmission_mylar**2)
    Spectrum_weighted = np.ma.fix_invalid(Spectrum_weighted,
copy=True,fill_value=0.)
    Spectrum_weighted /= np.max(Spectrum_weighted)
    #-----------------------------------------------------
    # Calculate photon flux at sample position
    # quantum efficiency of Pilatus (1000um Si)
    trans_si_photo = Spectrum_weighted*np.exp(-mu_photo_si*
rho_si*thickness_pilatus_sensor)
    efficiency_pilatus = 1 - np.sum(trans_si_photo)/np.sum(
Spectrum_weighted)
    # absorption in air between sample and detector
    trans_air = Spectrum_weighted*np.exp(-mu_air*rho_air*
thickness_air)
    transmission_air = np.sum(trans_air)/np.sum(
Spectrum_weighted)
    #-----------------------------------------------------
    #Load pilatus images
    flats_list = os.listdir(path)
    nb_flats = len(flats_list)
    flats = mam.steps_into_array(int(path[-5:]),nb_flats,
path,detector=’pilatus’)
    #plot figure of Pilatus image with ROI
    fig,ax = plt.subplots()
    ax.imshow(flats[0],cmap=’gray’)
    #Indicate the ROI used for the calculation
```

```
    rect = patches.Rectangle((ROI[2],ROI[0]),ROI[3]-ROI[2],ROI[1]-ROI[0],linewidth=1,edgecolor='r',facecolor='none')
    ax.add_patch(rect)
    fig.show()
    #calculate flux
    mean_flux_per_pixel = np.mean(flats[:,ROI[0]:ROI[1],ROI[2]:ROI[3]].reshape((ROI[1]-ROI[0])*(ROI[3]-ROI[2])*nb_flats))
    mean_flux_per_mm2_per_exposure = mean_flux_per_pixel/(pixel_size*pixel_size)
    #correction factor geometry (flux at pilatus vs. sample position)
    correction_geometry = (distance_IP/(distance_IP-thickness_air))**2
    corrected_flux=mean_flux_per_mm2_per_exposure*correction_geometry/(efficiency_pilatus*transmission_air)
    #-----------------------------------------------------
    # Air Kerma taking into account the spectrum
    flux=flux_per_energy_bin(Spectrum_weighted,corrected_flux)
    air_kerma = mu_en_rho_air*SpecEnergy*flux*100*1000*1.602e-16*1000 #correct for cm^2->mm^2, g->kg, keV->J
    return SpecEnergy, air_kerma

def K_and_scinti_counts(filepath,ROI_pilatus):
    #Use a Pilatus flatfield to correlate counts measured with ScintiBloc to Air Kerma.
    #Returns two arrays for air kerma per energy bin: one for energy and one for air kerma
    #Calculate photon flux from flatfield
    pilatus_path = filepath + '/pilatus'
    folderlist = os.listdir(pilatus_path)
    flat_folder = '%s/%s' % (pilatus_path, folderlist[0])
    energy_bins,air_kerma_bins = calculate_air_kerma_simulated_spectrum(flat_folder,ROI_pilatus)
    counter_path = '%s/scintibloc/%s/%s.txt' % (filepath,folderlist[0],folderlist[0])
    scintibloc_counts_list = np.loadtxt(counter_path,unpack=True,usecols=[0])
    scinticounts_pilatus = np.mean(scintibloc_counts_list)
    return energy_bins,air_kerma_bins,scinticounts_pilatus

def calculate_MGD(sample_identifier,basepath,pilatus_identifier,ROI_pilatus,glandularity,breast_thickness):
```

```
    #Calculates the MGD in mGy.
    #The air kerma is calculated from the average flux during a flat field series taken with the pilatus detector (on the same day)
    #This is correlated to the average scintibloc counts during that scan.
    #From the estimated air kerma per scintibloc counts, the MGD is calculated for the sample scan for the average scintibloc counts during the whole scan.
    # Take all Fields into account to calculate average scintibloc counts for whole scan
    counter_path = basepath + '%s/scintibloc' % sample_identifier
    folderlist = os.listdir(counter_path)
    nb_fields = len(folderlist)-2 #2 subtract flat field before and after scan
    scintibloc_counts = ()
    for i in range(nb_fields):
        counter_path_i = counter_path + '/%s/%s.txt' % (folderlist[i+1],folderlist[i+1])
        scintibloc_counts_i = np.loadtxt(counter_path_i,unpack=True,usecols=[0])
        scintibloc_counts = np.append(scintibloc_counts,scintibloc_counts_i)
    try:
        nb_steps=len(scintibloc_counts_i)
    except:
        nb_steps = 1
    average_scintibloc_counts = np.mean(scintibloc_counts)
    # the air kerma is estimated from flux on the pilatus
    energy_bins,air_kerma_bins,scinticounts_pilatus = K_and_scinti_counts('%s%s' % (basepath,pilatus_identifier),ROI_pilatus)
    # assume that scintibloc counts are linear, estimate air kerma for calculated average counts during sample scan
    air_kerma_bins = air_kerma_bins*average_scintibloc_counts/scinticounts_pilatus
    # calculate MGD (interpolation for intermediate thicknesses and glandularities)
    pDgN_kerma = nb_steps*interpolate_normalized_glandular_dose(energy_bins,air_kerma_bins,glandularity,breast_thickness)
    return pDgN_kerma
```

Bibliography

[Achterhold et al., 2013] Achterhold, K., Bech, M., Schleede, S., Potdevin, G., Ruth, R., Loewen, R., and Pfeiffer, F. (2013). Monochromatic computed tomography with a compact laser-driven X-ray source. *Scientific Reports*, 3:1313. (Cited on pages 7, 99, and 112.)

[Adams et al., 1973] Adams, D. F., Fraser, D. B., and Abrams, H. L. (1973). The Complications of Coronary Arteriography. *Circulation*, 48(3):609–618. (Cited on page 101.)

[Als-Nielsen and McMorrow, 2011] Als-Nielsen, J. and McMorrow, D. (2011). *Elements of Modern X-ray Physics*. Wiley, 2nd edition. (Cited on pages 11, 12, 13, 14, 16, 17, 34, 35, and 38.)

[Andersen and Kak, 1984] Andersen, A. H. and Kak, A. C. (1984). Simultaneous algebraic reconstruction technique (SART): a superior implementation of the ART algorithm. *Ultrasonic Imaging*, 6:81–94. (Cited on page 31.)

[Anton et al., 2013] Anton, G., Bayer, F., Beckmann, M. W., Durst, J., Fasching, P. A., Haas, W., Hartmann, A., Michel, T., Pelzer, G., Radicke, M., Rauh, C., Rieger, J., Ritter, A., Schulz-Wendtland, R., Uder, M., Wachter, D. L., Weber, T., Wenkel, E., and Wucherer, L. (2013). Grating-based darkfield imaging of human breast tissue. *Zeitschrift für Medizinische Physik*, 23(3):228–235. (Cited on pages 128 and 148.)

[Arfelli et al., 2000] Arfelli, F., Bonvicini, V., Bravin, A., Cantatore, G., Castelli, E., Dalla Palma, L., Di Michiel, M., Fabrizioli, M., Longo, R., Menk, R. H., Olivo, A., Pani, S., Pontoni, D., Poropat, P., Prest, M., Rashevsky, A., Ratti, M., Rigon, L., Tromba, G., Vacchi, A., Vallazza, E., and Zanconati, F. (2000). Mammography with synchrotron radiation: phase-detection techniques. *Radiology*, 215:286–293. (Cited on pages 18 and 128.)

[Arfelli et al., 1998] Arfelli, F., Bonvicini, V., Bravin, A., Cantatore, G., Castelli, E., Dalla Palma, L., Di Michiel, M., Longo, R., Olivo, A., Pani, S., Pontoni, D., Poropat, P., Prest, M., Rashevsky, A., Tromba, G., and Vacchi, A. (1998). Mammography of a phantom and breast tissue with synchrotron radiation and a linear-array silicon detector. *Radiology*, 208(3):709–715. (Cited on pages 19, 134, and 141.)

[Attwood, 2007] Attwood, D. (2007). *Soft X-Rays and Extreme Ultraviolet Radiation: Principles and Applications*. Cambridge University Press, New York, NY, USA, 1st edition. (Cited on pages 11, 14, 15, 33, 35, 38, 45, and 94.)

[Bacher et al., 1995] Bacher, W., Menz, W., and Mohr, J. (1995). The liga technique and its potential for microsystems - a survey. *IEEE Transactions on Industrial Electronics*, 42(5):431–441. (Cited on page 73.)

[Baum et al., 2015] Baum, T., Eggl, E., Malecki, A., Schaff, F., Potdevin, G., Gordijenko, O., Grande García, E., Burgkart, R., Rummeny, E. J., Noël, P. B., Bauer, J. S., and Pfeiffer, F. (2015). X-ray Dark-Field Vector Radiography: A Novel Technique for Osteoporosis Imaging. *Journal of Computer Assisted Tomography*, 39:286–289. (Cited on page 164.)

[Bech et al., 2009] Bech, M., Bunk, O., David, C., Ruth, R., Rifkin, J., Loewen, R., Feidenhans'l, R., and Pfeiffer, F. (2009). Hard X-ray phase-contrast imaging with the Compact Light Source based on inverse Compton X-rays. *Journal of Synchrotron Radiation*, 16:43–7. (Cited on pages 7, 30, 64, and 111.)

[Bech et al., 2012] Bech, M., Schleede, S., Potdevin, G., Achterhold, K., Bunk, O., Jensen, T. H., Loewen, R., Ruth, R., and Pfeiffer, F. (2012). Experimental validation of image contrast correlation between ultra-small-angle X-ray scattering and grating-based dark-field imaging using a laser-driven compact X-ray source. *Photonics and Lasers in Medicine*, 1(1):47–50. (Cited on page 111.)

[Beister et al., 2012] Beister, M., Kolditz, D., and Kalender, W. A. (2012). Iterative reconstruction methods in X-ray CT. *Physica Medica*, 28(2):94108. (Cited on page 31.)

[Berger et al., 2010] Berger, M. J., Hubbell, J. H., Seltzer, S. M., Chang, J., Coursey, J. S., Sukumar, R., Zucker, D. S., and Olsen, K. (2010). XCOM: Photon Cross Section Database (version 1.5). (Cited on page 136.)

[Bonse and Hart, 1965] Bonse, U. and Hart, M. (1965). An X-ray interferometer. *Applied Physics Letters*, 6(8):155–156. (Cited on page 18.)

[Boone, 1999] Boone, J. M. (1999). Glandular breast dose for monoenergetic and high-energy x-ray beams: Monte Carlo assessment. *Radiology*, 203:23–37. (Cited on page 132.)

[Boone, 2002] Boone, J. M. (2002). Normalized glandular dose (DgN) coefficients for arbitrary X-ray spectra in mammography: computer-fit values of Monte Carlo derived data. *Medical Physics*, 29(5):869–875. (Cited on pages 132, 133, 137, 138, 139, and 152.)

[Braig, 2015] Braig, E. (2015). Advanced X-Ray Modalities Applied to Preclinical Breast Tissue Imaging. Master's thesis, Technical University of Munich. (Cited on page 74.)

[Bravin et al., 2007] Bravin, A., Keyriläinen, J., Fernández, M., Fiedler, S., Nemoz, C., Karjalainen-Lindsberg, M.-L., Tenhunen, M., Virkkunen, P., Leidenius, M., von Smitten, K., Sipilä, P., and Suortti, P. (2007). High-resolution CT by diffraction-enhanced x-ray imaging: mapping of breast tissue samples and comparison with their histopathology. *Physics in Medicine and Biology*, 52(8):2197–2211. (Cited on page 128.)

[Buhr et al., 2012] Buhr, H., Büermann, L., Gerlach, M., Krumrey, M., and Rabus, H. (2012). Measurement of the mass energy-absorption coefficient of air for x-rays in the range from 3 to 60 keV. *Physics in Medicine and Biology*, 57(24):8231–47. (Cited on pages 136 and 152.)

[Burger et al., 2017] Burger, K., Ilicic, K., Dierolf, M., Günther, B., Walsh, D. W. M., Schmid, E., Eggl, E., Achterhold, K., Gleich, B., Combs, S. E., Molls, M., Schmid, T. E., Pfeiffer, F., and Wilkens, J. J. (2017). Spatial dose redistribution using a compact synchrotron x-ray source increases cell survival and cytogenetic integrity. *Submitted*. (Cited on page 164.)

[Buzug, 2008] Buzug, T. M. (2008). *Computed Tomography: From Photon Statistics To Modern Cone-Beam CT*. Springer Verlag. (Cited on page 16.)

[Carstens et al., 2014] Carstens, H., Lilienfein, N., Holzberger, S., Jocher, C., Eidam, T., Limpert, J., Tünnermann, A., Weitenberg, J., Yost, D. C., Alghamdi, A., Alahmed, Z., Azzeer, A., Apolonski, A., Fill, E., Krausz, F., and Pupeza, I. (2014). Megawatt-scale average-power ultrashort pulses in an enhancement cavity. *Optics letters*, 39(9):2595–8. (Cited on page 46.)

[Castelli et al., 2011] Castelli, E., Tonutti, M., Arfelli, F., Longo, R., Quaia, E., Rigon, L., Sanabor, D., Zanconati, F., Dreossi, D., Abrami, A., Quai, E., Bregant, P., Casarin, K., Chenda, V., Menk, R. H., Rokvic, T., Vascotto, A., Tromba, G., and Cova, M. A. (2011). Mammography with synchrotron radiation: first clinical experience with phase-detection technique. *Radiology*, 259(3):684–694. (Cited on pages 128 and 161.)

[Chapman et al., 1997] Chapman, D., Thomlinson, W., Johnston, R. E., Washburn, D., Pisano, E., Gmur, N., Zhong, Z., Menk, R., Arfelli, F., and Sayers, D. (1997). Diffraction enhanced x-ray imaging. *Physics in Medicine and Biology*, 42(11):2015–2025. (Cited on page 18.)

[Cheng et al., 2007] Cheng, A. S. H., Pegg, T. J., Karamitsos, T. D., Searle, N., Jerosch-Herold, M., Choudhury, R. P., Banning, A. P., Neubauer, S., Robson, M. D., and Selvanayagam, J. B. (2007). Cardiovascular Magnetic Resonance Perfusion Imaging at 3-Tesla for the Detection of Coronary Artery Disease. A Comparison With 1.5-Tesla. *Journal of the American College of Cardiology*, 49(25):2440–2449. (Cited on page 101.)

[Chi et al., 2017] Chi, Z., Yan, L., Du, Y., Zhang, Z., Huang, W., Chen, H., and Tang, C. (2017). Recent progress of phase-contrast imaging at Tsinghua Thomson-scattering X-ray source. *Nuclear Instruments and Methods in Physics Research Section B: Beam Interactions with Materials and Atoms*. (Cited on page 39.)

[Cloetens et al., 1999] Cloetens, P., Ludwig, W., Baruchel, J., Guigay, J. P., Pernot-Rejmankova, P., Salome-Pateyron, M., Schlenker, M., Buffiere, J. Y., Maire, E., and Peix, G. (1999). Hard x-ray phase imaging using simple propagation of a coherent synchrotron radiation beam. *Journal of Physics D: Applied Physics*, 32:A145–A151. (Cited on page 19.)

[Cont, 2016] Cont, D. (2016). X-Ray Beam Characterization at the Munich Compact Light Source. Master's thesis, Technical University of Munich. (Cited on pages 74 and 135.)

[Dance et al., 1999] Dance, D., Skinner, C., and Carlsson, G. (1999). Breast dosimetry. *Applied Radiation and Isotopes*, 50(1):185–203. (Cited on pages 132, 134, and 142.)

[Dance, 1990] Dance, D. R. (1990). Monte Carlo calculation of conversion factors for the estimation of mean glandular breast dose. *Physics in Medicine and Biology*, 35(9):1211–1219. (Cited on pages 131, 132, and 150.)

[Dance and Sechopoulos, 2016] Dance, D. R. and Sechopoulos, I. (2016). Dosimetry in x-ray-based breast imaging. *Physics in Medicine and Biology*, 61(19):R271–R304. (Cited on page 131.)

[Dance et al., 2000] Dance, D. R., Skinner, C. L., Young, K. C., Beckett, J. R., and Kotre, C. J. (2000). Additional factors for the estimation of mean glandular breast dose using the UK mammography dosimetry protocol. *Physics in Medicine and Biology*, 45(11):3225–3240. (Cited on pages 131, 132, and 150.)

[David et al., 2007] David, C., Weitkamp, T., Pfeiffer, F., Diaz, A., Bruder, J., Rohbeck, T., Groso, A., Bunk, O., Stampanoni, M., and Cloetens, P. (2007). Hard X-ray phase imaging and tomography using a grating interferometer. *Spectrochimica Acta Part B: Atomic Spectroscopy*, 62(6-7):626–630. (Cited on page 111.)

[Davis et al., 1995] Davis, T. J., Gao, D., Gureyev, T. E., Stevenson, A. W., and Wilkins, S. W. (1995). Phase-contrast imaging of weakly absorbing materials using hard X-rays. *Nature*, 373(6515):595–598. (Cited on page 18.)

[Dierolf et al., 2010] Dierolf, M., Menzel, A., Thibault, P., Schneider, P., Kewish, C. M., Wepf, R., Bunk, O., and Pfeiffer, F. (2010). Ptychographic X-ray computed tomography at the nanoscale. *Nature*, 467(7314):436–439. (Cited on page 5.)

[Dierolf, 2015] Dierolf, M. J. (2015). *Ptychographic X-ray Microscopy and Tomography.* PhD thesis, Technical University of Munich. (Cited on page 28.)

[Dix et al., 1986] Dix, W.-R., Engelke, K., Glüer, C.-C., Graeff, W., Höppner, C., Stellmaschek, K.-H., Wroblewski, T., Bleifeld, W., Höhne, K., and Kupper, W. (1986). NIKOS - A system for non-invasive examination of coronary arteries by means of digital subtraction angiography with synchrotron radiation. *Nuclear Instruments and Methods in Physics Research A: Accelerators, Spectrometers, Detectors and Associated Equipment*, 246:702–712. (Cited on page 9.)

[Donath et al., 2013] Donath, T., Brandstetter, S., Cibik, L., Commichau, S., Hofer, P., Krumrey, M., Lüthi, B., Marggraf, S., Müller, P., Schneebeli, M., Schulze-Briese, C., and Wernecke, J. (2013). Characterization of the PILATUS photon-counting pixel detector for X-ray energies from 1.75 keV to 60 keV. *Journal of Physics: Conference Series*, 425(6):62001. (Cited on pages 138 and 152.)

[Drever et al., 1983] Drever, R. W. P., Hall, J. L., Kowalski, F. V., Hough, J., Ford, G. M., Munley, A. J., and Ward, H. (1983). Laser phase and frequency stabilization using an optical resonator. *Applied Physics B*, 31(2):97–105. (Cited on page 52.)

[Eggl et al., 2016a] Eggl, E., Dierolf, M., Achterhold, K., Jud, C., Günther, B., Braig, E., Gleich, B., and Pfeiffer, F. (2016a). The Munich Compact Light Source: Initial performance measures. *Journal of Synchrotron Radiation*, 23(5):1137–1142. (Cited on pages 6, 39, 49, 54, 79, 80, 81, 97, 108, 152, 161, and 163.)

[Eggl et al., 2017a] Eggl, E., Grandl, S., Sztrókay-Gaul, A., Dierolf, M., Jud, C., Heck, L., Burger, K., Günther, B., Achterhold, K., Mayr, D., Wilkens, J. J., Auweter, S. D., Gleich, B., Hellerhoff, K., Reiser, M. F., Pfeiffer, F., and Herzen, J. (2017a). Dose-compatible grating-based phase-contrast mammography with a compact synchrotron source. *Submitted*. (Cited on pages 127, 149, and 164.)

[Eggl et al., 2015a] Eggl, E., Malecki, A., Schaff, F., Potdevin, G., Noël, P. B., Bauer, J. S., Gordijenko, O., Grande García, E., Burgkart, R., Rummeny, E. J., Baum, T., and Pfeiffer, F. (2015a). Prediction of Vertebral Failure Load by Using X-Ray Vector Radiographic Imaging. *Radiology*, 275(2):553–561. (Cited on pages 19 and 164.)

[Eggl et al., 2017b] Eggl, E., Mechlem, K., Braig, E., Kulpe, S., Dierolf, M., Günther, B., Achterhold, K., Herzen, J., Gleich, B., Rummeny, E., Noël, P. B., Pfeiffer, F., and Münzel, D. (2017b). Mono-energy coronary angiography with a compact synchrotron source. *Scientific Reports*, 7:42211. (Cited on pages 101, 105, 106, 107, 129, 150, 161, and 163.)

[Eggl et al., 2016b] Eggl, E., Schleede, S., Bech, M., Achterhold, K., Grandl, S., Sztrókay, A., Hellerhoff, K., Mayr, D., Loewen, R., Ruth, R. D., Reiser, M. F., and Pfeiffer, F. (2016b). X-ray phase-contrast tomosynthesis of a human ex-vivo breast slice with an inverse compton x-ray source. *European Physics Letters*, 116(6):68003. (Cited on pages 127, 134, 140, 143, 144, 145, 146, 147, and 164.)

[Eggl et al., 2015b] Eggl, E., Schleede, S., Bech, M., Achterhold, K., Loewen, R., Ruth, R. D., and Pfeiffer, F. (2015b). X-ray phase-contrast tomography with a compact laser-driven synchrotron source. *Proceedings of the National Academy of Sciences of the United States of America*, 112(18):5567–5572. (Cited on pages 95, 99, 111, 114, 115, 117, 118, and 163.)

[ESRF, 2017] ESRF (2017). European Synchrotron Radiation Facility. http://www.esrf.eu. (Cited on page 6.)

[Feldkamp et al., 1984] Feldkamp, L. A., Davis, L. C., and Kress, J. W. (1984). Practical cone-beam algorithm. *Journal of the Optical Society of America A*, 1(6):612–619. (Cited on page 29.)

[Figueroa et al., 2008] Figueroa, S. D., Winkelmann, C. T., Miller, W. H., Volkert, W. A., and Hoffman, T. J. (2008). TLD assessment of mouse dosimetry during micro-CT imaging. *Medical Physics*, 35(9):3866–3874. (Cited on page 124.)

[Gennaro et al., 2010] Gennaro, G., Toledano, A., di Maggio, C., Baldan, E., Bezzon, E., La Grassa, M., Pescarini, L., Polico, I., Proietti, A., Toffoli, A., and Muzzio, P. C. (2010). Digital breast tomosynthesis versus digital mammography: a clinical performance study. *European Radiology*, 20(7):1545–1553. (Cited on page 140.)

[Gilbert, 1972] Gilbert, P. (1972). Iterative methods for the three-dimensional reconstruction of an object from projections. *Journal of Theoretical Biology*, 36(1):105–117. (Cited on page 30.)

[Gordon et al., 1970] Gordon, R., Bender, R., and Herman, G. T. (1970). Algebraic Reconstruction Techniques (ART) for three-dimensional electron microscopy and X-ray photography. *Journal of Theoretical Biology*, 29(3):471–481. (Cited on page 30.)

[Gradl et al., 2017] Gradl, R., Dierolf, M., Hehn, L., Günther, B., Yildirim, A. O., Gleich, B., Achterhold, K., Pfeiffer, F., and Morgan, K. S. (2017). Propagation-based Phase-Contrast X-ray Imaging at a Compact Light Source. *Submitted.* (Cited on page 164.)

[Grandl et al., 2015] Grandl, S., Scherer, K., Sztrókay-Gaul, A., Birnbacher, L., Willer, K., Chabior, M., Herzen, J., Mayr, D., Auwerter, S. D., Pfeiffer, F., Bamberg, F., and Hellerhoff, K. (2015). Improved visualization of of breast cancer features in multifocal carcinoma using phase-contrast and dark-field mammography: an ex-vivo study. *European Radiology*, 25(12):3659–3668. (Cited on page 128.)

[Gruberg et al., 2000] Gruberg, L., Mintz, G. S., Mehran, R., Dangas, G., Lansky, A. J., Kent, K. M., Pichard, A. D., Satler, L. F., and Leon, M. B. (2000). The prognostic implications of further renal function deterioration within 48 h of interventional coronary procedures in patients with pre-existent chronic renal insufficiency. *Journal of the American College of Cardiology*, 36(5):1542–1548. (Cited on page 101.)

[Guan et al., 2014] Guan, H., Xu, Q., Garson, A., and Anastasio, M. (2014). Depth resolution properties of in-line X-ray phase-contrast tomosynthesis. *Proceedings of SPIE*, 9033:90330. (Cited on page 140.)

[Günther, 2017] Günther, B. (2017). Private communication. (Cited on page 65.)

[Hahn et al., 2015] Hahn, D., Thibault, P., Fehringer, A., Bech, M., Koehler, T., Pfeiffer, F., and Noël, P. B. (2015). Statistical iterative reconstruction algorithm for X-ray phase-contrast CT. *Scientific Reports*, 5:10452. (Cited on pages 31, 113, 116, and 117.)

[Hammerstein et al., 1979] Hammerstein, G. R., Miller, D. W., White, D. R., Masterson, M. E., Woodard, H. Q., and Laughlin, J. S. (1979). Absorbed Radiation Dose in Mammography. *Radiology*, 130(2):485–491. (Cited on pages 132 and 134.)

[Hammonds et al., 2011] Hammonds, J. C., Price, R. R., Donnelly, E. F., and Pickens, D. R. (2011). Phase-contrast digital tomosynthesis. *Medical Physics*, 2353:3–5. (Cited on page 140.)

[Hauser et al., 2014] Hauser, N., Wang, Z., Kubik-Huch, R. A., Trippel, M., Singer, G., Hohl, M. K., Roessl, E., Koehler, T., van Stevendaal, U., Wieberneit, N., and Stampanoni, M. (2014). A Study on Mastectomy Samples to Evaluate Breast Imaging Quality and Potential Clinical Relevance of Differential Phase Contrast Mammography. *Investigative Radiology*, 49(3):131–137. (Cited on page 128.)

[Hendrick et al., 1999] Hendrick, R., Bassett, L., and Botsco, M. (1999). *Mammography quality control manual.* American College of Radiology, Preston, USA. (Cited on page 160.)

[Hernandez et al., 2015] Hernandez, A. M., Seibert, J. A., and Boone, J. M. (2015). Breast dose in mammography is about 30% lower when realistic heterogeneous glandular distributions are considered. *Medical Physics*, 42(11):6337–6348. (Cited on page 135.)

[Herzen et al., 2009] Herzen, J., Donath, T., Pfeiffer, F., Bunk, O., Padeste, C., Beckmann, F., Schreyer, A., and David, C. (2009). Quantitative phase-contrast tomography of a liquid phantom using a conventional x-ray tube source. *Optics Express*, 17(12):10010. (Cited on pages 112 and 124.)

[Hoshino et al., 2012] Hoshino, M., Uesugi, K., and Yagi, N. (2012). Phase-contrast X-ray microtomography of mouse fetus. *Biology Open*, 1(3):269–74. (Cited on page 111.)

[Huang and Ruth, 1998] Huang, Z. and Ruth, R. D. (1998). Laser-electron storage ring. *Physical Review Letters*, 80(5):976–979. (Cited on pages 6, 48, 111, 128, and 140.)

[Hubbell and Seltzer, 1995] Hubbell, J. H. and Seltzer, S. M. (1995). Tables of X-ray mass attenuation coefficients and mass energy-absorption coefficients 1 keV to 20 MeV for elements Z=1 to 92 and 48 additional substances of dosimetric interest. Technical Report NISTIR-5632, National Institute of Standards and Technology(NIST). (Cited on page 103.)

[IAEA, 2007] IAEA (2007). International Atomic Energy Agency. Dosimetry in Diagnostic Radiology: an International Code of Practice. Technical Report 457, International Atomic Energy Agency, Vienna. (Cited on page 130.)

[Jensen et al., 2010] Jensen, T. H., Bech, M., Bunk, O., Donath, T., David, C., Feidenhans'l, R., and Pfeiffer, F. (2010). Directional x-ray dark-field imaging. *Physics in Medicine and Biology*, 55(12):3317–3323. (Cited on page 25.)

[Jud et al., 2017] Jud, C., Braig, E., Dierolf, M., Eggl, E., Günther, B., Achterhold, K., Gleich, B., Rummeny, E. J., Noël, P. B., Pfeiffer, F., and Muenzel, D. (2017). Trabecular bone anisotropy imaging with a compact laser-undulator synchrotron x-ray source. *Submitted.* (Cited on page 164.)

[Juneman et al., 2012] Juneman, E., Saleh, L., Thai, H., Goldman, S., and Movahed, M. R. (2012). Successful coronary angiography with adequate image acquisition using a combination of gadolinium and a power injector in a patient with severe iodine contrast allergy. *Experimental and Clinical Cardiology*, 17(1):17–19. (Cited on page 101.)

[Kak and Slaney, 1988] Kak, A. C. and Slaney, M. (1988). *Principles of Computerized Tomographic Imaging*. IEEE Service Center, Piscataway, NJ. (Cited on pages 27 and 28.)

[Kalender et al., 2012] Kalender, W. A., Beister, M., Boone, J. M., Kolditz, D., Vollmar, S. V., and Weigel, M. C. C. (2012). High-resolution spiral CT of the breast at very low dose: Concept and feasibility considerations. *European Radiology*, 22(1):1–8. (Cited on pages 140 and 164.)

[Kälsch et al., 2008] Kälsch, H., Kälsch, T., Eggebrecht, H., Konorza, T., Kahlert, P., and Erbel, R. (2008). Gadolinium-based coronary angiography in patients with contraindication for iodinated x-ray contrast medium: A word of caution. *Journal of Interventional Cardiology*, 21(2):167–174. (Cited on pages 101 and 108.)

[Kapteyn et al., 2005] Kapteyn, H. C., Murnane, M. M., and Christov, I. P. (2005). Extreme Nonlinear Optics: Coherent X-rays from Lasers. *Physics Today*, 58(3):39–46. (Cited on page 39.)

[Karlsson et al., 1976] Karlsson, M., Nygren, K., Wickman, G., and Hettinger, G. (1976). Absorbed dose in mammary radiography. *Acta Radiologica: Therapy, Physics, Biology*, 15:252–258. (Cited on page 131.)

[Keyrilainen et al., 2010] Keyrilainen, J., Bravin, A., Fernandez, M., Tenhunen, M., Virkkunen, P., and Suortti, P. (2010). Phase-contrast X-ray imaging of breast. *Acta Radiologica*, 51(8):866–884. (Cited on page 128.)

[Klein and Nishina, 1929] Klein, O. and Nishina, T. (1929). Über die Streuung von Strahlung durch freie Elektronen nach der neuen relativistischen Quantendynamik von Dirac. *Zeitschrift für Physik*, 52(11-12):853–868. (Cited on page 13.)

[Kneip et al., 2010] Kneip, S., McGuffey, C., Martins, J. L., Martins, S. F., Bellei, C., Chvykov, V., Dollar, F., Fonseca, R., Huntington, C., Kalintchenko, G., Maksimchuk, A., Mangles, S. P. D., Matsuoka, T., Nagel, S. R., Palmer, C. A. J., Schreiber, J., Phuoc, K. T., Thomas, A. G. R., Yanovsky, V., Silva, L. O., Krushelnick, K., and Najmudin, Z. (2010). Bright spatially coherent synchrotron X-rays from a table-top source. *Nature Physics*, 6(12):980–983. (Cited on pages 6 and 39.)

[Koehler et al., 2015] Koehler, T., Daerr, H., Martens, G., Kuhn, N., Löscher, S., van Stevendaal, U., and Roessl, E. (2015). Slit-scanning differential x-ray phase-contrast mammography: Proof-of-concept experimental studies. *Medical Physics*, 42(4):1959–1965. (Cited on page 128.)

[Kulpe, 2017] Kulpe, S. (2017). Digital Subtraction Angiography and K-Edge Imaging at the Munich Compact Light Source. Master's thesis, Technical University of Munich. (Cited on page 109.)

[Kuroda et al., 2011] Kuroda, R., Toyokawa, H., Yasumoto, M., Ikeura-Sekiguchi, H., Koike, M., Yamada, K., Yanagida, T., Nakajyo, T., Sakai, F., and Mori, K. (2011).

Quasi-monochromatic hard X-ray source via laser Compton scattering and its application. *Nuclear Instruments and Methods in Physics Research, Section A: Accelerators, Spectrometers, Detectors and Associated Equipment*, 637(1 SUPPL.):S183–S186. (Cited on pages 39, 108, and 161.)

[Lee et al., 2013] Lee, J. E., Wang, C., Xu, S., Cho, Y. W., Wang, L., Feng, X., Baldridge, A., Sartorelli, V., Zhuang, L., Peng, W., and Ge, K. (2013). H3K4 mono- and di-methyltransferase MLL4 is required for enhancer activation during cell differentiation. *eLIFE*, 2:e01503. (Cited on pages 118 and 119.)

[Li et al., 2014] Li, K., Ge, Y., Garrett, J., Bevins, N., Zambelli, J., and Chen, G.-H. (2014). Grating-based phase contrast tomosynthesis imaging: Proof-of-concept experimental studies. *Medical Physics*, 41:011903. (Cited on pages 140 and 149.)

[Lindfors et al., 2008] Lindfors, K. K., Boone, J. M., Nelson, T. R., Yang, K., Kwan, A. L. C., and Miller, D. F. (2008). Dedicated breast CT: Initial clinical experience. *Radiology*, 246(3):725–733. (Cited on page 140.)

[Loewen, 2003] Loewen, R. (2003). A Compact Light Source: Design and Technical Feasibility Study of a Laser-Electron Storage Ring X-ray Source. *SLAC-Report 632, Stanford University, USA.* (Cited on pages 39, 49, and 98.)

[Loewen, 2017] Loewen, R. (2017). Private communication. (Cited on pages 45, 46, 96, 98, 99, and 135.)

[Loewen et al., 2015] Loewen, R., Ruth, R. D., Gifford, M., and Weigenand, A. (2015). MuCLS Training. (Cited on pages 39 and 49.)

[Longo et al., 2014] Longo, R., Tonutti, M., Rigon, L., Arfelli, F., Dreossi, D., Quai, E., Zanconati, F., Castelli, E., Tromba, G., and Cova, M. A. (2014). Clinical study in phase- contrast mammography: image-quality analysis. *Philosophical Transactions of the Royal Society A: Mathematical, Physical and Engineering Sciences*, 372(2010):20130025. (Cited on pages 9, 128, 149, and 161.)

[Lyncean, 2017] Lyncean (2017). Lyncean Technologies Inc., USA. http://www.lynceantech.com. (Cited on page 39.)

[Maksimenko et al., 2007] Maksimenko, A., Yuasa, T., Ando, M., and Hashimoto, E. (2007). Refraction-based tomosynthesis: proof of the concept. *Applied Physics Letters*, 91:234108. (Cited on page 140.)

[Malecki et al., 2013] Malecki, A., Potdevin, G., Biernath, T., Eggl, E., Grande García, E., Baum, T., Noël, P. B., Bauer, J. S., and Pfeiffer, F. (2013). Coherent superposition in grating-based directional dark-field imaging. *PloS ONE*, 8(4):e61268. (Cited on page 25.)

[Malecki et al., 2014] Malecki, A., Potdevin, G., Biernath, T., Eggl, E., Willer, K., Lasser, T., Maisenbacher, J., Gibmeier, J., Wanner, A., and Pfeiffer, F. (2014). X-ray tensor tomography. *Europhysics Letters*, 105(3):38002. (Cited on page 25.)

[McCullough et al., 1997] McCullough, P. A., Wolyn, R., Rocher, L. L., Levin, R. N., and O'Neill, W. W. (1997). Acute Renal Failure After Coronary Intervention: Incidence, Risk Factors, And Relationship to Mortality. *The American Journal of Medicine*, 103(4):368–375. (Cited on page 101.)

[Michel et al., 2013] Michel, T., Rieger, J., Anton, G., Bayer, F., Beckmann, M. W., Durst, J., Fasching, P. A., Haas, W., Hartmann, A., Pelzer, G., Radicke, M., Rauh, C., Ritter, A., Sievers, P., Schulz-Wendtland, R., Uder, M., Wachter, D. L., Weber, T., Wenkel, E., and Zang, A. (2013). On a dark-field signal generated by micrometer-sized calcifications in phase-contrast mammography. *Physics in Medicine and Biology*, 58:2713–32. (Cited on page 128.)

[Modregger et al., 2007] Modregger, P., Lübbert, D., Schäfer, P., and Köhler, R. (2007). Spatial resolution in Bragg-magnified X-ray images as determined by Fourier analysis. *physica status solidi (a)*, 204(8):2746–2752. (Cited on pages 153 and 157.)

[Mohr et al., 2012] Mohr, J., Grund, T., Kunka, D., Kenntner, J., Leuthold, J., Meiser, J., Schulz, J., and Walter, M. (2012). High aspect ratio gratings for x-ray phase contrast imaging. *AIP Conference Proceedings*, 1466:41–50. (Cited on page 73.)

[Momose, 1995] Momose, A. (1995). Demonstration of phase-contrast x-ray computed tomography using an x-ray interferometer. *Nuclear Instruments and Methods In Physics Research A: Accelerators, Spectrometers, Detectors and Associated Equipment*, 352:622–628. (Cited on page 18.)

[Momose et al., 2003] Momose, A., Kawamoto, S., Koyama, I., Hamaishi, Y., Takai, K., and Suzuki, Y. (2003). Demonstration of x-ray Talbot interferometry. *Japanese Journal of Applied Physics, Part 2: Letters*, 42(7 B). (Cited on pages 19 and 111.)

[Momose et al., 2009] Momose, A., Yashiro, W., Maikusa, H., and Takeda, Y. (2009). High-speed X-ray phase imaging and X-ray phase tomography with Talbot interferometer and white synchrotron radiation. *Optics Express*, 17(15):12540–12545. (Cited on page 111.)

[Momose et al., 2006] Momose, A., Yashiro, W., Takeda, Y., Suzuki, Y., and Hattori, T. (2006). Phase tomography by X-ray talbot interferometry for biological imaging. *Japanese Journal of Applied Physics, Part 1: Regular Papers and Short Notes and Review Papers*, 45(6 A):5254–5262. (Cited on page 111.)

[NCRP, 2004] NCRP (2004). A guide to mammography and other breast imaging procedures. Technical report, National Council on Radiation Protection and Measurements, Bethesda, MD, USA. (Cited on page 149.)

[Nielsen et al., 2012] Nielsen, M. S., Lauridsen, T., Thomsen, M., Jensen, T. H., Bech, M., Christensen, L. B., Olsen, E. V., Hviid, M., Feidenhans'l, R., and Pfeiffer, F. (2012). X-ray tomography using the full complex index of refraction. *Physics in Medicine and Biology*, 57(19):5971–9. (Cited on page 124.)

[Nosratieh et al., 2015] Nosratieh, A., Hernandez, A., Shen, S. Z., Yaffe, M. J., Seibert, J. A., and Boone, J. M. (2015). Mean glandular dose coefficients (DgN) for x-ray spectra used in contemporary breast imaging systems. *Physics in Medicine and Biology*, 60(18):7179–90. (Cited on pages 133, 134, and 152.)

[Oliva et al., 2009] Oliva, P., Golosio, B., Stumbo, S., Bravin, A., and Tomassini, P. (2009). Compact x-ray sources for mammographic applications: Monte Carlo simulations of image quality. *Medical Physics*, 36(11):5149–5161. (Cited on pages 128 and 129.)

[Olivo et al., 2001] Olivo, A., Arfelli, F., Cantatore, G., Longo, R., Menk, R. H., Pani, S., Prest, M., Poropat, P., Rigon, L., Tromba, G., Vallazza, E., and Castelli, E. (2001). An innovative digital imaging set-up allowing a low-dose approach to phase contrast applications in the medical field. *Medical Physics*, 28(8):1610. (Cited on page 19.)

[Olivo and Castelli, 2014] Olivo, A. and Castelli, E. (2014). X-ray phase contrast imaging: From synchrotrons to conventional sources. *Rivista del Nuovo Cimento della Societa Italiano di Fisica*, 37(9):467–508. (Cited on pages 128 and 161.)

[Olivo et al., 2013] Olivo, A., Gkoumas, S., Endrizzi, M., Hagen, C., Szafraniec, M., Diemoz, P., Munro, P., Ignatyev, K., Johnson, B., Horrocks, J., Vinnicombe, S., Jones, J., and Speller, R. (2013). Low-dose phase contrast mammography with conventional x-ray sources. *Medical Physics*, 40:090701. (Cited on pages 19 and 128.)

[Olivo and Speller, 2007] Olivo, A. and Speller, R. (2007). A coded-aperture technique allowing x-ray phase contrast imaging with conventional sources. *Applied Physics Letters*, 91(7):49–51. (Cited on page 19.)

[Ose et al., 2005] Ose, K., Doue, T., Zen, K., Hadase, M., Sawada, T., Azuma, A., and Matsubara, H. (2005). 'Gadolinium' as an alternative to iodinated contrast media for X-ray angiography in patients with severe allergy. *Circulation Journal : Official Journal of the Japanese Circulation Society*, 69(4):507–509. (Cited on page 101.)

[Paganin et al., 2002] Paganin, D., Mayo, S. C., Gureyev, T. E., Miller, P. R., and Wilkins, S. W. (2002). Simultaneous phase and amplitude extraction from a single defocused image of a homogeneous object. *Journal of Microscopy*, 206(1):33–40. (Cited on page 19.)

[Parodi and Ferreira, 2000] Parodi, J. C. and Ferreira, L. M. (2000). Gadolinium-based contrast: An alternative contrast agent for endovascular interventions. *Annals of Vascular Surgery*, 14(5):480–483. (Cited on page 101.)

[Perry et al., 2008] Perry, N., Broeders, M., de Wolf, C., Törnberg, S., Holland, R., and von Karsa, L. (2008). European guidelines for quality assurance in breast cancer screening and diagnosis. *Annals of Oncology: Official Journal of the European Society for Medical Oncology (ESMO)*, 19(4):614–622. (Cited on page 127.)

[Pfeiffer et al., 2008] Pfeiffer, F., Bech, M., Bunk, O., Kraft, P., Eikenberry, E. F., Brönnimann, C., Grünzweig, C., and David, C. (2008). Hard-X-ray dark-field imaging using a grating interferometer. *Nature Materials*, 7(2):134–7. (Cited on pages 19, 24, 26, 111, 128, and 152.)

[Pfeiffer et al., 2007a] Pfeiffer, F., Bunk, O., David, C., Bech, M., Le Duc, G., Bravin, A., and Cloetens, P. (2007a). High-resolution brain tumor visualization using three-dimensional x-ray phase contrast tomography. *Physics in Medicine and Biology*, 52(23):6923–30. (Cited on page 7.)

[Pfeiffer et al., 2007b] Pfeiffer, F., Kottler, C., Bunk, O., and David, C. (2007b). Hard X-Ray Phase Tomography with Low-Brilliance Sources. *Physical Review Letters*, 98(10):108105. (Cited on pages 7, 30, 111, and 141.)

[Pfeiffer et al., 2006] Pfeiffer, F., Weitkamp, T., Bunk, O., and David, C. (2006). Phase retrieval and differential phase-contrast imaging with low-brilliance X-ray sources. *Nature Physics*, 2(4):258–261. (Cited on pages 7, 19, 24, 26, 111, 113, 116, 128, and 141.)

[Pinzer et al., 2012] Pinzer, B. R., Cacquevel, M., Modregger, P., McDonald, S. A., Bensadoun, J. C., Thuering, T., Aebischer, P., and Stampanoni, M. (2012). Imaging brain amyloid deposition using grating-based differential phase contrast tomography. *NeuroImage*, 61(4):1336–1346. (Cited on page 111.)

[Pogorelsky, 2016] Pogorelsky, I. (2016). Progress and Prospects of a Compton X-ray Source Driven by a High-Power CO2 Laser. In Rocca, J., Menoni, C., and Marconi, M., editors, *X-Ray Lasers 2014*, pages 127–132. Springer. (Cited on page 39.)

[Popmintchev et al., 2012] Popmintchev, T., Chen, M.-C., Popmintchev, D., Arpin, P., Brown, S., Católicauskas, S., Andriukaitis, G., Balčiunas, T., Mücke, O. D., Pugzlys, A., Baltuška, A., Shim, B., Schrauth, S. E., Gaeta, A., Hernández-García, C., Plaja, L., Becker, A., Jaron-Becker, A., Murnane, M. M., and Kapteyn, H. C. (2012). Bright Coherent Ultrahigh Harmonics in the keV X-ray Regime from Mid-Infrared Femtosecond Lasers. *Science*, 336(6086):1287–1291. (Cited on pages 6 and 39.)

[PTW Freiburg, 2016] PTW Freiburg (2016). Ionizing Radiation Detectors: Including Codes of Practice. Technical report, PTW Freiburg. (Cited on page 139.)

[Ramachandran and Lakshminarayanan, 1971] Ramachandran, G. N. and Lakshminarayanan, A. V. (1971). Three-Dimensional Reconstruction from Radiographs and Electron Micrographs: Application of Convolutions Instead of Fourier Transforms. *Proceedings of the National Academy of Sciences of the United States of America*, 68(9):2236–2240. (Cited on page 29.)

[Reusch, 2016] Reusch, T. (2016). Private communication. (Cited on pages 36 and 103.)

[Robinson and Harder, 2009] Robinson, I. and Harder, R. (2009). Coherent X-ray diffraction imaging of strain at the nanoscale. *Nature Materials*, 8(4):291–298. (Cited on page 5.)

[Rodt et al., 2011] Rodt, T., Luepke, M., Boehm, C., von Falck, C., Stamm, G., Borlak, J., Seifert, H., and Galanski, M. (2011). Phantom and cadaver measurements of dose and dose distribution in micro-CT of the chest in mice. *Acta Radiologica*, 52(1):75–80. (Cited on page 124.)

[Roessl et al., 2014] Roessl, E., Daerr, H., Koehler, T., Martens, G., and van Stevendaal, U. (2014). Clinical boundary conditions for grating-based differential phase-contrast mammography. *Philosophical Transactions of the Royal Society A: Mathematical, Physical and Engineering Sciences*, 372(2010):1–7. (Cited on page 128.)

[Rubenstein et al., 1986] Rubenstein, E., Hofstadter, R., Zeman, H. D., Thompson, A. C., Otis, J. N., Brown, G. S., Giacomini, J. C., Gordon, H. J., Kernoff, R. S., and Harrison, D. C. (1986). Transvenous coronary angiography in humans using synchrotron radiation. *Proceedings of the National Academy of Sciences of the United States of America*, 83(24):9724–9728. (Cited on page 9.)

[Sayin et al., 2007] Sayin, T., Turhan, S., Akyürek, O., and Kilickap, M. (2007). Gadolinium: nonionic contrast media (1:1) coronary angiography in patients with impaired renal function. *Angiology*, 58(5):561–4. (Cited on page 101.)

[Scherer et al., 2014] Scherer, K., Birnbacher, L., Chabior, M., Herzen, J., Mayr, D., Grandl, S., Sztrókay-Gaul, A., Hellerhoff, K., Bamberg, F., and Pfeiffer, F. (2014). Bi-directional x-ray phase-contrast mammography. *PLoS ONE*, 9(5):e93502. (Cited on page 128.)

[Scherer et al., 2016] Scherer, K., Braig, E., Ehn, S., Schock, J., Wolf, J., Birnbacher, L., Chabior, M., Herzen, J., Mayr, D., Grandl, S., Sztrókay-Gaul, A., Hellerhoff, K., and Pfeiffer, F. (2016). Improved Diagnostics by Assessing the Micromorphology of Breast Calcifications via X-Ray Dark-Field Radiography. *Scientific Reports*, 6:36991. (Cited on page 128.)

[Scherer et al., 2015] Scherer, K., Willer, K., Gromann, L., Birnbacher, L., Braig, E., Grandl, S., Sztrókay-Gaul, A., Herzen, J., Mayr, D., Hellerhoff, K., and Pfeiffer, F. (2015). Toward Clinically Compatible Phase-Contrast Mammography. *PloS ONE*, 10(6):e0130776. (Cited on pages 19 and 128.)

[Scherer, 2015] Scherer, K. H. (2015). *Grating-Based X-Ray Mammography.* PhD thesis, Technical University of Munich. (Cited on page 75.)

[Schleede, 2013] Schleede, S. (2013). *X-ray Phase-Contrast Imaging at a Compact Laser-Driven Synchrotron Source.* PhD thesis, Technical University of Munich. (Cited on page 43.)

[Schleede et al., 2012] Schleede, S., Bech, M., Achterhold, K., Potdevin, G., Gifford, M., Loewen, R., Limborg, C., Ruth, R., and Pfeiffer, F. (2012). Multimodal hard X-ray imaging of a mammography phantom at a compact synchrotron light source. *Journal of Synchrotron Radiation*, 19:525–529. (Cited on pages 111 and 134.)

[Schleede et al., 2014] Schleede, S., Bech, M., Grandl, S., Sztrókay, A., Herzen, J., Mayr, D., Stockmar, M., Potdevin, G., Zanette, I., Rack, A., Weitkamp, T., and Pfeiffer, F. (2014). X-ray phase-contrast tomosynthesis for improved breast tissue discrimination. *European Journal of Radiology*, 83:531–536. (Cited on pages 140, 141, 143, 145, 146, 147, and 148.)

[Schleede et al., 2013] Schleede, S., Meinel, F. G., Bech, M., Herzen, J., Achterhold, K., Potdevin, G., Malecki, A., Adam-Neumair, S., Thieme, S. F., Bamberg, F., Nikolaou, K., Bohla, A., Yildirim, A. O., Loewen, R., Gifford, M., Ruth, R., Eickelberg, O., Reiser, M., and Pfeiffer, F. (2013). Emphysema diagnosis using X-ray dark-field imaging at a laser-driven compact synchrotron light source. *Proceedings of the National Academy of Sciences of the United States of America*, 109(44):17880–17885. (Cited on pages 19, 111, and 129.)

[Schlegel and Bille, 1999] Schlegel, W. and Bille, J. (1999). *Medizinische Physik 2*. Springer Verlag. (Cited on pages 129, 130, 131, 139, and 152.)

[Schoonjans et al., 2011] Schoonjans, T., Brunetti, A., Golosio, B., Sanchez del Rio, M., Sol, V. A., Ferrero, C., and Vincze, L. (2011). The xraylib library for x-ray-matter interaction cross sections: new developments and applications. *Spectrochimica Acta Part B: Atomic Spectroscopy*, 66(11-12):776–784. (Cited on pages 17 and 136.)

[Schröter et al., 2017] Schröter, T. J., Koch, F. J., Meyer, P., Kunka, D., Meiser, J., Willer, K., Gromann, L., De Marco, F., Herzen, J., Noël, P., Yaroshenko, A., Hofmann, A., Pfeiffer, F., and Mohr, J. (2017). Large field-of-view tiled grating structures for x-ray phase-contrast imaging. *Review of Scientific Instruments*, 88(2):029901. (Cited on page 161.)

[Sechopoulos, 2013] Sechopoulos, I. (2013). A review of breast tomosynthesis. Part II. Image reconstruction, processing and analysis, and advanced applications. *Medical Physics*, 40(1):014302. (Cited on page 149.)

[Siegel et al., 2012] Siegel, R., Naishadham, D., and Jemal, A. (2012). Cancer statistics 2012. *CA: A Cancer Journal for Clinicians*, 62(1):10–29. (Cited on page 127.)

[Siegman, 1986] Siegman, A. E. (1986). *Lasers*. University Science Books, Mill Valley, California, USA. (Cited on page 53.)

[Snigirev et al., 1995] Snigirev, A., Snigireva, I., Kohn, V., Kuznetsov, S., and Schelokov, I. (1995). On the possibilities of x-ray phase contrast microimaging by coherent high-energy synchrotron radiation. *Review of Scientific Instruments*, 66(12):5486–5492. (Cited on page 19.)

[Spinosa et al., 1999] Spinosa, D. J., Matsumoto, A. H., Hagspiel, K. D., Angle, F. J., and Hartwell, G. D. (1999). Gadolinium-Based Contrast Agents in Angiography and Interventional Radiology. *AJR. American Journal of Roentgenology*, 173(November):1403–1409. (Cited on page 101.)

[Stampanoni et al., 2011] Stampanoni, M., Wang, Z., Thuring, T., David, C., Roessl, E., Trippel, M., Kubik-Huch, R. A., Singer, G., Hohl, M. K., and Hauser, N. (2011). The first analysis and clinical evaluation of native breast tissue using differential phase-contrast mammography. *Investigative Radiology*, 46(12):801–806. (Cited on pages 128 and 148.)

[Stepanek, 1998] Stepanek, J. (1998). Parametric study of laser Compton-backscattering from free relativistic electrons. *Nuclear Instruments and Methods in Physics Research, Section A: Accelerators, Spectrometers, Detectors and Associated Equipment*, 412(1):174–182. (Cited on page 41.)

[Stout et al., 2014] Stout, N. K., Lee, S. J., Schechter, C. B., Kerlikowske, K., Alagoz, O., Berry, D., Buist, D. S. M., Cevik, M., Chisholm, G., De Koning, H. J., Huang, H., Hubbard, R. A., Miglioretti, D. L., Munsell, M. F., Trentham-Dietz, A., Van Ravesteyn, N. T., Tosteson, A. N. A., and Mandelblatt, J. S. (2014). Benefits, harms, and costs for breast cancer screening after US implementation of digital mammography. *Journal of the National Cancer Institute*, 106(6):dju092. (Cited on page 127.)

[Sun and Wu, 2011] Sun, C. and Wu, Y. K. (2011). Theoretical and simulation studies of characteristics of a Compton light source. *Physical Review Special Topics - Accelerators and Beams*, 14(4):1–17. (Cited on pages 42 and 43.)

[Sun et al., 2013] Sun, J., Liu, P., Irvine, S., Pinzer, B., Stampanoni, M., and Xu, L. X. (2013). Preliminary comparison of grating-based and in-line phase contrast X-ray imaging with synchrotron radiation for mouse kidney at TOMCAT. *Journal of Instrumentation*, 8:C06003. (Cited on page 111.)

[Sunaguchi et al., 2011] Sunaguchi, N., Yuasa, T., Huo, Q., Ichihara, S., and Ando, M. (2011). Refraction-contrast tomosynthesis imaging using dark-field imaging optics. *Applied Physics Letters*, 99(10):97–100. (Cited on page 140.)

[Tajima and Dawson, 1979] Tajima, T. and Dawson, J. M. (1979). Laser Electron Accelerator. *Physical Review Letters*, 43(4):267–270. (Cited on page 39.)

[Takeda et al., 1994] Takeda, T., Itai, Y., Yoshioka, H., Umetani, K., Ueda, K., and Akisada, M. (1994). Synchrotron radiation cine K-edge energy subtraction coronary arteriography using an iodine filter method. *Medical and Biological Engineering and Computing*, 32(July):462–468. (Cited on page 109.)

[Talbot, 1836] Talbot, W. H. F. (1836). Facts relating to optical science. *The London and Edinburgh Philosophical Magazine and Journal of Science Series III*, 9(51). (Cited on page 20.)

[Tang et al., 2009] Tang, C., Huang, W., Li, R., Du, Y., Yan, L., Shi, J., Du, Q., Yu, P., Chen, H., Du, T., Cheng, C., and Lin, Y. (2009). Tsinghua Thomson scattering X-ray source. *Nuclear Instruments and Methods in Physics Research, Section A: Accelerators, Spectrometers, Detectors and Associated Equipment*, 608(1 SUPPL.):70–74. (Cited on page 39.)

[Tapfer et al., 2012] Tapfer, A., Bech, M., Velroyen, A., Meiser, J., Mohr, J., Walter, M., Schulz, J., Pauwels, B., Bruyndonckx, P., Liu, X., Sasov, A., and Pfeiffer, F. (2012). Experimental results from a preclinical X-ray phase-contrast CT scanner. *Proceedings of the National Academy of Sciences of the United States of America*, 109(39):15691–6. (Cited on pages 112, 113, and 124.)

[Tapfer et al., 2013] Tapfer, A., Braren, R., Bech, M., Willner, M., Zanette, I., Weitkamp, T., Trajkovic-Arsic, M., Siveke, J. T., Settles, M., Aichler, M., Walch, A., and Pfeiffer, F. (2013). X-ray phase-contrast CT of a pancreatic ductal adenocarcinoma mouse model. *PLoS ONE*, 8(3):e58439. (Cited on pages 7 and 141.)

[Tavakol et al., 2012] Tavakol, M., Ashraf, S., and Brener, S. J. (2012). Risks and complications of coronary angiography: a comprehensive review. *Global Journal of Health Science*, 4(1):65–93. (Cited on page 101.)

[Teerstra et al., 2010] Teerstra, H., Loo, C. E., van den Bosch, M. A., van Tinteren, H., Rutgers, E. J., Muller, S. H., and Gilhuijs, K. G. (2010). Breast tomosynthesis in clinical practice: initial results. *European Radiology*, 20(1):16–24. (Cited on page 140.)

[Tegze and Faigel, 1996] Tegze, M. and Faigel, G. (1996). X-ray holography with atomic resolution. *Nature*, 380(6569):49–51. (Cited on page 5.)

[Thibault et al., 2008] Thibault, P., Dierolf, M., Menzel, A., Bunk, O., David, C., and Pfeiffer, F. (2008). High-Resolution Scanning X-ray Diffraction Microscopy. *Science*, 321(5887):379–382. (Cited on page 5.)

[Thomsen et al., 2004] Thomsen, H. S., Morcos, S. K., and van der Molen, A. J. (2004). Effect of iodinated contrast media on thyroid function in adults. *European Radiology*, 14(5):902907. (Cited on page 101.)

[Tucker et al., 1991] Tucker, D. M., Barnes, G. T., and Chakraborty, D. P. (1991). Semiempirical model for generating tungsten target x-ray spectra. *Medical Physics*, 18(2):211–218. (Cited on page 103.)

[Umetani et al., 1993] Umetani, K., Ueda, K., Takeda, T., and Itai, Y. (1993). Iodine filter imaging system for subtraction angiography using synchrotron radiation. *Nuclear Instruments and Methods In Physics Research A: Accelerators, Spectrometers, Detectors and Associated Equipment*, 335:569–579. (Cited on page 109.)

[Variola, 2011] Variola, A. (2011). The ThomX Project. In *2nd International Particle Accelerator Conference (IPAC'11)*, pages 1903–1905. (Cited on pages 39, 108, and 161.)

[Variola et al., 2014] Variola, A., Haissinski, J., Loulergue, A., and Zomer, F. (2014). ThomX Technical Design Report. Technical report. (Cited on page 39.)

[Venkatesan et al., 2009] Venkatesan, A., Chu, P., Kerlikowske, K., Sickles, E. A., and Smith-Bindman, R. (2009). Positive predictive value of specific mammographic findings according to reader and patient variables. *Radiology*, 250(3):648–57. (Cited on page 127.)

[Viermetz, 2015] Viermetz, M. (2015). Optimization of a High Sensitivity X-Ray Phase-Contrast Computed Tomography Setup. Master's thesis, Technical University of Munich. (Cited on page 76.)

[Warren et al., 2012] Warren, L. M., Mackenzie, A., Cooke, J., Given-Wilson, R. M., Wallis, M. G., Chakraborty, D. P., Dance, D. R., Bosmans, H., and Young, K. C. (2012). Effect of image quality on calcification detection in digital mammography. *Medical Physics*, 39(6):3202–3213. (Cited on page 131.)

[Weitkamp et al., 2006] Weitkamp, T., David, C., Kottler, C., Bunk, O., and Pfeiffer, F. (2006). Tomography with grating interferometers at low-brilliance sources. *Proceedings of SPIE*, 6318. (Cited on pages 20, 21, 68, 69, and 70.)

[Weitkamp et al., 2005] Weitkamp, T., Diaz, A., David, C., Pfeiffer, F., Stampanoni, M., Cloetens, P., and Ziegler, E. (2005). X-ray phase imaging with a grating interferometer. *Optics Express*, 13(16):6296–6304. (Cited on pages 5, 19, 68, and 111.)

[Wenz et al., 2015] Wenz, J., Schleede, S., Khrennikov, K., Bech, M., Thibault, P., Heigoldt, M., Pfeiffer, F., and Karsch, S. (2015). Quantitative X-ray phase-contrast microtomography from a compact laser-driven betatron source. *Nature Communications*, 6:7568. (Cited on page 39.)

[Wiedemann, 2007] Wiedemann, H. (2007). *Particle accelerator physics: Third edition*. Springer. (Cited on page 49.)

[Willmott, 2011] Willmott, P. (2011). *An Introduction to Synchrotron Radiation: Techniques and Applications*. John Wiley and Sons, Ltd. (Cited on pages 12, 13, 33, 34, 37, 38, and 39.)

[Wu et al., 1991] Wu, X., Barnes, G. T., and Tucker, D. M. (1991). Spectral dependence of glandular tissue dose in screen-film mammography. *Radiology*, 179(1):143–148. (Cited on pages 131, 132, and 133.)

[Wu et al., 1994] Wu, X., Gingold, E. L., Barnes, G. T., and Tucker, D. M. (1994). Normalized average glandular dose in molybdenum target-rhodium filter and rhodium target-rhodium filter mammography. *Radiology*, 193(1):83–89. (Cited on pages 131 and 132.)

[Yaffe and Mainprize, 2011] Yaffe, M. J. and Mainprize, J. G. (2011). Risk of radiation-induced breast cancer from mammographic screening. *Radiology*, 258(1):98–105. (Cited on page 131.)

[Yaroshenko et al., 2015] Yaroshenko, A., Hellbach, K., Yildirim, A. A. Ö., Conlon, T. M. T., Fernandez, I. E. I., Bech, M., Velroyen, A., Meinel, F. G., Auweter, S., Reiser, M. F., Eickelberg, O., and Pfeiffer, F. (2015). Improved In vivo Assessment of Pulmonary Fibrosis in Mice using X-Ray Dark-Field Radiography. *Scientific Reports*, 5:17492. (Cited on page 19.)

[Yashiro et al., 2010] Yashiro, W., Terui, Y., Kawabata, K., and Momose, A. (2010). On the origin of visibility contrast in x-ray Talbot interferometry. *Optics Express*, 18(16):16890–16901. (Cited on page 7.)

[Young and Oduko, 2016] Young, K. C. and Oduko, J. M. (2016). Radiation doses received in the united kingdom breast screening programme in 2010 to 2012. *The British Journal of Radiology*, 89(1058):20150831. (Cited on page 131.)

[Zanette et al., 2012] Zanette, I., Bech, M., Rack, A., Le Duc, G., Tafforeau, P., David, C., Mohr, J., Pfeiffer, F., and Weitkamp, T. (2012). Trimodal low-dose X-ray tomography. *Proceedings of the National Academy of Sciences of the United States of America*, 109(26):10199–10204. (Cited on page 111.)

[Zhou et al., 2014] Zhou, H., Wan, B., Grubisic, I., Kaplan, T., and Tjian, R. (2014). TAF7L modulates brown adipose tissue formation. *eLIFE*, 3:e02811. (Cited on pages 118 and 119.)

[Zhu et al., 2010] Zhu, P., Zhang, K., Wang, Z., Liu, Y., Liu, X., Wu, Z., McDonald, S. A., Marone, F., and Stampanoni, M. (2010). Low-dose, simple, and fast grating-based X-ray phase-contrast imaging. *Proceedings of the National Academy of Sciences of the United States of America*, 107(31):13576–13581. (Cited on page 111.)

List of Figures

List of Tables

Acronyms

ABI analyzer-based imaging. 19, 20

AP anteroposterior. 155, 157

ART algebraic reconstruction technique. 31

BPM beam position monitor. 51

BW bandwidth. 33, 36, 37, 96, 97

CAD computer-aided design. 48

CC cranio-caudal. 131, 150, 157

CCD charge-coupled device. 57, 65, 116

CDI coherent diffraction imaging. 35

CEO carrier-envelope offset. 57, 65

cevAC-Mx clinical ex-vivo absorption-contrast mammography. 150, 154, 155, 157, 158, 160

CI crystal interferometer. 19

civAC-Mx clinical in-vivo absorption-contrast mammography. 154, 155, 157

CLS Compact Light Source. 38–42, 64, 66, 98, 99, 103, 105, 108, 111, 112, 114, 124, 129, 134, 140, 142, 145, 148, 163

CMOS complementary metal-oxide-semiconductor. 75

CNR contrast-to-noise-ratio. 102, 104, 105, 108, 141, 145, 147, 148, 153, 158, 160–164

CT Computed Tomography. 5, 7, 9, 11, 27, 28, 31, 66, 103, 111, 112, 114, 116, 119, 135, 140

DCIS ductal carcinoma in situ. 155, 157

DEI diffraction-enhanced imaging. 19

EI edge-illumination. 20

ESRF European Synchrotron Radiation Facility. 6, 36, 37, 145, 148

FBP Filtered Backprojection. 27, 30, 31, 113, 116, 117, 124, 141, 149

FOV field of view. 7, 65

FSR free spectral range. 53

FWHM full width at half maximum. 69, 70, 79, 96, 97

G0 source grating. 26

G1 phase grating. 20–24, 69, 73, 140, 149, 152

G2 analyzer grating. 22, 73, 140, 152

GBI grating-based imaging. 19, 20

GUI graphical user interface. 57

H&E hematoxylin-eosin. 118, 119, 141, 146, 155

HV high voltage. 131

HVL half value layer. 132

IAEA International Atomic Energy Agency. 130

IP interaction point. 48, 52, 96

IPS integrated protection system. 54

IR infrared. 42, 51, 66

kerma kinetic energy released per unit mass. 129–132, 136, 137, 139, 153

KES K-edge subtraction. 9, 66, 107, 109, 163

LAD left anterior descending. 107

LCX left circumflex. 107

lp linepairs. 157

mAC-Mx monochromatic absorption-contrast mammography. 157, 158, 160

mgbAC-Mx monochromatic grating-based absorption-contrast mammography. 155, 157, 160

mgbDFC-Mx monochromatic grating-based dark-field-contrast mammography. 155, 157, 160

mgbDPC-Mx monochromatic grating-based differential phase-contrast mammography. 155, 157, 160

MGD mean glandular dose. 131, 132, 137, 138, 141, 150, 152–154

MLO mediolateral-oblique. 131, 150

MRI Magnetic Resonance Imaging. 101, 150, 154, 155

MSB Munich School of Bioengineering. 54, 85

MuCLS Munich Compact Light Source. 6, 7, 9, 10, 33, 34, 37, 39, 41, 43, 46–48, 54, 55, 59, 61, 64, 65, 67, 68, 70, 73–76, 79, 82, 85, 88–90, 92, 93, 95, 96, 98–109, 111, 112, 119, 124, 127, 129, 132–139, 149, 150, 152, 153, 158, 160–164

Nd:YAG neodymium-doped yttrium aluminium garnet. 52

Nd:YLF neodymium-doped yttrium lithium fluoride. 51

NIST National Institut of Standards and Technology. 103

NLCG non-linear conjugate gradients. 120

NST no special type. 155, 157

OSSPS ordered subsets separable paraboloidal surrogate. 120

PBI propagation-based imaging. 20

PCI phase-contrast imaging. 19, 35

PDH Pound-Drever-Hall. 52, 57

PMMA polymethyl methacrylate. 96, 98, 99, 135, 139

PSF point-spread function. 74, 82

QE quantum efficiency. 136

RF radio-frequency. 51, 52, 54, 55, 62, 99

rms root mean square. 82

ROI region of interest. 76, 81, 82, 103–105, 113, 135, 141, 145, 147, 153

SART simultaneous algebraic reconstruction technique. 31

SIR statistical iterative reconstruction. 31, 120

SIRT simultaneous iterative reconstruction technique. 31

SLAC Stanford Linear Accelerator. 100

SYRMEP Synchrotron Radiation for Medical Physics. 128, 129, 161

TUM	Technische Universität München. 54
UPS	uninterruptible power supply. 54
UV	ultraviolet. 51
XBPM	x-ray beam position monitor. 65, 164
XGI	x-ray grating interferometer. 20, 68, 73, 119

Publications and scientific presentations

All publications and scientific presentations related to this thesis are listed chronologically here. The list of publications is categorized into first-authored and co-authored publications.

First-authored publications (peer-reviewed)

Elena Eggl, Susanne Grandl, Anikó Sztrókay-Gaul, Martin Dierolf, Christoph Jud, Lisa Heck, Karin Burger, Benedikt Günther, Klaus Achterhold, Doris Mayr, Jan J. Wilkens, Sigrid D. Auweter, Bernhard Gleich, Karin Hellerhoff, Maximilian F. Reiser, Franz Pfeiffer and Julia Herzen. Dose-compatible grating-based phase-contrast mammography with a compact synchrotron source. *Submitted* (2017).

Elena Eggl, Korbinian Mechlem, Eva Braig, Stephanie Kulpe, Martin Dierolf, Benedikt Günther, Klaus Achterhold, Julia Herzen, Bernhard Gleich, Ernst J. Rummeny, Peter B. Noël, Franz Pfeiffer, and Daniela Muenzel. Mono-energy coronary angiography with a compact sychrotron source. *Scientific Reports* **7**:42211 (2017).

Elena Eggl, Simone Schleede, Martin Bech, Klaus Achterhold, Susanne Grandl, Anikó Sztrókay, Karin Hellerhoff, Doris Mayr, Roderick Loewen, Ronald D. Ruth, Maximilian F. Reiser, and Franz Pfeiffer. X-ray phase-contrast tomosynthesis of a human ex-vivo breast slice with an inverse Compton x-ray source. *European Physics Letters* **116**(6):68003 (2016).

Elena Eggl, Martin Dierolf, Klaus Achterhold, Christoph Jud, Benedikt Günther, Eva Braig, Bernhard Gleich, and Franz Pfeiffer. The Munich Compact Light Source: initial performance measures. *Journal of Synchrotron Radiation* **23**:1137-1142 (2016).

Elena Eggl, Andreas Malecki, Florian Schaff, Guillaume Potdevin, Peter B. Noël, Jan S. Bauer, Olga Gordijenko, Eduardo Grande García, Rainer Burgkart, Ernst J. Rummeny, Thomas Baum, and Franz Pfeiffer. Prediction of Vertebral Failure Load by Using X-Ray Vector Radiographic Imaging. *Radiology* **275**:53-561 (2015).

Elena Eggl, Simone Schleede, Martin Bech, Klaus Achterhold, Roderick Loewen, Ronald D. Ruth, and Franz Pfeiffer. X-ray phase-contrast tomography with a compact laser-driven synchrotron source. *Proceedings of the National Academy of Sciences of the United States of America* **112** (18):5567-5572 (2015).

Co-authored publications (peer-reviewed)

Christoph Jud, Eva Braig, Martin Dierolf, Elena Eggl, Benedikt Günther, Klaus Achterhold, Bernhard Gleich, Ernst J. Rummeny, Peter B. Noël, Franz Pfeiffer and Daniela Muenzel. Trabecular bone anisotropy imaging with a compact laser-undulator synchrotron x-ray source. *Submitted* (2017).

Karin Burger, Katarina Ilicic, Martin Dierolf, Benedikt Günther, Dietrich W. Walsh, Ernst Schmid, Elena Eggl, Klaus Achterhold, Bernhard Gleich, Stephanie E. Combs, Michael Molls, Thomas E. Schmid, Franz Pfeiffer and Jan J. Wilkens. Spatial dose redistribution using a compact synchrotron X-ray source increases cell survival and cytogenetic integrity. *Submitted* (2017).

Matthias Wieczorek, Jürgen Frikel, Jakob Vogel, Elena Eggl, Felix Kopp, Peter B. Noël, Franz Pfeiffer, Laurent Demaret, and Tobias Lasser. X-ray computed tomography using curvelet sparse regularization. *Medical Physics* **42**:1555-1565 (2015).

Thomas Baum, Elena Eggl, Andreas Malecki, Florian Schaff, Guillaume Potdevin, Olga Gordijenko, Eduardo Grande García, Rainer Burgkart, Ernst J. Rummeny, Peter B. Noël, Jan S. Bauer, and Franz Pfeiffer. X-ray Dark-Field Vector Radiography – A Novel Technique for Osteoporosis Imaging. *Journal of Computer Assisted Tomography* **39**:286-289 (2015).

Andreas Malecki, Elena Eggl, Florian Schaff, Guillaume Potdevin, Thomas Baum, Eduardo Grande García, Jan S. Bauer, and Franz Pfeiffer. Correlation of X-Ray Dark-Field Radiography to Mechanical Sample Properties. *Microscopy and Microanalysis* **20**(5):1528-1533 (2014).

Andreas Malecki, Guillaume Potdevin, Thomas Biernath, Elena Eggl, Konstantin Willer, Tobias Lasser, Jens Maisenbacher, Jens Gibmeier, Alexander Wanner, and Franz Pfeiffer. X-ray tensor tomography. *European Physics Letters* **105**:38002 (2014).

Florian Schaff, Andreas Malecki, Guillaume Potdevin, Elena Eggl, Peter B. Noël, Thomas Baum, Eduardo Grande García, Jan S. Bauer, and Franz Pfeiffer. Correlation of X-Ray Vector Radiography to Bone Micro-Architecture. *Scientific Reports* **4**:3695 (2014).

Hans Liebl, Thomas Baum, Dimitrios C. Karampinos, Janina Patsch, Andreas Malecki, Florian Schaff, Elena Eggl, Ernst J. Rummeny, Franz Pfeiffer, and Jan S. Bauer. Emerging Research on Bone Health Using High-Resolution CT and MRI. *Current Radiology Reports* **2**(1) (2013).

Andreas Malecki, Guillaume Potdevin, Thomas Biernath, Elena Eggl, Eduardo Grande García, Thomas Baum, Peter B. Noël, Jan S. Bauer, and Franz Pfeiffer. Coherent Superposition in Grating-Based Directional Dark-Field Imaging. *PLoS ONE* **8**(4):e61268 (2013).

Conference proceedings

Elena Eggl, Korbinian Mechlem, Eva Braig, Stephanie Kulpe, Martin Dierolf, Benedikt Günther, Klaus Achterhold, Julia Herzen, Bernhard Gleich, Ernst J. Rummeny, Peter B. Noël, Franz Pfeiffer, and Daniela Muenzel. Mono-Energy Coronary Angiography with a Compact Light Source, *Proceedings of SPIE* **101324L** (2017).

Christoph Jud, Eva Braig, Martin Dierolf, Elena Eggl, Benedikt Günther, Klaus Achterhold, Bernhard Gleich, Ernst J. Rummeny, Peter B. Noël, Franz Pfeiffer and Daniela Muenzel. X-ray vector radiography of a human hand. *Proceedings of SPIE* **101325U** (2017).

Poster presentations and awards

Elena Eggl, Korbinian Mechlem, Eva Braig, Stephanie Kulpe, Martin Dierolf, Benedikt Günther, Klaus Achterhold, Julia Herzen, Bernhard Gleich, Ernst J. Rummeny, Peter B. Noël, Franz Pfeiffer, and Daniela Muenzel. Mono-Energy Coronary Angiography with a Compact Light Source, *SPIE Medical Imaging, Orlando, FL, U.S.A., February 2017.*

Awards: SPIE Poster Award, Honorable Mention, SPIE Medical Imaging, February 2017 for “Mono-Energy Coronary Angiography with a Compact Light Source”

Acknowledgments

A lot of people contributed to this thesis in one way or another and I would like to express my gratitude to any one of them. I would like to thank...

- Franz Pfeiffer for offering me this interesting PhD topic and providing me with the opportunity to work and do research at one of the most fascinating x-ray sources that exist worldwide. Thank you for your academic support and for involving me in the MuCLS acceptance testing process, from which I learned many things. Thank you for providing the financial support to carry out experiments with the best possible equipment and to share our findings at various conferences.
- Franz Pfeiffer, Klaus Achterhold, Martin Dierolf and Bernhard Gleich for their efforts to make it possible for the MuCLS to be installed at the IMETUM/MSB facility. I would like to acknowledge the funding through MAP/CALA for making the MuCLS to be installed at TUM.
- the MuCLS operators, especially Martin Dierolf and Benedikt Günther, for their efforts that the MuCLS would reliably produce x-rays during experiments.
- in addition, Martin Dierolf for his support with getting the experimental setups and detectors up and running, and for the endless hours he spent troubleshooting MuCLS and IT issues, and for always having an open ear for my questions.
- the staff of Lyncean Technologies Inc. for their technical support – remotely and during on-site service visits – with the MuCLS and for training us to operate the MuCLS.
- Rod Loewen for patiently answering all of my questions on the MuCLS and for his detailed explanations about MuCLS operation.
- our collaborators, without whom the experiments would not have been possible:
  - Susanne Grandl, Anikó Sztrókay, Doris Mayr, Sigrid Auweter, Karin Hellerhoff and Maximilian F. Reiser from the Klinikum Großhadern for the collaboration on the mammography project;
  - Daniela Muenzel, Peter B. Noël, Thomas Baum, Jan S. Bauer and Ernst J. Rummeny from the radiology department of the Klinikum for working together on the angiography and osteoporosis projects;
  - Danays Kunka, Pascal Meyer and Jürgen Mohr from the Karlsruhe Nano Micro Facility of KIT for providing us with excellent gratings.
- Simone Schleede for her preceding work at the CLS and for passing her projects on to me in such a well-organized way, which made it much easier for me to get the “old ”results into publications.

- Christoph Jud for working together on the grating interferometer at the MuCLS and Kai Scherer for fruitful discussion that helped us with optimizing the interferometer setup.
- Korbinian Mechlem for providing the code for the angiography simulations.
- Lorenz Hehn for his help with the reconstructions of the bird samples.
- Julia Herzen for her support with the mammography project.
- everyone who proofread my manuscripts or my thesis (in no particular order and not exclusively): Martin Dierolf, Klaus Achterhold, Christoph Jud, Benedikt Günther, Irene Zanette, Karin Burger, Daniela Muenzel, Rod Loewen, Susanne Grandl, and Franz Pfeiffer.
- Nelly de Leiris for her help with all organizational issues and when ordering stuff.
- the E17 group, especially my fellow IMETUM Großraumbüro mates, for providing such a great working atmosphere and sharing many nice evenings at the E17 Stammtisch, the Sudelfeld seminar days or at conferences, which I have been able to enjoy for the last 6.5 years ever since I started working in the group as a Bachelor student.
- Karin Burger for many many afternoon visits to the coffee shop at Maschinenbau and for the great times we spent sharing rooms during seminar days or conferences.
- of course also the coffee shop at Maschinenbau for their great Cappuccino which saved many of my afternoons.
- Karin Burger, Regine Gradl and Simone Ferstl for organizing my PhD defense which was a very nice event.
- Martin Dierolf, Klaus Achterhold and Franz Pfeiffer for making the acceptance test visits so enjoyable even though the frustration was high at some points. It still makes me smile when I think back to Good Morning Breakfasts, burritos, burgers, and giant pizzas and cake slices.
- last but not least, my family: My parents, for their support throughout my whole studies. Klaus, for encouraging me and for being such a wonderful Dad, taking care of Hannah while I was at “Unitä ”. Hannah and also baby-in-belly for providing me with the motivation to finish my thesis in time and for keeping my life in perspective.